



**Some pages of this thesis may have been removed for copyright restrictions.**

If you have discovered material in Aston Research Explorer which is unlawful e.g. breaches copyright, (either yours or that of a third party) or any other law, including but not limited to those relating to patent, trademark, confidentiality, data protection, obscenity, defamation, libel, then please read our [Takedown policy](#) and contact the service immediately ([openaccess@aston.ac.uk](mailto:openaccess@aston.ac.uk))

# SYNTHESIS AND IN-SITU ATR STUDIES OF NANOSTRUCTURED TITANIA PHOTOCATALYSTS FOR THE DEGRADATION OF AQUEOUS ORGANIC POLLUTANTS

Brunella Barbero

Doctor of Philosophy

Aston University

European Bioenergy Research Institute  
(EBRI)

September 2017

©Brunella Barbero, 2017

Brunella Barbero asserts her moral right to be identified as the author of this thesis. This copy of the thesis has been supplied on condition that anyone who consults it is understood to recognise that its copyright belongs to its author and that no quotation from the thesis and no information derived from it may be published without appropriate permission or acknowledgement.

Aston University  
EBRI (European Bioenergy Research Institute)

# SYNTHESIS AND IN-SITU ATR STUDIES OF NANOSTRUCTURED TITANIA PHOTOCATALYSTS FOR THE DEGRADATION OF AQUEOUS ORGANIC POLLUTANTS

Brunella Barbero  
Doctor of Philosophy

September 2017

## Summary

Water is a crucial resource for life but only 3% of global water is fresh and this small amount is ever decreasing due to unwise human activities. Traditional biological treatments require further chemical processing to degrade recalcitrant molecules and the processing of such chemicals necessitates large energy inputs and high costs. Heterogeneous photocatalysis provides a green solution as it harnesses the power of natural sunlight.

Titanium dioxide is one of the most extensively studied photocatalysts due to low toxicity, chemical stability and low cost. Despite the powerful intrinsic oxidating ability drawbacks in commercial titania materials stem from the relatively high band gap energy and low surface areas. To overcome this, in this research the aim is to synthesis a novel material which can maximize the efficiency of photocatalytic processes applied to depollution of waste water. Mesoporous silicas with tunable parameters were employed as supports for the anchoring of surface titania species, in order to improve the available active surface area of the catalyst. Highly sophisticated analytical techniques common to the fields of surface science and heterogeneous catalysis were applied to fully characterize the prepared materials and determine structure-function relationships.

Screening for the photocatalytic activity of the synthesized materials was performed in jacketed quartz batch reactor irradiated by a UV-vis light source against common organic dyes. Photoactivity of the prepared materials was investigated alongside commercially available titania catalysts to act as benchmarks.

In heterogeneous catalysis it is vital to study the interaction between the surface of the catalyst and the probe molecules, including adsorptive and desorptive processes occurring at the solid-liquid interface. ATR-IR spectroscopy was used to investigate this aspect of our reaction, allowing for real time monitoring of reaction kinetics with the use of an innovative flow cell chamber, fit with a quartz window allowing for *in-situ* UV irradiation.

## Keywords

Advanced oxidation processes (AOPs), waste water treatment, hierarchical photocatalyst, UV-vis light, ATR-IR spectroscopy.

To Placido and Rossana.  
For me, ocean and lighthouse.

*In memory of my amazing dad, Placido Barbero (14 June 1952 - 2 December 2017).*

*I miss him every day but I'm glad that he saw this process through to its completion, offering the support to make it possible in every sense.*

*Thanks for teaching me that the key of life is the enjoyment.*



## Acknowledgments

To start I would like to thank my supervisors, Professor Karen Wilson and Professor Adam F. Lee for giving me the opportunity to conduct this research. Thanks to all the SMAC group members with whom I have worked, in particular Dr. Mark Isaacs, for his valuable comments, suggestions, unlimited help and support throughout this work. Individually I would like also to thank Dr Chris Parlett, for his contribution collecting the STEM images shown in this thesis and his great advice every time that I need. I am also truly thankful to Dr Amin Osatiashtiani and Dr Kumar Santosh for their great kindness and for accepting the task of review this work and for helping in the final thesis writing.

Special thank goes to Dr. Donna Chen which, at the start of this PhD in Cardiff University, with her guidance, her ever-glowing enthusiasm and interest in my work has been a great motivation over the last 4 years.

Thanks also go to the FP7 scholarship for funding my PhD and to all the members of the PCATDES project for the precious contributions to my research work, the fun time and the amazing trips. In this respect I would like to mention Dr. Raul Quesada-Cabrera, Dr. Carlos Sotelo Vazquez and Emir Bouleghlimat and thank them for their spirit, help and friendship.

I would also like to thank Prof Javier Marugán of King Juan Carlos University in Madrid who gave me the opportunity to carry out some part of my research in his group; I learned a lot from his positive and motivating attitude. The time in Madrid may have been brief but it was a lot of fun.

The biggest thank goes to my family and friends. Without their support and encouragement I am sure I would not be where I am today.

Thanks to Serena, who motivated me to do always my best (and more!) without saying a word or pressuring me but just being the amazing strong woman she is. (Love ya sista!)

Mum and Dad, this work is dedicated to you. Thanks for always encouraging me to do whatever I want and for being understanding even during the darkest times. You are absolutely amazing! Last but no least I have to mention the great guy who stops me from running away when I was already halfway to the end of my PhD but completely fed up with everything. Gracias David, you have the invaluable power to make me laugh about the worst and the most complicated situations (sometimes with the additional support of a glass of vermouth!). Believing in me and forcing me out of my comfort zone every day, you gave me the confidence and the positive vibes to push through to the end. Tu energía me encanta! Tqm, words cannot express.

## List of contents

<b>List of Abbreviations</b>	<b>10</b>
<b>List of Equations, Figures and Tables</b>	<b>11</b>
<b>Chapter 1 Introduction</b>	<b>23</b>
1.1 Water: the environmental problem	24
1.1.1 Water pollution	25
1.1.2 Water quality	25
1.2 Water treatments	26
1.2.1 Conventional water treatments	26
1.2.1.1 Disadvantages of conventional wastewater treatment plants	27
1.2.2 Advanced oxidation processes (AOPs)	28
1.3 Heterogeneous photocatalysis	30
1.3.1 Definition and mechanism	30
1.3.2 Catalysts for photocatalytic reactions	33
1.4 Titanium dioxide as photocatalyst	34
1.4.1 Trends to improve TiO <sub>2</sub> activity	36
1.5 Photocatalyst supports	37
1.5.1 Porous structure	37
1.5.2 Mesoporous SBA-15	39
1.5.3 Hierarchical SBA-15	42
1.6 Probe molecules	42
1.6.1 Organic dyes	42
1.6.2 Carboxylic acids	44
1.7 Thesis aim	46
1.8 References	47
<b>Chapter 2 Experimental</b>	<b>57</b>
2.1 Catalyst preparation	58

2.1.1	SBA-15 synthesis.....	58
2.1.2	Polystyrene (PS) beads synthesis.....	58
2.1.3	TLCT macro-mesoporous SBA-15 synthesis.....	59
2.1.4	Titania grafting .....	59
2.2	Catalyst characterization.....	60
2.2.1	Inductively coupled plasma mass spectroscopy .....	60
2.2.2	X-ray fluorescence spectroscopy (XRF) .....	60
2.2.3	Powder X-ray diffraction (XRD).....	61
2.2.4	X-ray photoemission spectroscopy (XPS).....	64
2.2.5	Nitrogen porosimetry .....	65
2.2.6	Diffuse reflectance UV–vis spectroscopy (DRUVS).....	68
2.2.7	Vibrational spectroscopy.....	71
2.2.7.1	Raman spectroscopy.....	72
2.2.7.2	Diffuse reflectance infra-red Fourier transform spectroscopy .....	73
2.2.7.3	Attenuated total reflectance spectroscopy (ATR- IR).....	74
2.2.8	Microscopy analysis.....	76
2.2.8.1	Scanning electron microscopy (SEM).....	76
2.2.8.2	Scanning transmission electron microscopy (STEM).....	78
2.3	Photocatalytic reaction .....	79
2.3.1	Photo-oxidation of methyl orange.....	79
2.3.2	Photo-oxidation of propanoic acid.....	81
2.3.2.1	ATR flow reactor.....	81
2.3.2.2	Thin film preparation .....	83
2.3.2.3	Batch reactor.....	84
2.4	Reference.....	87
<b>Chapter 3 Titania grafted on mesoporous silica support.....</b>		<b>90</b>
3.1	Introduction.....	91
3.2	Results and discussion.....	93

3.2.1	Characterisation of parent SBA-15.....	93
3.2.2	Characterisation of TiO <sub>2</sub> -SBA-15 catalysts.....	93
3.2.2.1	Effect of mesopore size.....	97
3.2.2.1.1	Elemental analysis.....	98
3.2.2.1.2	X-ray photoelectron spectroscopy.....	98
3.2.2.1.3	Nitrogen porosimetry.....	101
3.2.2.1.4	X-ray diffraction.....	103
3.2.2.1.5	Raman analysis .....	106
3.2.2.1.6	ATR IR spectroscopy.....	106
3.2.2.1.7	Scanning transmission electron microscopy.....	107
3.2.2.1.8	UV-vis diffuse reflectance spectroscopy .....	109
3.2.2.2	Effect of titania loading .....	112
3.2.2.2.1	Elemental analysis.....	113
3.2.2.2.2	X-ray photoelectron spectroscopy.....	113
3.2.2.2.3	Nitrogen porosimetry.....	116
3.2.2.2.4	X-ray diffraction.....	118
3.2.2.2.5	Raman analysis .....	120
3.2.2.2.6	ATR IR Spectroscopy.....	121
3.2.2.2.7	Scanning transmission electron microscopy.....	122
3.2.2.2.8	UV-vis diffuse reflectance spectroscopy .....	123
3.2.3	Photocatalytic degradation of methyl orange.....	126
3.2.3.1	Effect of mesopore size .....	126
3.2.3.2	Effect of titania loading .....	129
3.3	Conclusions.....	132
3.4	References.....	133
<b>Chapter 4 Titania grafted on hierarchical silica support.....</b>		<b>138</b>
4.1	Introduction.....	139
4.2	Results and discussion.....	139

4.2.1	Characterisation of polystyrene beads .....	141
4.2.2	Characterisation of the TLCT-MM-SBA-15 supports.....	142
4.2.3	Characterisation of TiO <sub>2</sub> grafted supports.....	147
4.2.3.1	Effect of macropores size.....	147
4.2.3.1.1	Elemental analysis.....	147
4.2.3.1.2	X-ray photoelectron spectroscopy.....	147
4.2.3.1.3	Nitrogen porosimetry.....	149
4.2.3.1.4	Powder X-ray diffraction.....	151
4.2.3.1.5	ATR IR spectroscopy.....	151
4.2.3.1.6	Scanning transmission electron microscopy.....	152
4.2.3.1.7	UV-vis diffuse reflectance spectroscopy .....	154
4.2.3.2	Effect of titania loading .....	156
4.2.3.2.1	Elemental analysis.....	157
4.2.3.2.2	X-ray photoelectron spectroscopy.....	157
4.2.3.2.3	Nitrogen porosimetry.....	159
4.2.3.2.4	Powder X-ray diffraction.....	159
4.2.3.2.5	ATR IR spectroscopy.....	162
4.2.3.2.6	Scanning transmission electron microscopy.....	162
4.2.3.2.7	UV-vis diffuse reflectance spectroscopy .....	163
4.2.4	Photocatalytic degradation of methyl orange (MO).....	166
4.2.4.1	Effect of macropores size.....	166
4.2.4.2	Effect of titania loading .....	169
4.3	Conclusions.....	172
4.4	References.....	173
 <b>Chapter 5 In situ ATR IR study of liquid phase propanoic acid photooxidation on TiO<sub>2</sub> nanoparticles.....</b>		<b>178</b>
5.1	Introduction.....	179
5.2	Results and Discussions.....	179

5.2.1	Adsorption kinetics and equilibrium studies.....	182
5.2.2	Optimization of working conditions.....	182
5.2.2.1	Effect of propanoic acid concentration.....	184
5.2.2.2	Effect of flow rate.....	187
5.2.2.3	Effect of temperature.....	188
5.2.3	Adsorption and photodecomposition of propanoic acid on P-25, anatase and rutile TiO <sub>2</sub> nanoparticles.....	191
5.2.3.1	Propanoic acid adsorption.....	192
5.2.3.2	Propanoic acid photodecomposition.....	201
5.2.3.2.1	Batch reactor.....	202
5.2.3.2.2	ATR flow reactor.....	203
5.2.3.2.3	Proposed reaction mechanism.....	209
5.2.4	Effect of pH.....	211
5.3	Conclusions.....	216
5.4	References.....	219
<b>Chapter 6 Conclusions and future work.....</b>		<b>222</b>
6.1.	Conclusions.....	223
6.2.	Future work.....	225
<b>Appendix.....</b>		<b>226</b>

## **List of Abbreviations**

**AOP** - Advanced oxidation processes

**ATR** - Attenuated total reflectance

**BET** - Brunauer, Emmett and Teller Adsorption Theory

**BJH** - Barrett, Joyner and Halenda Pore Size Distribution Method

**DRIFTS** - Diffuse reflection infrared Fourier transform spectroscopy

**EDX** - Energy dispersive X-ray analysis

**HOMO** - Highest occupied molecular orbital

**ICP-OES** - Inductively coupled plasma optical emission spectroscopy

**LUMO** - Lowest unoccupied molecular orbital

**SEM** - Scanning electron microscopy

**STEM** - Scanning transmission electron microscope

**UV-vis** - Ultraviolet visible light

**XPS** - X-ray photoelectron spectroscopy

**XRF** - X-ray fluorescence

**XRD** - Powder X-ray diffraction

# List of Equations, Figures and Tables

## Chapter 1 Introduction

<b>Figure 1.1</b> World map of the freshwater stress in 1995 and 2025.[2]	24
<b>Figure 1.2</b> Scheme of a conventional waste water treatment	27
<b>Table 1.1</b> Oxidation potential of some water treatment oxidants.[12]	28
<b>Figure 1.3</b> Advanced oxidation processes (AOPs) classification.	29
<b>Figure 1.4</b> Relative disposition of the CB (LUMO) and VB (HOMO) for an insulator, a semiconductor and a conductor.	31
<b>Equation 1.1</b> Charge carrier generation	31
<b>Figure 1.5</b> Main processes occurring on a semiconductor particle: (a) photogeneration of electron/hole pair; (b) carriers migration at the surface of the semiconductor; (c-d) electron/ hole recombination in the bulk and at surface, respectively.	32
<b>Equation 1.2</b> Direct hole attack to the adsorbed substrate (S)	32
<b>Equation 1.3</b> Oxidation of adsorbed water by the hole	32
<b>Equation 1.4</b> Oxidation of surface hydroxyl ion by the hole	32
<b>Equation 1.5</b> Reduction of oxygen by the electron	32
<b>Figure 1.6</b> Band positions of some typical photocatalysts (at pH= 7 in aqueous solutions).[29]	33
<b>Figure 1.7</b> Representations of the crystal structures of the common $\text{TiO}_2$ polymorphs: anatase (tetragonal, $a = 0.3785 \text{ nm}$ , $c = 0.9513 \text{ nm}$ ) (a), rutile (tetragonal, $a = 0.4593 \text{ nm}$ , $c = 0.2959 \text{ nm}$ ) (b), and brookite (orthorhombic, $a = 0.9181 \text{ nm}$ , $b = 0.5455 \text{ nm}$ , $c = 0.5142 \text{ nm}$ ) (c). Adapted from reference [38].	35
<b>Figure 1.8</b> Classification of porous materials according with the pores size (IUPAC standard).	37
<b>Equation 1.6</b> Hydrolysis of the alkoxide group	38
<b>Equation 1.7</b> Alcohol condensation	38
<b>Equation 1.8</b> Water condensation	38
<b>Figure 1.9</b> Schematic stepwise of the two main formation mechanisms of SBA-15: self-assembly (a) and cooperative self-assembly (b) route.	39
<b>Figure 1.10</b> Advantages of hierarchical nanostructures in heterogeneous photocatalysis. Figure adapted from reference. [29]	40
<b>Figure 1.11</b> Liquid crystal templating route to form macro-mesoporous silica using P-123 as soft template for the mesophase and polystyrene beads to introduce a macropore network.	41
<b>Table 1.2</b> Methyl Orange properties.	42



<b>Equation 1.9</b> Hydroxyl radical attack	43
<b>Figure 1.12</b> Pictorial representation of direct dye degradation process.	44
<b>Equation 1.10</b> Direct hole attack to dye	43
<b>Equation 1.11</b> Direct electron attack to dye	43
<b>Table 1.3</b> Propanoic acid proprieties.	45
<b>Equation 1.12</b> Photo-Kolbe mechanism	45
<b>Equation 1.13</b> Hydroxyl radical attack	45

## Chapter 2 Experimental

<b>Figure 2.1</b> Illustrative representation of X-ray fluorescence mechanism	61
<b>Figure 2.2</b> Constructive and destructive interference of X-ray photons (a);schematic of X-ray interaction with a crystal lattice (b).	62
<b>Equation 2.1</b> Bragg's equation	62
<b>Equation 2.2</b> Pythagoras theorem	62
<b>Equation 2.3</b> Scherrer equation	63
<b>Figure 2.3</b> Schematic representation of cross sectional SBA-15 pore channels, layer spacing and unit cell	63
<b>Figure 2.4</b> Graphical representation of photoelectron ejection.	64
<b>Equation 2.4</b> Kinetic energy	64
<b>Equation 2.5</b> Total angular momentum	65
<b>Equation 2.6</b> BET linear	67
<b>Figure 2.5</b> Six types of gas physisorption isotherms.[14]	66
<b>Equation 2.7</b> Monolayer volume	67
<b>Equation 2.8</b> Definition of constant, C	67
<b>Equation 2.9</b> BET surface area calculation	67
<b>Equation 2.10</b> Kelvin's equation	67
<b>Equation 2.11</b> Pore radius	68
<b>Figure 2.6</b> Schematic of interaction of the incident beam and the sample surface.	69
<b>Equation 2.12</b> Band gap evaluation	70
<b>Equation 2.13</b> Kubelka-Munk function	70
<b>Figure 2.7</b> Schematic of direct and indirect band gap energy.	70
<b>Figure 2.8</b> UV–vis diffuse reflectance spectra (a) and Tauc plot for indirect	

semiconductor (b).	71
<b>Figure 2.9</b> Energy level diagram for Rayleigh and Raman scattering	72
<b>Figure 2.10</b> Schematic drawing the optical path through the DRIFTS apparatus (a) detail of the interaction between the incident beam and the surface of the powder sample (b).	73
<b>Equation 2.14</b> Hooke's law	74
<b>Equation 2.15</b> Reduced mass	74
<b>Figure 2.11</b> Graphical representation of the interaction between IR beam and the sample with the formation of the evanescent wave.	75
<b>Equation 2.16</b> Critical angle	75
<b>Equation 2.17</b> Penetration depth	75
<b>Table 2.1</b> General properties of ATR crystals	76
<b>Figure 2.12</b> Illustrative representation of X-ray interaction with the sample surface and the different signal emitted.	77
<b>Equation 2.18</b> Schematic STEM microscope configuration.[30]	78
<b>Figure 2.13</b> Set up of the photoreactor for dye degradation (a) and detail of MO reaction solution during the irradiation time (b).	80
<b>Figure 2.14</b> UV-vis absorbance spectra of MO standard solutions (a); calibration plot to determine the concentration of unknown samples (b)	81
<b>Equation 2.19</b> Lambert-Beer law	80
<b>Equation 2.20</b> Percentage of MO degradation	81
<b>Figure 2.15</b> Set up of the ATR flow cell for in-situ measurements (right) and detail of the UV array and the base plate with the ZnSe crystal (left)	82
<b>Figure 2.16</b> Light intensity calibration obtained controlling the emission of the UV array through the remote control and measuring the actual intensity with a light meter (a); lightmeter used for the measurement (b).	83
<b>Equation 2.21</b> Etching of the ATR crystal	83
<b>Figure 2.17</b> ZnSe crystal before (left) and after coating (right) with the TiO <sub>2</sub> thin film	84
<b>Figure 2.18</b> Batch photoreactor (a) and detail of the UV array (b)	85
<b>Table 2.2</b> List of compounds detected by refractive index detector on HPLC	85
<b>Figure 2.19</b> Calibration of reactants and potential products detected by refractive index detector (RID) on HPLC	86
<b>Equation 2.22</b> Conversion	86
<b>Equation 2.23</b> Yield	87
<b>Equation 2.24</b> Selectivity	87

### Chapter 3 Titania grafted on mesoporous silica support

<b>Figure 3.1</b> Schematic drawing of the self-assembly of the surfactant P-123 during the synthesis of SBA-15 (a) and dependence of the microporosity and mesopore size from the aging temperature (b).	93
<b>Figure 3.2</b> Stacked isotherm plot of SBA-15 aged at different temperature (a) stacked BJH pore size distributions for the mesoporous silica supports (b).	94
<b>Table 3.1</b> Structural and textural properties of the SBA-15 support aged at three different temperatures	95
<b>Figure 3.3</b> Effect of aging temperature on SBA-15 pore volume (total, mesopore and micropore volume) (a); surface area and pore size (b)	95
<b>Figure 3.4</b> Offset XRD patterns at low (a) and wide (b) angle of SBA-15 supports synthesized with different mesopore sizes.	96
<b>Figure 3.5</b> Evolution of the evaluated wall thickness ( $t_{\text{wall}}$ ) (a) and representative ordered hexagonal structure of SBA-15 (b)	96
<b>Table 3.2</b> Pore spacing ( $a_0$ ), interlayer spacing ( $d_{10}$ ) and wall thickness ( $t_{\text{wall}}$ ) of the supports synthesized at different aging temperature	97
<b>Table 3.3</b> Bulk elemental analysis for the Ti-SBA-15-n (n=1,2) composites.	98
<b>Table 3.4</b> Surface composition of the Ti-SBA-15-X-n samples	98
<b>Figure 3.6</b> Ti 2p (a) and O 1s (b) XPS stack plot for Ti-SBA-15-5-n. The spectra of bulk anatase and of the SBA-15 parent support are reported for comparison.	99
<b>Table 3.5</b> Comparison of the surface and bulk Ti wt. % content for the Ti-SBA-15-n composites	100
<b>Figure 3.7</b> Si 2p XP spectra for the Ti-SBA-15-5-n samples and parent support (a), and the detail of the Si 2p region for the Ti-SBA-15-5-2 sample (b).	100
<b>Figure 3.8</b> Stacked isotherm plots (a) and BJH pore size distributions of Ti-SBA-15-5-n and the relative parent support (b).	101
<b>Figure 3.9</b> Stacked isotherm plots (a) and BJH pore size distributions of Ti-SBA-15-6-n and the relative parent support.	102
<b>Figure 3.10</b> Stacked isotherm plots (a) and BJH pore size distributions of Ti-SBA-15-7-n and the relative parent support.	102
<b>Table 3.6</b> Textural properties of composites materials.	103
<b>Figure 3.11</b> Offset low angle XRD pattern of titania coated SBA-15 (2nd grafting cycle) compared with the each parent support (a,b and c), wall thickness as a function of aging time for the parent SBA-15 and TiO <sub>2</sub> -grafted (2 <sup>nd</sup> cycle) materials (d).	104
<b>Table 3.7</b> Evaluated pore spacing ( $a_0$ ), interlayer spacing ( $d_{10}$ ) and wall thickness ( $t_{\text{wall}}$ ) of the three supports synthesized at different aging temperature and the related grafted materials.	105
<b>Figure 3.12</b> Offset of wide angle XRD patterns of the composites materials and their support in comparison with the spectrum of pure anatase (the stars mark the anatase	

reflection peaks) for the three series of support (a,b,c), sketch showing the SBA-15 material (light grey) coated with TiO <sub>2</sub> particles by two cycles of graftings (purple dots) (d).	105
<b>Figure 3.13</b> Raman spectra of the parent SBA-15-5 and Ti-SBA-15-n (n=1-2) (a) and detail of the SBA-15-5 spectrum (b).	106
<b>Figure 3.14</b> ATR IR spectra of Ti-SBA-15-n samples, the support and the commercial benchmark of TiO <sub>2</sub> P-25 in the range of 2800-400 cm <sup>-1</sup> (a) and 400-1600 cm <sup>-1</sup> (b).	107
<b>Figure 3.15</b> Representative bright field STEM images of the channel (on the right) and the open mesoporous structure (on the left) of the SBA-15 7 (a,b) and Ti-SBA-15-7-2 (c,d).	108
<b>Figure 3.16</b> Pore spacing distributions, normal and cumulative statistical distributions for (a) SBA-15 7, (b) Ti-SBA-15 7-2, (c) comparison between TEM and XRD measurements. Pore size distributions, normal and cumulative statistical distributions for (d) SBA-15 7, (e) Ti-SBA-15 7-2 and (f) comparison between TEM and porosimetry measurements.	109
<b>Figure 3.17</b> Electronic energy states of a semiconductor in the transition from nanosized to bulk crystals.	110
<b>Figure 3.18</b> UV-vis spectra of Ti-SBA-15-X-n samples, Degussa P-25, bulk anatase and mesoporous SBA-15.	111
<b>Table 3.8</b> Titania content (wt.%), band gap (E <sub>g</sub> ), corresponding wavelengths value (λ <sub>E<sub>g</sub></sub> ) and the band edge for the parent support, Ti-SBA-15-X-n and the bulk references materials.	112
<b>Figure 3.19</b> Kubelka-Munk function for band gap evaluation (a), spectrum of SBA-15 (b).	111
<b>Figure 3.20</b> Comparison on the wt. % of TiO <sub>2</sub> values obtained from XRF and ICP analysis.	113
<b>Table 3.9.</b> Bulk elemental analysis for the Ti-SBA-15-n (n=1-5) composites.	113
<b>Table 3.10</b> Surface composition of the Ti-SBA-15-n materials.	114
<b>Figure 3.21</b> Ti 2p XP spectra for the Ti-SBA-15-5-n samples and parent support.	114
<b>Figure 3.22</b> O 1s XPS stack plot for Ti-SBA-15-n (n=1-5). The spectrum of the parent SBA-15 is reported for comparison (a); variation of surface species with increasing TiO <sub>2</sub> film thickness (b).	115
<b>Figure 3.23</b> Si 2p XP spectra for the Ti-SBA-15-5-n samples and parent support (a). Surface Ti/Si atomic ratio (from XPS) versus bulk Ti/Si atomic ratio (from XRF). Solid line shows the expected values for a homogeneous Ti distribution within the solid (b).	116
<b>Figure 3.24</b> Stacked isotherm plots (a) and BJH pore size distributions for Ti-SBA-15-5-n and the relative parent support (b).	116
<b>Figure 3.25</b> Effect of Ti loading on mesopore and micropore volume and evolution of titania film thickness with the number of grafting cycles.	118
<b>Table 3.11</b> Structural and textural properties of the parent SBA-15 and the grafted	

samples	116
<b>Figure 3.26</b> Offset low angle XRD patterns of parent SBA-15 and the TiO <sub>2</sub> grafted sample (a); evolution of the evaluated wall thickness ( $t_{\text{wall}}$ ) and pore spacing with the increasing of titania grafting cycles (b).	119
<b>Table 3.12</b> Pore spacing ( $a_0$ ) and pore wall thickness ( $t_{\text{wall}}$ ) calculated from XRD and N <sub>2</sub> adsorption-desorption analyses.	119
<b>Figure 3.27</b> Offset of wide angle XRD patterns of the composites materials and their support in comparison with the pattern of pure anatase (the gray star marks the (101) anatase reflection peaks).	120
<b>Figure 3.28</b> Raman spectra of the parent SBA-15-7 and Ti-SBA-15-n (n=1-5).	121
<b>Figure 3.29</b> ATR FT-IR spectra of Ti-SBA-15-n samples and the parent support.	121
<b>Table 3.13</b> Vibrational mode assignments of Ti-SBA-15-n catalysts	122
<b>Figure 3.30</b> Representative TEM images of Ti-SBA-15-5. Arrows show crystalline TiO <sub>2</sub> nanoparticles (a); higher magnification and inset with detail of TiO <sub>2</sub> nanoparticle observed inside the SBA-15 channel (b).	123
<b>Figure 3.31</b> UV-vis spectra of Ti-SBA-15-X-n samples, TiO <sub>2</sub> P-25, bulk anatase and parent SBA-15 (a) and evolution of UV absorption edge with the increasing of TiO <sub>2</sub> loading (b)	124
<b>Table 3.14</b> TiO <sub>2</sub> content, band gap ( $E_g$ ), corresponding wavelengths value ( $\lambda_{Eg}$ ) and the band edge for the parent support, Ti-SBA-15-X-n and the TiO <sub>2</sub> references.	125
<b>Figure 3.32</b> Kubelka-Munk function for band gap evaluation of the TiO <sub>2</sub> based catalyst, the bare mesoporous support and two commercial references (a), trend of the band gap value with the increasing of titania loading (b).	124
<b>Figure 3.33</b> Reduction of MO concentration with irradiation time over the three series of Ti-SBA-15-x-n, bulk anatase and Degussa P-25 and one of the parent support (SBA-15-7).	126
<b>Figure 3.34</b> Initial rate ( $r^0$ ) normalised for the mass of catalyst as function of the pore size.	127
<b>Figure 3.35</b> Variation of the dye degradation rate with irradiation time of methyl orange solution.	128
<b>Figure 3.36</b> Initial rate ( $r^0$ ) for the MO degradation normalised for the mass of TiO <sub>2</sub> .	129
<b>Figure 3.37</b> Reduction in MO concentration with irradiation time by using different catalysts at different wt. % of TiO <sub>2</sub> and two references (Degussa P-25 and bulk anatase).	129
<b>Figure 3.38</b> Variation of the dye degradation rate with irradiation time of MO solution.	130
<b>Figure 3.39</b> Initial rate ( $r^0$ ) for the MO degradation normalised for the mass of catalyst as function of the TiO <sub>2</sub> loading.	131
<b>Figure 3.40</b> Initial rate ( $r^0$ ) for the MO degradation normalised for the mass of TiO <sub>2</sub> .	132

## Chapter 4 Titania grafted on hierarchical silica support

<b>Figure 4.1</b> Representative STEM images of polystyrene beads of 200nm size (before the centrifuge step) (a) and the relative particle size distributions for 500 particles (b).	141
<b>Figure 4.2</b> Representative STEM images of polystyrene beads of 400nm size (before the centrifuge step) (a) and the relative particle size distributions for 500 particles (b).	142
<b>Figure 4.3</b> Representative STEM images of polystyrene beads of 600nm size (before the centrifuge step) (a) and the relative particle size distributions for 500 particles (b).	143
<b>Table 4.1</b> Textural properties of the MM- SBA-15 support	143
<b>Figure 4.4</b> Stacked isotherms of MM-SBA-15 supports (a) and stacked BJH size distribution plots (b).	144
<b>Figure 4.5</b> Low angle XRD patterns of the silica supports (a), trend of increasing of $t_{wall}$ and $a_0$ with increasing of macropore size in comparison with the values for the SBA-15 (b).	145
<b>Table 4.2</b> Pore spacing ( $a_0$ ), interlayer spacing ( $d_{10}$ ) and wall thickness ( $t_{wall}$ ) of the hierarchical supports with different macropores size. The sample SBA-15-7 is reported for comparison.	145
<b>Figure 4.6</b> SEM image of macro-mesoporous SBA-15 obtained with PS beads of different sizes: 200 nm(a), 400 nm (b) and 600 nm (c). The plot shows that measured macropores are smaller than the size of PS bead templates previously measured from the STEM pictures (d)	146
<b>Table 4.3</b> Bulk elemental analysis for the hierarchical composites with different macropores size.	147
<b>Table 4.4</b> Surface composition of the hierarchical composites	147
<b>Figure 4.7</b> Ti 2p region from XPS analysis of 200-1 and bulk anatase (a), and O 1s region from of titania grafted on macroporous SBA-15 and the correspondent bare support.	148
<b>Figure 4.8</b> Si 2p region from XPS analysis of 200-1 and parent support.	149
<b>Table 4.5</b> Comparison of the surface and bulk Ti wt. % content for the hierarchical composites	149
<b>Figure 4.9</b> Stacked isotherm plots of hierarchical SBA-15 with different macropore sizes (black lines): MM-200 (1), MM-400 (3) and MM-600 (5); and the relative grafted composite samples (200-1(2), 400-1 (4) and 600-1 (6)) (a); stacked BJH mesopore size distributions (b).	150
<b>Table 4.6</b> Textural properties of the parent MM- SBA-15 and the grafted samples	150
<b>Figure 4.10</b> Offset of wide angle XRD patterns of the grafted materials in comparison with the spectrum of bulk anatase (a). Evolution of the anatase crystallite size with the number of titania graftings evaluated by the Scherrer equation (b).	151
<b>Figure 4.11</b> ATR IR spectra of the grafted samples, the MM-200 support, the mesoporous support (SBA-15 7) and the TiO <sub>2</sub> P-25 in the range of 2950-4000 cm <sup>-1</sup> (a),	

400-1600 $\text{cm}^{-1}$ (b).	152
<b>Table 4.7</b> Assigned vibrational modes for the $\text{TiO}_2$ grafted MM-SBA-15	152
<b>Figure 4.12</b> Representative bright field TEM images of channel (a) and the hierarchical macro/mesoporous structure of the 200-1(b).	153
<b>Figure 4.13</b> Representative bright field TEM images of the hierarchical macro/mesoporous structure of the 400-1(a) and the 600-1 (b) samples.	153
<b>Figure 4.14</b> Schematic figure of photonic crystal with silica inverse opal structure.	154
<b>Figure 4.15</b> DRUV-vis reflectance spectra (%R) of hierarchical silica supports with different macropores size in comparison with the mesoporous SBA-15 (a) shift of the stop band position as function of the macropore size (b).	155
<b>Figure 4.16</b> Kubelka-Munk function for band gap evaluation (a) and absorption spectra (primary y-axis) of the $\text{TiO}_2$ on MM-SBA-15 support and the reflectance spectra (secondary y-axis) for the corresponding supports (b).	156
<b>Table 4.8</b> Bulk elemental analysis for the hierarchical composites with different $\text{TiO}_2$ loading.	157
<b>Table 4.9</b> Surface composition of the 400-n materials (n=1-3).	157
<b>Figure 4.17</b> Ti 2p XPS stack plots of the composites catalysts obtained from the 1st and the 3rd grafting cycles. The spectrum of bulk anatase is reported for comparison (a) O 1s XPS stack plots of the three grafting cycles and the relative bare support (b).	158
<b>Figure 4.18</b> Si 2p XPS stack plots for the 1st and the 3rd grafting cycle of the composites catalyst. The spectrum of the bare support MM-400 is reported for comparison (a) highlight of the Si 2p region for the 3rd grafting cycle (b).	159
<b>Table 4.10</b> Comparison of the surface and bulk Ti wt. % content for the MM-n composites	159
<b>Figure 4.19</b> Stacked isotherm plots of MM-n (n=1-3) composites samples and the parent MM-400 (a) BJH pore size distributions (b)	160
<b>Figure 4.20</b> Offset of wide angle XRD patterns of the grafted materials in comparison with the spectrum of pure anatase (a); evolution of the anatase crystallite size with the number of titania graftings evaluated by the Scherrer equation (b).	161
<b>Table 4.11</b> Textural properties of the parent MM- SBA-15 and the grafted samples	161
<b>Figure 4.21</b> ATR IR spectra of $\text{TiO}_2$ grafted samples and the bare support MM-400 in the range of wavenumber of 2950-4000 $\text{cm}^{-1}$ (a) and of 400-1600 $\text{cm}^{-1}$ (b)	162
<b>Figure 4.22</b> Representative HRTEM images of MM-400 after titania 400-3 (a and d), 400-1 (b) and 400-2 (c).	163
<b>Figure 4.23</b> Absorption spectra of all the $\text{TiO}_2$ grafted MM-400 samples (a); Kubelka-Munk functions for the band gap evaluation (b).	164
<b>Figure 4.24</b> Diffuse reflectance spectra (%R) of the $\text{TiO}_2$ grafted MM-400 samples with different $\text{TiO}_2$ loading and the corresponding support MM-400. The PBG region has been enhanced for clarity.	164
<b>Figure 4.25</b> The stop band position as a function of the titania loading.	165

<b>Figure 4.26</b> Absorption spectra (primary y-axis) of the TiO <sub>2</sub> grafted MM-400 samples and the reflectance spectra (secondary y-axis) for the correspondent support	166
<b>Figure 4.27</b> Degradation of MO concentration with irradiation time over the three series of synthesized catalyst from supports with different macropores size, two references (bulk anatase and Degussa P-25) and two parent supports (MM-SBA-15 and SBA-15). Photolysis test of MO under UV without catalyst is also reported together with the comparison with the 1st grafting cycle on SBA-15-7.	167
<b>Figure 4.28</b> Variation of the dye degradation rate with irradiation time of methyl orange solution for the grafted samples with different macropores size.	167
<b>Figure 4.29</b> Initial rate ( $r^0$ ) normalised for the mass of catalyst (a) and the mass of TiO <sub>2</sub> (b) as function of the macropore diameters.	168
<b>Figure 4.30</b> Degradation of MO concentration with irradiation time over the three TiO <sub>2</sub> -grafted catalysts from the support MM-400, two references (bulk anatase and Degussa P-25) and the parent support. Photolysis test of MO under UV without catalyst is also reported.	170
<b>Figure 4.31</b> Variation of the dye degradation rate with irradiation time of methyl orange solution for the grafted samples with different TiO <sub>2</sub> loading, the MM-400 support and UV-vis test.	170
<b>Figure 4.32</b> Initial rate ( $r^0$ ) of MO degradation normalised for the mass of catalyst as function of the TiO <sub>2</sub> loading for the two families of catalyst (meso and macro/meso TiO <sub>2</sub> -coated SBA-15) (a)	172

## Chapter 5 In situ ATR IR study of liquid phase propanoic acid photooxidation on TiO<sub>2</sub> nanoparticles

<b>Figure 5.1</b> Schematic drawing of the experimental setup of the ATR IR cell for solid-liquid interface investigations and an example of the IR spectra collected for pure PA (a), PA in liquid phase (b) and PA adsorbed on P-25 surface (c).	181
<b>Equation 5.1</b> Langmuir kinetic model	182
<b>Equation 5.2</b> Surface coverage	182
<b>Figure 5.2</b> Time dependence of absorbance (at 1712 cm <sup>-1</sup> ) during the adsorption (a) and desorption (b) time and the relative fitting obtained with exponential function in Origin 9.	183
<b>Equation 5.3</b> Langmuir affinity constant	183
<b>Figure 5.3</b> ATR IR spectra of dried TiO <sub>2</sub> thin film on ZnSe surface (a), water (b) and water saturated thin film (c).	184
<b>Table 5.1</b> IR absorption bands and vibrational mode assignments of propanoic acid.	185
<b>Figure 5.4</b> ATR-IR spectra of propanoic acid dissolved in water in the range of concentration between 0.1 M and 10 <sup>-2</sup> M (a), calibration lines calculated from the peak area of the characteristic vibrational modes of propanoic acid in solution (b)	185
<b>Figure 5.5</b> ATR IR spectra of propanoic acid adsorbed on TiO <sub>2</sub> P-25 under equilibrium conditions (bold line) and spectra of the acid at the same concentration	



in solution (dotted line) (a). Adsorption affinity constant ( $k_L$ ) from the kinetic experiment performed at different propanoic acid concentration (b).	187
<b>Figure 5.6</b> Different adsorption modes of propanoic acid on $\text{TiO}_2$ .	187
<b>Figure 5.7</b> ATR IR spectra of 0.1M propanoic acid solution adsorbed on $\text{TiO}_2$ P-25 under equilibrium conditions (bold line) reached at different flow rates and spectra of the acid at the same concentration in solution (dotted line)(a). Equilibrium constant ( $k_{eq}$ ) evaluated from the Langmuir model for the three surface complexes. (b)	188
<b>Figure 5.8</b> ATR-FTIR spectra of adsorbed propionic acid over $\text{TiO}_2$ P-25 collected at the equilibrium ( $t=30$ min) at different temperature. The spectrum of propanoic acid in solution at room temperature (black dotted line) was reported for comparison (a). Value of equilibrium constants (evaluated from the Langmuir model) are reported for the three surface complexes (b).	189
<b>Figure 5.9</b> Temperature dependence of $\Delta G_{ads}^\circ$ calculated from the Langmuir eq.	190
<b>Equation 5.4</b> Gibbs free energy.	190
<b>Figure 5.10</b> Series of ATR-IR spectra recorded during adsorption of propanoic acid solution on $\text{TiO}_2$ P-25 in the dark for 30 min. IR region: $2500\text{-}3850\text{ cm}^{-1}$ (a) and $1000\text{-}1850\text{ cm}^{-1}$ (b).	192
<b>Equation 5.5</b> Surface protonation of $\text{TiO}_2$ at acidic pH.	193
<b>Equation 5.6</b> Surface deprotonation of $\text{TiO}_2$ at basic pH	193
<b>Figure 5.11</b> Simplified figure of the protonation and deprotonation of hydroxylated $\text{TiO}_2$ surface leading to positive and negative net charge at the surface.	193
<b>Figure 5.12</b> Adsorption/desorption time profile of the most relevant bands of adsorbed propanoic acid on $\text{TiO}_2$ P-25 obtained by measuring the peak area at different times.	194
<b>Figure 5.13</b> ATR-IR absorption spectra of propanoic acid adsorbed on P-25, anatase, rutile and physical mix 80%A-20%R $\text{TiO}_2$ nanoparticle thin film	195
<b>Figure 5.14</b> ATR IR spectra changes obtained during the adsorption of propanoic acid on anatase, (a) and the corresponding spectra in the desorption step (b). The arrow indicates evolution of spectra with increasing time.	196
<b>Figure 5.15</b> ATR IR spectra changes obtained during the adsorption of propanoic acid on rutile, (a) and the corresponding spectra in the desorption step (b). The arrow indicates evolution of spectra with increasing time.	196
<b>Figure 5.16</b> ATR IR spectra changes obtained during the adsorption of propanoic acid on physical mixture 80% anatase-20% rutile, (a) and the corresponding spectra in the desorption step (b). The arrow indicates evolution of spectra with increasing time.	197
<b>Figure 5.17</b> Time dependence of absorbance of propanoic acid on different $\text{TiO}_2$ nanoparticle. Adsorption and desorption data points were obtained from the measured area of the absorption peaks of propionic acid and propionate bonded to the surface (a, b, c). Schematic representation of surface bound species related with the desorption rate (d).	198

<b>Table 5.2</b> Maximum absorbance value for each component ( $A_{\max}$ ), value for each component normalised for the surface area ( $A_{\max} \cdot SA^{-1}$ ), residual coverage in the end of the desorption step ( $\theta_r$ ), adsorption/desorption rate constant ( $k_a$ , $k_d$ ) and half-live value ( $t^{1/2}$ ).	199
<b>Figure 5.18</b> IR spectra in 1300–1700 $\text{cm}^{-1}$ spectral region for pyridine adsorbed on P-25, anatase and rutile (a) and plot of surface Lewis acid density for the different $\text{TiO}_2$ samples.(b)	200
<b>Figure 5.19</b> Comparison of the photocatalytic activity of the different photocatalysts under UV light (a) and reaction profile of propionic acid with relative formed intermediates detected by HPLC analysis of $\text{TiO}_2$ P-25 (b), anatase (c) and rutile (d ).	202
<b>Table 5.3</b> Experimental results of the propanoic acid photooxidation over $\text{TiO}_2$ samples.	203
<b>Figure 5.20</b> shows the ATR IR spectra obtained during photodegradation of propanoic acid on $\text{TiO}_2$ P-25	204
<b>Figure 5.21</b> Stacked ATR IR spectra obtained in different conditions (from the top): (1) after 60 min of irradiation, (2) equilibrium in the dark, (1-2) spectrum obtained (2) from the difference of the latter two, (3) equilibrium in the dark of formic acid (3) over P-25.	205
<b>Figure 5.22</b> Evolution of the peak areas of propanoic acid at $\nu(\text{C-O}) \sim 1227 \text{ cm}^{-1}$ and $\nu(\text{C-C}) \sim 1080 \text{ cm}^{-1}$ (p, in black) and formate (f, in red) and water (w, in blue), during the irradiation time.	206
<b>Figure 5.23</b> ATR-IR spectra recorded at different time during the photodegradation of propanoic acid on anatase under UV (365 nm) in the 2500-3900 $\text{cm}^{-1}$ (a) and 1000–1850 $\text{cm}^{-1}$ (b) region.	207
<b>Figure 5.24</b> ATR-IR spectra recorded at different time during the photodegradation of propanoic acid on anatase under UV (365 nm) in the 2500-3900 $\text{cm}^{-1}$ (a) and 1000–1850 $\text{cm}^{-1}$ (b) region.	208
<b>Figure 5.25</b> Evolution of the peak areas related to the H-bonded acid $\nu(\text{C=O})$ and propionate in bridging $\nu(\text{COO}^-)$ configuration.	208
<b>Figure 5.26</b> Illustration of OH-radical-mediated photocatalysis on anatase (left) and rutile (right), image from Reference [38].	209
<b>Figure 5.27</b> Proposed reaction mechanism for of propanoic acid over $\text{TiO}_2$ P-25.	210
<b>Figure 5.28</b> Conversion-selectivity plot for the three $\text{TiO}_2$ samples (a); evolution during the irradiation time of the peak area ratio $\nu(\text{CO}_2)/\nu(\text{C-C})$ evaluated for P-25 and anatase (b).	211
<b>Figure 5.29</b> Comparison of the photocatalytic degradation of propionic acid over $\text{TiO}_2$ P-25 at different pH under UV light (a) Trend of the initial rate with the pH value (b).	212
<b>Table 5.4</b> Experimental results of the propanoic acid photooxidation over P-25 at different pH.	212
<b>Figure 5.30</b> Reaction profile of oxidation propionic acid over $\text{TiO}_2$ P-25 with relative intermediates detected by HPLC analysis at pH 6 (a) and 8 (b).	213
<b>Figure 5.31</b> ATR-FTIR spectra of propionic acid at pH 3 and 8 in aqueous	

solution (dotted lines) and adsorbed on TiO <sub>2</sub> P-25 nanoparticle (bold lines)	213
<b>Figure 5.32</b> Schematic illustration of the adsorption of carboxylic acid on the TiO <sub>2</sub> surface relatively to the pH of the solution and isoelectric point (IEP) of TiO <sub>2</sub>	214
<b>Figure 5.33</b> ATR-IR spectra recorded at different time during the photodegradation of propanoic acid on TiO <sub>2</sub> P-25 under UV (365 nm) at pH 8 in the 2500-3900cm <sup>-1</sup> (a) and 1000–1850 cm <sup>-1</sup> (b) region. Spectra were collected during 2 hours illumination at different times and spectra of TiO <sub>2</sub> samples saturated with propanoic acid solution prior to illumination were used as background in each measurement.	215
<b>Figure 5.34</b> Conversion-selectivity plot for the three pH values (a); evolution during the irradiation time of the peak area ratio $\nu(\text{CO}_2)/\nu(\text{C-C})$ .	216

## Appendix

<b>Figure 1</b> Evolution during the time of the spectra obtained from the subtraction ( $\text{UV}_{\text{time}} - \text{Ads}_{\text{dark}}$ ) from the experiment of propanoic acid over TiO <sub>2</sub> P-25.	227
<b>Figure 2</b> Evolution during the time of the spectra obtained from the subtraction ( $\text{UV}_{\text{time}} - \text{Ads}_{\text{dark}}$ ) from the experiment of propanoic acid over anatase.	228
<b>Figure 3</b> Evolution during the time of the spectra obtained from the subtraction ( $\text{UV}_{\text{time}} - \text{Ads}_{\text{dark}}$ ) from the experiment of propanoic acid over rutile.	228

# *Chapter 1*

## *Introduction*

## 1. Introduction

### 1.1 Water: the environmental problem

Over two third of the Earth's surface is covered by water but the amount of fresh water available to the world population represents only 2.5 % of all water on the planet. It is worth noting that most of this fresh water is trapped in glaciers and snowfields, leaving only 0.007 % of the planet's fresh water available to be used by human beings. The increasing demand for clean water together with its scarcity and misuse caused by the expansion of industries, human population swelling and long-term droughts have become a serious issue worldwide. The World Health Organisation (WHO) estimates that over 2.5 billion people have a very limited access to clean water and millions of people die every year because of diseases caused by bacteriologically damaged water.[1]

In 2000 the member states of the United Nations (UN) gathered together to define a series of eight time-bound targets, with a deadline of 2015, that have become known as the Millennium Development Goals (MDG). Goal 7, to ensure the environmental sustainability, included a target that challenged the global community to halve, by 2015, the proportion of people without sustainable access to safe drinking water. In 2015, 6.6 billion people use an improved drinking water source but despite the achievements of the MDG period, a great deal remains to be done. Global water demand is largely influenced by population growth, urbanization, food and energy security policies, and macro-economic processes. As the population continues to rise, the number of people affected by water stress and water scarcity is expected to rise sharply. **Figure 1.1** shows the amount of water withdrawal as a percentage of the total available supply, at the national level in 1995 and in 2025 (projected amounts). Overall, the percentages are expected to rise substantially by 2025



**Figure 1.1** World map of the freshwater stress in 1995 and 2025.[2]

As the overall demand for water grows, also the quantity of wastewater produced and its overall pollution load are continuously increasing worldwide. Over 80% of the world's wastewater, and over 95% in some least developed countries, is released to the environment without treatment.

On the 22 March 2017, on the occasion of the World Water Day, the UN released the World Water Development Report (WWDR) entitled *Wastewater: The Untapped Resource*, demonstrating how the improvement of wastewater management can generate social, environmental and economic benefits essential for sustainable development.[3] One of a few attractive options is the possible reuse of onsite rural wastewater or the treated municipal wastewater from treatment plants for agricultural and industrial activities.[4, 5] The wastewater problem could be addressed by using conventional water treatment methods, but they are highly expensive and energy intensive making them largely inaccessible in developing countries. Therefore, highly efficient and low cost water treatment technologies must be developed and optimised to address the fresh water shortage.

### **1.1.1 Water pollution**

The major sources of water pollution are from human settlements, industrial and agricultural activities, which produce a large number of contaminant compounds classified into three main groups:

1. bacteria, virus, protozoa and all agents which cause diseases;
2. inorganic compounds which are water soluble, such as acids, salts and toxic metals (cadmium, lead, mercury). Radioactive waste also belongs to this group;
3. organic compounds, such as saturated, unsaturated and aromatic hydrocarbons; they constitute oils, detergents and emulsifiers, plastics and pesticides.

Most of the contaminants are characterized by their persistence, bioaccumulation and toxicity. Nowadays water pollution is aggravated by population growth and rapid urbanization and it is expected to get worse over coming decades.

### **1.1.2 Water quality**

Water quality may be defined by its physical, chemical, and biological properties. Physical parameters include colour, odour, temperature, and turbidity. The content of insoluble contaminants, such as solids, oils and grease, also fall into this category; solids may be further classified into suspended and dissolved solids. Chemical parameters are usually associated with the biochemical oxygen demand (BOD), chemical oxygen demand (COD), total organic carbon (TOC)

and total oxygen demand (TOD); but also with more general properties including salinity, hardness, pH, acidity and alkalinity, as well as concentrations of ionized metals such as iron and manganese, and anionic species such as chlorides, sulfates, sulfides, nitrates and phosphates. Bacteriological parameters include the presence of coliforms, fecal coliforms, specific pathogens, and viruses.

## **1.2 Water treatments**

### **1.2.1 Conventional water treatments**

The most common approach to treat water consists in a combination of physical, chemical and biological processes. These treatments are divided into preliminary, primary, secondary and tertiary and a simple scheme is shown in **Figure 1.2**. Preliminary treatment is basically mechanical and its main function is to protect the downstream equipment and to enhance the efficiency of the subsequent stages by removing large materials, suspended or floating solids as sand and wood. Primary treatment is designed to eliminate suspended solids by the physical processes of sedimentation. Sedimentation removes a good percentage of organic and inorganic pollutants which can contribute a high reduction in COD ( $\text{g.l}^{-1}$ ). Some organic nitrogen, organic phosphorus and heavy metals associated with solids are also removed during primary sedimentation, producing a mud potentially contaminated. Colloidal and dissolved compounds are not affected. The effluent of primary treatment contains mainly colloidal and dissolved organic and inorganic solids. The secondary treatment consists of biological treatment by employing many different types of microorganisms in a controlled environment. Generally this stage consists in an aerobic biological treatment techniques with the objective to remove the colloidal and dissolved organic matter present in the effluent with a removal efficiency of 70- 90% BOD (Biological Oxygen Demand,  $\text{g.l}^{-1}$ ). Tertiary treatment improves the quality of the effluents destroying the remaining organic contaminants and no-biodegradable compounds. This stage removes nitrogen, phosphorus and brings bacteria down and it generally includes chemical oxidation, reverse osmosis, microfiltration, nanofiltration etc. In some cases these techniques are used in combination with primary and secondary treatment (i.e: chemical addition in primary and secondary treatment). The most common tertiary treatments are briefly described below.

1. Chlorination has been the most commonly and widely used water treatment method in the last decades to decontaminate wastewater streams. This treatment consists in the addition of chlorine ( $\text{Cl}_2$ ) or hypochlorite ( $\text{ClO}$ ) to water in order to destroy pathogenic microorganisms. Unfortunately, this disinfection method generates mutagenic and carcinogenic products well-known as disinfection by-products (DBPs).[6]
2. Membrane reactors assure physical separation of microorganisms, organic and inorganic compounds and they intrinsically require small operational energy. However these systems are affected by membrane fouling, increasing significantly the hydraulic resistance of the system.[7, 8] Therefore the membranes require frequent cleaning and maintenance

processes, adding significant operational costs. Moreover the output of this process is a concentrated stream (i.e. ca 10% volume of treated water) containing active pathogenic microorganisms which may cause a significant damage in feed stream or deposition place.[8]

3. Reverse osmosis and nanofiltration can remove dissolved and no-biodegradable compounds. These processes are based on the implementation of a different pressure to the two side of a membrane: water can pass throughout the membrane which is impenetrable to the solute. The membrane cost and the energy consumption to obtain the difference of pressure, are the main drawback of this process.
4. Ultraviolet (UV) light can be used instead of chlorine because damage to the genetic structure of bacteria, viruses, and other pathogens making them incapable of reproduction. The key disadvantages of UV disinfection are the need for frequent lamp maintenance and replacement, and the need for a highly treated effluent to ensure that the target microorganisms are not shielded from the UV radiation.

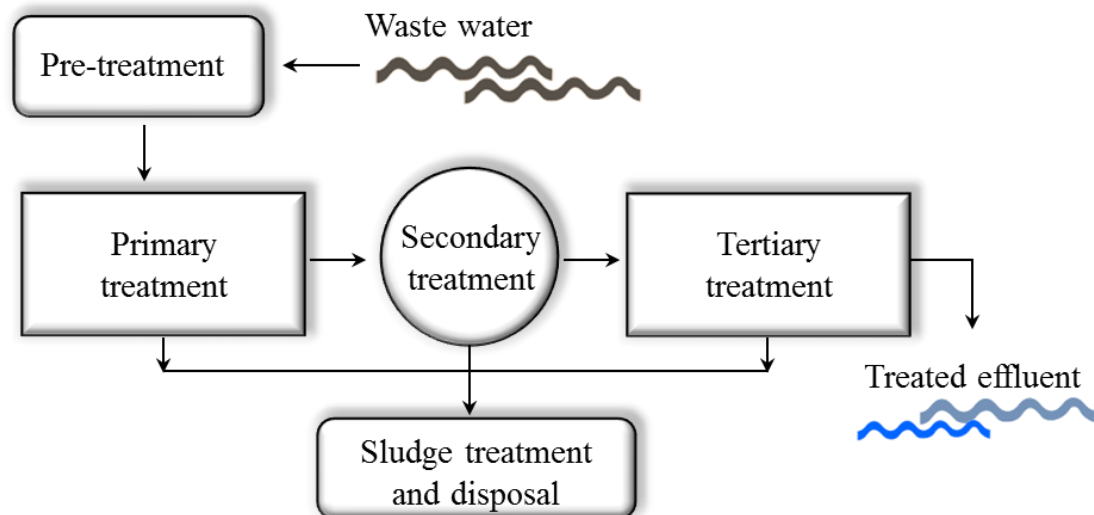


**Figure 1.2** Scheme of a conventional waste water treatment

#### **1.2.1.1 Disadvantages of conventional wastewater treatment plants**

Despite the fact that the commonly used tertiary treatment methods can achieve the legislative required standards, they generally require high operational and maintenance costs and intensive energy. Another problem is the possible formation of DBPs. As mention before, chlorination, used to remove pathogen agents from treated water, leads to the formation, with the natural organic compounds of the water (i.e. fulvic and humic acids), of chloride hydrocarbon considered carcinogenic. These compounds are generally removed with active carbon which later need to be burned, this stage produce chlorine oxides which can form carcinogenic dioxins. Also chemical and membrane methods (i.e., ozonation, nanofiltration and reverse osmosis) can generate toxic secondary contaminants which are introduced to ecosystems. Therefore, there is a clear need to



develop and implement cost-effective and flexible water treatment technologies which can provide the complete degradation of the water contaminants.

### 1.2.2 Advanced oxidation processes (AOPs)

Advanced oxidation processes (AOPs) are a class of oxidation techniques, which usually operate at or near ambient temperature and pressure,[9] all characterized by the same chemical feature: production of hydroxyl ( $\text{HO}^\bullet$ ) radicals. Hydroxyl radicals are highly reactive species, with little selectivity of attack and with rate constants ranging from  $10^8$  to  $10^9 \text{ M}^{-1}.\text{s}^{-1}$ . [10, 11] These oxidant species are effective for the treatment of many compounds in water due to their high oxidation strength. The hydroxyl radical's oxidation potential (2.80 V) is only surpassed by that of the fluorine molecule (**Table 1.1**).

**Table 1.1** Oxidation potential of some water treatment oxidants.[12]

Species	Symbol	Oxidation potential / Volts
Fluorine	$\text{F}_2$	3.00
Hydroxyl radical	$\text{HO}^\bullet$	2.80
Ozone	$\text{O}_3$	2.07
Hydrogen peroxide	$\text{H}_2\text{O}_2$	1.76
Permanganate ion	$\text{MnO}_4^-$	1.68
Hypochlorous acid	$\text{HOCl}$	1.49
Chlorine	$\text{Cl}_2$	1.36
Chlorine dioxide	$\text{ClO}_2$	0.95
Oxygen	$\text{O}_2$	0.40

It is important to highlight that AOPs do not replace the traditional processes but they can be exploited in an integrated approach with biological treatment systems for the oxidative degradation of toxic or refractory substances.

Therefore only wastes with relatively small COD contents ( $\leq 5 \text{ g. l}^{-1}$ ) can be suitably treated by means of advanced oxidation techniques. Higher COD contents would require the consumption of too large amounts of expensive reactants. The main advantage of using AOPs is the possibility to achieve the complete mineralization of organic contaminants to  $\text{CO}_2$  and water. Some of these technologies employ the UV light in conjunction with other chemical additives to improve the efficiency of the process. Among different available AOPs, those driven by light seem to be the

most popular technologies for wastewater treatment as shown by the large amount of data available in the literature.[13] An example of AOPs classification is offered in **Figure 1.3**.

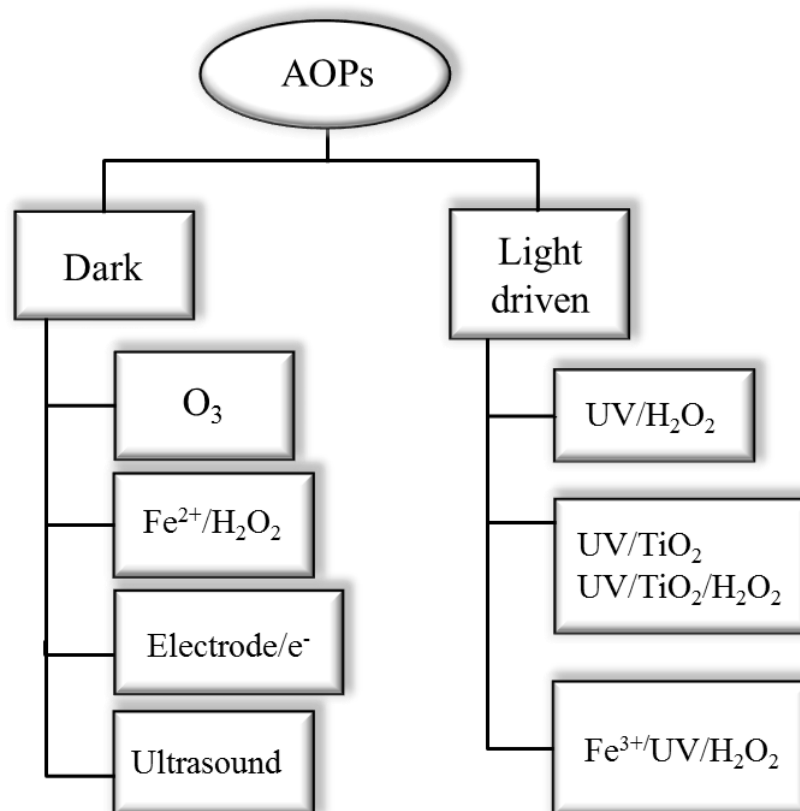


**Figure 1.3** Advanced oxidation processes (AOPs) classification.

Some of the commercially available AOP technologies are: ozonation ( $O_3$ ), hydrogen peroxide ( $H_2O_2$ ),  $UV/H_2O_2$  and photocatalysis utilizing either ultraviolet (UV) or solar irradiation with titanium dioxide ( $TiO_2$ ). However choose best-performing AOP for water treatment involves the evaluation of several parameters, such as:

- nature and physical-chemical properties of the water (or wet matrix) to treat and the pollutant to remove together with its biodegradability;
- presence of radical scavengers (i.e. carbonate);[14]
- presence of compounds which absorb UV radiation or suspended solid which can scatter the irradiated light;[15]
- pH of the solution which can influence the rate of radical generation.[14]

Due to fast development of light related technologies, the photochemical AOPs are positioning themselves on a privileged situation to compete with other available technologies. In particular, photocatalytic degradation processes, assisted by a semiconductor metal oxide (normally as photocatalyst) and oxygen (as primary oxidizing agent), earn increasing importance in the area of wastewater treatment as the most emerging destructive technology.[16]

### 1.3 Heterogeneous photocatalysis

The first contribution for understanding the heterogeneous photocatalytic processes happened in 1972 with the pioneering research of Fujishima and Honda.[17] They discovered the possibility to obtain photocatalytic dissociation of water (water splitting) on  $\text{TiO}_2$  electrodes. Although the primary objective of these studies involved energy applications mainly related to the production of hydrogen, this finding opened the frontiers of titania photocatalysis for other type of applications. Only four years later, Carey et al.[18] first reported the photocatalytic degradation of organic molecules, biphenyl and chlorobiphenyl derivatives, in the presence of  $\text{TiO}_2$ . Over the last decades, heterogeneous photocatalysis has garnered a significant amount of research interest due to the extremely wide range of applications, such as: organic synthesis, water splitting, photoreduction, hydrogen transfer, metal deposition, disinfection and anti-cancer therapy, water detoxification, gaseous pollutant removal, etc.[19, 20]

#### 1.3.1 Definition and mechanism

In heterogeneous photocatalysis, when a semiconductive material is irradiated with light at proper wavelength generates on its surface a series of reductive and oxidative reactions able to produce highly reactive species ( $\text{HO}^\bullet$ ,  $\text{O}^{\bullet-}$ ,  $\text{HO}_2^\bullet$ ). The peculiarity of photocatalytic reactions, when compared to conventional catalysis, consists in the way the catalyst is activated, with thermal activation being replaced by photonic activation.

Photocatalysts are usually semiconductors, which are materials with electrical properties intermediate between those of metals and insulators; this is due to a special configuration of the energy levels of electrons in semiconductors.[21] Band theory describes the energy levels of electrons within a solid organized in a bands structure, where the highest occupied molecular orbital (HOMO) is called valence band (VB) and the lowest unoccupied molecular orbital (LUMO) is called conduction band (CB). The energy difference between the bottom of the conduction band and the top of the valence band in a semiconductor is called band gap energy ( $E_g$ ).[22] In semiconductors the energy gap lies between 0-4 eV. Materials with zero band-gap are metals or semimetals, while those with an energy level gap larger than 4 eV are more frequently known as insulators.[22] On **Figure 1.4** a scheme of the electronic bands in solids is depicted.

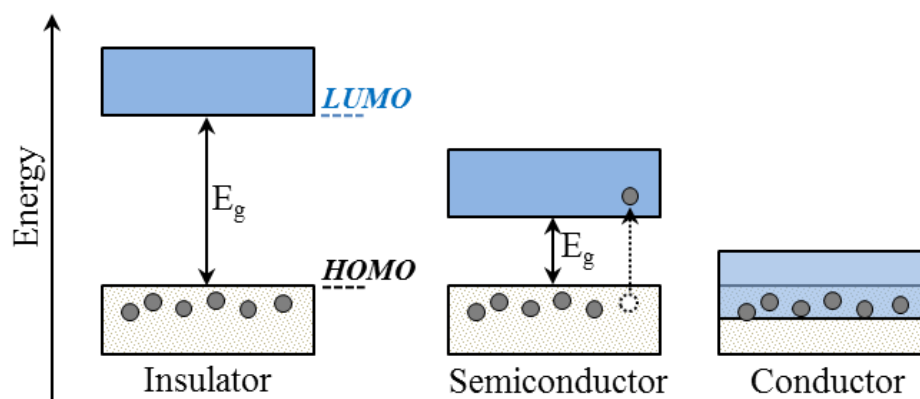


**Figure 1.4** Relative disposition of the CB (LUMO) and VB (HOMO) for an insulator, a semiconductor and a conductor.

In presence of light a semiconductor is activated when absorbs a photon with energy equal or higher than the band gap energy ( $E_{hv} \geq E_g$ ). The absorption leads to a charge separation due to the promotion of an electron ( $e^-$ ) from the valence band (VB) to the conduction band (CB), thus generating in the VB an electronic vacancy or positive hole ( $h^+$ ). The  $h_{VB}^+$  and  $e_{CB}^-$  are powerful oxidizing and reducing agents, respectively. This first step is called charge carrier generation. (Equation 1.1)

#### Equation 1.1 Charge carrier generation

**Figure 1.5** shows the main processes which may occur in the bulk or at the surface of the photocatalyst after the electron-hole pair ( $e^- - h^+$ ) generation (a). In first place the generated carriers needs to migrate from the bulk to the surface of the catalyst to be available for the following interaction with the other compounds present in the system (b). However these processes must compete with the major deactivation processes involving electron/hole recombination, which may occur in the bulk or at the surface of the photocatalyst in few nanosecond with simultaneous heat dispersion (c-d).[23]

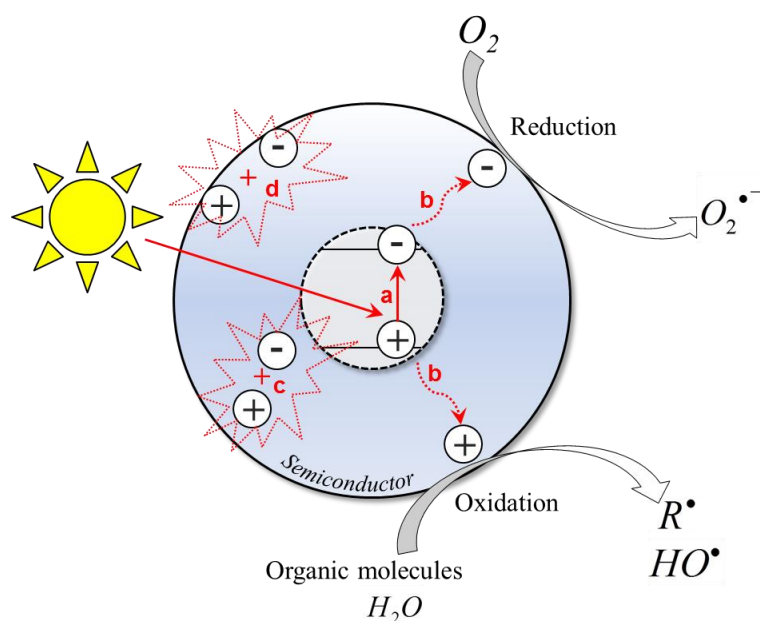


**Figure 1.5** Main processes occurring on a semiconductor particle: (a) photogeneration of electron/hole pair; (b) carriers migration at the surface of the semiconductor; (c-d) electron/ hole recombination in the bulk and at surface, respectively.

Once at the surface the ( $e^-$  -  $h^+$ ) can either directly attack the pollutant adsorbed by the catalyst surface or generate highly oxidizing species as a consequence of the interaction between the charge carriers with adsorbed oxygen and water molecule. Generally the holes mediate the oxidation of organic molecules and water by the formation of hydroxyl radicals ( $HO^\bullet$ ), and the electrons mediate reduction reactions by the formation of superoxide radicals ( $O_2^{\bullet-}$ ).<sup>[24]</sup> The main reactions can be described by the following equations:

**Equation 1.2** Direct hole attack to the adsorbed substrate (S)



**Equation 1.3** Oxidation of adsorbed water by the hole



**Equation 1.4** Oxidation of surface hydroxyl ion by the hole

**Equation 1.5** Reduction of oxygen by the electron

These mechanisms that take place at surface and interfacial areas of the  $\text{TiO}_2$  catalyst allow the degradation of contaminants and one must notice that the main contribution to the photocatalytic degradation of organic contaminant in water is given by the formation of highly reactive hydroxyl radicals ( $\text{HO}^\bullet$ ), possible only in the presence of water and dissolved oxygen.[25]

### 1.3.2 Catalysts for photocatalytic reactions

The semiconductors that are most commonly used as photocatalysts are oxides or sulfides of the transition metals.[26] In the last few decades several semiconductors have been successfully reported as photocatalysts for environmental applications, including titanium dioxide ( $\text{TiO}_2$ ), zinc oxide ( $\text{ZnO}$ ), zirconium dioxide ( $\text{ZrO}_2$ ), iron (III) oxide ( $\text{Fe}_2\text{O}_3$ ), cerium oxide ( $\text{CeO}_2$ ), tungsten trioxide ( $\text{WO}_3$ ), zinc sulfide ( $\text{ZnS}$ ), cadmium sulfide ( $\text{CdS}$ ).[27] It is commonly acknowledged that a semiconductor photocatalytic material should possess five essential property requirements, which are: being photoactive, able to be excited by visible and/or near-UV light, biologically and chemically inert (i.e., not prone to photocorrosion), non-toxic and inexpensive.[28]

**Figure 1.6** shows the band gap energies and redox potentials (voltage vs. standard hydrogen electrode (NHE) at pH 7) of some of the most common semiconductors used as catalysts. The lower edge of the conduction band (grey colour) and upper edge of the valence band (white colour) are presented along with the band gap in electron volts. The wider a band gap is the more energy (short wavelength) is needed to activate the transfer of electrons between bands. The band gap value defines the range of irradiation wavelengths in which the semiconductor is active as photocatalyst. Furthermore, for organic pollution degradation purposes, the redox potential of hydroxyl radicals should lie in its bandgap.

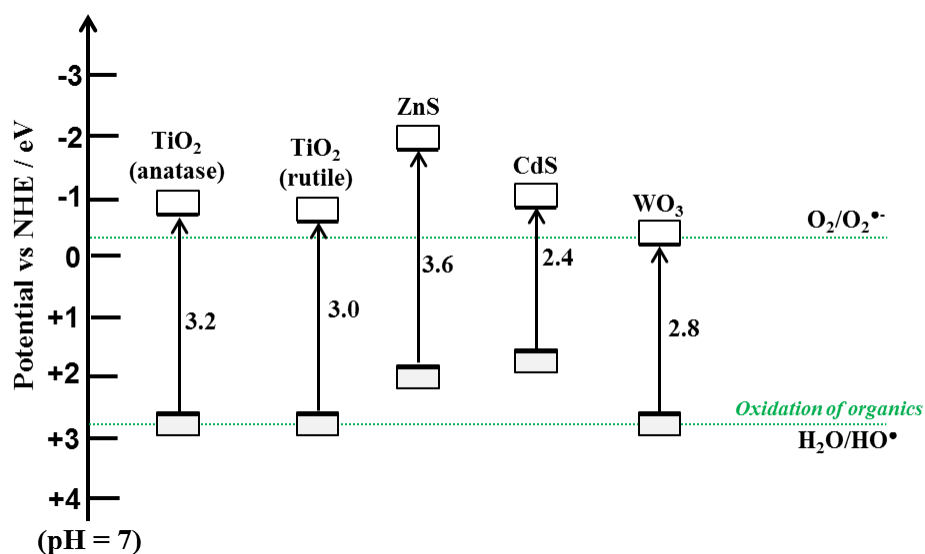


**Figure 1.6** Band positions of some typical photocatalysts (at pH= 7 in aqueous solutions).[29]

Although these semiconductor have been widely tested as heterogeneous photocatalysts, their use for large-scale applications is restricted because of one or more of the following reasons:[26]

- instability in aqueous medium that leads to the decomposition of the catalyst;
- large band gap that often necessitates the use of UV light;
- high rate of electron-hole recombination.

For example, materials such as CdS has a relatively shorter band gap (2.4 eV), but it is insufficiently stable in aqueous media, since it readily undergoes photoanodic corrosion realising toxic  $\text{Cd}^{2+}$  ions in water.[30, 31] Similar behaviour was observed also for  $\text{WO}_3$  and  $\alpha\text{-Fe}_2\text{O}_3$  (hematite), both active in the visible region, but probably because of corrosion show significantly low activity in aqueous media.[32] Although ZnO and  $\text{TiO}_2$  have similar band gap energies (3.2 eV), the former shows some instability in illuminated aqueous solutions, with formation of  $\text{Zn}(\text{OH})_2$  on the particle surface leading to the deactivation of the catalyst, thus its tendency for photodissolution is a problem that affects its efficiency as a photocatalyst.[33, 34] Because it has a strong oxidizing power under UV irradiation, high chemical stability, low cost and low toxicity  $\text{TiO}_2$  is the most used photocatalyst for environmental applications. In the next section, a detailed description about this remarkable material is presented.

#### 1.4 Titanium dioxide as photocatalyst

Titanium dioxide ( $\text{TiO}_2$ ) is the most commercially utilised semiconductor material. It was discovered in the year 1821, and is reported to be one amongst the top 20 inorganic chemicals of industrial importance.[35] Because of its brightness and a very high refractive index it is widely used as a pigment to provide whiteness and opacity to paints, plastics, papers, inks, food, etc.  $\text{TiO}_2$  is also commonly used in cosmetic and skincare products, and it is present in many types of sunblock products to avoid the effect of UV light over the skin. However, despite the vast number of applications of  $\text{TiO}_2$ , the most studied and promising is its exceptional photocatalytic response for environmental remediation applications.[36] The overall photocatalytic performance of  $\text{TiO}_2$  has been suggested to depend on some specific parameters such as phase, crystallinity, particle size and surface area.[37] The crystalline phase of  $\text{TiO}_2$  is one of the most important factors influencing its photocatalytic performance and this semiconductor exists in nature as three main crystalline polymorphs; anatase, rutile and brookite. **Figure 1.7** illustrates the unit cell structures of three  $\text{TiO}_2$  crystals.



**Figure 1.7** Representations of the crystal structures of the common  $\text{TiO}_2$  polymorphs: anatase (tetragonal,  $a = 0.3785 \text{ nm}$ ,  $c = 0.9513 \text{ nm}$ ) (a), rutile (tetragonal,  $a = 0.4593 \text{ nm}$ ,  $c = 0.2959 \text{ nm}$ ) (b), and brookite (orthorhombic,  $a = 0.9181 \text{ nm}$ ,  $b = 0.5455 \text{ nm}$ ,  $c = 0.5142 \text{ nm}$ ) (c). Adapted from reference [38].

Anatase and rutile  $\text{TiO}_2$ , both with tetragonal structure, show different lattice configuration: hexagonal close packing (hcp) and cubic close packing (ccp), respectively. In their structures, the basic building block consists of a titanium ion ( $\text{Ti}^{4+}$ ) surrounded by six oxygen ( $\text{O}^{2-}$ ) but in anatase, the Ti–O distances are shorter ( $1.934$  and  $1.980 \text{ \AA}$  versus  $1.949$  and  $1.980 \text{ \AA}$  in rutile) while the Ti–Ti distances are greater than that in rutile ( $3.79$  and  $3.04 \text{ \AA}$  versus  $3.57$  and  $2.96 \text{ \AA}$ ). These differences in lattice structure lead to different electronic band structure and band gap energy,  $3.2 \text{ eV}$  for anatase and  $3.0$  for rutile, thus different photocatalytic behaviours.[39] Despite the higher band gap energy, anatase is generally reported to exhibit the greater photocatalytic activity compared to rutile.[40, 41] Brookite has an orthorhombic crystal structure and its band gap value is  $3.13 \text{ eV}$ .[42] This  $\text{TiO}_2$  form is quite rare in comparison with the other two and due to its low stability and difficulty in preparation it is not yet of commercial interest and it is less common for photocatalytic application. Moreover of the three different phases, rutile has been identified as a stable form while anatase and brookite are defined as metastable, as they can be transform to rutile phase upon calcination at temperatures exceeding  $\sim 600^\circ \text{C}$  .[40, 43] Thermal treatments allow to have mixed titania phases which are also commercially available.

Degussa P-25 is a successful commercialized  $\text{TiO}_2$  with a typical phase-mixed structure composed of anatase and rutile in a ratio of 4:1.[44] This catalyst is a standard benchmark for photocatalytic applications and it has been extensively used in many fields showing in most of the applications greater activity compared to pure anatase.[43, 44] Several studies have demonstrated that the intimate contact of the two phases can lead to a better response to light absorption and charge carrier, enhancement of charge separation and greater interactions at solid-liquid interface with adsorbed species.[45-47]

However  $\text{TiO}_2$  has been reported to be an excellent photocatalyst, there are still several limitations which need substantial improvement and that are hindering its large scale application. One of the major drawbacks is the narrow photocatalytic region ( $\lambda < 400 \text{ nm}$ ) of



TiO<sub>2</sub> which has the band gap of ~3.2 eV (corresponding to a wavelength of 388 nm). Thus the catalyst results to be active only in the UV region, which is less than 5% of the overall solar intensity.[39] The challenge is to avoid the UV lamps as light source and promote the use of visible and/or solar light as an alternative economical source of illumination especially for water and waste water treatment. Another big limitation is the fast recombination of photogenerated holes and electrons that reduces the overall efficiency of the process (low photonic yield). Moreover, since heterogenous photocatalysis occurs on the surface of TiO<sub>2</sub>, mass transfer limitation has to be minimized and surface area improved in order to have a good interaction with organic pollutants in water. The non-porous structure and the relatively low surface area of commercial TiO<sub>2</sub> (i.e. 50 m<sup>2</sup>.g<sup>-1</sup> for Degussa P-25) can result in slow photocatalytic degradation rates. Besides, the TiO<sub>2</sub> nanoparticles (~20-30 nm) may undergo aggregation due to the instability of the nanosized particle, which may hamper the light incidence on the active centres reducing its catalytic activity.[48] Furthermore, in water depollution, the use of suspensions requires a final step to separate the photocatalyst from the treated water, which is one of the main challenges in regards to both the economic and safety concern.

#### **1.4.1 Trends to improve TiO<sub>2</sub> activity**

In the last few decades, there has been a constant investigation to improve the photoactivity of TiO<sub>2</sub> based photocatalysts. The adopted strategies can be summarized as either morphological modifications, such as increasing surface area and porosity of the catalyst, or as chemical modifications, by incorporation of additional components in the TiO<sub>2</sub> structure (i.e. doping, metal coating and surface sensitization). Chemical modifications have been widely explored with the aim to obtain a visible light active (VLA) TiO<sub>2</sub>; however the overall efficiency of the photocatalytic process can be significantly enhanced by controlling the semiconductor morphology as the activity of TiO<sub>2</sub> largely depends on its crystal structure, surface area, particle size distribution, porosity and hydroxyl density. The approach of the present work is to control the morphology of the catalyst by designing TiO<sub>2</sub> supported materials, with the objective of obtaining an efficient photodegradation system with the following advantages:

- high specific surface area
- improved molecular transport/diffusion
- enhanced light harvesting
- strong adsorption affinity towards the pollutants
- good sedimentation ability for catalyst recovery and recycling.

## 1.5 Photocatalyst supports

Various materials have been explored as supports for  $\text{TiO}_2$  catalyst particles for the photodegradation of pollutants from wastewater. High surface area materials such as silica,[49, 50] alumina,[51] zeolites,[52] clays,[53] activated carbon,[54] carbon fibers and carbon nanotubes,[55, 56] have been used to prepare  $\text{TiO}_2$ -based composite catalysts. Among these materials, silica supports have been commonly used to simplify the separation of the photocatalyst after the reaction from the aqueous media.[49, 57, 58] Moreover strict control of synthesis and preparation parameters can be applied, tuning the physical properties of this kind of support; in particular the attainable high surface area of silica can markedly improve the catalytic activity by increasing the number of active sites for molecules to adsorb and the  $\text{TiO}_2$  surface readily available for the reaction.[59] Many researchers used SBA-15 as a support for photocatalytic applications because of its unique properties like large pore size, high surface area, thermal stability and framework delocalization capacity by attracting electrons compared to any other silicious porous materials.[60, 61]

### 1.5.1 Porous structure

According to IUPAC (International Union of Pure and Applied Chemistry) pores can be classified into three categories: micropores (below 2 nm in diameter), mesopores (between 2 and 50 nm) and macropores (greater than 50 nm).[62] (**Figure 1.8**)

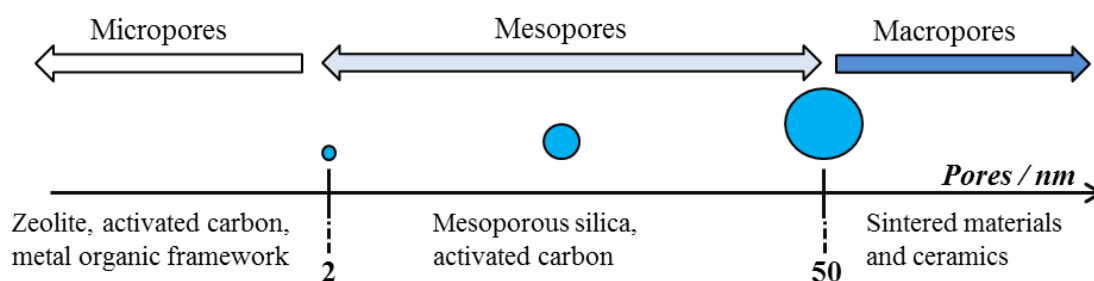


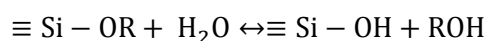
**Figure 1.8** Classification of porous materials according with the pores size (IUPAC standard).

### 1.5.2 Mesoporous SBA-15

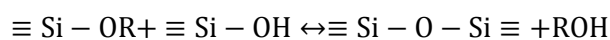
In 1992 researchers of the Mobil Oil Corporation reported the synthesis of a new kind of material in the form of ordered mesoporous silica-based and silica-alumina-based families known collectively as M41S.[63, 64] The synthesis of M41S is very versatile and allows, by suitably varying some synthetic parameters (i.e. pH, temperature) and the type and the concentration of some reagents (i.e. surfactant or source of silica), to obtain ordered mesoporous systems characterized by different morphological and structural properties. In the 1998 the Stucky group

from University of Santa Barbara (CA) produced a mechanically stable, porous silica material with well-defined 2D hexagonal structure and large surface area, called SBA-15 (Santa Barbara Amorphous). The synthesis of SBA-15 materials by Zhao et al.[65] became one of the most promising developments in the research field of this century. Compared with the other member of the family of mesoporous materials, the SBA-15 showed enhanced hydrothermal stability with thicker silica walls and larger pores,[66, 67] founding a wide range of application such as catalyst support.[60, 68]

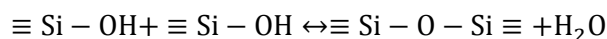
SBA-15 is synthesised in acid media (pH ~1) by using a triblock copolymer, as non-ionic structure directing agent (SDA),[65] which, during the condensation of the silica precursor, helps the formation of the mesostructured network. Block copolymers are amphiphilic molecules, which mean they are composed of a hydrophilic and a hydrophobic part, and the ratio between this two components influences micelles array, pore shape and architecture.[69] Pluronic P-123 is the symmetric triblock copolymer commonly used in the synthesis of SBA-15 as a soft template and it is made up from poly(ethylene oxide)-poly(propylene oxide)-poly(ethylene oxide) chains (PEO<sub>20</sub>-PPO<sub>70</sub>-PEO<sub>20</sub>).[65, 70] Firstly, P-123 surfactant is dissolved in acidic aqueous media and, due to its amphiphilicity nature, forms micelles in aqueous solutions to lower the free energy in the system. The micelles consist of a hydrophobic PPO core surrounded by hydrophilic PEO chains that form a corona around the core. Then silica source, normally tetraethylorthosilicate (TEOS) or tetramethoxysilane (TMOS), is added to the solution and the alkoxides start to hydrolyses (**Equation 1.6**) and polymerises to form a silica network (**Equation 1.7** and **Equation 1.8**). Both steps can be controlled by varying the pH and by adding salts to the aqueous solutions.



**Equation 1.6** Hydrolysis of the alkoxide group



**Equation 1.7** Alcohol condensation



**Equation 1.8** Water condensation

The hydrolysis rate changes depending on the nature of the silica precursor; in general, short alkyl chains hydrolyse faster than long chains, e.g. TMOS has a faster hydrolysis rate than TEOS. By tuning the hydrolysis and condensation rates, the properties of the silica gel can be controlled. The silica mesostructure formation mechanism has been discussed in several papers;[63, 69-72] however, in all the proposed mechanism, condensation followed by polymerization of silica leads to mesostructure and the main difference is the way in which the surfactants interact with the inorganic species. At the moment two main theories have been developed. One is based on the

liquid crystal templating (LCT) mechanism,[73] suggested by Beck et al. in which the formation of SBA-15 is assumed to be similar to the one of MCM-41. In this route the self-assembly process of the template results the formation of liquid crystal mesophase. Micelles start as spherical and arrange themselves in a hexagonal pattern, when the silica precursor is added it starts to condense on them to form the silica walls. On the other hand, Flodström et al.[74, 75] proposed a ‘cooperative self-assembly’ mechanism which takes place between the template and the mineral network precursor yielding the organised mesostructure. Silica hydrolysis followed by polymerisation generates attractive forces between micelles, which eventually coalesce forming cylindrical aggregates defining the 2D hexagonal pattern.[75] Among the different proposed approaches, this second mechanism is the most popular one adopted for the SBA-15 formation. Once this step is completed, the temperature is increased usually between 80– 130 °C and the hydrothermal treatment begins. The effect of this step is twofold: first, following the formation of the hexagonal structure, the PEO chains are trapped into the silica network [76, 77] and they are the source for the micropores in the final material; secondly hydrothermal treatment decreases the shrinkage of the silica walls upon calcination. The final step of the synthesis is the removal of the surfactants and calcination is the most common way to remove it from SBA-15. During the calcination, which is performed in air, the material is heated to 550 °C using a slow ramp rate (rr ~1 °C.min<sup>-1</sup>) to avoid damaging the mesoporous architecture and this temperature is held for 5 h before the material is cooled down to room temperature. Schematic formation mechanisms of SBA-15 are depicted in **Figure 1.9**.

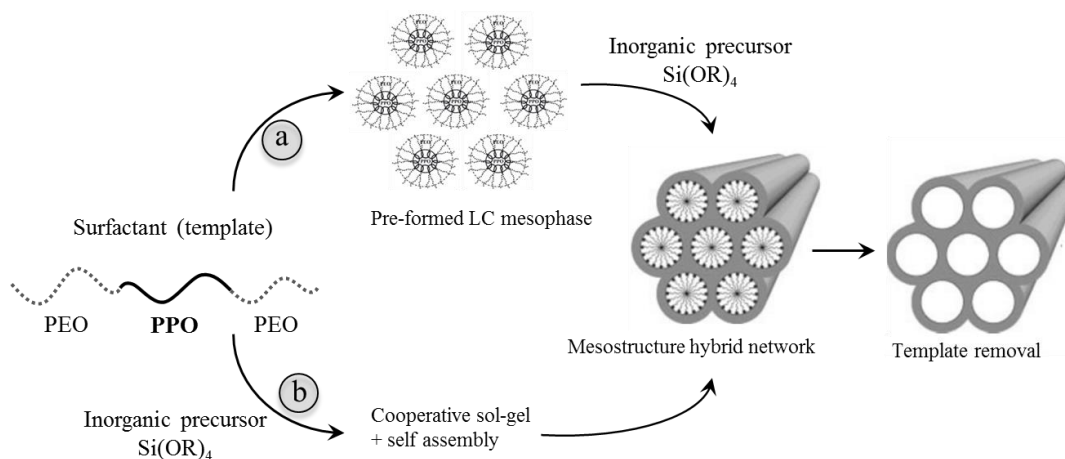


**Figure 1.9** Schematic stepwise of the two main formation mechanisms of SBA-15: self-assembly (a) and cooperative self-assembly (b) route.

### 1.5.3 Hierarchical SBA-15

In heterogeneous photocatalysis the advantages of hierarchical structures lead to enhancement of the overall photocatalytic efficiency which are summarized in **Figure 1.10**.

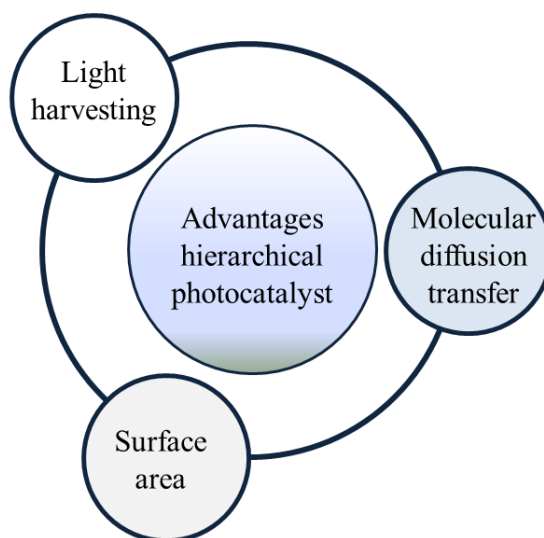


**Figure 1.10** Advantages of hierarchical nanostructures in heterogeneous photocatalysis. Figure adapted from reference. [29]

In first place, as discussed in the previous section (**Section 1.4.1**), increasing the surface area of semiconductors has been proven to be one of the most efficient approaches for enhancing their photocatalytic activity.[61, 78] It is well known that macro-mesoporous materials exhibit smaller surface areas compared to materials with only meso- and micropore structure but for the majority of them the specific surface area is still considerably high and lies in the range of 100–500 m<sup>2</sup> g<sup>-1</sup>. [79] Moreover hierarchical macro-mesoporous structures have additional features such as high surface area to volume ratio, large accessible surface area and better permeability, which improves the number of both adsorption and catalytic sites.[80] Furthermore hierarchical structures with meso- and macropores offers excellent transport paths for organic molecule in water, which are partially due to the reduced length of the mesopore channels but also to the increasing of accessible surface area.[81] Thus the reactant molecules can easily diffuse into the reaction sites and the products can also freely move out of them,[82, 83] improving the overall photoactivity of the process. Apart from improving surface area and mass transport, increasing of light harvesting has also been proven to be one of the most efficient approaches for enhancing photocatalytic activity through the fabrication of hierarchical structures.[72, 84] Enhancement of light collection and absorption is of great importance for photocatalytic materials and it believed to be due to the so-called light-scattering effects, which lead to a significant improvement in light trapping within the solid structure increasing the probability of light absorption.[81, 85] In addition, ordered macroporous materials can influence the propagation and velocity of electromagnetic radiation due to the modular variation in refractive index within their architecture which can be exploited to trap light and increase absorption to enhance the photocatalytic efficiency. This material characterized by periodic 1D, 2D or 3D structures are well known as photonic crystals (PCs) and they show two important features. The first is the existence of a photonic band gap (PBG), that is, a range of forbidden frequencies. Photons within this particular energy region cannot propagate through the

crystal and are, consequently, reflected (light trapping). The second is the slow photon effect which can actually improve the effective absorption of photons by reducing their velocity within the lattice of the PC. If the band gap of the semiconductor material is overlap with the edge of the PBG, increased photon absorption is predicted.[86] Photonic crystal based photocatalyst will be discussed further in **Chapter 4**.

So far, a great number of hierarchical semiconductors have been designed and synthesized and many attempts have been made to obtain a photocatalyst with highly controlled hierarchical morphologies, introducing in ordered mesostructures large templates such as polystyrene beads,[87-89]polymer emulsions,[90-92]and silica spheres.[93] In this work polystyrene (PS) beads of size 200 – 600 nm were used as hard templates, in order to obtain macropore structures with periodicities ranging from around 180 – 500 nm. Thus hierarchical macroporous-mesoporous SBA-15 (MM-SBA-15) has been prepared using a dual templating method of liquid crystal surfactants to form the mesopores, and a polystyrene bead template which is calcined to leave behind macropores.[94] As discussed above (**Section 1.5.2**) a large number of studies have been carried out to investigate the formation of mesostructures on the basis of surfactant self-assembly and its interactions with inorganic species and two mechanisms are generally accepted: true liquid crystal templating (TLCT)[95] and cooperative liquid-crystal template. For the fabrication of MM-SBA-15, the used concentration of surfactant was so high that under the synthesis conditions (pH and temperature) a lyotropic liquid crystalline phase is formed without requiring the presence of silica precursor. This is typically described as a TLCT strategy for the SBA-15 synthesis. Macropores were introduced adding polystyrene beads during the templating of the mesopore network.[95] A general preparative route for the formation of hierarchical MM-SBA-15 through TLCT is reported in **Figure 1.11**. First, surfactant molecules assemble to form regular micellar array leading to the formation of micelle liquid crystals. Then the silica precursor (TMOS) and the hard template (PS beads) were added and the condensation of inorganic silica precursor over the micelle liquid crystals and the polystyrene spheres leads to formation of macro-mesostructure, the precursor infiltration was followed by removal of methanol under vacuum. Finally, removal by calcination of the surfactant micelle and PD beads templates gives the mesoporous silica structures.[69, 96, 97]

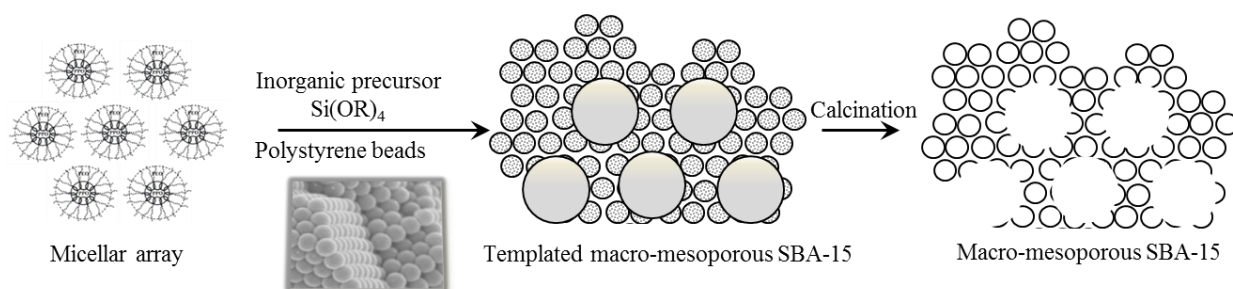


**Figure 1.11** Liquid crystal templating route to form macro-mesoporous silica using P-123 as soft template for the mesophase and polystyrene beads to introduce a macropore network.

## 1.6 Probe molecules

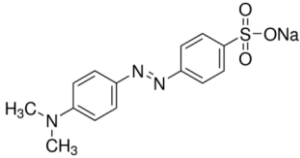
### 1.6.1 Organic dyes

Large quantities of highly coloured and toxic dye effluents are produced from different industries all around the world and extensive studies have been conducted on dyes degradation in aqueous system because. The release of these untreated effluents can cause serious pollution to environment and aquatic organisms.[98, 99] Dyes are usually the first contaminant to be recognized in industrial wastewater due to their high visibility even in very small concentrations (< 1 ppm).[100] and colour removal is the most complex and difficult task in water treatment. They are used in many industries like textile, paper, plastic, leather, ceramic, cosmetics, ink, food processing etc.[101] There are many classes of dyes commercially available and many ways to classify them. However the most appropriate system for the classification of dyes is by their chemical structure, which determines the colour, properties and uses of dyes, and provides the only rational basis of a classification of these compounds.[102]

In the field of photocatalysis the most studied dyes are the thiazine dyes (i.e. methylene blue), the xanthenes (i.e. rhodamine B) and the azo dyes (i.e. methyl orange). Azo dyes are by far the most important class, accounting for over 50-70% of all market of dyes. These contain one or more azo bonds (-N=N-) in their structure.[103] In this work, the photocatalytic test were performed using methyl orange (MO) as test compound, i.e. the photocatalytic activity of the synthesized TiO<sub>2</sub> based catalysts was tested based on the photodegradation rates of methyl orange solutions under UV-vis irradiation. This dye is one of the most stable azo dyes under irradiation and the results revealed that the percentage of MO molecules decomposed was actually due to the photoactivity of catalysts in solution and not to direct photolysis of the target compound. Methyl Orange is a very intensely colored compound and is commonly used in dyeing and printing textiles industry.

Its molecular formula is C<sub>14</sub>H<sub>14</sub>N<sub>3</sub>NaO<sub>3</sub>S with molar mass of 327.33 g.mol<sup>-1</sup>, and its molecular structure is shown in **Table 1.2** (the molecular size was evaluated with Chemdraw3D software).

**Table 1.2** Methyl Orange properties.

Name	Chemical structure	Size / nm	Molecular weight / g.mol <sup>-1</sup>	Density / g.cm <sup>-3</sup>	Absorption λ <sub>max</sub> / nm
Methyl orange		1.54	327.33	1.28	464

The photocatalytic reactions were followed by decolorization of MO aqueous solution. In azo dyes, colour disappearance usually reflects an attack on the azo bond (-N=N-) which strongly adsorb

light at 464 nm; thus the disappearance of this peak in the UV-vis absorption spectra can be easily followed by spectrophotometric measurements.[104] It is believed that hydroxyl radicals play an essential role in the fission of the  $-N=N-$  conjugated system, as the double bond in azo dyes is mainly vulnerable to electrophilic attack by highly reactive radicals.[105] The reaction usually proceeds with the opening of the aromatic rings.[106, 107] Therefore, aromatic amines or phenolic compounds are often observed as intermediate products. The ring opening yields a variety of carboxylic acids, which eventually decarboxylate by the photo-Kolbe reaction to  $CO_2$ . [108] However there are two mechanisms generally accepted regarding photocatalyzed dye degradation reactions. The first possible route is the indirect mechanism for dye degradation in presence of UV-active catalyst, which consisted of photon absorption by the photocatalyst followed by carrier generation and formation of active species on catalyst surface (hydroxyl radicals, superoxide radicals, hydroperoxyl radicals). Moreover both oxidation and reduction of dye can commonly take place on the surface of the photoexcited semiconductor photocatalyst.[109] The main reactions responsible of indirect dye degradation are represented by the equations below.

**Equation 1.9** Hydroxyl radical attack

**Equation 1.10** Direct hole attack to dye

**Equation 1.11** Direct electron attack to dye

The second route is a self-sensitization (or direct) mechanism, which involves the dye excitation under visible light photon ( $\lambda > 400$  nm) from the ground state (Dye) to an excited state (Dye\*). This excited state dye is further converted into an unstable dye cation radical (Dye $^{\bullet+}$ ) by an electron injection into the conduction band of  $TiO_2$ . [110] These trapped electrons located in the CB can react with the dissolved oxygen promoting the formation of superoxide radical anions ( $O_2^{\bullet-}$ ) which in turn result into hydroxyl radicals. These  $HO^{\bullet}$  radicals result to be the mainly responsible for the oxidation of the dye and the other organic product in the system.[111] The overall direct mechanism is represented in **Figure 1.12**.



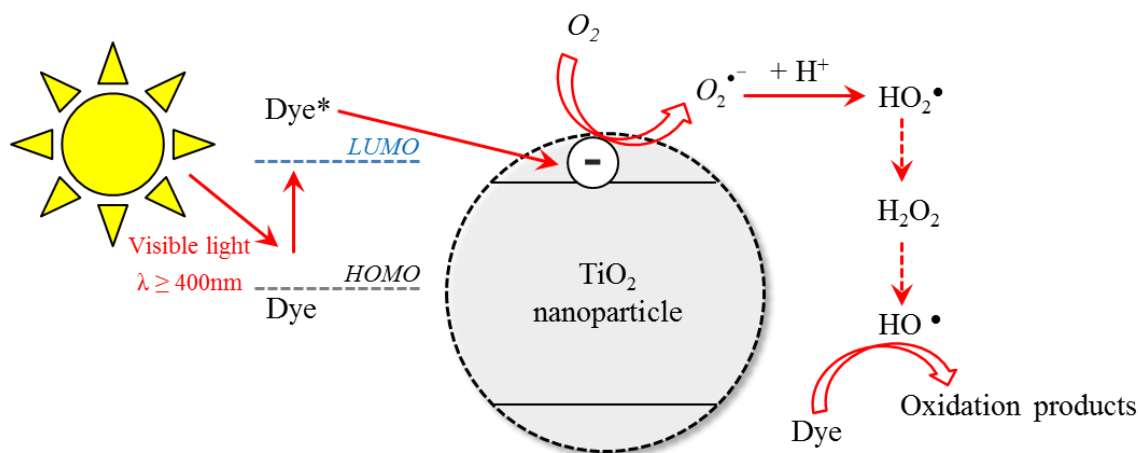


**Figure 1.12** Pictorial representation of direct dye degradation process.

According to many studies, the first described mechanism is generally prevalent over the self-sensitization route with a much more pronounced and faster contribution to the dye degradation process.[112]

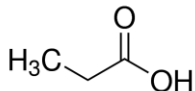
### 1.6.2 Carboxylic acids

Carboxylic acids are classified by the chemical structure  $R\text{-COOH}$  and, depending on the kind of substituents group (R), they can have different physical and chemical properties. In particular, aliphatic and aromatic carboxylic acids are widely used in various chemical process industries and, due to the environmental restrictions and the potential hazardous effects on flora and fauna, they need to be removed from the industrial effluents before disposal to natural water bodies. Treatment of waste water containing most widely-used industrial organic acids such as formic acid, acetic acid and propionic acid has been recognized as a significant expense to the industry and environment.[113] These carboxylic acids are fundamental materials in the chemical industry and are most widely used in the field of food and beverages as an acidulant and also in pharmaceutical and chemical industries (i.e. dye- and paint-producing, petrochemical and pigment industries).[114] Several procedures and techniques have been adopted for degradation and mineralization of short-chain carboxylic acids from contaminated waters and heterogeneous photocatalysis using  $\text{TiO}_2$  under UV light irradiation has been one of the most extensively studied techniques.[115] However the details of the photodegradation mechanism of carboxylic acid in liquid phase is not entirely clear yet, even in the cases of most simple saturated straight-chain carboxylic acids with less than five carbon atoms.[108, 116]

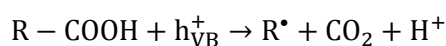
In this work propanoic acid ( $\text{C}_3\text{H}_6\text{O}_2$ ) was chosen as model substrate in order to explore the photodegradation mechanism over different  $\text{TiO}_2$  phases under UV LED irradiation. Adsorption and photodecomposition of propanoic acid were investigated combining studies in flow and batch

system using *in-situ* spectroscopy techniques and analytical methods to clarify the effect of interactions at solid-liquid interface and the degradation reaction mechanism. Propanoic acid was chosen as model substrate for these experiments as it meets some important criteria, such as being soluble in water, stable under UV irradiation (no photolysis), easy to detect by UV and IR spectroscopy techniques. Moreover its main degradation product is acetic acid which is stable enough to achieve high concentration in solution to be readily detected. Molecular formula and general properties of propanoic acid are reported in **Table 1.3**.

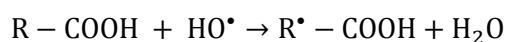
**Table 1.3** Propanoic acid properties.

Name	Chemical structure	Size / nm	Molecular weight / g.mol <sup>-1</sup>	Density / g.cm <sup>-3</sup>	Acidity / pK <sub>a</sub>
Propanoic acid		0.37	74.08	0.98	4.88

Furthermore the understanding of the photodegradation mechanism of carboxylic acids is important because, in spite of the complexity of initial organic pollutants in waste water, in TiO<sub>2</sub> photocatalyzed processes, these compounds are always observed to accumulate and account for the majority of converted initial substrates besides CO<sub>2</sub>. [117] It is generally accepted that the photodecomposition of carboxylic acids is usually initiated via two main routes. The first route is the decarboxylation by means of so-called photo-Kolbe mechanism [118], which is exclusively originated from hole oxidation and it consists on the loss of the carboxylic group released as CO<sub>2</sub> and the formation of a carbon centred radical (R<sup>•</sup>). A second possible route involves the hydroxylation by means of generated hydroxyl radicals followed by Kolbe's decarboxylation. In this case the first HO<sup>•</sup> attack generates an alkyl radical and a water molecule. The possible initiation reactions of carboxylic acids degradation are represented by the equations below.



**Equation 1.12** Photo-Kolbe mechanism



**Equation 1.13** Hydroxyl radical attack

After one of these initial steps the reaction can evolve in different ways based on the experimental conditions (i.e. presence of oxygen) and the nature of the catalyst. [119, 120] In all the previous

reports the subject of surface adsorption of propionic acid and its relation to photoreactivity were hardly discussed.[121-123] Without knowing the surface adsorption, the adsorbed species directly involved in photoreactions may not be exactly assigned. In this thesis a detailed investigation of reaction pathway of propanoic acid over  $\text{TiO}_2$  is presented in **Chapter 5**.

## 1.7 Thesis aim

As outlined earlier in this chapter, heterogeneous photocatalysis offers many advantages on removal of pollutants present in wastewaters and the need for developing an economical and effective immobilized titania photocatalyst has driven this research. The overall aim of this work was to investigate the optimal strategy to synthesize a smart photocatalyst tuning its structural and optical properties. The synthesized  $\text{TiO}_2$  based catalysts were characterized and then the catalytic performances tested on photo-oxidation of organic dye in water under UV-vis light.

The first part of this work was focused on the controlling of the structural proprieties of the host support with high surface area. Composite photocatalysts consisting of semiconductor nanoparticles dispersed on ordered silica hosts were the first material to be studied.  $\text{TiO}_2$ -coated mesoporous SBA-15 was fabricated varying two main parameters: pores size of SBA-15 and then the  $\text{TiO}_2$  loading. The development of a composite material with high surface area was thought to be an interesting and promising avenue.

The following step was to improve the optical proprieties of the photocatalyst distributing  $\text{TiO}_2$  nanoparticles in photonic hosts with high surface area. Hierarchical SBA-15 with ordered macro-mesoporous architecture was fabricated from polystyrene sphere templates, with a range of stop bands in the visible region obtained varying the macropores size and the  $\text{TiO}_2$  loading. The shift of the stop band and the effect of overlap of the stop band position and the band gap of the semiconductor on the rate of dye degradation were also analyses and discussed.

However despite the importance of heterogeneous photocatalysis as strategy for water treatment, not enough is known about reactions occurring at the catalytic solid-liquid interface. Shortage of information on the molecular level can hinder a more rational design of the catalyst and process. For this reason the last part of the presented work has the aim to shed some light on the processes occurring at the solid-liquid interface by using in-situ spectroscopy. Photocatalysis by  $\text{TiO}_2$  was probed in situ using propanoic acid as target molecule, in order to identify the adsorption modes on the different titania phases and the reaction intermediates not always detectable in solution, because their life-cycle can be restricted to the interface. In this thesis, ATR IR technique is used to probe the solid-liquid interface and through the innovative design of the ATR flow cell reactor operando photocatalytic studies were performed.

## 1.8 References

- [1] S. Malato, P. Fernandez-Ibanez, M. I. Maldonado, J. Blanco, and W. Gernjak, "Decontamination and disinfection of water by solar photocatalysis: Recent overview and trends," *Catalysis Today*, vol. 147, pp. 1-59, Sep 15 2009.
- [2] W.C.Change.(2016).Available:[https://www.wccc-corp.com/single\\_post/2016/08/09/Water-stress-in-Africa-to-hit-64-per-cent-by-2025](https://www.wccc-corp.com/single_post/2016/08/09/Water-stress-in-Africa-to-hit-64-per-cent-by-2025)
- [3] W. U. N. W. W. A. P. UNESCO, "The United Nations World Water Development Report 2017: Wastewater, The Untapped Resource," 22 March 2017 2017.
- [4] L. Lapena, M. Cerezo, and P. Garciaaugustin, "Possible Reuse of Treated Municipal Waste-Water for Citrus Spp Plant Irrigation," *Bulletin of Environmental Contamination and Toxicology*, vol. 55, pp. 697-703, Nov 1995.
- [5] R. M. Bradley, S. Weeraratne, and T. M. M. Mediwake, "Water use projections in developing countries," *Journal American Water Works Association*, vol. 94, pp. 52-+, Aug 2002.
- [6] F. Edition, "Guidelines for drinking-water quality."
- [7] J. C. Crittenden, K. J. Howe, D. W. Hand, G. Tchobanoglous, and R. R. Trussell, *Principles of Water Treatment*: John Wiley & Sons, Incorporated, 2012.
- [8] M. M. Pendergast and E. M. Hoek, "A review of water treatment membrane nanotechnologies," *Energy & Environmental Science*, vol. 4, pp. 1946-1971, 2011.
- [9] W. H. Glaze and J. W. Kang, "Advanced oxidation processes. Description of a kinetic model for the oxidation of hazardous materials in aqueous media with ozone and hydrogen peroxide in a semibatch reactor," *Industrial & engineering chemistry research*, vol. 28, pp. 1573-1580, 1989.
- [10] F. Ross and A. B. Ross, "Selected specific rates of reactions of transients from water in aqueous solution. III. Hydroxyl radical and perhydroxyl radical and their radical ions," Notre Dame Univ., IN (USA). Radiation Lab.1977.
- [11] W. R. Haag and C. C. D. Yao, "Rate constants for reaction of hydroxyl radicals with several drinking water contaminants," *Environmental Science & Technology*, vol. 26, pp. 1005-1013, 1992/05/01 1992.
- [12] C. Huang, C. Dong, and Z. Tang, "Advanced chemical oxidation: its present role and potential future in hazardous waste treatment," *Waste management*, vol. 13, pp. 361-377, 1993.
- [13] A. Stasinakis, "Use of selected advanced oxidation processes (AOPs) for wastewater treatment—a mini review," 2008.
- [14] J. Hoigné, "Inter-calibration of OH radical sources and water quality parameters," *Water Science and Technology*, vol. 35, pp. 1-8, 1997.

- [15] E. J. Rosenfeldt, K. G. Linden, S. Canonica, and U. Von Gunten, "Comparison of the efficiency of OH radical formation during ozonation and the advanced oxidation processes  $O_3/H_2O_2$  and UV/ $H_2O_2$ ," *Water research*, vol. 40, pp. 3695-3704, 2006.
- [16] G. Palmisano, V. Augugliaro, M. Pagliaro, and L. Palmisano, "Photocatalysis: a promising route for 21st century organic chemistry," *Chemical Communications*, pp. 3425-3437, 2007.
- [17] A. Fujishima and K. Honda, "Electrochemical photolysis of water at a semiconductor electrode," *nature*, vol. 238, pp. 37-38, 1972.
- [18] J. H. Carey, J. Lawrence, and H. M. Tosine, "Photodechlorination of PCB's in the presence of titanium dioxide in aqueous suspensions," *Bulletin of Environmental Contamination and Toxicology*, vol. 16, pp. 697-701, 1976.
- [19] A. O. Ibadon and P. Fitzpatrick, "Heterogeneous photocatalysis: recent advances and applications," *Catalysts*, vol. 3, pp. 189-218, 2013.
- [20] D. F. Ollis, "Photocatalytic purification and remediation of contaminated air and water," *Comptes Rendus de l'Académie des Sciences - Series IIC - Chemistry*, vol. 3, pp. 405-411, 2000/11/01/ 2000.
- [21] P. Y. Yu and M. Cardona, *Fundamentals of semiconductors: physics and materials properties*: Springer, 1996.
- [22] P. Y. Yu and M. Cardona, *Fundamentals of semiconductors: physics and materials properties*: Springer, 2010.
- [23] K. Ozawa, M. Emori, S. Yamamoto, R. Yukawa, S. Yamamoto, R. Hobara, *et al.*, "Electron-Hole Recombination Time at TiO<sub>2</sub> Single-Crystal Surfaces: Influence of Surface Band Bending," *The Journal of Physical Chemistry Letters*, vol. 5, pp. 1953-1957, 2014/06/05 2014.
- [24] R. Vinu and G. Madras, "Environmental remediation by photocatalysis," *Journal of the Indian Institute of Science*, vol. 90, pp. 189-230, 2012.
- [25] A. Sclafani and J. M. Herrmann, "Comparison of the photoelectronic and photocatalytic activities of various anatase and rutile forms of titania in pure liquid organic phases and in aqueous solutions," *Journal of Physical Chemistry*, vol. 100, pp. 13655-13661, Aug 8 1996.
- [26] R. J. Tayade, R. G. Kulkarni, and R. V. Jasra, "Transition metal ion impregnated mesoporous TiO<sub>2</sub> for photocatalytic degradation of organic contaminants in water," *Industrial & engineering chemistry research*, vol. 45, pp. 5231-5238, 2006.
- [27] J. M. Herrmann, "Heterogeneous photocatalysis: State of the art and present applications," *Topics in Catalysis*, vol. 34, pp. 49-65, May 2005.
- [28] D. S. Bhatkhande, V. G. Pangarkar, and A. A. C. M. Beenackers, "Photocatalytic degradation for environmental applications - a review," *Journal of Chemical Technology and Biotechnology*, vol. 77, pp. 102-116, Jan 2002.

- [29] X. Li, J. Yu, and M. Jaroniec, "Hierarchical photocatalysts," *Chemical Society Reviews*, vol. 45, pp. 2603-2636, 2016.
- [30] D. Beydoun, R. Amal, G. Low, and S. McEvoy, "Role of nanoparticles in photocatalysis," *Journal of Nanoparticle Research*, vol. 1, pp. 439-458, Dec 1999.
- [31] N. Serpone, "Brief Introductory-Remarks on Heterogeneous Photocatalysis," *Solar Energy Materials and Solar Cells*, vol. 38, pp. 369-379, Aug 1995.
- [32] M. A. Fox and M. T. Dulay, "Heterogeneous Photocatalysis," *Chemical Reviews*, vol. 93, pp. 341-357, Jan-Feb 1993.
- [33] B. Neppolian, H. C. Choi, S. Sakthivel, B. Arabindoo, and V. Murugesan, "Solar/UV-induced photocatalytic degradation of three commercial textile dyes," *Journal of Hazardous Materials*, vol. 89, pp. 303-317, Jan 28 2002.
- [34] R. Comparelli, E. Fanizza, M. L. Curri, P. D. Cozzoli, G. Mascolo, and A. Agostiano, "UV-induced photocatalytic degradation of azo dyes by organic-capped ZnO nanocrystals immobilized onto substrates," *Applied Catalysis B-Environmental*, vol. 60, pp. 1-11, Sep 1 2005.
- [35] S. Riyas, V. A. Yasir, and P. N. M. Das, "Crystal structure transformation of TiO<sub>2</sub> in presence of Fe<sub>2</sub>O<sub>3</sub> and NiO in air atmosphere," *Bulletin of Materials Science*, vol. 25, pp. 267-273, 2002.
- [36] U. Diebold, "The surface science of titanium dioxide," *Surface science reports*, vol. 48, pp. 53-229, 2003.
- [37] J. M. Herrmann, C. Guillard, and P. Pichat, "Heterogeneous photocatalysis : an emerging technology for water treatment," *Catalysis Today*, vol. 17, pp. 7-20, 1993/05/26/ 1993.
- [38] Q. Guo, C. Zhou, Z. Ma, Z. Ren, H. Fan, and X. Yang, "Fundamental Processes in Surface Photocatalysis on TiO<sub>2</sub>," in *Heterogeneous Photocatalysis: From Fundamentals to Green Applications*, J. C. Colmenares and Y.-J. Xu, Eds., ed Berlin, Heidelberg: Springer Berlin Heidelberg, 2016, pp. 361-416.
- [39] A. L. Linsebigler, G. Lu, and J. T. Yates Jr, "Photocatalysis on TiO<sub>2</sub> surfaces: principles, mechanisms, and selected results," *Chemical reviews*, vol. 95, pp. 735-758, 1995.
- [40] J.-G. Li, T. Ishigaki, and X. Sun, "Anatase, brookite, and rutile nanocrystals via redox reactions under mild hydrothermal conditions: phase-selective synthesis and physicochemical properties," *The Journal of Physical Chemistry C*, vol. 111, pp. 4969-4976, 2007.
- [41] F. Labat, P. Baranek, C. Domain, C. Minot, and C. Adamo, "Density functional theory analysis of the structural and electronic properties of TiO<sub>2</sub> rutile and anatase polytypes: Performances of different exchange-correlation functionals," *The Journal of chemical physics*, vol. 126, p. 154703, 2007.

- [42] D. Reyes-Coronado, G. Rodriguez-Gattorno, M. E. Espinosa-Pesqueira, C. Cab, R. de Coss, and G. Oskam, "Phase-pure TiO(2) nanoparticles: anatase, brookite and rutile," *Nanotechnology*, vol. 19, Apr 9 2008.
- [43] J. Zhang, Q. Xu, Z. Feng, M. Li, and C. Li, "Importance of the relationship between surface phases and photocatalytic activity of TiO<sub>2</sub>," *Angewandte Chemie International Edition*, vol. 47, pp. 1766-1769, 2008.
- [44] D. C. Hurum, A. G. Agrios, K. A. Gray, T. Rajh, and M. C. Thurnauer, "Explaining the enhanced photocatalytic activity of Degussa P25 mixed-phase TiO<sub>2</sub> using EPR," *The Journal of Physical Chemistry B*, vol. 107, pp. 4545-4549, 2003.
- [45] W.-K. Wang, J.-J. Chen, X. Zhang, Y.-X. Huang, W.-W. Li, and H.-Q. Yu, "Self-induced synthesis of phase-junction TiO<sub>2</sub> with a tailored rutile to anatase ratio below phase transition temperature," vol. 6, p. 20491, 02/11/online 2016.
- [46] R. I. Bickley, T. Gonzalez-Carreno, J. S. Lees, L. Palmisano, and R. J. D. Tilley, "A structural investigation of titanium dioxide photocatalysts," *Journal of Solid State Chemistry*, vol. 92, pp. 178-190, 1991/05/01/ 1991.
- [47] T. Ohno, K. Sarukawa, K. Tokieda, and M. Matsumura, "Morphology of a TiO<sub>2</sub> Photocatalyst (Degussa, P-25) Consisting of Anatase and Rutile Crystalline Phases," *Journal of Catalysis*, vol. 203, pp. 82-86, 2001/10/01/ 2001.
- [48] Q. H. Zhang, L. Gao, and S. Zheng, "The photocatalytic properties of nanocrystalline TiO<sub>2</sub> in the rutile phase," *Acta Chimica Sinica*, vol. 59, pp. 1909-1913, 2001.
- [49] M.-J. López-Muñoz, R. van Grieken, J. Aguado, and J. Marugán, *Role of the support on the activity of silica-supported TiO<sub>2</sub> photocatalysts: Structure of the TiO<sub>2</sub>/SBA15 photocatalysts* vol. 101, 2005.
- [50] P. Pucher, M. Benmami, R. Azouani, G. Krammer, K. Chhor, J. F. Bocquet, *et al.*, "Nano-TiO<sub>2</sub> sols immobilized on porous silica as new efficient photocatalyst," *Applied Catalysis a-General*, vol. 332, pp. 297-303, Nov 20 2007.
- [51] S. Sakthivel, M. Shankar, M. Palanichamy, B. Arabindoo, and V. Murugesan, "Photocatalytic decomposition of leather dye: comparative study of TiO<sub>2</sub> supported on alumina and glass beads," *Journal of Photochemistry and Photobiology A: Chemistry*, vol. 148, pp. 153-159, 2002.
- [52] S. Sampath, H. Uchida, and H. Yoneyama, "Photocatalytic degradation of gaseous pyridine over zeolite-supported titanium dioxide," *Journal of Catalysis*, vol. 149, pp. 189-194, 1994.
- [53] J. Ménesi, L. Körösi, É. Bazsó, V. Zöllmer, A. Richardt, and I. Dékány, "Photocatalytic oxidation of organic pollutants on titania-clay composites," *Chemosphere*, vol. 70, pp. 538-542, 2008/01/01/ 2008.
- [54] K. Woan, G. Pyrgiotakis, and W. Sigmund, "Photocatalytic carbon-nanotube-TiO<sub>2</sub> composites," *Advanced Materials*, vol. 21, pp. 2233-2239, 2009.

- [55] H. Uchida, S. Itoh, and H. Yoneyama, "Photocatalytic decomposition of propyzamide using TiO<sub>2</sub> supported on activated carbon," *Chemistry Letters*, vol. 22, pp. 1995-1998, 1993.
- [56] P. Fu, Y. Luan, and X. Dai, "Preparation of activated carbon fibers supported TiO<sub>2</sub> photocatalyst and evaluation of its photocatalytic reactivity," *Journal of Molecular Catalysis A: Chemical*, vol. 221, pp. 81-88, 2004.
- [57] K. Gude, V. Gun'ko, and J. Blitz, *Adsorption and photocatalytic decomposition of methylene blue on surface modified silica and silica-titania* vol. 325, 2008.
- [58] C. Anderson and A. J. Bard, "Improved photocatalytic activity and characterization of mixed TiO<sub>2</sub>/SiO<sub>2</sub> and TiO<sub>2</sub>/Al<sub>2</sub>O<sub>3</sub> materials," *The Journal of Physical Chemistry B*, vol. 101, pp. 2611-2616, 1997.
- [59] Y. Li and S.-J. Kim, "Synthesis and characterization of nano titania particles embedded in mesoporous silica with both high photocatalytic activity and adsorption capability," *The Journal of Physical Chemistry B*, vol. 109, pp. 12309-12315, 2005.
- [60] S. Perathoner, P. Lanzafame, R. Passalacqua, G. Centi, R. Schlögl, and D. S. Su, "Use of mesoporous SBA-15 for nanostructuring titania for photocatalytic applications," *Microporous and Mesoporous Materials*, vol. 90, pp. 347-361, 2006.
- [61] W. Wang and M. Song, "Photocatalytic activity of titania-containing mesoporous SBA-15 silica," *Microporous and Mesoporous Materials*, vol. 96, pp. 255-261, 2006/11/26/ 2006.
- [62] J. Rouquerol, D. Avnir, D. H. Everett, C. Fairbridge, M. Haynes, N. Pernicone, *et al.*, "Guidelines for the Characterization of Porous Solids," *Characterization of Porous Solids Iii*, vol. 87, pp. 1-9, 1994.
- [63] C. Kresge, M. Leonowicz, W. Roth, and J. Vartuli, "Ordered mesoporous molecular sieves synthesized by a liquid-crystal template mechanism," *nature*, vol. 359, pp. 710-712, 1992.
- [64] J. Beck, J. Vartuli, W. J. Roth, M. Leonowicz, C. Kresge, K. Schmitt, *et al.*, "A new family of mesoporous molecular sieves prepared with liquid crystal templates," *Journal of the American Chemical Society*, vol. 114, pp. 10834-10843, 1992.
- [65] D. Zhao, Q. Huo, J. Feng, B. F. Chmelka, and G. D. Stucky, "Nonionic Triblock and Star Diblock Copolymer and Oligomeric Surfactant Syntheses of Highly Ordered, Hydrothermally Stable, Mesoporous Silica Structures," *Journal of the American Chemical Society*, vol. 120, pp. 6024-6036, 1998/06/01 1998.
- [66] A. Y. Khodakov, V. L. Zholobenko, R. Bechara, and D. Durand, "Impact of aqueous impregnation on the long-range ordering and mesoporous structure of cobalt containing MCM-41 and SBA-15 materials," *Microporous and Mesoporous Materials*, vol. 79, pp. 29-39, Apr 1 2005.
- [67] T. Linssen, K. Cassiers, P. Cool, and E. F. Vansant, "Mesoporous templated silicates: an overview of their synthesis, catalytic activation and evaluation of the stability," *Advances in Colloid and Interface Science*, vol. 103, pp. 121-147, Apr 25 2003.



- [68] H. Ding, H. Sun, and Y. Shan, "Preparation and characterization of mesoporous SBA-15 supported dye-sensitized TiO<sub>2</sub> photocatalyst," *Journal of Photochemistry and Photobiology A: Chemistry*, vol. 169, pp. 101-107, 2005.
- [69] Y. Wan, Y. Shi, and D. Zhao, "Designed synthesis of mesoporous solids via nonionic-surfactant-templating approach," *Chemical Communications*, pp. 897-926, 2007.
- [70] D. Zhao, J. Feng, Q. Huo, N. Melosh, G. H. Fredrickson, B. F. Chmelka, *et al.*, "Triblock copolymer syntheses of mesoporous silica with periodic 50 to 300 angstrom pores," *science*, vol. 279, pp. 548-552, 1998.
- [71] J. Frasc, B. Lebeau, M. Soulard, J. Patarin, and R. Zana, "In Situ Investigations on Cetyltrimethylammonium Surfactant/Silicate Systems, Precursors of Organized Mesoporous MCM-41-Type Siliceous Materials," *Langmuir*, vol. 16, pp. 9049-9057, 2000/11/01 2000.
- [72] G. J. d. A. Soler-Illia, C. Sanchez, B. Lebeau, and J. Patarin, "Chemical strategies to design textured materials: from microporous and mesoporous oxides to nanonetworks and hierarchical structures," *Chemical reviews*, vol. 102, pp. 4093-4138, 2002.
- [73] H. G. Schimmel, G. J. Kearley, M. G. Nijkamp, C. T. Visserl, K. P. de Jong, and F. M. Mulder, "Hydrogen adsorption in carbon nanostructures: Comparison of nanotubes, fibers, and coals," *Chemistry-a European Journal*, vol. 9, pp. 4764-4770, Oct 6 2003.
- [74] K. Flodström, H. Wennerström, and V. Alfredsson, "Mechanism of Mesoporous Silica Formation. A Time-Resolved NMR and TEM Study of Silica- Block Copolymer Aggregation," *Langmuir*, vol. 20, pp. 680-688, 2004.
- [75] K. Flodström, C. V. Teixeira, H. Amenitsch, V. Alfredsson, and M. Lindén, "In Situ Synchrotron Small-Angle X-ray Scattering/X-ray Diffraction Study of the Formation of SBA-15 Mesoporous Silica," *Langmuir*, vol. 20, pp. 4885-4891, 2004/06/01 2004.
- [76] G. Prieto, A. Martínez, R. Murciano, and M. A. Arribas, "Cobalt supported on morphologically tailored SBA-15 mesostructures: the impact of pore length on metal dispersion and catalytic activity in the Fischer-Tropsch synthesis," *Applied Catalysis A: General*, vol. 367, pp. 146-156, 2009.
- [77] Y.-l. Su, J. Wang, and H.-z. Liu, "Formation of a Hydrophobic Microenvironment in Aqueous PEO-PPO-PEO Block Copolymer Solutions Investigated by Fourier Transform Infrared Spectroscopy," *The Journal of Physical Chemistry B*, vol. 106, pp. 11823-11828, 2002/11/01 2002.
- [78] L. Zhang, W. Wang, L. Zhou, and H. Xu, "Bi<sub>2</sub>WO<sub>6</sub> Nano- and Microstructures: Shape Control and Associated Visible-Light-Driven Photocatalytic Activities," *Small*, vol. 3, pp. 1618-1625, 2007.
- [79] J. Yu, L. Zhang, B. Cheng, and Y. Su, "Hydrothermal preparation and photocatalytic activity of hierarchically sponge-like macro-/mesoporous titania," *The Journal of Physical Chemistry C*, vol. 111, pp. 10582-10589, 2007.

- [80] S. Luo, F. Chai, L. Zhang, C. Wang, L. Li, X. Liu, *et al.*, "Facile and fast synthesis of urchin-shaped Fe<sub>3</sub>O<sub>4</sub>@Bi<sub>2</sub>S<sub>3</sub> core-shell hierarchical structures and their magnetically recyclable photocatalytic activity," *Journal of Materials Chemistry*, vol. 22, pp. 4832-4836, 2012.
- [81] J. Du, X. Lai, N. Yang, J. Zhai, D. Kisailus, F. Su, *et al.*, "Hierarchically ordered macro-mesoporous TiO<sub>2</sub>-graphene composite films: improved mass transfer, reduced charge recombination, and their enhanced photocatalytic activities," *ACS nano*, vol. 5, pp. 590-596, 2010.
- [82] M. D. Hernández-Alonso, F. Fresno, S. Suárez, and J. M. Coronado, "Development of alternative photocatalysts to TiO<sub>2</sub>: challenges and opportunities," *Energy & Environmental Science*, vol. 2, pp. 1231-1257, 2009.
- [83] W. Ho, C. Y. Jimmy, and S. Lee, "Synthesis of hierarchical nanoporous F-doped TiO<sub>2</sub> spheres with visible light photocatalytic activity," *Chemical Communications*, pp. 1115-1117, 2006.
- [84] T. Kamegawa, Y. Ishiguro, H. Seto, and H. Yamashita, "Enhanced photocatalytic properties of TiO<sub>2</sub>-loaded porous silica with hierarchical macroporous and mesoporous architectures in water purification," *Journal of Materials Chemistry A*, vol. 3, pp. 2323-2330, 2015.
- [85] S. Kumar, C. M. A. Parlett, M. A. Isaacs, D. V. Jowett, R. E. Douthwaite, M. C. R. Cockett, *et al.*, "Facile synthesis of hierarchical Cu<sub>2</sub>O nanocubes as visible light photocatalysts," *Applied Catalysis B: Environmental*, vol. 189, pp. 226-232, 2016/07/15/2016.
- [86] H. Kisch, "Semiconductor photocatalysis—mechanistic and synthetic aspects," *Angewandte Chemie International Edition*, vol. 52, pp. 812-847, 2013.
- [87] W. Cai, J. Yu, and M. Jaroniec, "Template-free synthesis of hierarchical spindle-like  $\gamma$ -Al<sub>2</sub>O<sub>3</sub> materials and their adsorption affinity towards organic and inorganic pollutants in water," *Journal of Materials Chemistry*, vol. 20, pp. 4587-4594, 2010.
- [88] Y. Jiao, Y. Liu, F. Qu, and X. Wu, "Dendritic  $\alpha$ -Fe<sub>2</sub>O<sub>3</sub> hierarchical architectures for visible light driven photocatalysts," *CrystEngComm*, vol. 16, pp. 575-580, 2014.
- [89] Q. Xiang, J. Yu, and M. Jaroniec, "Tunable photocatalytic selectivity of TiO<sub>2</sub> films consisted of flower-like microspheres with exposed {001} facets," *Chemical Communications*, vol. 47, pp. 4532-4534, 2011.
- [90] P. J. Hagerman, D. Hagerman, and J. Zubietta, "Organic-Inorganic Hybrid Materials: From "Simple" Coordination Polymers to Organodiamine-Templated Molybdenum Oxides," *Angewandte Chemie International Edition*, vol. 38, pp. 2638-2684, 1999.
- [91] H. Zhang, G. Hardy, Y. Khimyak, M. Rosseinsky, and A. Cooper, "Synthesis of hierarchically porous silica and metal oxide beads using emulsion-templated polymer scaffolds," *Chemistry of materials*, vol. 16, pp. 4245-4256, 2004.

- [92] B. P. Binks, "Macroporous silica from solid-stabilized emulsion templates," *Advanced Materials*, vol. 14, pp. 1824-1827, 2002.
- [93] S. Zhang, L. Chen, S. Zhou, D. Zhao, and L. Wu, "Facile Synthesis of Hierarchically Ordered Porous Carbon via in Situ Self-Assembly of Colloidal Polymer and Silica Spheres and Its Use as a Catalyst Support," *Chemistry of Materials*, vol. 22, pp. 3433-3440, 2010/06/08 2010.
- [94] J.-P. Dacquin, J. Dhainaut, D. Duprez, S. Royer, A. Lee, and K. Wilson, *An Efficient Route to Highly Organized, Tunable Macroporous-Mesoporous Alumina* vol. 131, 2009.
- [95] S. G. Wainwright, C. M. A. Parlett, R. A. Blackley, W. Zhou, A. Lee, K. Wilson, *et al.*, *True liquid crystal templating of SBA-15 with reduced microporosity* vol. 172, 2013.
- [96] F. Hoffmann, M. Cornelius, J. Morell, and M. Fröba, "Silica-based mesoporous organic–inorganic hybrid materials," *Angewandte Chemie International Edition*, vol. 45, pp. 3216-3251, 2006.
- [97] G. S. Attard, J. C. Glyde, and C. G. Goltner, "Liquid-crystalline phases as templates for the synthesis of mesoporous silica," *Nature*, vol. 378, pp. 366-368, 11/23/print 1995.
- [98] J. Levec and A. Pintar, "Catalytic wet-air oxidation processes: a review," *Catalysis Today*, vol. 124, pp. 172-184, 2007.
- [99] I. Ali, M. Asim, and T. A. Khan, "Low cost adsorbents for the removal of organic pollutants from wastewater," *Journal of environmental management*, vol. 113, pp. 170-183, 2012.
- [100] G. Liu, X. Li, J. Zhao, H. Hidaka, and N. Serpone, "Photooxidation pathway of sulforhodamine-B. Dependence on the adsorption mode on TiO<sub>2</sub> exposed to visible light radiation," *Environmental science & technology*, vol. 34, pp. 3982-3990, 2000.
- [101] K. Ranganathan, K. Karunakaran, and D. Sharma, "Recycling of wastewaters of textile dyeing industries using advanced treatment technology and cost analysis—case studies," *Resources, Conservation and Recycling*, vol. 50, pp. 306-318, 2007.
- [102] E. Wich, "The Colour Index," *Color Research & Application*, vol. 2, pp. 77-80, 1977.
- [103] M. Singh, R. Sharma, and U. Banerjee, "Biotechnological applications of cyclodextrins," *Biotechnology advances*, vol. 20, pp. 341-359, 2002.
- [104] M. Styliadi, D. I. Kondarides, and X. E. Verykios, "Pathways of solar light-induced photocatalytic degradation of azo dyes in aqueous TiO<sub>2</sub> suspensions," *Applied Catalysis B: Environmental*, vol. 40, pp. 271-286, 2003/02/28/ 2003.
- [105] H. Chun and W. Yizhong, "Decolorization and biodegradability of photocatalytic treated azo dyes and wool textile wastewater," *Chemosphere*, vol. 39, pp. 2107-2115, 1999.
- [106] J. Lü, J.-X. Lin, X.-L. Zhao, and R. Cao, "Photochromic hybrid materials of cucurbituril and polyoxometalates as photocatalysts under visible light," *Chemical Communications*, vol. 48, pp. 669-671, 2012.

- [107] M. R. Hoffmann, S. T. Martin, W. Choi, and D. W. Bahnemann, "Environmental applications of semiconductor photocatalysis," *Chemical reviews*, vol. 95, pp. 69-96, 1995.
- [108] B. Kraeutler and A. J. Bard, "Heterogeneous photocatalytic decomposition of saturated carboxylic acids on titanium dioxide powder. Decarboxylative route to alkanes," *Journal of the American Chemical Society*, vol. 100, pp. 5985-5992, 1978.
- [109] K. Vinodgopal, I. Bedja, S. Hotchandani, and P. V. Kamat, "A photocatalytic approach for the reductive decolorization of textile azo dyes in colloidal semiconductor suspensions," *Langmuir*, vol. 10, pp. 1767-1771, 1994.
- [110] A. Ajmal, I. Majeed, R. Malik, H. Idriss, and M. Nadeem, *ChemInform Abstract: Principles and Mechanisms of Photocatalytic Dye Degradation on TiO<sub>2</sub> Based Photocatalysts: A Comparative Overview* vol. 4, 2014.
- [111] G. Sivalingam, K. Nagaveni, M. Hegde, and G. Madras, "Photocatalytic degradation of various dyes by combustion synthesized nano anatase TiO<sub>2</sub>," *Applied Catalysis B: Environmental*, vol. 45, pp. 23-38, 2003.
- [112] J. Zhao, T. Wu, K. Wu, K. Oikawa, H. Hidaka, and N. Serpone, "Photoassisted degradation of dye pollutants. 3. Degradation of the cationic dye rhodamine B in aqueous anionic surfactant/TiO<sub>2</sub> dispersions under visible light irradiation: evidence for the need of substrate adsorption on TiO<sub>2</sub> particles," *Environmental science & technology*, vol. 32, pp. 2394-2400, 1998.
- [113] S. Kumara and B. Babub, "Separation of Carboxylic Acids from Waste Water via Reactive Extraction."
- [114] B. Wu, J. Zhang, Z. Wei, S. Cai, and Z. Liu, "Chemical alignment of oxidatively shortened single-walled carbon nanotubes on silver surface," *The Journal of Physical Chemistry B*, vol. 105, pp. 5075-5078, 2001.
- [115] S. Horikoshi, F. Hojo, H. Hidaka, and N. Serpone, "Environmental remediation by an integrated microwave/UV illumination technique. 8. Fate of carboxylic acids, aldehydes, alkoxycarbonyl and phenolic substrates in a microwave radiation field in the presence of TiO<sub>2</sub> particles under UV irradiation," *Environmental science & technology*, vol. 38, pp. 2198-2208, 2004.
- [116] R. Prakash, R. A. Rather, M. Kaur, and B. Pal, "Oxidative degradation of aliphatic carboxylic acids by photocatalysis with bare and Ag-loaded TiO<sub>2</sub> under UV light irradiation," *Particulate Science and Technology*, pp. 1-5, 2016.
- [117] V. Gandhi, M. Mishra, and P. Joshi, *Titanium Dioxide Catalyzed Photocatalytic Degradation of Carboxylic Acids from Waste Water: A Review* vol. 712, 2012.
- [118] B. Kraeutler and A. J. Bard, "Heterogeneous Photocatalytic Decomposition of Saturated Carboxylic-Acids on TiO<sub>2</sub> Powder - Decarboxylative Route to Alkanes," *Journal of the American Chemical Society*, vol. 100, pp. 5985-5992, 1978.

- [119] B. Wen, Y. Li, C. C. Chen, W. H. Ma, and J. C. Zhao, "An Unexplored O-2-Involved Pathway for the Decarboxylation of Saturated Carboxylic Acids by TiO<sub>2</sub> Photocatalysis: An Isotopic Probe Study," *Chemistry-a European Journal*, vol. 16, pp. 11859-11866, 2010.
- [120] Y. Nosaka, M. Kishimoto, and J. Nishino, "Factors governing the initial process of TiO<sub>2</sub> photocatalysis studied by means of in-situ electron spin resonance measurements," *Journal of Physical Chemistry B*, vol. 102, pp. 10279-10283, Dec 10 1998.
- [121] C. B. Mendive, D. W. Bahnemann, and M. A. Blesa, "Microscopic characterization of the photocatalytic oxidation of oxalic acid adsorbed onto TiO<sub>2</sub> by FTIR-ATR," *Catalysis Today*, vol. 101, pp. 237-244, Apr 15 2005.
- [122] P. Z. Araujo, C. B. Mendive, L. A. G. Rodenas, P. J. Morando, A. E. Regazzoni, M. A. Blesa, *et al.*, "FT-IR-ATR as a tool to probe photocatalytic interfaces," *Colloids and Surfaces a-Physicochemical and Engineering Aspects*, vol. 265, pp. 73-80, Sep 1 2005.
- [123] A. G. Young and A. J. McQuillan, "Adsorption/Desorption Kinetics from ATR-IR Spectroscopy. Aqueous Oxalic Acid on Anatase TiO<sub>2</sub>," *Langmuir*, vol. 25, pp. 3538-3548, Mar 17 2009.

## *Chapter 2*

### *Experimental*

## **2. Experimental**

### **2.1 Catalyst preparation**

#### **2.1.1 SBA-15 synthesis**

The preparation of SBA-15 was achieved using an established literature procedure by Zhao et al.[1] The SBA-15 has been synthesized by using a 2.6 wt. % solution of Pluronic P-123 triblock copolymers (poly(ethylene glycol)-poly(propylene glycol)-poly(ethylene glycol) (Sigma Aldrich), dissolved in acidic solution 1.6 M of hydrochloric acid (32%wt HCL, Sigma Aldrich) with a pH=1. The dissolved P-123 forms micelles that are suitable as soft templates to make structured mesoporous materials. The solution was prepared in a sealed flask and stirred for 2 hours, at 500 rpm and 35°C. Tetraethyl orthoxysilicate (TEOS) was then added to the mixture as silica source at a molar ratio of 60:1[TEOS]: [P-123] and stirred for an additional 24 hours under the same conditions.

Three batches were made with identical methods up until this step. The pore size and the thickness of the silica wall can be adjusted by varying the aging temperature. Therefore, three mixtures were aged at 80,100 and 120 °C for 24 hours in an oven in a sealed flask. The solids were recovered from each mixture by filtration, washed with ethanol and dried in the oven at 80 °C overnight. Removal of the P-123 framework was performed by calcination at 500 °C in a muffle furnace for 6 hours with a ramp rate of 1 °C.min<sup>-1</sup>.

#### **2.1.2 Polystyrene (PS) beads synthesis**

The emulsion polymerisation approach by Vaudreuil and co-workers [2] was adopted to generate monodisperse polystyrene (PS) beads. Polystyrene beads will be employed as a hard template to introduce macropores into the framework of SBA-15. The reactants for this synthesis procedure were styrene as main monomer, divinylbenzene as co-monomer and potassium persulfate as the initiator of the reaction. The reaction was performed on a large scale in a 2 L jacketed Radleys' reactor ready system at 90°C. The deionised water (1.275 L) was first introduced in the vessel flask, along with a condenser, thermocouple and a nitrogen line at 1.5 bar pressure under stirring at 300 rpm and the reactor was left outgassing at room temperature for overnight. In order to fully extract polymerisation inhibitors from the as-supplied monomer reagents, Styrene (Sigma Aldrich, 140 ml) and divinylbenzene (Sigma Aldrich, 27 ml) were washed three times with 0.1M NaOH and another three times with deionised water (using about the same volume of the monomer) and then added to the reaction vessel. Potassium persulfate (Sigma Aldrich, 0.35 g) was dissolved in deionized water (20 ml) at 80 °C. After 30 minutes of stirring at 300 rpm in the reactor at 90 °C, the potassium persulfate solution was added. After stirring under N<sub>2</sub> for 22 hours, the resultant

solid was recovered and separated by centrifugation at 8000 rpm for 3 hours. The beads were dried overnight at 80 °C, yielding approximately 70 grams.

### 2.1.3 TLCT macro-mesoporous SBA-15 synthesis

Macro-mesoporous SBA-15 (MM-SBA-15) was synthesised using the true liquid crystal template (TLCT) method which included the P-123 as soft template to obtain the mesophase and a hard macropore template of polystyrene spheres. The hierarchical material was obtained using an adapted protocol of Attard et al.[3] Pluronic P-123 (2 g) was mixed with hydrochloric acid acidified water (pH 2, 2 g, 2M) and sonicated for 3 hours at 40 °C to yield a homogeneous gel. The sol-gel exhibits a hexagonal mesophase. Tetramethoxysilane (TMOS), used as silica source, was then added (1.02 cm<sup>3</sup> 1:4 mole ratio to H<sub>2</sub>O) and mixed for 10 minutes to form a homogeneous liquid. Polystyrene beads (6 g, synthesis described in **Section 2.1.2**) were then added to the liquid. The evolved methanol was removed under a light vacuum (0.12 bar) at 40 °C to form a viscous gel. The gel was aged for 24 hours at room temperature to complete condensation, before a calcination treatment at 500 °C for 6 hours in air (ramp rate 3 °C min<sup>-1</sup>). A successful synthesis produces approximately 2.0 g of silica support (white solid).

### 2.1.4 Titania grafting

The grafting of titania was achieved using a modified procedure by Landau et al[4] in which triethylamine (TEA, Sigma Aldrich) was used to activate surface silanols on the silica and allow the reaction to proceed at lower temperatures (85 °C). The synthetic procedure involved mixing titanium isopropoxide (TTIP, Sigma-Aldrich) in anhydrous toluene (Sigma-Aldrich, water content < 0.002%) in the presence of TEA with SBA-15 or MM-SBA-15 material under stirring at 85 °C for 6 hours and under nitrogen flow. The procedure was conducted under an inert environment as the employed Ti precursor, titanium isopropoxide, hydrolyzes instantly upon contact with moisture forming large titania particles in the presence of water rather than the intended uniform coating. The concentration of titanium isopropoxide in toluene was 145 g.l<sup>-1</sup>, the molar ratio between TTIP and SBA-15 was fixed at 3.5 and the mass ratio TEA / SBA-15 at 1.5.

After the reaction, the solid was separated by filtration, washed with toluene (300 ml) and inserted in a 0.5 wt% water-ethanol solution under stirring for 24 hours for the final re-hydration of the grafted surface. The resultant solid was washed with ethanol (150 ml), dried in an oven to 120 °C and calcined raising the temperature for 1 h at 250 °C, 400 °C and finally for 4 h at 500 °C. Upon completion of the calcination procedure, TiO<sub>2</sub> would then be grafted on the surface.



## **2.2 Catalyst characterization**

### **2.2.1 Inductively coupled plasma optical emission spectroscopy (ICP-OES)**

Inductively coupled plasma-optical emission spectroscopy (ICP-OES) was employed to analyse the bulk composition of the TiO<sub>2</sub> based materials. ICP-OES is a technique in which the composition of elements in samples can be determined using plasma and a spectrometer.

Solid samples were dissolved or digested using a combination of acids, usually metal ions in 10 wt. % HNO<sub>3</sub>, in a closed microwave system, thus retaining potentially volatile analyte species. A peristaltic pump sends the resulting sample solution to a nebuliser and then into the core of argon plasma, which is created through electromagnetic induction and where temperatures of approximately 10000°C are attained. Thus, sample atoms break up in ions, lose electrons and recombine in the plasma, generating radiations at the characteristic wavelengths of the involved element, analysed in an adequate optical chamber. Calibration curves, obtained *via* different concentration standards, allow quantification of the unknown concentration in the analysed solution.

#### **Instrument and analysis specification:**

ICP- OES was performed using Thermo iCAP 7000 ICP-OES and a calibrated to an elemental standard (Sigma Aldrich, 1000 ppm) made up to give concentrations of 1, 10, 25, 50 and 100 ppm. Samples were digested in nitric in a microwave digester prior analysis.

### **2.2.2 X-ray fluorescence spectroscopy (XRF)**

X-ray fluorescence (XRF) is a non-destructive analytical technique used to determine the elemental composition of the synthesised materials.

The solid sample was irradiated with high energy X-rays from the controlled X-ray tube. X-rays with sufficiently high energy interact with atoms in their ground state causing emission of core electron, which leave behind an electron hole. The hole in the lower energy shell decreases atomic stability, which is overcome by the demotion of a high energy shell electron to the hole (demoted electron); this process generates excess energy, which is released as a secondary (or fluorescent) X-ray photon.[5] The energy of this X-ray is equal to the specific difference in energy between two quantum states of the electron and the XRF analysis is based on the measurement of this energy. Each of the elements present in the sample produces a set of characteristic fluorescent X-rays ('finger print') that is unique for that specific element. The result of this analysis is a graphical representation of X-ray intensity peaks as function of energy peaks. The peak energy identifies the

element (qualitative analysis) and the peak height/intensity is generally indicative of its concentration (quantitative analysis). Emission lines in the XRF spectra typically identify K-L and L-M transitions, according to IUPAC nomenclature, as shown in **Figure 2.1**.

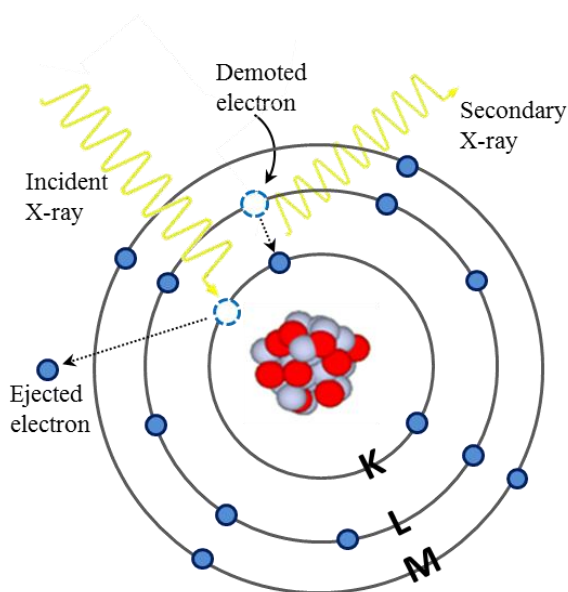


**Figure 2.1** Illustrative representation of X-ray fluorescence mechanism

#### **Instrument specification:**

XRF analysis was carried out via X-ray fluorescence on a Bruker S8 Tiger instrument, with the mass percentage of each element determined by SPECTRA software.

#### **2.2.3 Powder X-ray diffraction (XRD)**

Powder X-ray diffraction (XRD) is a non-destructive analytical technique, which due to the wavelengths within the Ångström range, can be used for phase identification of a crystalline material and can provide information on unit cell dimensions.[6]

This technique is based on the fact that when X-rays interact with a crystalline substance, a diffraction pattern can be obtained because of the similarity in the distance between atoms and X-ray wavelengths. An X-ray beam is projected towards the sample and the detector moves around a set angle, covering a range of  $2\theta$  values which are of interest. X-ray diffraction patterns result from the constructive and destructive interference of monochromatic X-rays upon scattering within a crystal lattice. The atoms in a crystalline material are arranged in a regular motif, resulting in planes of atoms which will scatter the incoming X-rays by different amounts depending on the plane spacing ( $d$ ) (**Figure 2.2**).

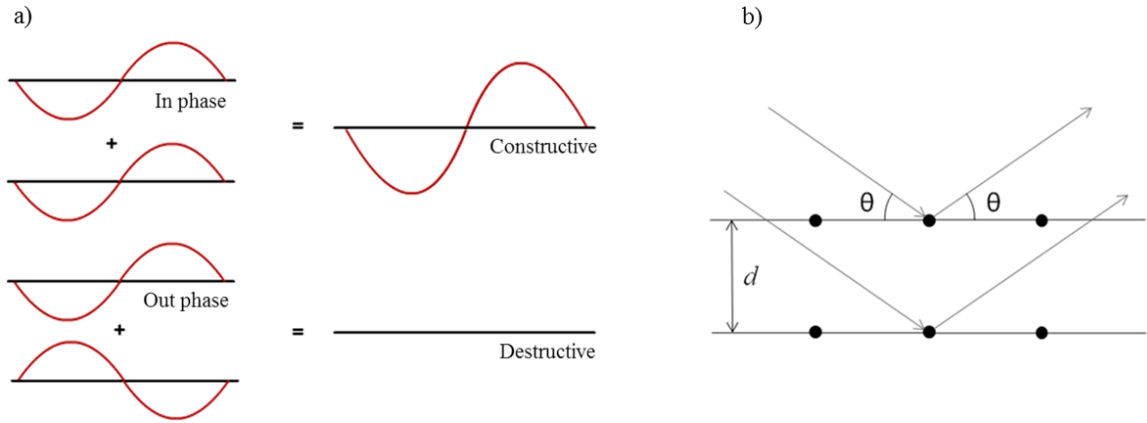


**Figure 2.2** Constructive and destructive interference of X-ray photons (a); schematic of X-ray interaction with a crystal lattice (b).

According to Bragg's law, the angle at which the X-ray is diffracted is dependent on the wavelength of the x-ray beam and the distance between lattice planes. This is mathematically explained by Bragg's equation (**Equation 2.1**):[7]

**Equation 2.1** Bragg's equation.

Where  $n$  is an order of reflection (multiplication integer),  $\lambda$  is the wavelength of the x-ray incident source ( $\lambda_{\text{cu}} = 0.154\text{nm}$ ),  $\theta$  is the diffraction Bragg's angle and  $d$  is the lattice spacing.

Upon calculation of layer spacing, the unit cell size (or pore spacing) could be calculated using the following equation derived from Pythagoras theorem: (**Equation 2.2**)

$$\sqrt{3}$$

**Equation 2.2** Pythagoras theorem.

Furthermore, as it is illustrated in **Figure 2.3**, if the pore diameter is measured (for example, by means of  $N_2$  porosimetry) the wall thickness ( $t_{\text{wall}}$ ) could be calculated by subtracting pore diameter from unit cell size.

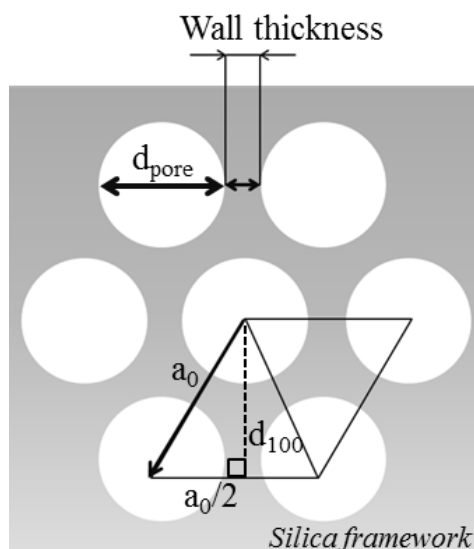


**Figure 2.3** Schematic representation of cross sectional SBA-15 pore channels, layer spacing and unit cell

Determination of averaged sizes of the crystalline particles in a solid material can also be obtained for the most intense peaks in the patterns using the Scherrer formula.[8, 9] In this equation the width of an individual X-ray reflection is inversely related to the size of the crystallites (**Equation 2.3**):

---

**Equation 2.3** Scherrer equation

where  $L$  = crystallite size (nm),  $B$  = FWHM of diffraction peak,  $S = 0.15$  (systematic broadening caused by diffractometer),  $\theta$  is the Bragg angle,  $k$  is known as the shape factor and  $\lambda$  is the wavelength of the X-ray. For this work, shape factor used is 0.9, which assumes roughly spherical particles. The wavelength  $\lambda$  for the X ray radiation produced by the copper tube is 0.154 nm.

**Instrument specification:**

XRD patterns were recorded on a Bruker D8 Advance diffractometer fitted with a LynxEye high-speed strip detector, both using Cu  $K\alpha$  (1.54 Å) sources with a nickel filter, calibrated against Quartz  $SiO_2$  standards. Low angle patterns were recorded over a range of  $2\theta = 0.3-8^\circ$  (step size  $0.01^\circ$ , scan speed  $0.014^\circ.s^{-1}$ ) and wide angle patterns over a range of  $2\theta = 25-75^\circ$  (step size  $0.02^\circ$ , scan speed  $0.020^\circ.s^{-1}$ ).

## 2.2.4 X-ray photoemission spectroscopy (XPS)

X-ray photoelectron spectroscopy (XPS) is a surface sensitive, analytical technique that provides information regarding elemental composition, oxidation state, and local elemental environment of a wide array of materials.

In XPS analysis, the sample to be studied is exposed to an X-ray photon beam. Usually, the  $K\alpha$  emission of Al ( $h\nu = 1486.6$  eV) or Mg ( $h\nu = 1253.6$  eV) are used.[10] As a result of this impact, a photoelectron is ejected leaving behind a core hole. (**Figure 2.4**) This creates an excited ionic state, which then relaxes into the final ground state as outer electrons fill the core holes.[11] The binding energy of a core electron is affected by chemical bonding and changes in oxidation state of the atom which results in a chemical shift in the detected photoelectron kinetic energy. In other words, if the positive charge on the atom is increased through electron withdrawing species bound to the surface or increased oxidation state, the binding energy of the core electron is also increased.[12]

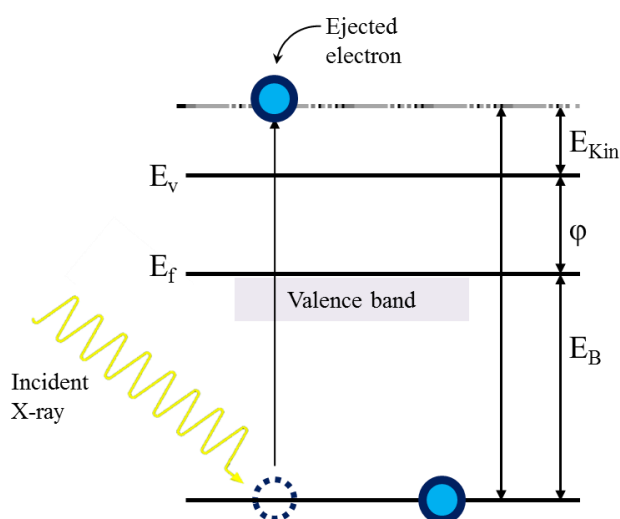


**Figure 2.4** Graphical representation of photoelectron ejection.

The kinetic energies of released photoelectrons can be measured and the binding energies calculated using **Equation 2.4**:

$$- \phi$$

**Equation 2.4** Kinetic energy.

where  $h\nu$  is the energy of the incoming photon,  $E_B$  the initial binding energy,  $\phi$  the work-function of the spectrometer.

The calculated binding energies can be referenced to a database of standards from the National Institute of Standards and Technology (NIST) photoelectron spectroscopy database to determine

chemical identity and garner information regarding chemical environment.[13] The final appearance of the XPS spectrum is greatly affected by the orbital in which a photoelectron is generated. When emission occurs from a non-s orbital ( $l > 0$ ), spin coupling interactions between orbital angular momentum ( $l$ ) and the spin of the ejected electron ( $s$ ) arise, the sum of which is known as the total angular momentum ( $j$ ). (**Equation 2.5**)

$$j = l + s$$

**Equation 2.5** Total angular momentum.

As the spin of the electron can be clockwise ( $+ \frac{1}{2}$ ) or anti-clockwise ( $- \frac{1}{2}$ ), two  $j$  values are produced. s orbitals do not possess any distinct orbital angular momentum ( $l = 0$ ), thus appearing as singlet peaks, but for all other orbitals the effect of spin coupling splits the resultant XPS peak into doublet form. These new peaks have a defined ratio equal to  $2j + 1$ . For example, if observing photoemission from a 2p orbital, for which the orbital angular momentum,  $l$ , is 1,  $j$  would be calculated to be either  $3/2$  or  $1/2$ .

#### **Instrument specification:**

XPS analysis was performed on a Kratos Axis HSi x-ray photoelectron spectrometer fitted with a charge neutraliser and magnetic focusing lens employing Al K $\alpha$  monochromated radiation (1486.6 eV). Spectral fitting was performed using CasaXPS version 2.3.14. Binding energies were corrected to adventitious C 1s at 284.6 eV. Errors were estimated by varying a Shirley background across reasonable limits.

### **2.2.5 Nitrogen porosimetry**

Porosimetry analysis is used to determine textural physical characteristics of materials such as surface area, pores diameter and pores volume.

Nitrogen gas was employed as the probe molecule and added to the free-space above the sample at a series of known pressures; the amount of gas adsorbed onto the surface of the sample up to the saturation pressure is measured. Vacuum is then applied in known stages, the gas removed and desorption of nitrogen is measured, which may result in hysteresis behaviour due to capillary condensation. By plotting the amount of adsorbate against the partial pressure of the system, an isotherm can be constructed, which can provide information regarding the material structure and properties.[14] The gas adsorption isotherms are classified by International Union of Pure and Applied Chemistry (IUPAC) into six types,[15] shown in **Figure 2.5**.

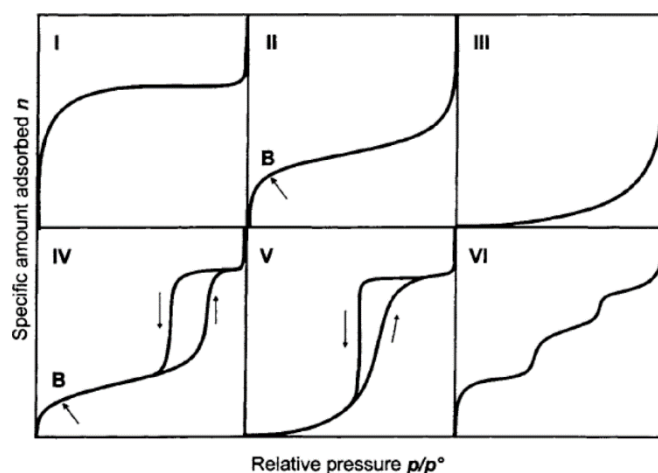


**Figure 2.5** Six types of gas physisorption isotherms.[14]

Type I is the Langmuir isotherm commonly observed in microporous materials (e.g. zeolite and activated carbon), of which the steep increase of adsorbed quantity at low relative pressure indicates that the available microporous volume is occupied. Type-II, and -IV isotherms are possible similar materials, in which multi-layer adsorption (starting at B) might occur in the middle relative pressure range. Type II is indicative of a non-porous or macroporous material (e.g. nonporous alumina and silica), while type IV is typical for mesoporous materials (e.g. mesoporous alumina and silica). Type-III and -V isotherms indicate the weak adsorbate-adsorbent interactions. The first is the result of stronger adsorbate-adsorbate interactions than adsorbate-adsorbent (e.g. graphite/water), the latter of porous materials and materials that have the weak interaction between the adsorbate and adsorbent (e.g. activated carbon/water). Types IV and V are characterized by presence of hysteresis loop which implies the occurrence of capillary condensation within mesopores. Finally type VI exhibits a stepwise profile which might be associated with layer-by-layer adsorption on a uniform surface.[16]

Surface areas were calculated using the Brunauer–Emmet–Teller (BET). BET is an extended version of the Langmuir adsorption model. Langmuir assumed that energy of adsorption for the first monolayer is generally considerably larger than that of the second and higher layers, thus forming multilayer is only possible at much higher pressures than the pressure required for formation of the first monolayer.[16] According to BET model, the molecules in the first layer were assumed to act as sites for the second-layer molecules, and so on to infinite layers. It is also assumed that the adsorption behaviour of all layers above the first monolayer is the same.[17] BET surface areas were evaluated from the measured of monolayer capacity over the range  $P/P_0 = 0.03–0.18$  and the resultant equation forms a  $y = mx + c$  format, as shown in the following equations:.

$$\frac{P}{V(P - P_0)} = \frac{C - 1}{V_m C} \cdot \left(\frac{P}{P_0}\right) + \frac{1}{V_m C}$$

**Equation 2.6** BET linear

$P$  = pressure;  $P_0$  = saturation pressure;  $V$  = volume adsorbed;  $V_m$  = monolayer volume;  $C$  = multilayer adsorption parameter

$$V_m = \frac{1}{(\text{Gradient} + \text{Intercept})}$$

**Equation 2.7** Monolayer volume

$$C = \frac{\text{Gradient}}{\text{Intercept}} + 1$$

**Equation 2.8** Definition of constant,  $C$

Surface areas are calculated from **Equation 2.9** using the monolayer volume, and assume  $N_2$  molecules close pack and occupy  $0.162 \text{ nm}^2$ . [17]

$$SA = \frac{V_m \sigma N_A}{mv}$$

**Equation 2.9** BET surface area calculation

$SA$  = surface area,  $V_m$  = monolayer volume,  $\sigma$  =  $N_2$  area;  $N_A$  = Avogadro number;  $m$  = sample mass;  $v$  = gas molar volume.

Calculation of the mesopore distribution was calculated from the desorption branch of the type IV isotherm, applying the Barrett, Joyner and Halenda (BJH) method. This method involves the area of the isotherm at relative pressure above 0.2 as it models the formation of multilayers and parallel capillary condensation within the pore structure of the material. When  $P/P_0 > 0.2$ , a rapid rise in  $N_2$  adsorption is observed as the mesopores saturate by capillary condensation. The pressure required for saturation is dependent on the pore diameter and the radius of curvature of the resulting meniscus formed by the condensed  $N_2$ . The quantitative expression of this phenomenon is given by Kelvin's equation [18]:

$$r_k = - \frac{2\gamma v_l}{RT} \cos \theta \ln \left( \frac{P}{P_0} \right)$$

**Equation 2.10** Kelvin's equation.



where  $r_k$  is Kelvin radius which represents the radius of curvature of a hemispherical meniscus,  $\gamma$  is surface tension of condensed phase at temperature  $T$ ,  $v_l$  is the molar volume of the liquid and  $\theta$  is contact angle of liquid with pore wall which is often considered zero assuming perfect wetting.

In particular case when the pore is cylindrical shape, it would be fair to assume that the condensate has a hemispherical meniscus with radius of  $r_k$ . But because there has been already some physisorption taken place,  $r_k$  will not be equal to pore radius,  $r_p$ . Therefore considering that the multilayer has a thickness of  $t$  and assuming the contact angle is zero ( $\theta=0$ ),  $r_p$  can be calculated from the following equation:

$$r_p = r_k + t$$

**Equation 2.11** Pore radius.

Applying this modification to Kelvin equation based on a cylindrical pore model (**Equation 2.11**) has been a basis for many methods applied for mesopore analysis, including the Barrett–Joyner–Halenda (BJH) method, which is the simplest and by far the most frequently used.[16]

The volume of micropores has been calculated using method developed by Lippens and de Boer which is mostly known as t-plot. Microporosity was assessed using the t-plot method, this assumes for a known monolayer volume subsequent adsorbate layer volumes can be calculated.[20] Computer modelled expected multi-layer thickness, using parameters for a nonporous reference, is plotted against the actual volume adsorbed for corresponding pressures. Extrapolation to the y-axis, which dissects at zero if monolayer accessibility is unrestricted, allows micropore volume to be determined.[18]

#### **Instrument specification:**

Quantachrom Nova 4200 instrument at 77 K. After outgassing approximately 80 mg of catalyst which was accurately weighed into the sample tube, at 120 °C for at least 2 h. Subsequently, the data were processed using NOVWin software version 2.2. Samples were degassed at 120 °C for 4 h prior to N<sub>2</sub> adsorption at –196 °C.

### **2.2.6 Diffuse reflectance UV–vis spectroscopy (DRUVS)**

Diffuse reflectance UV–vis spectroscopy (DRUVS) is a bulk technique based on the onset of UV/vis spectra that aims to directly measure the band gap energies and the absorption edge of nanostructured materials.

Diffuse reflectance spectroscopy is based on the interaction between an incident beam and a powdered sample, and measured the reflected radiant energy that has been partially absorbed, transmitted and partially scattered by the surface of the sample, with no defined angle of reflection. (**Figure 2.6**). The reflectance spectrum of a reference standard, like a white disk of spectralon (100% reflected light), should always be recorded prior to that of any other sample.

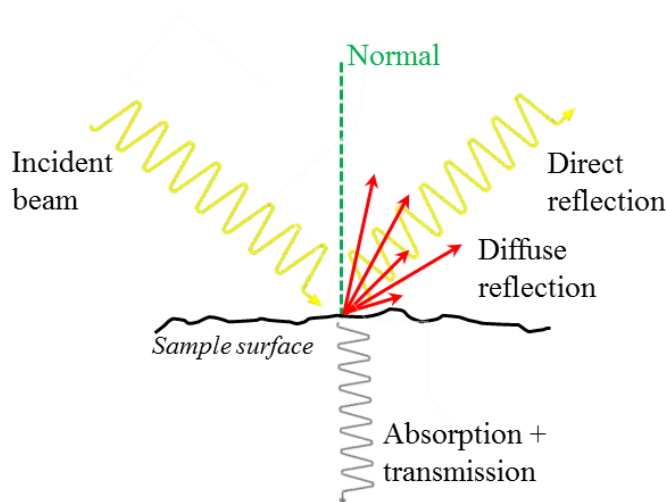


**Figure 2.6** Schematic of interaction of the incident beam and the sample surface.

The term band gap refers to the energy difference between the top of the valence band (VB) to the bottom of the conduction band (CB); in order for an electron to jump from a VB to a CB, it requires a specific minimum amount of energy for the transition, the band gap energy.[19]

The band gap of a semiconductor is always one of two types, a direct band gap or an indirect band gap. The minimal-energy state in the conduction band and the maximal-energy state in the valence band are each characterized by a certain crystal momentum ( $k$ -vector). In a direct band gap semiconductor, the top of the valence band and the bottom of the conduction band occur at the same value of momentum, after light absorption an electron can directly emit a photon. If the  $k$ -vector is different between the two bands, the band gap is called indirect; a photon cannot be emitted because the electron must pass through an intermediate state and transfer momentum to the crystal lattice. However this difference between the two types of band gaps is most important in design of optical devices. A diagram illustrating the band gap is shown in **Figure 2.7**.

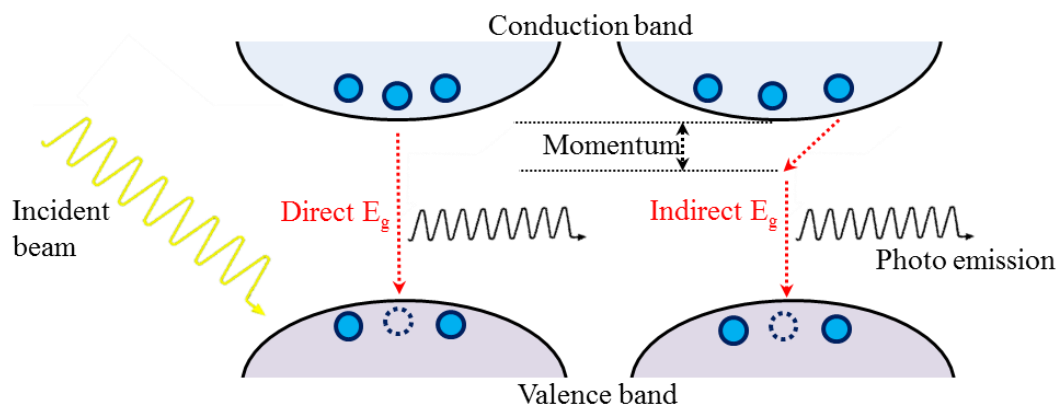


**Figure 2.7** Schematic of direct and indirect band gap energy.

Band gaps were calculated using **Equation 2.12**: [20, 21]

**Equation 2.12** Band gap evaluation

where  $\alpha$ ,  $h\nu$ ,  $E_g$  and  $A$  are absorption coefficient, light frequency, band gap, and a proportionality constant respectively, and variable  $\eta$  depends on the nature of the optical transition during photon absorption.

For indirect band gap materials such as anatase  $\text{TiO}_2$ ,  $E_g$  can be estimated from a Tauc plot of  $(h\nu)^{0.5}$  versus  $h\nu$ , [22] with the optical absorption coefficient obtained from the Kubelka–Munk function obtained from **Equation 2.13** below, by fitting a tangent to the band edge as shown in **Figure 2.8**:

**Equation 2.13** Kubelka-Munk function

where  $R$  is the reflectance obtained from the DRUV measurement were performed in diffuse reflectance mode.

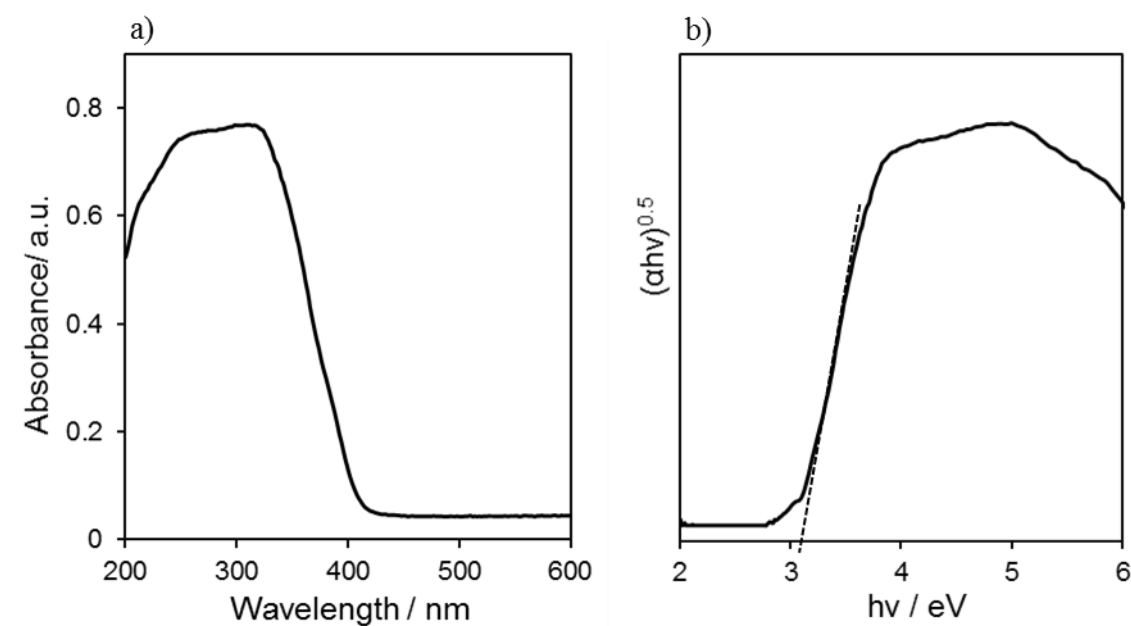


**Figure 2.8** UV–vis diffuse reflectance spectra (a) and Tauc plot for indirect semiconductor (b).

#### Instrument specification:

Ultraviolet-visible diffuse reflectance measurements have been acquired using a single beam Evolution 220 (Thermo Scientific) spectrometer equipped with an Integrating sphere. Optical properties of the powder sample were determined over the wavelength range 200–800 nm with spectralon disk as a standard reference material.

### 2.2.7 Vibrational spectroscopy

Vibrational spectroscopy is an energy sensitive method based on periodic changes of dipole moments (infrared spectroscopy, IR) or polarizabilities (Raman spectroscopy) caused by molecular vibrations of molecules or group of atoms.

These modes of vibration give rise to:

- absorption bands (IR) if the sample is irradiated with polychromatic light of suitable wavelengths upon changes of the dipole moment
- scattered light (Raman) if the sample is irradiated with a monochromatic light of a suitable wavelength upon a change of the polarizabilities.

Absorption bands and scattered light have characteristic energies to be determined and analysed.

### 2.2.7.1 Raman spectroscopy

Raman spectroscopy is an analytical technique that can provide detailed molecular information and crystallography information of a sample in non-destructive way. Raman spectroscopy is the measurement of the wavelength and intensity of inelastic scattering (or Raman scattering) of incident radiation from molecules and occurs when a photon interacts with the electric dipole of the molecule causing a change of its polarisability.[23]

The incident beam is usually a monochromatic light from a laser in the visible, near infrared, or near ultraviolet range. The laser light of known energy irradiates the samples and the incident photon excites the molecule into a virtual energy state before the photon scatters elastically or inelastically. Three different potential outcomes can be identified and are depicted in **Figure 2.9**.

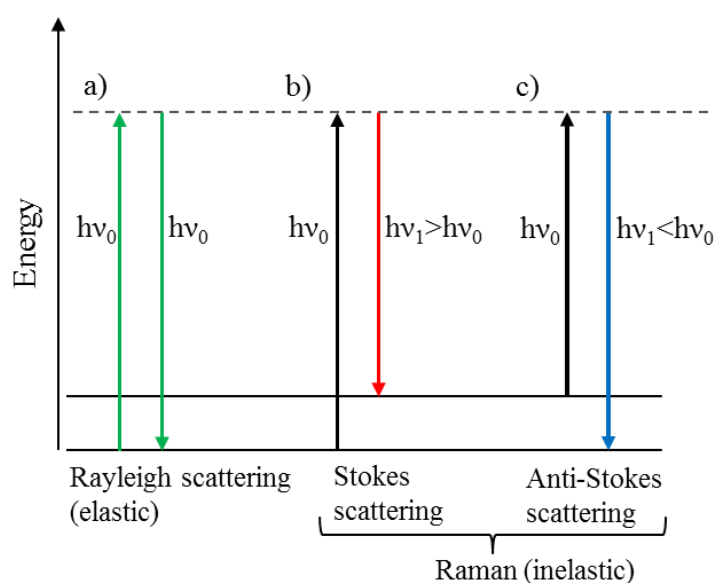


**Figure 2.9** Energy level diagram for Rayleigh and Raman scattering.

When the scattered photon has the same energy of the incoming photon, the scatter is elastic and it is also called Rayleigh scatter (a). In Stokes scatter (b), the energy from the photon is absorbed and the target molecule is promoted to a higher (virtual) energy state. Some of the energy from the incident photon is used by the molecule to excite it to higher level vibrational and rotational states; the rest is emitted as a photon of reduced energy. This photon is commonly called the Raman photon. Stokes scatter results when the molecule is excited from ground state ( $\nu_0$ ) and results in a molecule at a higher energy state ( $\nu_1$ ). Anti-Stokes scatter (c) results when a molecule in an excited state ( $\nu_1$ ) gains energy from the incident photon. It then decays back to a lower energy level, ground state ( $\nu_0$ ), with the emission of a higher energy photon than the incident radiation. Since very few molecules reside in the excited state, Anti-Stokes scatter does not predominate in a Raman Spectra.

Electromagnetic radiation from the irradiated sample is collected with a lens and sent through a monochromator. Elastic scattered radiation at the wavelength corresponding to Rayleigh scattering is filtered out by an optical filter, while the rest of the collected light is dispersed onto a detector. As a consequence of light interacting with molecular vibrations the energy of the laser photon being shifted up or down and this shift in energy gives information about the vibrational modes in the system.

#### **Instrument specification:**

Raman spectra were obtained on a InVia Raman Microscope Renishaw fitted with a 532 and 633 nm lasers, and Wire 3.4 software. Data was collected ranging between 100-1200  $\text{cm}^{-1}$ , employing 532 nm source and x20 lens magnification; samples were exposed for 10 sec to the beam source, recording 50 accumulations at 50 % laser power.

#### **2.2.7.2 Diffuse reflectance infra-red Fourier transform spectroscopy (DRIFT)**

Diffuse reflectance infrared Fourier transform spectroscopy (DRIFT) is a surface sensitive infrared spectroscopic technique used to probe the bonding mode of surface species.

The infrared beam is focussed onto the sample where it can interact with the material in several different ways. The beam can be scattered or reflected from neighbouring particles in the sample, or transmitted through particles, after which the beam can be scattered or reflected once more. Infrared radiation absorption causes an excitation of the vibrational modes of surface functional groups, either stretching or bending modes, through the adsorption of photons at a specific energy. This results in the generation of a dipole moment, which has a bond-specific wavenumber. Random orientation in powder sample generates multiple scattering angles, so a parabolic mirror is required to focus the reflected thus increasing sensitivity and signal to noise ratios.[24, 25] (**Figure 2.10**)

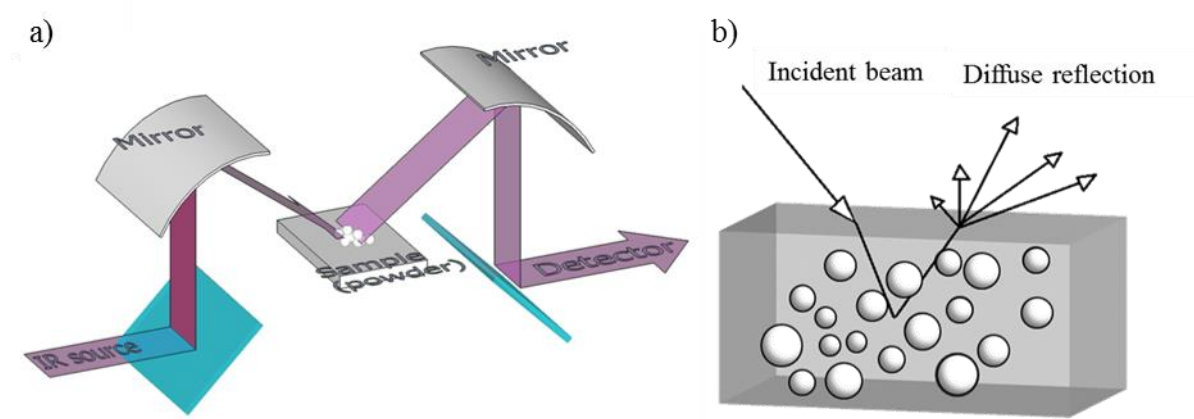


**Figure 2.10** Schematic drawing the optical path through the DRIFTS apparatus (a) detail of the interaction between the incident beam and the surface of the powder sample (b).

Hooke's law (**Equation 2.14**) can be applied in order to ascertain the relationship between the frequency ( $\nu$ ) of vibration with the associated bond strength ( $k$ ) and reduced mass of the target functional group ( $\mu$ ).[26]

$$\nu = \frac{1}{2\pi} \sqrt{\frac{k}{\mu}}$$

**Equation 2.14** Hooke's law

In the **Equation 2.15**,  $m_1$  and  $m_2$  indicate the mass of the bonded atoms in grams.

**Equation 2.15** Reduced mass

Titration of the surface of catalyst with probe molecules is a powerful technique for quantitative analysis of surface acidity (and basicity) of solid catalysts. Pyridine is a well-known probe molecule for characterization of nature of acid sites by DRIFTS and it was employed in this study for the measurement of acid sites density on the metal oxides surface.

#### **Instrument and analysis specification:**

DRIFT spectra were obtained using a Nicolet Avatar 370 MCT with Smart Collector accessory, mid/near infrared source and mercury cadmium telluride (MCT-A) photon detector at -196 °C (liquid N<sub>2</sub>). Samples were diluted with KBr powder (10 wt% in KBr) for analysis then loaded into an environmental cell and subjected to additional drying under vacuum at 110 °C for 10 min prior to measurements to remove moisture physisorbed during air exposure. Samples were scanned between 4000 and 650 cm<sup>-1</sup> *in vacuo* at a resolution of 4 cm<sup>-1</sup>.

Pyridine adsorption was performed by exposure of samples to pyridine vapour in a desiccator overnight. Excess physisorbed pyridine was removed in a vacuum oven prior to sample loading in the environmental cell, with spectra recorded at 25 °C *in vacuo*

#### **2.2.7.3 Attenuated total reflectance spectroscopy (ATR- IR)**

Attenuated total reflectance spectroscopy (ATR) allows qualitative or semi-quantitative analysis of samples with little or no sample preparation, which greatly speeds sample analysis and it can be used for solid and liquid samples allowing also the analysis at the interface.

ATR is an internal reflective technique, as the IR beam is coupled into a crystal called internal reflecting element (IRE) with high refracting index ( $n_{IRE}$ ). The IR beam reflects from the internal

surface of the IRE and creates an evanescent wave which projects orthogonally into the sample in intimate contact with the ATR crystal.

The refractive index of the crystal and the sample govern the basic phenomenon of the ATR technique, thus the internal reflection can only occur when the angle of the incident beam  $\theta$  is larger than the critical angle  $\theta_c$ . (**Equation 2.16**)

$$\left( \text{---} \right)$$

**Equation 2.16** Critical angle

The sample is in intimate contact with the IRE and has a lower refracting index ( $n_{\text{sample}} < n_{\text{IRE}}$ ). When  $\theta$  is larger than the critical angle  $\theta_c$ , the light is trapped in the IRE and is reflected one or multiple time until the radiation is returned attenuated by the crystal and the sample to the detector. This ATR phenomenon is shown graphically in **Figure 2.11**.

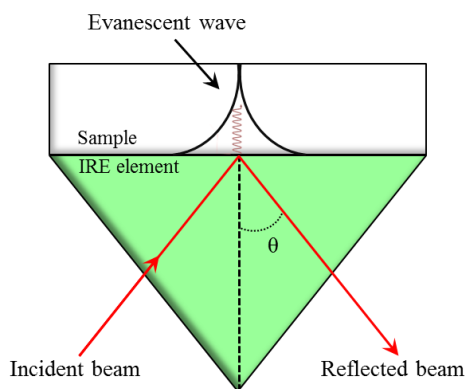


**Figure 2.11** Graphical representation of the interaction between IR beam and the sample with the formation of the evanescent wave.

**Equation 2.17** allow to evaluate the penetration depth of the evanescent wave in the sample, as function of angles of incidence and the refractive indices of the crystal and sample and the wavelength of the radiation:

$$\text{---} \frac{1}{2}$$

**Equation 2.17** Penetration depth

where  $\lambda$  is the wavelength of light and  $\theta$  is the angle of incidence of the IR beam relative to a perpendicular from the surface of the crystal. Typical depth of penetration in ATR ranges from about 0.5 microns up to about 5 microns depending upon these experimental values. The effective



pathlength of the spectrum collected varies with the wavelength of the radiation; typically the penetration depth is lower at higher wavenumbers.

Two configurations of ATR accessory were employed in this work. In a single bounce–ATR, a single internal reflection occurs using a diamond prism whereas multi-bounce ATR, undergoes multiple internal reflections (up to 20) using special ZnSe prisms. The multiple internal reflections produce more intensive spectra by multiple reflections and, hence it is useful for weak absorbers and it was employed for *in-situ* studies at liquid-solid interface, while the single bounce–ATR is suitable for strong absorbers and it was used to analyse the interface species of the composites catalysts (powder samples). **Table 2.1** summarizes some of the properties of these two materials used as ATR crystals.

**Table 2.1** General properties of ATR crystals

Material	Wave range / $\text{cm}^{-1}$	Refractive index (at $1000 \text{ cm}^{-1}$ )	Depth of penetration / $\mu\text{m}$ (at $45^\circ$ and $1000 \text{ cm}^{-1}$ )	pH range	
Diamond	25000-100	2.4	2	1	14
ZnSe	15000-650	2.4	2	5	9

#### **Instrument specification:**

ATR measurements were performed using a Thermo Scientific Nicolet iS50 spectrometers equipped with a single bounce diamond crystal and with a Smart Collector Accessory with horizontal multibounce ZnSe crystal, an infrared source and mercury cadmium telluride (MCT-A) photon detector cooled to  $-196^\circ\text{C}$ . Spectra were collected using OMNIC software.

## **2.2.8 Microscopy analysis**

### **2.2.8.1 Scanning electron microscopy (SEM)**

Scanning electron microscope (SEM) produces 3D images with resolution of  $\sim 2 \text{ nm}$  which provide information on the topography and morphology of the samples.

In this technique, an electron beam generated from a tungsten filament (electron gun) situated on top of the microscope interacts with the sample surface.[27] Electrons emitted by the gun are accelerated, typically by 1-30 kV, and they travel under vacuum passing first through a condenser and objective lenses which focus and direct the beam; then through a set of scanning coils and an aperture. The scanning coils are a set of lenses which are moving (rastering) the beam with very high precision. These electrons hit the sample and lose energy through interactions occurring in

multiple ways, generating high energy backscattering electrons, secondary electrons through inelastic scattering and X-ray radiation. Secondary electrons are emitted from the surface of the sample and recorded by a detector, allowing the producing of the SEM image.[27] The low energy, ~50 eV, of the secondary electrons means that their escape is impeded and therefore the technique is surface sensitive.

Image contrast is generated from the morphology of the sample: surfaces at 90° angles to the beam are brightest and as surfaces tilt towards being parallel to the beam increasingly darker areas are observed. This allows the production of a 3-D image of the sample surface. High energy backscattered electrons are generated through elastic scattering of the incident electron beam with atoms on the sample surface, contributing to the quality of the final image. The higher the atomic mass (or Z number) of the interacting nucleus, the stronger the diffraction effect and the brighter the image.[27] In this work, SEM has been used to study the successful formation of the macropores structure of the TLCT MM-SBA-15. **Figure 2.12** shows a schematic explanation about the working principles of a SEM microscope.

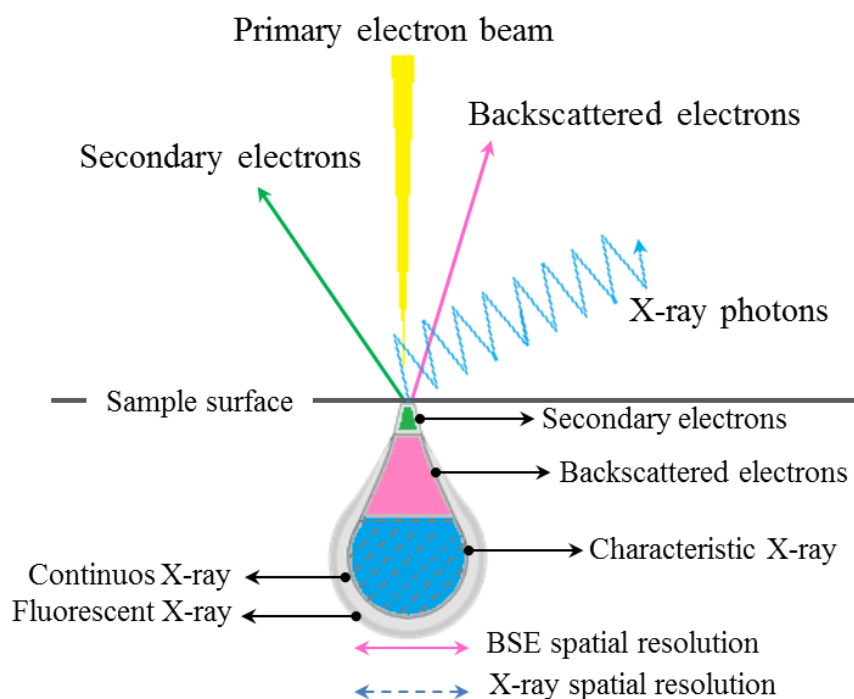


**Figure 2.12** Illustrative representation of X-ray interaction with the sample surface and the different signal emitted.

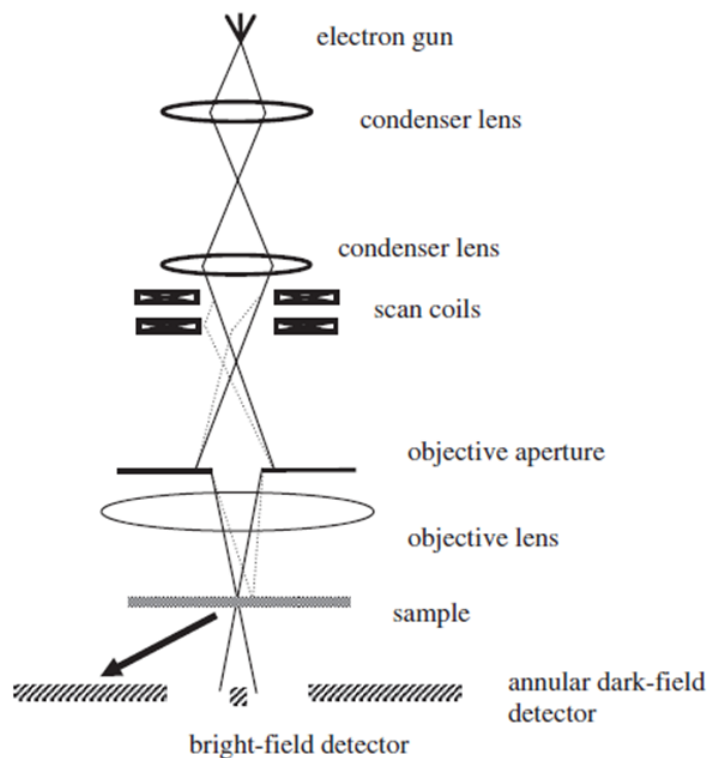
#### **Instrument specification:**

Scanning electron microscopy (SEM) images were recorded on a Carl ZEISS SUPRA 55-VP operating at 25 kV. Samples were supported on aluminium stubs each backed with carbon tape.

### 2.2.8.2 Scanning transmission electron microscopy (STEM)

As with SEM, scanning transmission electron microscopy (STEM) utilises a beam of electrons for imaging which scans over the sample rastering the surface. However, for the STEM, the high-energy electron beam is transmitted through the sample and any apparent absorption by the sample resulting in a change in transmitted beam intensity.

After the generation, the accelerated electron beam is adjusted and focused by the condenser lenses. An aperture is inserted to remove the wider scattered electrons and the size is chosen by the compromise the signal to noise ratio. The electron probe is controlled by the scan coils to scan over the selected region of the sample. When the probe strikes onto the sample, the elastically transmitted electrons exhibit different angles with the respect of the optical axis.[28] Below the sample, the high angle annular dark field (HAADF), bright field (BF) and electron energy loss detectors are positioned to collect different electron signal. The first is an annular detector that collects the electrons transmitted at higher scattering angles; the second is perpendicular to the transmitted beam and collects information about the electrons that leave the sample with a relatively low angle compared to the incident beam. On the contrary, an energy dispersive X-ray (EDX) detector is placed above the sample to collect the characteristic X-ray emitted from the sample. The produced 2D images are black and white and the contrast depended upon several variables, including thickness, atomic mass and density of the sample.[29]



**Equation 2.18** Schematic STEM microscope configuration.[30]

## **Instrument and analysis specification:**

High resolution TEM/STEM (HAADF) images were recorded on a JEOL 2100F FEG STEM operating at 200 k eV and equipped with a spherical aberration probe corrector (CEOS GmbH) and a Bruker XFlash 5030 EDX, with analysis carried out at the University of Birmingham. The samples were prepared by supporting a dispersion of the catalyst in ethanol onto a copper grid coated with a holey carbon Cu grid (Agar Scientific Ltd.). The data was processed using ImageJ software and Microsoft Excel.

## **2.3 Photocatalytic reaction**

### **2.3.1 Photo-oxidation of methyl orange**

Photocatalytic tests of the TiO<sub>2</sub> composites samples for the degradation of the methyl orange (MO) dye were carried out at room temperature in a sealed 120 ml quartz photoreactor. Thermostated water at 20°C was pumped continuously through the outer jacket of reactor to prevent overheating of the reaction mixture. The whole photocatalytic reactor was insulated in a wooden box to prevent the escape of harmful radiation and to minimise temperature fluctuations caused by draughts. (Figure 2.13)

Test solutions were prepared by mixing 50 ml of MO solution (15 ppm) and 50 mg of either mesoporous and the hierarchical synthesized materials or the commercial TiO<sub>2</sub> benchmark to form an aqueous dispersion. The obtained suspension was continuously stirred using a magnetic stirring bar at 300 rpm. Prior to irradiation, the test solution was kept in the dark for 60 min under constant stirring to establish the adsorption-desorption equilibrium. Subsequently, the reaction mixture was irradiated by a 200 W Oriel Instruments 66002 Hg-Xe arc lamp for 4 hours. The UV-source was placed at a fix distance from the reactor of 43 cm and with an average radiant flux of 25 mW.cm<sup>-2</sup>. Aliquots of the reaction mixture (0.5 ml) were periodically withdrawn and centrifuged to separate the catalyst, and UV-vis absorption spectra recorded on the filtrate to monitor the extent of MO reaction.

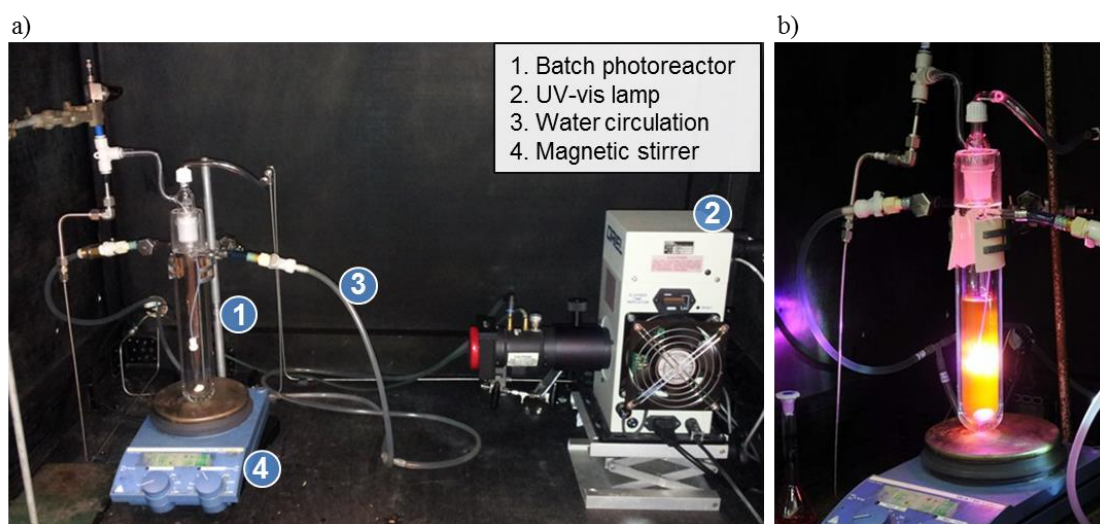


**Figure 2.13** Set up of the photoreactor for dye degradation (a) and detail of MO reaction solution during the irradiation time (b).

Post-reaction, photocatalysts were separated from the aqueous solution by centrifugation (6000 rpm, 15 min) prior to UV–vis analysis by Evolution 220 (Thermo Scientific) spectrophotometer. As MO absorbs light at certain wavelengths with  $\lambda_{\text{max}} = 464 \text{ nm}$ , during the photoreaction the degree of degradation was quantified from calibration curves constructed from standards solutions prepared at different dye concentrations. (**Figure 2.14a**)

The Lambert-Beer law states that the absorbance of a solution is directly proportional to the concentration of the absorbing species in the solution and the path length of light. Thus, for a fixed path length, UV/Vis spectroscopy can be used to determine the concentration of the dye in a solution. The general Lambert-Beer law could be written as the following:

$$\left[ \frac{0}{-} \right]$$

**Equation 2.19** Lambert-Beer law.

where  $A$  is the absorbance,  $I$  is the intensity of transmitted light,  $I_0$  is the incident intensity,  $\epsilon$  is the extinction coefficient of the sample ( $\text{L} \cdot \text{mol}^{-1} \cdot \text{cm}^{-1}$ ),  $l$  is the path length through the sample (cm), and  $[C]$  is the concentration of the species under consideration ( $\text{mol} \cdot \text{L}^{-1}$ ). In cases where the path length is always constant (i.e. cuvette size), the value of  $\epsilon$  and  $l$  can be combined to a term  $\alpha$  called the absorption coefficient and the equation for Lambert-Beer's law suited a linear equation with the general form of  $y = mx$ . Thus the unknown concentration of samples containing MO is then determined by measuring its absorbance and converting the obtained value in concentration using the absorption coefficient. (**Figure 2.14b**)

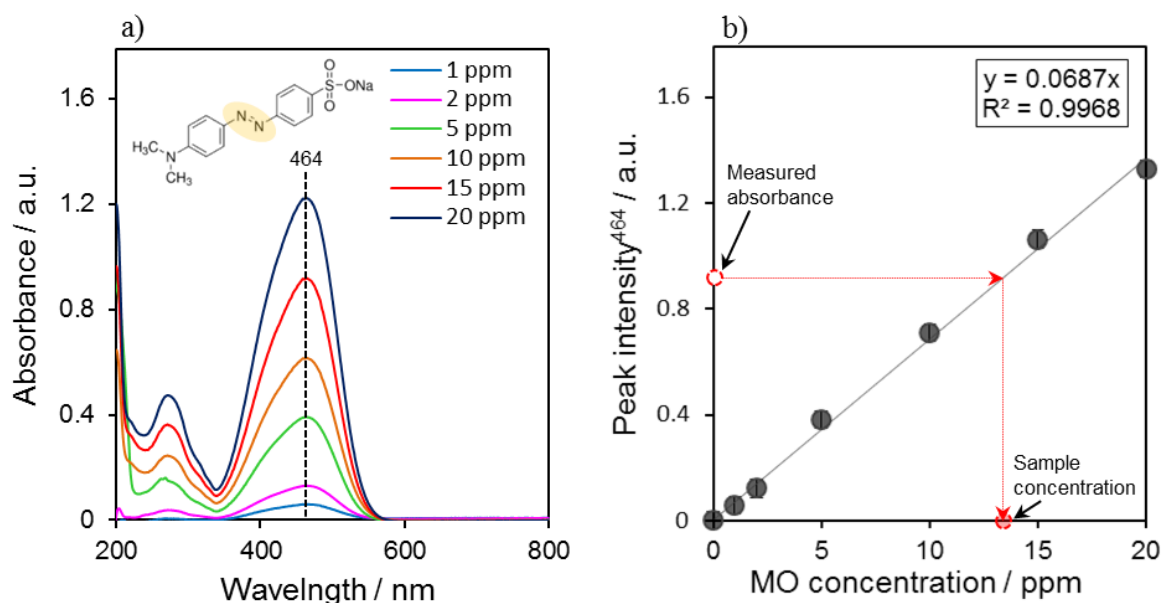


**Figure 2.14** UV-vis absorbance spectra of MO standard solutions (a); calibration plot to determine the concentration of unknown samples (b).

Furthermore, initial rate of reactions ( $r^0 \sim \text{ppm MO} \cdot \text{h}^{-1}$ ) were determined from the initial linear portion of the profile of conversion ( $t < 1 \text{ h}$ ) and the % of degradation was evaluated as below:

**Equation 2.20** Percentage of MO degradation

### 2.3.2 Photo-oxidation of propanoic acid

For studies of propanoic acid adsorption on  $\text{TiO}_2$  and photo-oxidation mechanisms at solid liquid interfaces *in-situ* a bespoke flow through cell was designed and applied in ATR-IR spectroscopy measurements; in parallel a batch reactor was used to test the catalytic performance of the catalysts and to detected reaction intermediates in solution. Both reactors were equipped with 365 nm LED array.

#### 2.3.2.1 ATR flow reactor

The ATR-IR experiments were conducted in a specially designed continuous flow cell, made from a horizontal ATR crystal mounted in a plate block. The flow cell was coupled to a 365 nm LED array, the top plate has a quartz window to allow light irradiation and sealed channels for external temperature controlled fluids to circulate through the cell body and thus control the temperature of the assembly. The cell was mounted on an attachment for ATR measurements within the sample compartment of a Thermo Scientific Nicolet iS50 FTIR spectrometer equipped with MCT detector.

Spectra were recorded at  $4\text{ cm}^{-1}$ . The ATR crystal for a liquid flow-through cell is made of Zinc Selenide (ZnSe) and has trapezoid shape and has dimensions of 80 mm x10 mm x2 mm, resulting in 20 reflections for a  $45^\circ$  reflection crystal. The sample compartment was closed and purged with nitrogen during the experiments to avoid  $\text{H}_2\text{O}$  and  $\text{CO}_2$  contamination.

Propanoic acid solution ( $0.05\text{ mol.l}^{-1}$ ,  $\text{pH} \approx 3.5$ ) was passed through the cell and over the  $\text{TiO}_2$  film in the dark for 30 min in order to reach equilibrium. The  $\text{pK}_a$  value of propanoic acid is 4.88. The spectra were measured at room temperature at a resolution of  $4\text{ cm}^{-1}$ , using the clean crystal spectrum as initial background. Based on the purpose of each experiment, if necessary the internal background/reference was changed to allow the more accurate observation of different changes in the collected spectra induced by several operative conditions. The spectrum taken as background will be always specified.

Water subtraction and manual baseline corrections were performed to eliminate the strong signal due to the solvent and in order to eliminate minor fluctuations due to instrumental instabilities, respectively. **Figure 2.15** shows the complete set-up of the ATR IR cell with a detail of the UV LED array and the base plate with the ZnSe crystal.

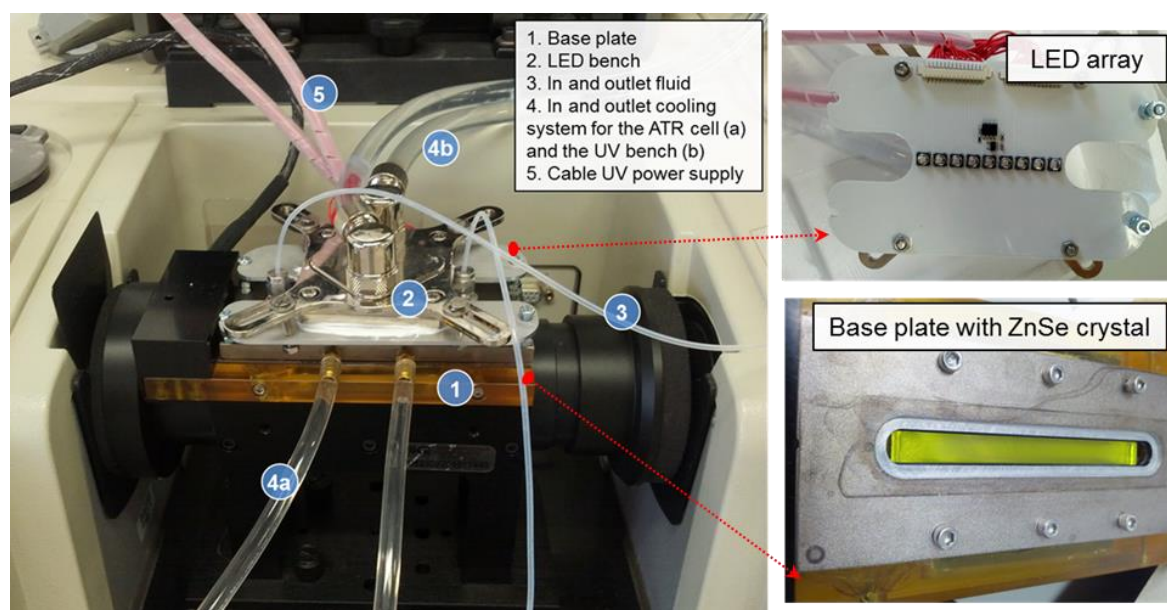


**Figure 2.15** Set up of the ATR flow cell for in-situ measurements (right) and detail of the UV array and the base plate with the ZnSe crystal (left)

Irradiation of the sample with UV light was carried out using a UV-LED array comprised of 9 LED bulbs in series with emission wavelength of 365 nm. Remote control and monitoring of operative conditions were performed using prototype software developed within Bath University, which allow the possibility of setting different intensity values in the range from 10 to  $100\text{ mW.cm}^{-2}$ . Measurements related to the intensity were performed using the light meter G&R Labs Model 200 equipped with a probe which detects light in the wavelength range of 190-550 nm. The power



settled for the photocatalytic test was  $\sim 25 \text{ mW.cm}^{-2}$ . **Figure 2.16** shows the results from the light intensity test.

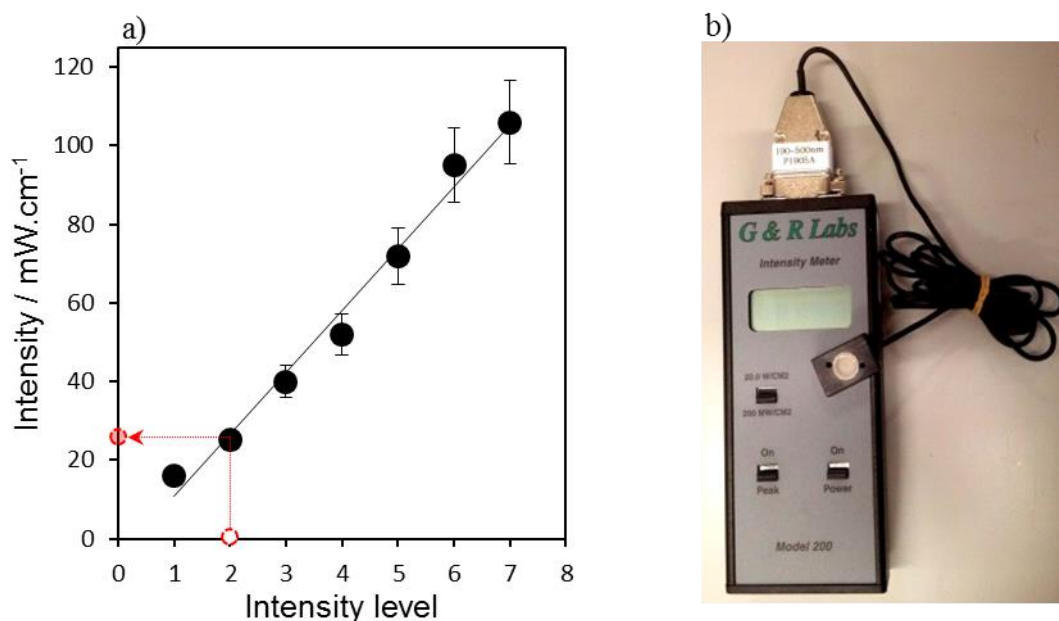
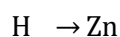


**Figure 2.16** Light intensity calibration obtained controlling the emission of the UV array through the remote control and measuring the actual intensity with a light meter (a); lightmeter used for the measurement (b).

After long irradiation times, the formation of a precipitate was noticed on the ZnSe crystal; this residue could be removed only by polishing the surface with diamond paste.

It is possible that the attack to the crystal surface is due to the  $\text{H}_2\text{Se}$  production linked with the low pH of propanoic acid solution. Under irradiation the inorganic compound can partially decompose to leave a residue of elemental  $\text{Se}^0$ . [31] (**Equation 2.21**)



**Equation 2.21** Etching of the ATR crystal.

Because of the probable attack of the crystal surface, the illumination time was kept to maximum 2 hours as a compromise to collect enough information of the kinetic degradation process and to protect the integrity of the crystal.

### 2.3.2.2 Thin film preparation

Slurry of the catalysts powder was prepared from about 60 mg catalyst and 10 ml water (Milli-Q, 18 M $\Omega$ cm). After sonication for 30 min  $\text{TiO}_2$  thin-films were formed by dropping the slurry onto a ZnSe crystal. The solvent was allowed to evaporate in a vacuum oven for 2 hours at 40 °C. After drying, loose catalyst particles were removed by gentle stream of water over the IRE. The procedure was repeated two times. Following the final drying step, the film was ready for use. A



new catalyst coating was prepared for each experiment. **Figure 2.17** shows the crystal before (left) and after (right) the coating.

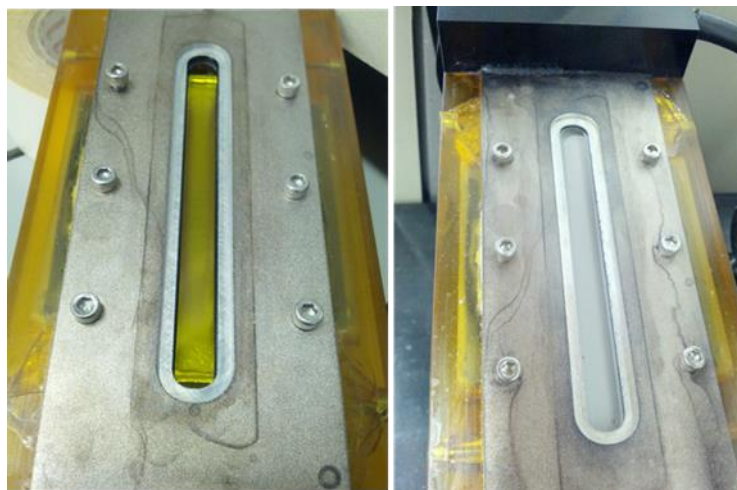


**Figure 2.17** ZnSe crystal before (left) and after coating (right) with the  $\text{TiO}_2$  thin film.

### 2.3.2.3 Batch reactor

In parallel with the ATR *in-situ* studies the photocatalytic tests of propanoic acid degradation were also performed in a batch reactor. The employed reactor is a double-walled pyrex reactor (ca. 500 ml) mounted with an outlet and an inlet port allowing water circulation and temperature control ( $20 \pm 1$  °C). Irradiation was provided by a UV-LED bench comprised of 36 LED bulbs with emission wavelength of 365 nm and designed and built in the same way of the LED array of the ATR flow cell in order to have the same light source and comparable results. **Figure 2.18** shows the actual set-up of the batch reactor used for photocatalytic tests.

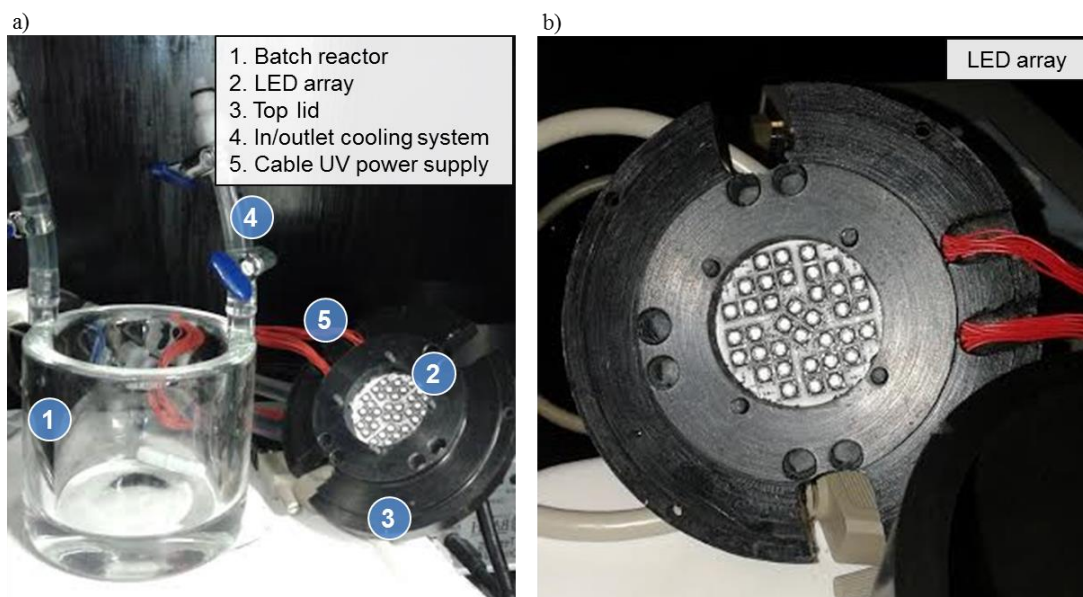


**Figure 2.18** Batch photoreactor (a) and detail of the UV array (b).

The initial concentrations of the substrate and the mass of catalyst were constant in all the experiments (5 mM propanoic acid and  $0.5 \text{ g.L}^{-3}$  of catalyst). During the degradation process, samples were withdrawn periodically and filtered prior to analysis on an Agilent 1200 series HPLC equipped with RI and diode array detectors and a Hi-Plex H column for analysis. A 5 mM aqueous solution of sulphuric acid was used as the eluent phase, with a flow rate of  $0.6 \text{ ml min}^{-1}$  and  $65^\circ\text{C}$  column temperature. Product yields were calculated from response factors determined from multi-point calibration curves. List of compounds that the HPLC was calibrated for and their response factors are given in **Table 2.2**. A representation of typical calibration curves is shown on **Figure 2.19**.

**Table 2.2** List of compounds detected by refractive index detector on HPLC

Compound	Detector	Retention time	Response factor
		min	$\text{M (nRIU.s)}^{-1}$
Propanoic acid	RI	21.3	8182.4
Acetic acid	RI	17.9	5762.8
Formic acid	RI	15.9	4279.6
Formaldehyde	RI	15.7	4660.9

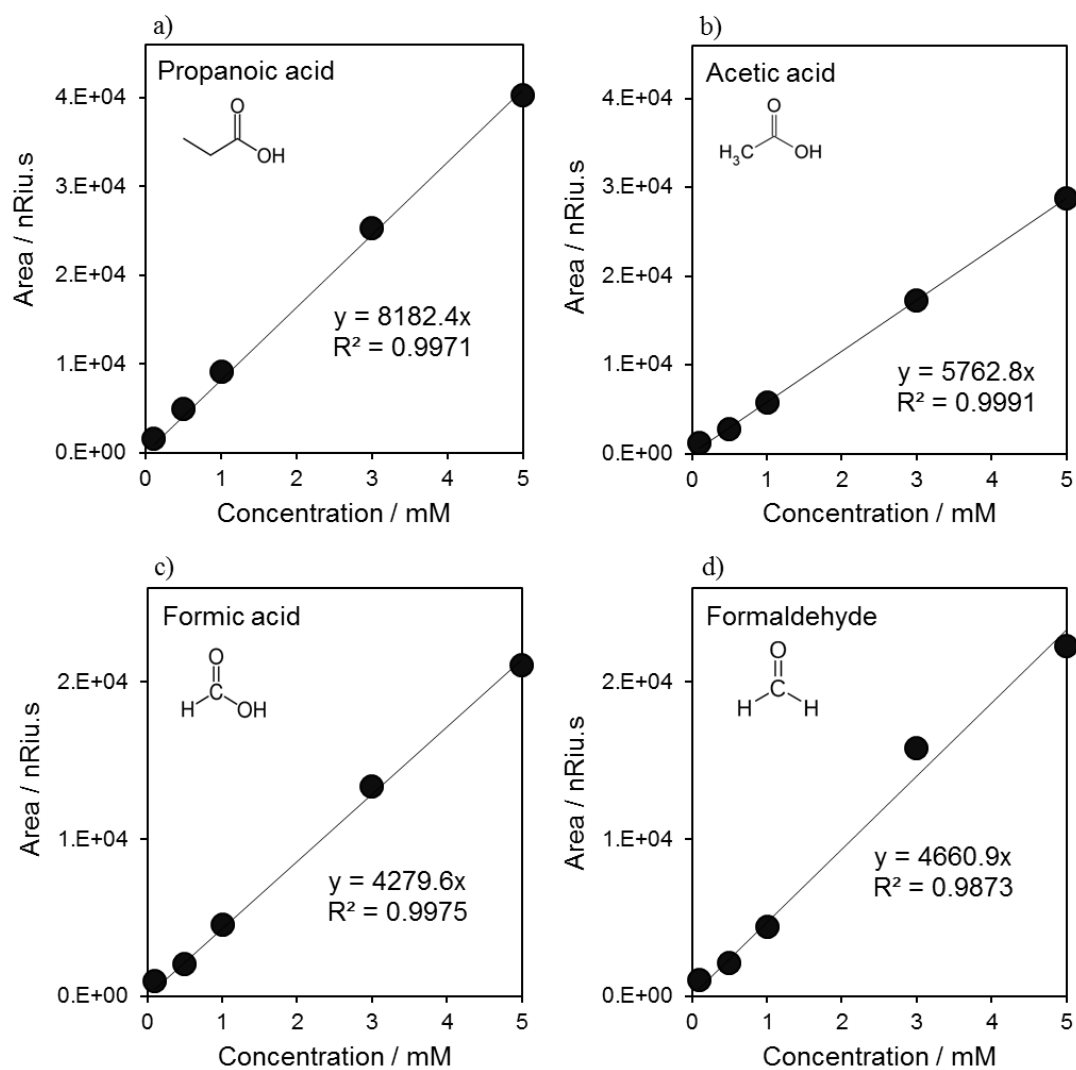


**Figure 2.19** Calibration of reactants and potential products detected by refractive index detector (RID) on HPLC.

Furthermore, initial rate of reactions ( $r^0$ ) were determined from the initial linear portion of the profile of conversion ( $t < 1$  h) and yields, conversion and selectivity (%) were calculated as below:

$$\text{Conversion} = \left( \frac{C_0 - C_t}{C_0} \right) \times 100$$

**Equation 2.22** Conversion

where  $C_0$  is the initial concentration of the reactant and  $C_t$  the concentration at time  $t$ .

$$\text{Yield} = \frac{C_t^p}{C_0^s} \times 100$$

**Equation 2.23** Yield

where  $C_0^s$  is the initial concentration of the substrate (i.e. propanoic acid) and  $C_t^p$  is the concentration of the product at time t. (i.e. acetic acid)

$$\text{Selectivity} = \frac{\text{yield}}{\text{reactant conversion}} \times 100$$

**Equation 2.24** Selectivity

## 2.4 Reference

- [1] D. Zhao, Q. Huo, J. Feng, B. F. Chmelka, and G. D. Stucky, "Nonionic Triblock and Star Diblock Copolymer and Oligomeric Surfactant Syntheses of Highly Ordered, Hydrothermally Stable, Mesoporous Silica Structures," *Journal of the American Chemical Society*, vol. 120, pp. 6024-6036, 1998/06/01 1998.
- [2] S. Vaudreuil, M. Bousmina, S. Kaliaguine, and L. Bonneviot, "Synthesis of macrostructured silica by sedimentation-aggregation," *Advanced Materials*, vol. 13, pp. 1310-1312, Sep 3 2001.
- [3] G. S. Attard, J. C. Glyde, and C. G. Goltner, "Liquid-Crystalline Phases as Templates for the Synthesis of Mesoporous Silica," *Nature*, vol. 378, pp. 366-368, Nov 23 1995.
- [4] M. V. Landau, E. Dafa, M. L. Kaliya, T. Sen, and M. Herskowitz, "Mesoporous alumina catalytic, material prepared by grafting wide-pore MCM-41 with an alumina multilayer," *Microporous and Mesoporous Materials*, vol. 49, pp. 65-81, Nov 15 2001.
- [5] J. M. Hollas, *Modern spectroscopy*: John Wiley & Sons, 2004.
- [6] B. D. Cullity, "Elements of X-Ray Diffraction," *American Journal of Physics*, vol. 25, pp. 394-395, 1957.
- [7] P. Atkins and J. de Paula, *Atkins' Physical Chemistry*: OUP Oxford, 2010.
- [8] H. Itoh, S. Utamapanya, J. V. Stark, K. J. Klabunde, and J. R. Schlup, "Nanoscale Metal-Oxide Particles as Chemical Reagents - Intrinsic Effects of Particle-Size on Hydroxyl Content and on Reactivity and Acid-Base Properties of Ultrafine Magnesium-Oxide," *Chemistry of Materials*, vol. 5, pp. 71-77, Jan 1993.
- [9] R. J. Matyi, L. H. Schwartz, and J. B. Butt, "Particle-Size, Particle-Size Distribution, and Related Measurements of Supported Metal-Catalysts," *Catalysis Reviews-Science and Engineering*, vol. 29, pp. 41-99, 1987.
- [10] J. Lynch, *Physico-chemical analysis of industrial catalysts: a practical guide to characterisation*: Editions Technip, 2003.

- [11] J. F. Watts, "X-ray photoelectron spectroscopy," *Vacuum*, vol. 45, pp. 653-671, 1994/06/01/ 1994.
- [12] K. W. Kolasinski, *Surface science: foundations of catalysis and nanoscience*: John Wiley & Sons, 2012.
- [13] J. Rumble, D. Bickham, and C. Powell, "The NIST x-ray photoelectron spectroscopy database," *Surface and interface analysis*, vol. 19, pp. 241-246, 1992.
- [14] K. S. W. Sing, D. H. Everett, R. A. W. Haul, L. Moscou, R. A. Pierotti, J. Rouquerol, *et al.*, "Reporting Physisorption Data for Gas Solid Systems with Special Reference to the Determination of Surface-Area and Porosity (Recommendations 1984)," *Pure and Applied Chemistry*, vol. 57, pp. 603-619, 1985.
- [15] J. Rouquerol, F. Rouquerol, P. Llewellyn, G. Maurin, and K. S. Sing, *Adsorption by powders and porous solids: principles, methodology and applications*: Academic press, 2013.
- [16] F. Rouquerol, J. Rouquerol, and K. Sing, "CHAPTER 3 - Methodology of Adsorption at the Gas-Solid Interface," in *Adsorption by Powders and Porous Solids*, ed London: Academic Press, 1999, pp. 51-92.
- [17] J. M. Thomas, "Handbook Of Heterogeneous Catalysis. 2., completely revised and enlarged Edition. Vol. 1-8. Edited by G. Ertl, H. Knözinger, F. Schüth, and J. Weitkamp," *Angewandte Chemie International Edition*, vol. 48, pp. 3390-3391, 2009.
- [18] P. A. Webb and C. Orr, *Analytical methods in fine particle technology*. Norcross, GA.: Micromeritics Instrument Corporation, 1997.
- [19] M. R. Hoffmann, S. T. Martin, W. Choi, and D. W. Bahnemann, "Environmental Applications of Semiconductor Photocatalysis," *Chemical Reviews*, vol. 95, pp. 69-96, 1995/01/01 1995.
- [20] B. D. Vezibicke, S. Patel, B. E. Davis, and D. P. Birnie, "Evaluation of the Tauc method for optical absorption edge determination: ZnO thin films as a model system," *physica status solidi (b)*, vol. 252, pp. 1700-1710, 2015.
- [21] A. L. Linsebigler, G. Lu, and J. T. Yates Jr, "Photocatalysis on TiO<sub>2</sub> surfaces: principles, mechanisms, and selected results," *Chemical reviews*, vol. 95, pp. 735-758, 1995.
- [22] J. Tauc, R. Grigorovici, and A. Vancu, "Optical Properties and Electronic Structure of Amorphous Germanium," *physica status solidi (b)*, vol. 15, pp. 627-637, 1966.
- [23] E. R. Lippincott, "Infrared Spectra of Inorganic and Coordination Compounds," *Journal of the American Chemical Society*, vol. 85, pp. 3532-3532, 1963.
- [24] B. Stuart, *Infrared spectroscopy*: Wiley Online Library, 2005.
- [25] H. Günzler and H.-U. Gremlich, *IR-Spektroskopie: Eine Einführung*: John Wiley & Sons, 2012.

- [26] J. T. Burke, "IR Spectroscopy or Hooke's Law at the Molecular Level - A Joint Freshman Physics-Chemistry Experience," *Journal of Chemical Education*, vol. 74, p. 1213, 1997/10/01 1997.
- [27] T. G. Rochow and P. A. Tucker, "Microscopical Stages," in *Introduction to Microscopy by Means of Light, Electrons, X Rays, or Acoustics*, ed Boston, MA: Springer US, 1994, pp. 233-255.
- [28] S. J. Pennycook, B. David, and C. B. Williams, "Transmission electron microscopy: a textbook for materials science," *Microscopy and Microanalysis*, vol. 16, p. 111, 2010.
- [29] P. Nellist and S. Pennycook, "The principles and interpretation of annular dark-field Z-contrast imaging," *Advances in imaging and electron physics*, vol. 113, pp. 147-203, 2000.
- [30] S. J. Pennycook, "A scan through the history of STEM," in *Scanning transmission electron microscopy*, ed: Springer, 2011, pp. 1-90.
- [31] C. B. Mendive, D. W. Bahnemann, and M. A. Blesa, "Microscopic characterization of the photocatalytic oxidation of oxalic acid adsorbed onto TiO<sub>2</sub> by FTIR-ATR," *Catalysis Today*, vol. 101, pp. 237-244, Apr 15 2005.

## *Chapter 3*

### *Titania grafted on mesoporous silica support*

### 3 Titania grafted on mesoporous silica support

#### 3.1 Introduction

**Chapter 1** highlighted the growing interest in the development of heterogeneous photocatalysts for waste water treatment. Among all the photoactive materials studied, semiconductor  $\text{TiO}_2$  is one of the most widely used.[1, 2]

$\text{TiO}_2$ -based photocatalysts have been recognized as a very promising material for the degradation of undesirable organic compounds in water under environmentally friendly conditions, using only light as the energy source.[1-4] Despite possessing excellent photocatalytic properties, commercial  $\text{TiO}_2$  suffers from poor physical properties which have much scope for improvement, through optimisation of the degree of crystallinity, particle size, specific surface area and porosity.[5, 6] Many researchers have tried to increase the specific surface area (SSA) of titania, with the objective being achieving more active sites per unit area and, consequently, a higher photocatalytic activity. Particularly, special attention has been devoted to SBA-15 as a support for  $\text{TiO}_2$ , because of its 2D hexagonal pore structure (with average diameters between 2 and 10 nm) and high surface area ( $\sim 800 \text{ m}^2.\text{g}^{-1}$ ).[7, 8]

When considering preparation techniques of a mixed-oxide composite catalyst, two methods are commonly employed: one-pot synthesis, *e.g.* addition of a titania precursor to the silica source during the synthesis of the mesoporous material, [9-11] and post-synthesis processing, resulting in the deposition of  $\text{TiO}_2$  particles with controlled size in the range 3–7 nm.[12-14]

The first method limits the amount of titanium oxide that can be incorporated in the silica walls, because of the fast hydrolysis of titanium oxide precursors over the micelles of the template. In addition, it is important to control the synthesis conditions to avoid the formation of large external  $\text{TiO}_2$  particles.

The second method can promote the formation of metal oxides in the channels or external surfaces of support, therefore special attention should be paid to the amount of deposited  $\text{TiO}_2$  to avoid pore blocking, which could hinder the access of reactant molecules to the catalytically active sites in the porous matrix.

Busuioc and co-workers[15] reported a post-synthesis deposition method to obtain anatase  $\text{TiO}_2$  nanoparticles with different sizes loaded onto SBA-15. These materials showed great adsorption properties and higher photocatalytic activity for the degradation of Rhodamine 6G under UV light irradiation compared with a bulk anatase. Dong and co-workers[16] prepared a 2D hexagonal composite catalysts by depositing anatase  $\text{TiO}_2$  on amorphous  $\text{SiO}_2$  with large meso-channels and high SSA. The photoactivity of the obtained materials was evaluated for the degradation of a wide range of different organic dyes under UV. The photoactivity of the obtained materials was tested during degradation of different organic dyes under UV light. The synthesis procedures employed in those experiments, however, did not allow control of particle size, particularly upon high  $\text{TiO}_2$



loading ( $> 20$  wt%). Control over particle size plays a key role on photocatalytic efficiency as it crucially affects charge recombination. Moreover, particles size bigger than the typical mesopores of SBA-15 ( $\sim 5$ - $10$  nm) cannot be dispersed inside the pores of the host support, losing the advantage of having a porous material with high internal surface area.

More recently, Besanscon and co-workers[17] studied the impact of dispersion of  $\text{TiO}_2$  on SBA-15 by varying  $\text{TiO}_2/\text{SiO}_2$  mass ratio during a post-synthesis impregnation process followed by a thermal treatment at  $400^\circ\text{C}$  in air. At a very high  $\text{TiO}_2$  loading ( $\sim 80$  wt. %), these composites exhibit greater activity for methyl orange degradation than commercial anatase, however,  $\text{N}_2$  sorption data and XRD analysis highlight the significant structural change of the host support upon thermal treatment process and the presence of crystallized anatase mainly outside the pore framework.

Also Zhang et al.[18] reported on the synthesis of titania supported on silica, focused on the nature and the localization of the  $\text{TiO}_2$  phase. They prepared titania-coated SBA-15 materials by successive grafting of titanium isopropoxide (1 to 4 graftings) to gradually increase the  $\text{TiO}_2$  loading ( $\sim 12$ - $34$  wt. %) and obtained a good uniform dispersion of the active phase inside and outside the support. Despite the good results achieved on the materials synthesis, optical properties and photocatalytic activity were not further investigated in their work.

In general, among the other post-synthesis methodologies, grafting leads to a better dispersion of the deposited  $\text{TiO}_2$  without altering the architecture of SBA-15 support and minimising pore blockage. In this study, titania-coated SBA-15 was prepared by a post-grafting procedure. A layer-by-layer grafting approach was taken in order to increase the loading of the active phase,[19, 20] ensuring a uniform and controlled dispersion of  $\text{TiO}_2$  as well as avoiding pore blocking of the SBA-15 support.

The effect of pore diameter and  $\text{TiO}_2$  film thickness was thoroughly investigated. The first section of this chapter discusses the layer-wise grafting of titania on SBA-15 in order to investigate diffusion kinetics. Subsequently, the effect of  $\text{TiO}_2$  film thickness was explored (up to five consecutive grafting cycles) using the SBA-15 synthesized with the largest pore diameter of  $7$  nm. Finally, the catalytic activity of the composites was evaluated by studying the photodegradation of methyl orange (MO) in water under UV-vis irradiation.

## 3.2 Results and discussion

### 3.2.1 Characterisation of parent SBA-15

SBA-15 mesoporous silica was prepared following the method reported by Zhao et al [21]. Full details of synthesis preparation are reported in **Chapter 2**.

It is well-known from previous studies that the temperature of the hydrothermal treatment has a significant impact of the final porosity of the sample because of the temperature-dependent behavior of the P-123 triblock copolymers [22, 23]. P-123 has a symmetric structure which is composed of a hydrophobic polypropylene oxide (PPO) center and two hydrophilic blocks of polyethylene oxide (PEO) and will form cylindrical micelles when placed in acidic media (water at pH=1). They are capable of forming both spherical and cylindrical micelles. As the hydrophobicity of the PEO blocks increases as a function of the temperature, the degree of hydration of these PEO blocks decreases at high temperatures. This implies a lower interaction with water molecules and a withdrawal of the PEO chains inside the hydrophobic core of the surfactant, resulting in a larger volume of the micelle core and therefore an expanded pore diameter within the SBA-15 material.[24, 25] . **(Figure 3.1)** The nomenclature used for the silica supports is defined as follows: SBA-15-X, where X = pore size (nm).

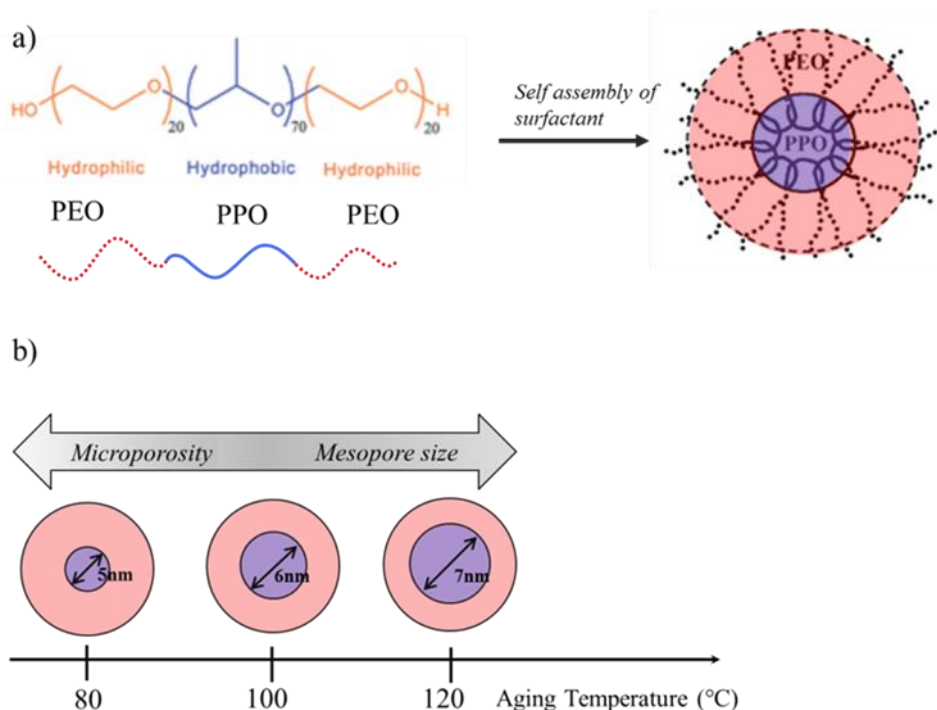


**Figure 3.1** Schematic drawing of the self-assembly of the surfactant P-123 during the synthesis of SBA-15 (a) and dependence of the microporosity and mesopore size from the aging temperature (b).

The successful pore expansion was first probed by N<sub>2</sub> porosimetry, for which adsorption isotherms of supports synthesized at different aging temperature (80,100 and 120°C) are reported in **Figure 3.2a**. The N<sub>2</sub> adsorption-desorption of SBA-15 shows a type IV isotherm according to IUPAC [26] which is indicative of an ordered mesoporous material with H1 type hysteresis loop, suggesting highly uniform mesopores.

**Figure 3.2b** shows a narrow pore size distribution with a clear shift to larger diameters with increasing aging temperature. As highlighted in the preceding paragraph, these materials are characterized by uniform cylindrical mesopores arranged in a 2D-hexagonally packed structure, the pore walls of which contain a high degree of microporosity due to the interpenetration of the PEO chain in the silica network.

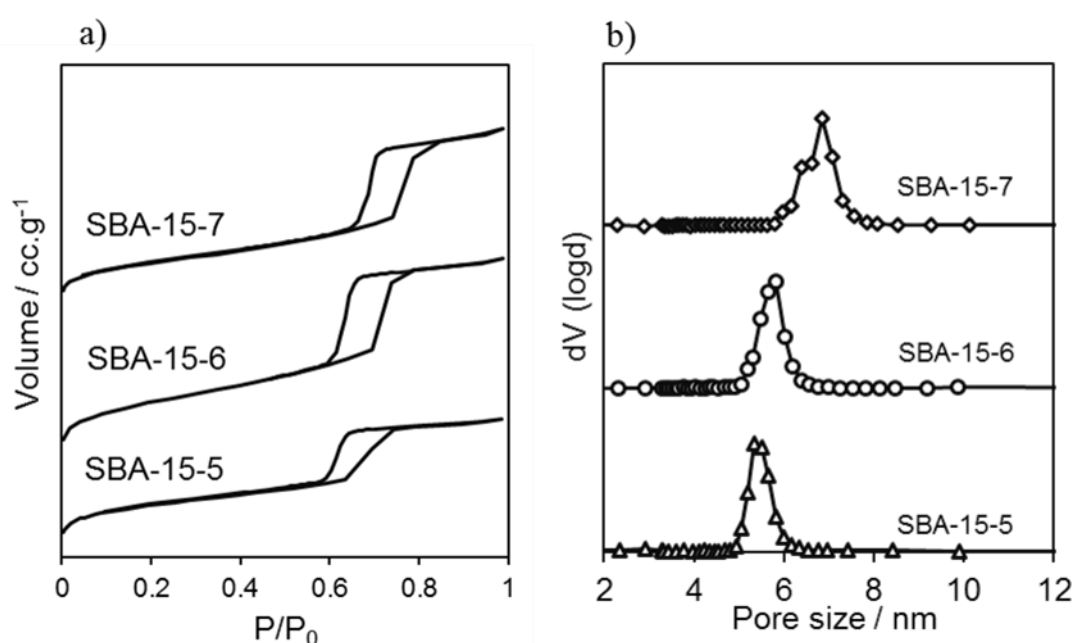


**Figure 3.2** Stacked isotherm plot of SBA-15 aged at different temperature (a) stacked BJH pore size distributions for the mesoporous silica supports (b).

There is a very clear relation between the aging temperature and the relative amount of micropores and mesopores: with increasing aging temperatures, the relative amount of micropores decreases. (

#### **Figure 3.3a)**

Microporosity is introduced to the silica walls through silica condensation around hydrophilic PEO chains and the subsequent removal of these chains. Due to increasing PEO hydrophobicity at high temperatures, the chains withdraw inside the hydrophobic PPO cores, leaving a lower volume of holes or voids in the silica walls. These holes are too unstable to resist the calcination step, so the micropores will only be generated at places when the PEO is actively penetrating the silica wall (at lower aging temperature). On the other hand the larger PPO core at higher temperatures enhances the contribution to the mesopore volume and diameter.

**Figure 3.3b** shows the evolution of the mesoporous surface area and the pore diameter with aging temperature.

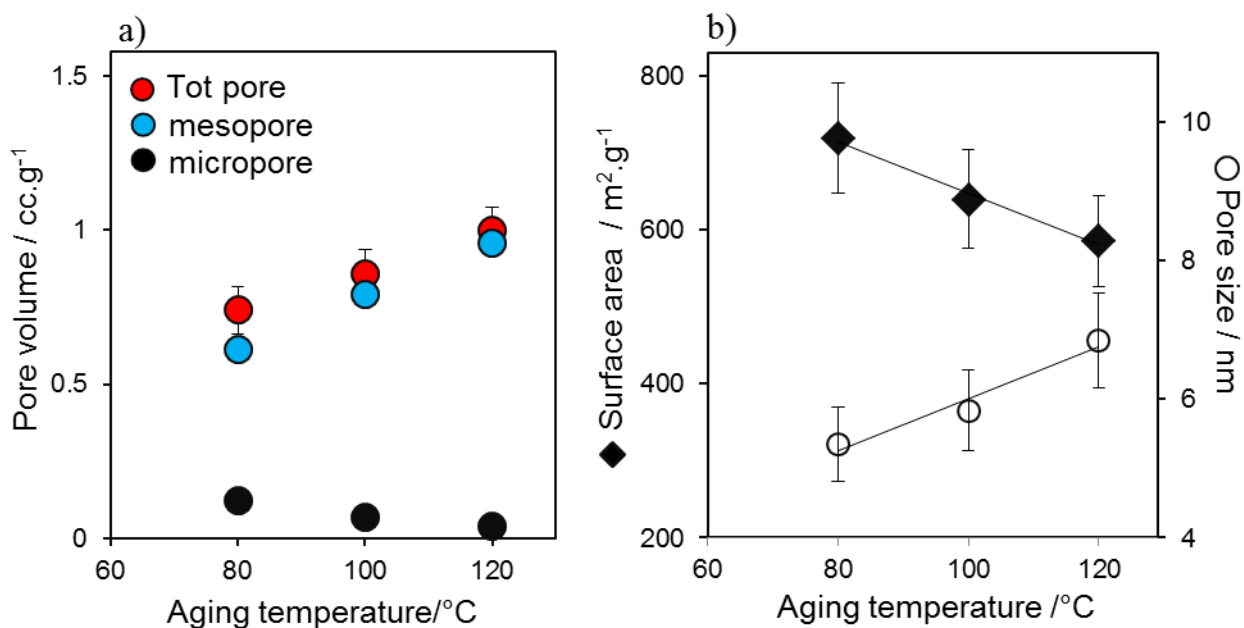


**Figure 3.3** Effect of aging temperature on SBA-15 pore volume (total, mesopore and micropore volume) (a); surface area and pore size (b).

These values are shown in **Table 3.1**,

**Table 3.1** Structural and textural properties of the SBA-15 support aged at three different temperatures

Sample	T <sub>aging</sub> / °C	Pore size / nm	S <sub>BET</sub> / m <sup>2</sup> g <sup>-1</sup>	V <sub>pore</sub> / cc g <sup>-1</sup>	V <sub>micro</sub> / cc g <sup>-1</sup>
SBA-15 5	80	5.4	719	0.7	0.13
SBA-15 6	100	5.9	640	0.9	0.07
SBA-15 7	120	6.8	585	1.0	0.04

**Figure 3.4** shows the XRD patterns for the SBA-15 supports with three mesopore sizes. The XRD patterns obtained in the low  $2\theta$  region for the three silica support clearly show diffraction peaks characteristic of the ( $d_{10}$ ), ( $d_{11}$ ) and ( $d_{20}$ ) diffraction planes of the 2D hexagonal pore structure. (**Figure 3.4a**) This established the presence of a hexagonally arranged, periodic mesoporous framework of the prepared SBA-15. In addition the wide angle XRD shows the typical broad reflection of amorphous silica. (**Figure 3.4b**)

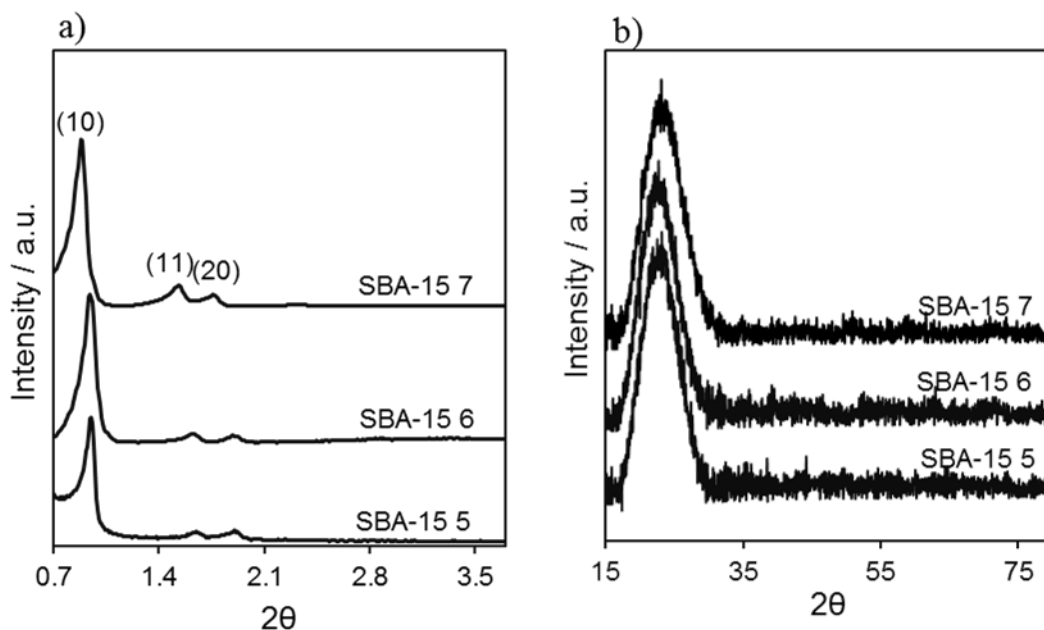


**Figure 3.4** Offset XRD patterns at low (a) and wide (b) angle of SBA-15 supports synthesized with different mesopore sizes.

The pore diameter increased and the silica wall thickness ( $t_{\text{wall}}$ ) decreased upon ageing temperature (**Figure 3.5a**).[23] **Figure 3.5b** illustrates a schematic representation of the cross-sectional channels of SBA-15, in which wall thickness ( $t_{\text{wall}}$ ), mesopore diameter ( $d_{\text{pore}}$ ) and the pore spacing ( $a_0$ ) are illustrated.

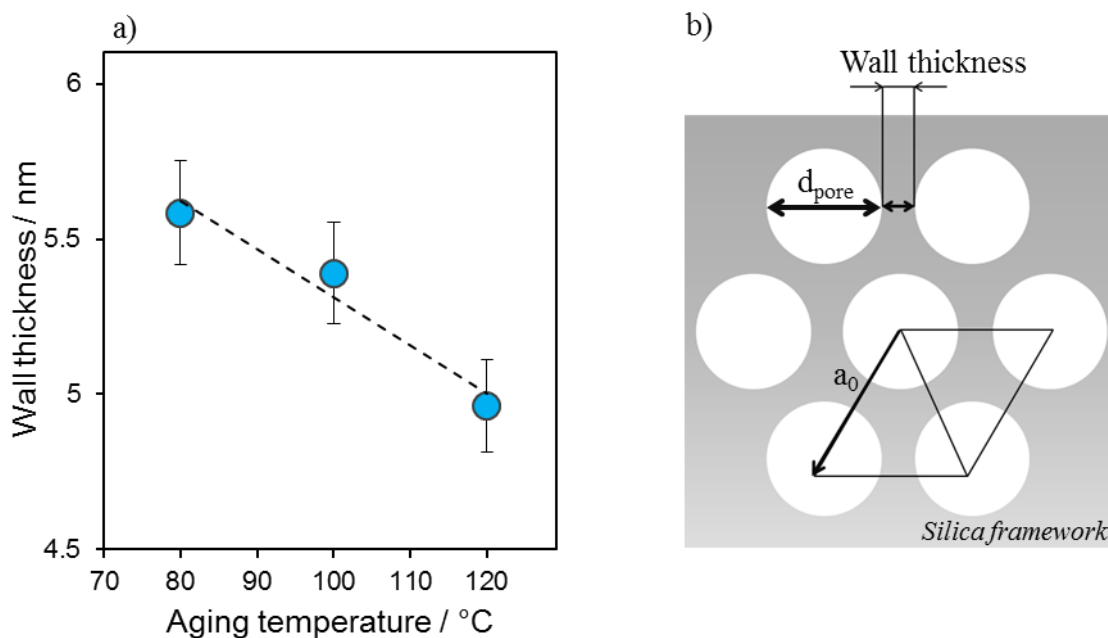


**Figure 3.5** Evolution of the evaluated wall thickness ( $t_{\text{wall}}$ ) (a) and representative ordered hexagonal structure of SBA-15 (b)

The calculated values are reported in **Table 3.2**.

**Table 3.2** Pore spacing ( $a_0$ ), interlayer spacing ( $d_{10}$ ) and wall thickness ( $t_{\text{wall}}$ ) of the supports synthesized at different aging temperature.

Sample	$2\theta$	$d_{(10)}^a / \text{nm}$	$a_0^b / \text{nm}$	$d_{\text{pore}}^c / \text{nm}$	$t_{\text{wall}}^d / \text{nm}$
SBA-15-5	0.95	9.4	10.9	5.4	5.6
SBA-15 6	0.94	9.6	11.1	5.9	5.4
SBA-15 7	0.88	10.2	11.8	6.8	5.0

<sup>a</sup>Interlayer spacing derived from Bragg's law, <sup>b</sup>pore spacing= $(2d_{10}/\sqrt{3})$ , <sup>c</sup>from BJH, <sup>d</sup>wall thickness= $a_0 - d_{\text{pore}}$

### 3.2.2 Characterisation of TiO<sub>2</sub>-SBA-15 catalysts

#### 3.2.2.1 Effect of mesopore size

A series of TiO<sub>2</sub>-SBA-15 composites were first synthesised using the SBA-15 supports with various pore diameters of 5, 6 and 7 nm. Two grafting cycles were performed on each support with the aim of investigating the physicochemical and optical properties of the supported materials and exploring the dispersion of the TiO<sub>2</sub> nanoparticles, in order to identify the optimal support for the further development of a smart catalyst for photocatalytic degradation of organic pollutants in water. Therefore, the supported TiO<sub>2</sub> samples were characterized by bulk and surface elemental analysis, XPS, N<sub>2</sub> porosimetry, XRD, ATR-IR spectroscopy, TEM and UV-vis diffusive reflectance spectroscopy. The nomenclature used for the composites catalyst is defined as follows:

Ti-SBA-15 X-n

where X = pore size (nm) of the silica support, n = number of grafting cycles.

### 3.2.2.1.1 Elemental analysis

XRF and ICP analysis were conducted on the composite Ti-SBA-15 materials to quantify their bulk composition. The values of wt.% of TiO<sub>2</sub> obtained from the two techniques are shown in **Table 3.3**.

**Table 3.3** Bulk elemental analysis for the Ti-SBA-15-n (n=1,2) composites.

Sample	TiO <sub>2</sub> loading / wt. %	
	XRF (% error)	ICP-OES
Ti-SBA-15 5-1	10.2 (1.41)	8.2
Ti-SBA-15 5-2	16.1(1.12)	13.2
Ti-SBA-15 6-1	9.5 (1.46)	11.9
Ti-SBA-15 6-2	20.0 (1)	17.4
Ti-SBA-15 7-1	12.0 (1.6)	10.7
Ti-SBA-15 7-2	18.4 (1.26)	15.4

### 3.2.2.1.2 X-ray photoelectron spectroscopy

XPS analysis was carried out to determine the surface composition and probe any changes to the surface chemistry (e.g. Ti oxidation state) and physical properties (e.g. spatial locale) upon incorporation of TiO<sub>2</sub> nanoparticles.

A summary of the surface elemental composition is presented in **Table 3.4**, confirming the increase in Ti loading with additional grafting cycle.

**Table 3.4** Surface composition of the Ti-SBA-15-X-n samples.

Sample	Si	O	Ti
	/ wt. %	/ wt. %	/ wt. %
Ti-SBA-15 5-1	45	49	6
Ti-SBA-15 5-2	42	46	11
Ti-SBA-15 6-1	43	47	9
Ti-SBA-15 6-2	39	49	12
Ti-SBA-15 7-1	45	47	7
Ti-SBA-15 7-2	41	48	10

Furthermore, **Figure 3.6a** show the Ti 2p region for the composite catalysts Ti-SBA-15-5-n in comparison with the spectrum of bulk anatase, which recorded a Ti 2p<sub>3/2</sub> peak position at 458.5 eV, which is in agreement with the literature value for the binding energy of Ti<sup>4+</sup>. [27]

The binding energy of the Ti 2p photoelectrons of Ti-SBA-15 samples was found to be higher in energy by approximately 0.8–1.9 eV. This shift towards a higher energy is due to the presence of

the interfacial species Ti-O-Si, and can be explained by the coordination of titanium (a more electronegative oxygen anion within the Ti-O-Si formation than that present within pure TiO<sub>2</sub> bulk species).[28] This phenomenon at the silica-titania interface due to the higher Pauling electronegativity of Si (1.9) versus Ti (1.54), resulting in the electron density being drawn away from titanium [29] The contribution from such polarized titanium atoms at the interface with SBA-15 found to decrease after only the 1<sup>st</sup> grafting cycle, which is most likely due to the addition of titania loading leading to the interfacial state being attenuated.

O 1s core level spectra are presented in **Figure 3.6b**. The O 1s region for bare SBA-15 can be deconvoluted into two species including oxygen in Si-O-Si at 532.8 eV, and a feature at a higher B.E. (533.3 eV) related to the presence of a hydroxyl species (Si-OH). The TiO<sub>2</sub>-grafted samples exhibit additional peak centred at 530 eV, attributed to Ti-O-Ti.[28, 30]

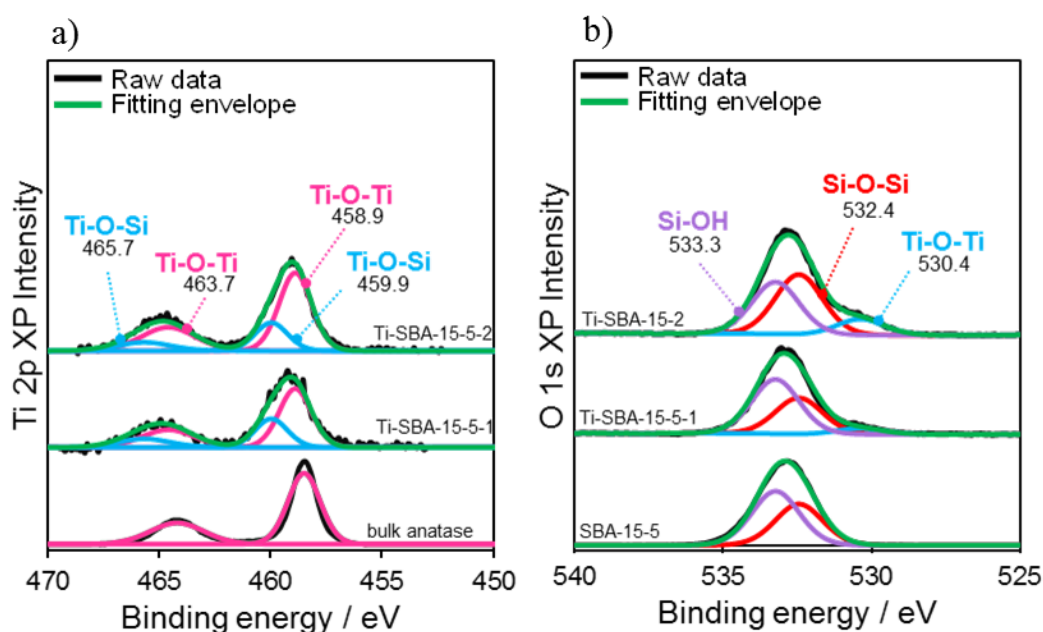


**Figure 3.6** Ti 2p (a) and O 1s (b) XPS stack plot for Ti-SBA-15-5-n. The spectra of bulk anatase and of the SBA-15 parent support are reported for comparison.

The corresponding Si 2p XP spectra are shown in **Figure 3.7**. The binding energy of the overall envelope decreases from 103.6 eV for pure SBA-15 by ~0.8 eV after each grafting cycle, and reaches the final value of 102.8 eV after the 2nd cycle. This shift in binding energy is consistent with that observed for the titanium signal, suggesting an interfacial species is being formed, and the contribution from bulk silica is being progressively screened by titania. This leads to the emergence of the silica environment at the interface, in which silicon atoms are linked via oxygen to less electronegative titanium. The Si 2p region was initially fit for SBA-15 with a Si 2p doublet (2p<sub>3/2</sub> = 103.6 eV, doublet separation = 0.6 eV). [31] Additionally, a secondary silicon phase was fit at 102.8 eV (green line) at higher binding energy, attributed to Si-O-Ti species. This secondary



species at a lower binding energy is resultant from electronic alterations to the silicon environment within the bridging layer.[32]

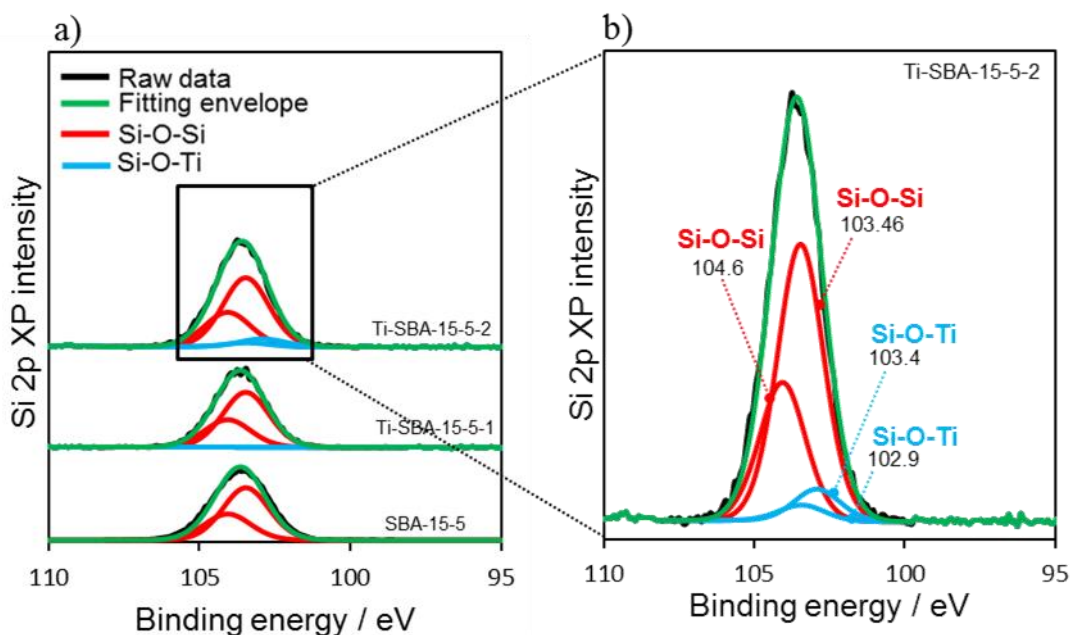


**Figure 3.7** Si 2p XPS spectra for the Ti-SBA-15-5-n samples and parent support (a), and the detail of the Si 2p region for the Ti-SBA-15-5-2 sample (b).

The surface and bulk compositions of the nanocomposite series evaluated by XPS and XRF respectively are summarised in **Table 3.5** below and the wt. % Ti surface:bulk ratio is reported. Surface Ti content was largely found to be exceeding that of the bulk content, which would suggest a surface enrichment of titania.

**Table 3.5** Comparison of the surface and bulk Ti wt. % content for the Ti-SBA-15-n composites.

Sample	Surface Ti <sup>a</sup> / wt. %	Bulk Ti <sup>b</sup> / wt. %	Bulk : Surface
Ti-SBA-15 5-1	5.8	4.5	0.8
Ti-SBA-15 5-2	10.5	10.0	1.0
Ti-SBA-15 6-1	8.8	7.0	0.8
Ti-SBA-15 6-2	12.2	13.0	1.1
Ti-SBA-15 7-1	7.3	4.0	0.6
Ti-SBA-15 7-2	10.3	9.0	0.9

<sup>a</sup> XPS, <sup>b</sup> XRF

### 3.2.2.1.3 Nitrogen porosimetry

Nitrogen porosimetry was employed to explore the impact of titania deposition on the textural properties of the three series of catalysts. It can be observed that the shapes of the recorded isotherms are retained after the grafting procedure, however the hysteresis loop caused by capillary condensation within the intrinsic mesopore regime (around  $P/P_0=0.6$ ) is progressively shifted toward lower relative pressures with increasing the number of grafting cycles, indicative of a decreasing mesopore diameter. (Figure 3.8a, Figure 3.9a, Figure 3.10a)

These results show that  $\text{TiO}_2$  is filling the mesopores forming a uniform coating. The reduction in mesopore diameter is also confirmed from the BJH analysis of the desorption curve which shows a progressive shift of the distribution curve towards smaller pore diameters (Figure 3.8b, Figure 3.9b, Figure 3.10b)

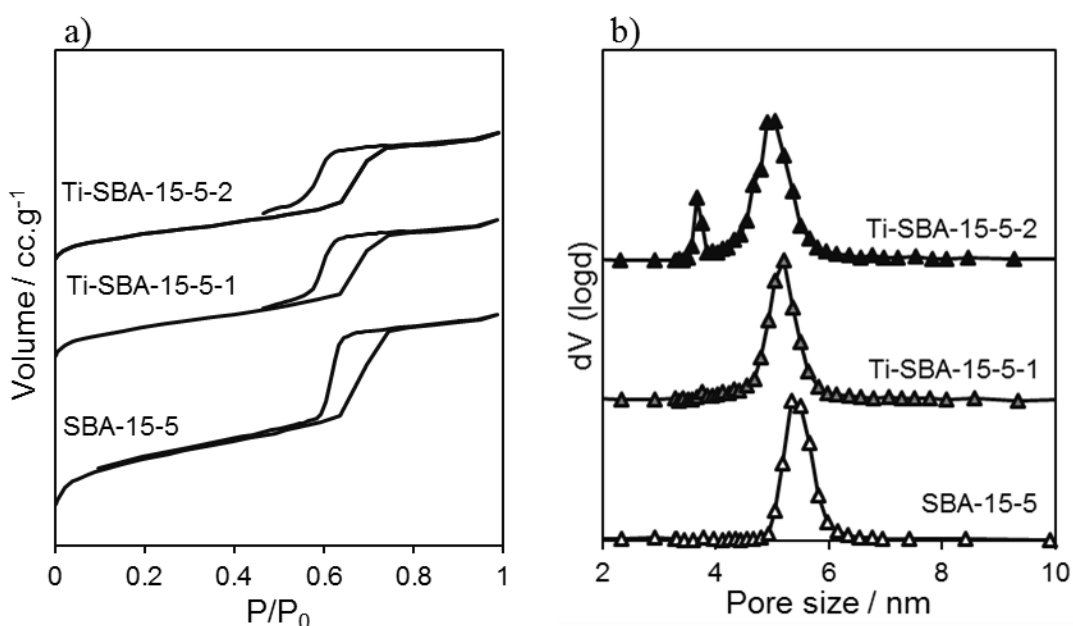


**Figure 3.8** Stacked isotherm plots (a) and BJH pore size distributions of Ti-SBA-15-5-n and the relative parent support (b).

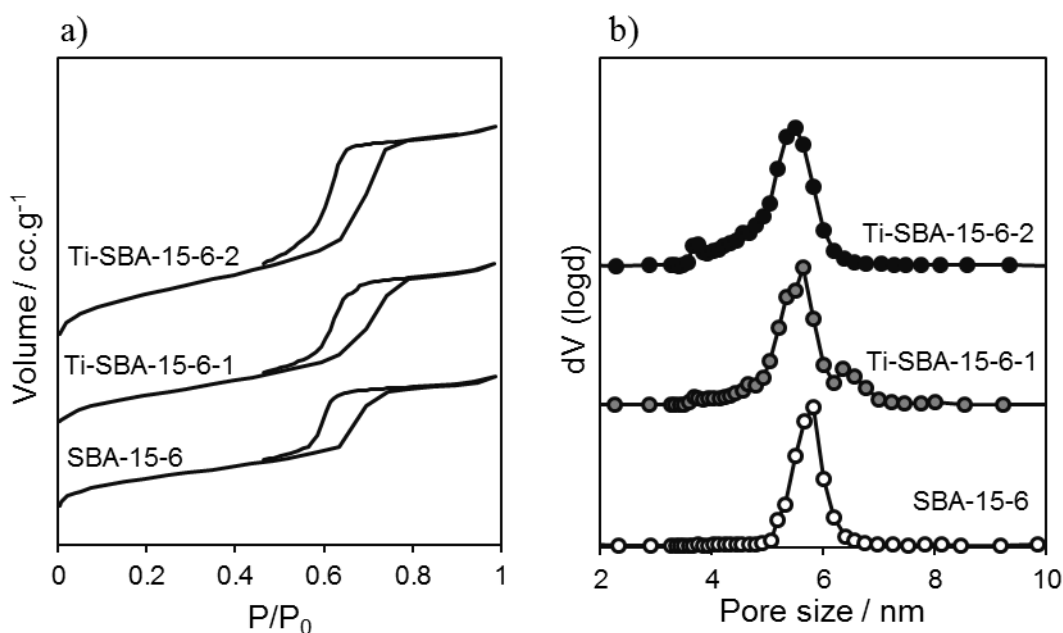


**Figure 3.9** Stacked isotherm plots (a) and BJH pore size distributions of Ti-SBA-15-6-n and the relative parent support.

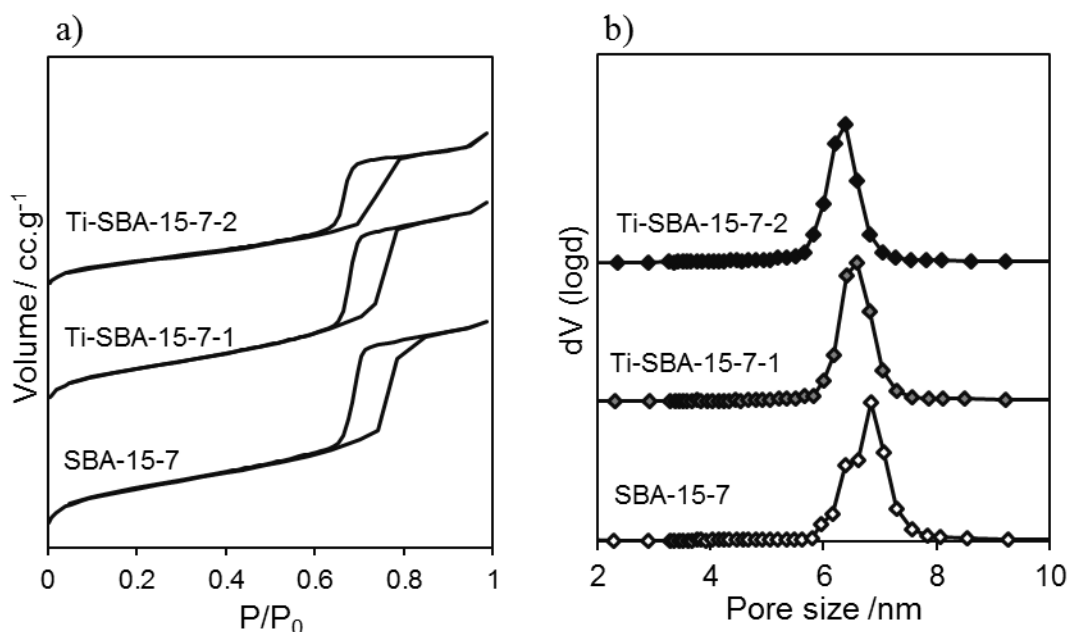


**Figure 3.10** Stacked isotherm plots (a) and BJH pore size distributions of Ti-SBA-15-7-n and the relative parent support.

Moreover, the plot of pore size distribution for the sample with the largest pore diameter (SBA-15-7) confirms that it retains its unimodal pore size distribution, which could suggest the possible formation of a homogenous titania layer. This means that the pore size of the silica supports is large enough to allow a uniform grafting inside the mesopores. Pore size distribution plots of the other two support aged at 80°C and 100°C exhibit a bimodal pore distribution, indicative of an uneven application of grafted titania layers within the inherent mesopore network.[18]

As shown in **Table 3.6** the surface area and the pore size of the grafted materials decreased with increasing number of performed grafting procedures.

**Table 3.6** Textural properties of composites materials.

Sample	$S_{\text{BET}}$ / $\text{m}^2 \text{g}^{-1}$	$d_p$ / nm	$V_{\text{total}}$ / $\text{cc g}^{-1}$	$V_{\text{micro}}$ / $\text{cc g}^{-1}$
SBA-15 5	719	5.4	0.7	0.13
Ti-SBA-15-5-1	517	5.2	0.7	0.05
Ti-SBA-15-5-2	366	4.9	0.5	0.04
SBA-15 6	640	5.9	0.9	0.07
Ti-SBA-15-6-1	471	5.7	0.7	0.02
Ti-SBA-15-6-2	420	5.5	0.6	0.03
SBA-15 7	748	6.8	1.0	0.04
Ti-SBA-15-7-1	558	6.6	1.1	0.02
Ti-SBA-15-7-2	484	6.2	0.8	0.02

#### 3.2.2.1.4 X-ray diffraction

The low angle XRD patterns in **Figure 3.11a-c** shows that the ordered mesostructures were retained upon two grafting procedures and an increase in wall thickness is observed between the parent and the grafted materials, confirming the presence of titania inside the mesopores. (**Figure 3.11d**)

The position of the (20) peak is unchanged relative to the (10) after grafting, indicating pore spacing is unaffected by the grafting, but a moderate decrease is evident in the intensities of all reflections of the composites materials, possibly due to X-ray absorption by the  $\text{TiO}_2$  matrix.[18]

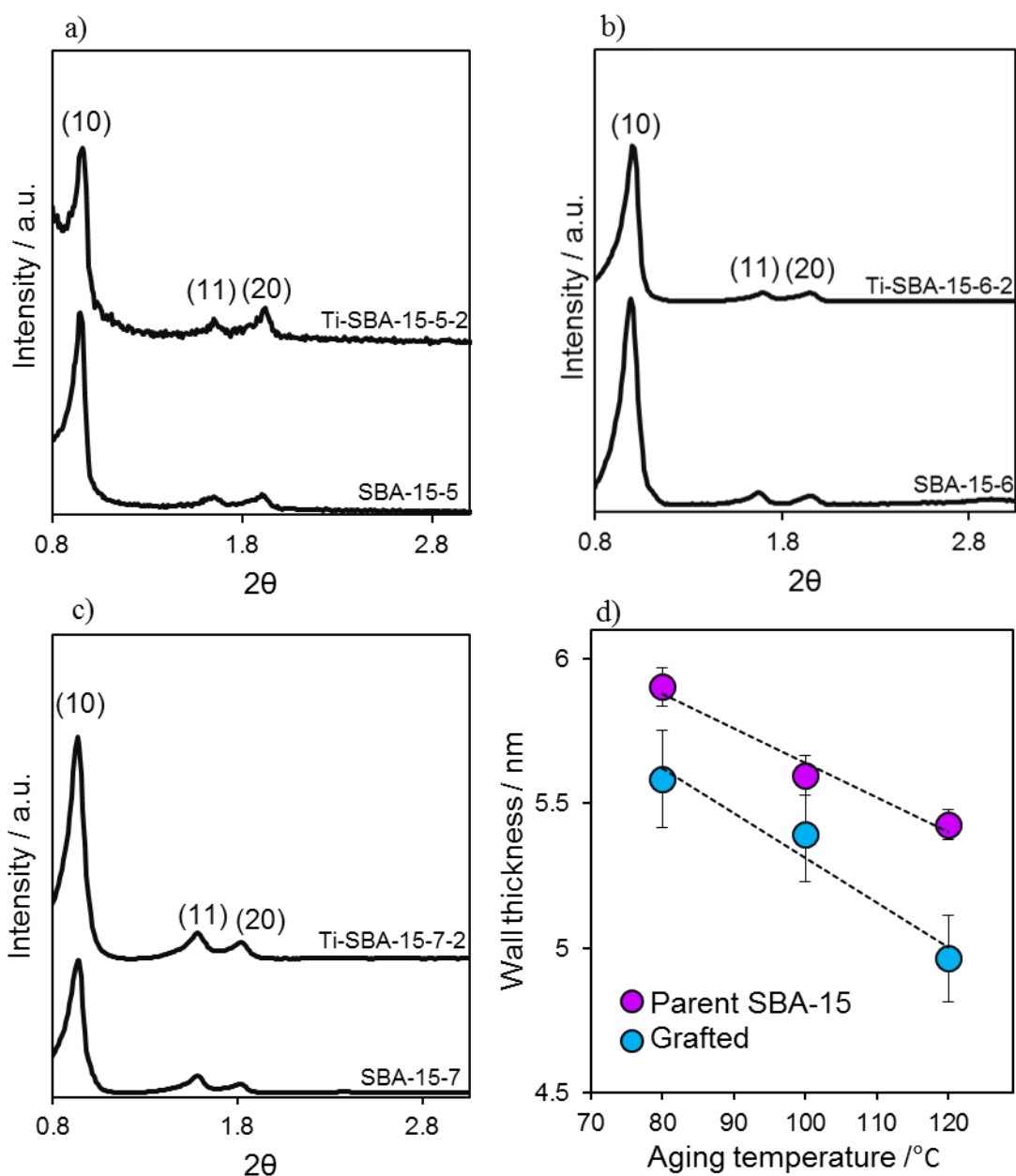


**Figure 3.11** Offset low angle XRD pattern of titania coated SBA-15 (2<sup>nd</sup> grafting cycle) compared with the each parent support (a,b and c), wall thickness as a function of aging time for the parent SBA-15s and TiO<sub>2</sub>-grafted (2<sup>nd</sup> cycle) materials (d).

The parameters evaluated from the XRD low angle are reported in **Table 3.7**.

**Table 3.7** Evaluated pore spacing ( $a_0$ ), interlayer spacing ( $d_{10}$ ) and wall thickness ( $t_{\text{wall}}$ ) of the three supports synthesized at different aging temperature and the related grafted materials.

Sample	$2\theta$	$d_{(10)} / \text{nm}$	$a_0 / \text{nm}$	$t_{\text{wall}} / \text{nm}$
SBA-15-5	0.9	9.4	10.9	5.6
Ti-SBA-15-5-2	0.9	9.3	10.8	5.9
SBA-15-6	0.9	9.6	11.0	5.4
Ti-SBA-15-6-2	0.9	9.5	10.9	5.6
SBA-15-7	0.8	10.2	11.8	5.0
Ti-SBA-15-7-2	0.8	10.2	11.8	5.4

From the collected wide angle XRD patterns, shown in **Figure 3.12**, no intense diffraction peaks corresponding to any  $\text{TiO}_2$  phase was observed from the grafted SBA-15, besides the (101) reflection peak of anatase (marked with the green star). As crystallites of a diameter below approximately 2 nm are undetectable by powder XRD with a  $\text{Cu K}\alpha$  X-ray tube, it can be concluded that the grafted  $\text{TiO}_2$  is either amorphous in nature or composed of very fine nanoparticulate moieties. The anatase diffraction peaks are slightly more pronounced for the Ti-SBA-15-5 sample. On the other hand, the sample with the largest pore size (7 nm) allows a better dispersion of the  $\text{TiO}_2$  on the support, avoiding the formation of large titania agglomerates.

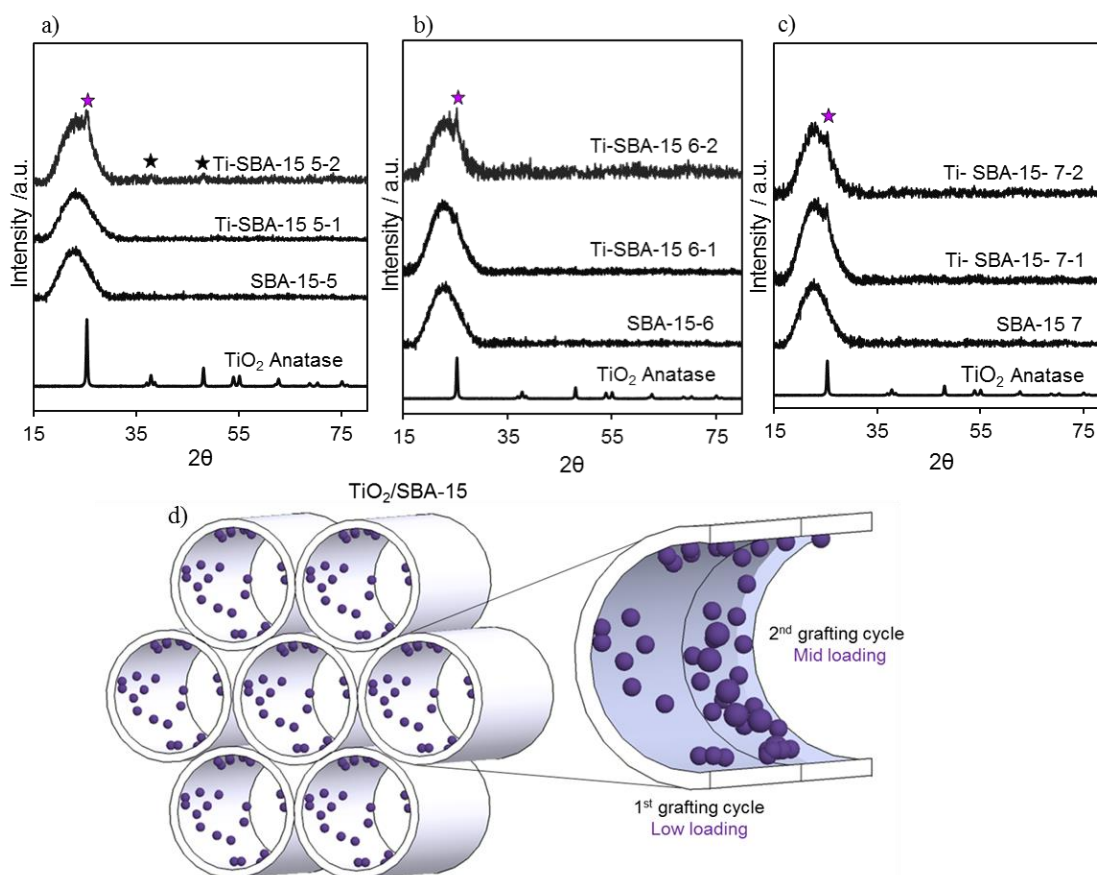


**Figure 3.12** Offset of wide angle XRD patterns of the composites materials and their support in comparison with the spectrum of pure anatase (the stars mark the anatase reflection peaks) for the

three series of support (a,b,c), sketch showing the SBA-15 material (light grey) coated with TiO<sub>2</sub> particles by two cycles of graftings (purple dots) (d).

### 3.2.2.1.5 Raman analysis

The crystal phase of the Ti-SBA-15-*n* photocatalysts for TiO<sub>2</sub> loading ≤10 wt. % was determined with Raman spectroscopy and the spectra of the series obtained from the grafting on SBA-15-5 are presented in **Figure 3.13a**.

The result indicates clearly that only the anatase phase of TiO<sub>2</sub> exists in these materials. The four different bands at 145, 400, 520 and 640 cm<sup>-1</sup> are assigned to anatase crystallites (in red).[33] On the other hand, silica typically possesses four main Raman features: the siloxane linkages at 452 and 803 cm<sup>-1</sup>, the three- and four-fold siloxane rings at ~ 605 and ~ 498 cm<sup>-1</sup>, the surface silanol groups at 980 cm<sup>-1</sup> and the antisymmetric mode of the Si-O-Si linkages at 1050 cm<sup>-1</sup>. [33] However the signal of SBA-15 is weak and only some of the typical silica vibrations could be identified (grey marked). (**Figure 3.13b**)

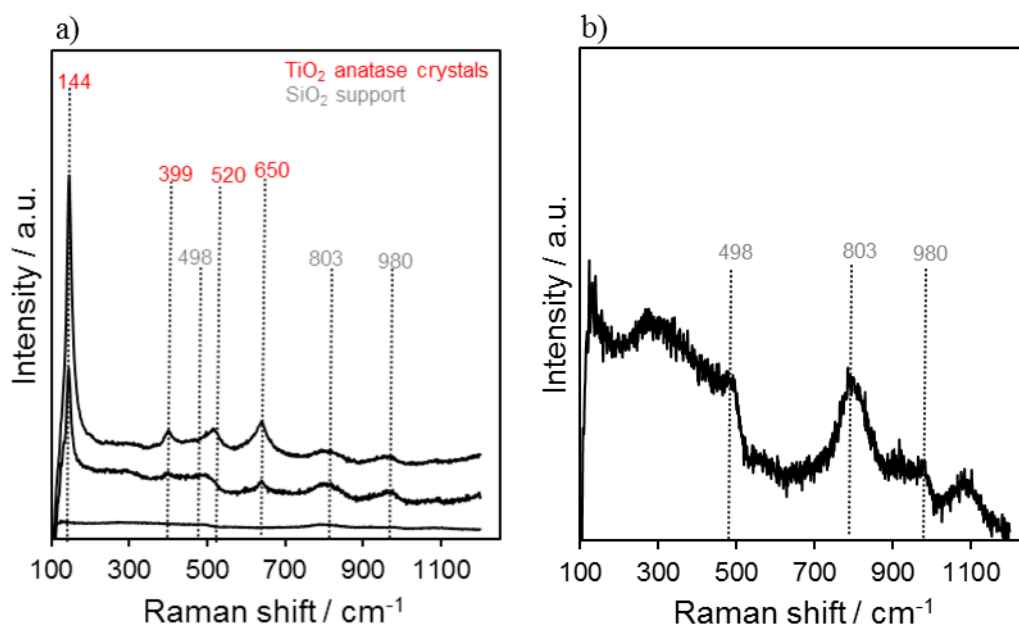


**Figure 3.13** Raman spectra of the parent SBA-15-5 and Ti-SBA-15-*n* (*n*=1-2) (a) and detail of the SBA-15-5 spectrum (b).

### 3.2.2.1.6 ATR IR spectroscopy

FT-IR spectra of the composites samples (black and red line) and the associated support SBA-15-7 (grey line) are shown in **Figure 3.14**. The spectrum of pure TiO<sub>2</sub> is reported for comparison (green line). The other catalysts obtained through grafting the supports with different pore sizes (Ti-SBA-15-5-*n* and Ti-SBA-15-6-*n*) exhibited the same trend.

In **Figure 3.14a** the peaks at  $3740\text{ cm}^{-1}$  and around  $3500\text{ cm}^{-1}$  is due to the stretching vibration of hydroxyl groups of Si-OH or Ti-OH, respectively.[34] In **Figure 3.14b** the IR absorption peaks at  $1072\text{ cm}^{-1}$  and  $800\text{ cm}^{-1}$  are attributed to  $\nu_{\text{as}}(\text{Si-O-Si})$  and  $\nu_{\text{s}}(\text{Si-O-Si})$  vibrations of silica framework of SBA-15, respectively.[18] Meanwhile, the band at ca.  $435\text{ cm}^{-1}$  corresponded to the characteristic tetrahedral bending of Si-O bond of pure SBA-15.[35] These three peaks are well defined in the spectrum of the bare support (grey line).

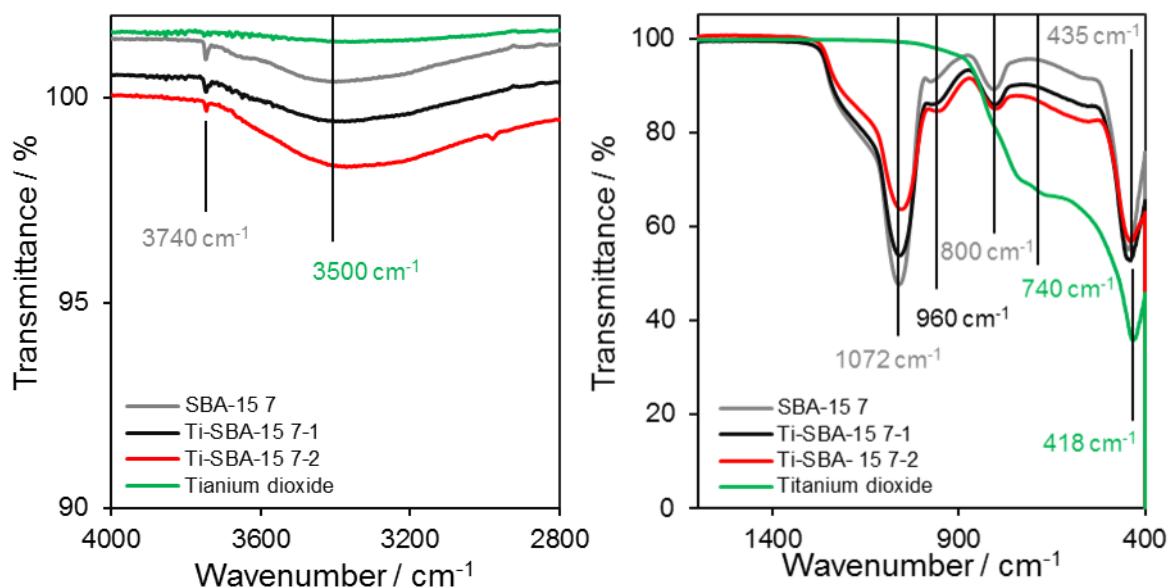


**Figure 3.14** ATR IR spectra of Ti-SBA-15-n samples, the support and the commercial benchmark of  $\text{TiO}_2$  P-25 in the range of  $2800\text{--}400\text{ cm}^{-1}$  (a) and  $400\text{--}1600\text{ cm}^{-1}$  (b).

The band at around  $960\text{ cm}^{-1}$  has been widely used to characterize the incorporation of metal ions in the silica framework as the stretching Si-O vibration mode is perturbed by the neighbouring metal ions.[36] In the spectrum of the bare support this band is very weak and can be assigned to the stretching  $\nu_{\text{as}}(\text{Si-OH})$ . Upon increasing the  $\text{TiO}_2$  loading the band became more evident with a small shift to a lower frequency. According to the literature, this can be direct evidence for the substitution of Ti ions in the SBA-15 framework and the band can be assigned to the stretching  $\nu_{\text{as}}(\text{Si-O-Ti})$  mode.[18] Also the peak at  $435\text{ cm}^{-1}$   $\delta(\text{Si-O})$  is perturbed by the increasing of titania loading, with a shift to a lower frequency of  $418\text{ cm}^{-1}$ , characteristic of the stretching  $\nu(\text{Ti-O})$ . In addition, a broad absorption in the range  $400\text{--}800\text{ cm}^{-1}$  grows with the Ti content. The band at c.a.  $740\text{ cm}^{-1}$  is commonly assigned to  $\nu(\text{Ti-O-Ti})$ , so this feature in the composite material is evidence of presence of  $\text{TiO}_2$  as a separate phase, and becomes more evident at higher  $\text{TiO}_2$  loading.

### 3.2.2.1.7 Scanning transmission electron microscopy

The parent SBA-15-7 and the corresponding composite material Ti-SBA-15 7-2 were imaged by STEM in order to further prove the retention of the ordered structure of the silica support following



the grafting procedure. Moreover, it could confirm the presence/absence of large titania agglomerates. (**Figure 3.15**)

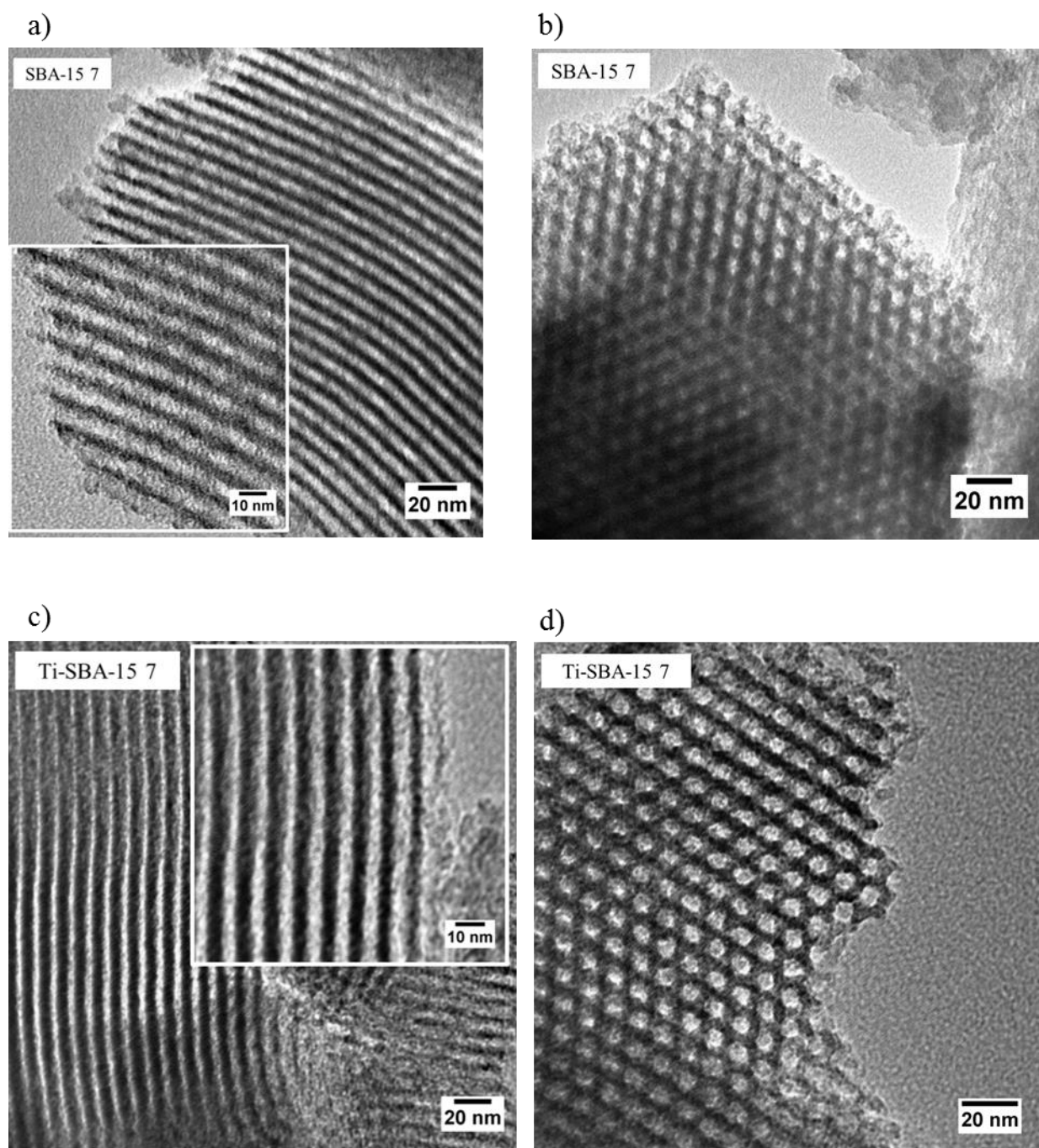


**Figure 3.15** Representative bright field STEM images of the channel (on the right) and the open mesoporous structure (on the left) of the SBA-15 7 (a,b) and Ti-SBA-15-7-2 (c,d).

The STEM images obtained using the high-angle annular dark field imaging clearly reveal regions of hexagonally arranged pore structures, as well as the channels consistent with porosimetry and low angle XRD results. It should be noted that large titania agglomerates were not observed in TEM images of the synthesised mesoporous silica after two cycles of  $\text{TiO}_2$  grafting. Furthermore pore size and a pore spacing distributions were measured using ImageJ software and compared with the data acquired from  $\text{N}_2$  adsorption and powder. (**Figure 3.16**)

Direct measurements from STEM images confirm that there is a clear decrease in pore diameter after two cycles of grafting, but no change in pore spacing, in agreement with the data obtained from XRD and porosimetry analysis

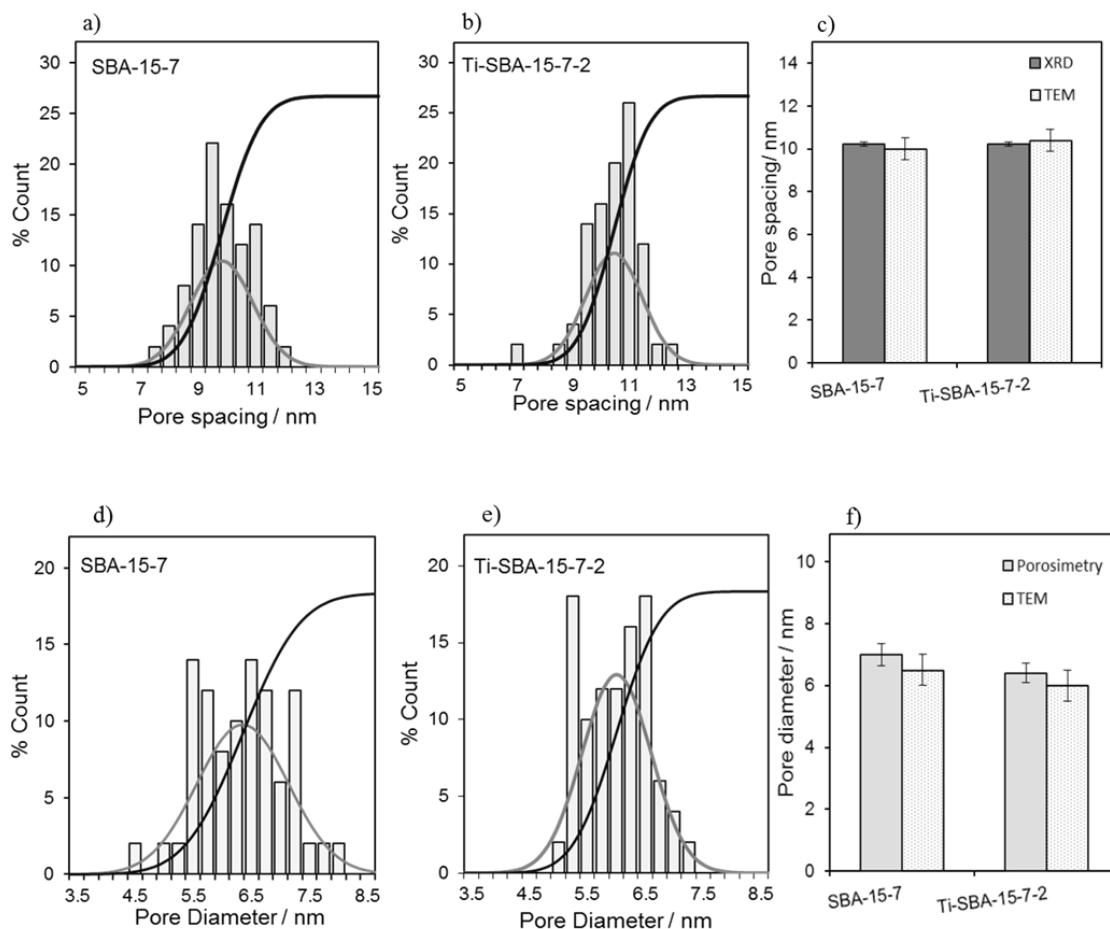


**Figure 3.16** Pore spacing distributions, normal and cumulative statistical distributions for (a) SBA-15 7, (b) Ti-SBA-15 7-2, (c) comparison between TEM and XRD measurements. Pore size distributions, normal and cumulative statistical distributions for (d) SBA-15 7, (e) Ti-SBA-15 7-2 and (f) comparison between TEM and porosimetry measurements.

### 3.2.2.1.8 UV-vis diffuse reflectance spectroscopy

UV-visible spectroscopy is commonly used for the assessment of Ti atoms environment on silica-based materials and to investigate the growth of the  $\text{TiO}_2$  particles on the support, since for semiconductors the band gap energy ( $E_g$ ) is expected to shift with the particles size according to the *quantum size effect*. **Figure 3.17** shows the optical properties size dependent of a semiconductor from the nanosized crystals to the bulk crystal. The term quantum size effect is frequently used when the size (radius) of solid particles is smaller than their Bohr radii to result in expansion of the bandgap. The Bohr radii for anatase particles have been estimated to be 2.5 nm.

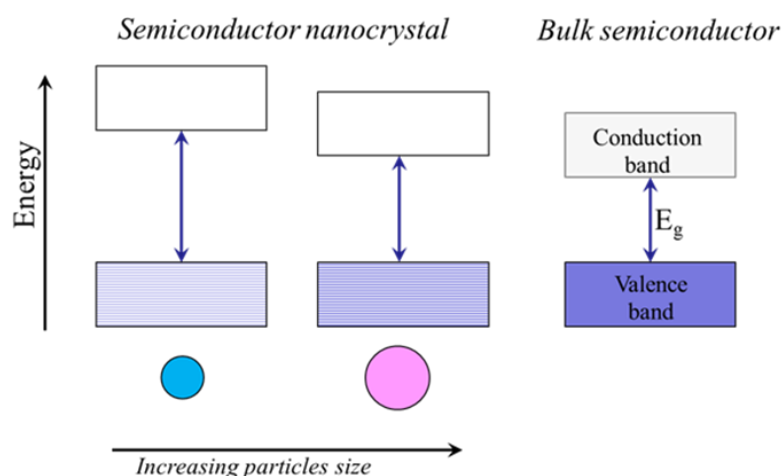


**Figure 3.17** Electronic energy states of a semiconductor in the transition from nanosized to bulk crystals.

**Figure 3.18** shows the DRUV-Vis spectra of the Ti-SBA-15-X-n samples in comparison with the spectra of the commercial TiO<sub>2</sub> Degussa P-25 and the bulk anatase. The spectrum of the parent mesoporous SBA-15 is also reported which is mainly transparent in the UV-vis region, the absorption observed in the range between 200 and 400 nm comes from titanium species. An absorption band of pure SBA-15 is seen around 210 nm (bold black line). As shown, the major adsorption band of TiO<sub>2</sub> (Degussa P-25 or pure anatase) is around 390 nm.[36, 37]

The adsorption band of TiO<sub>2</sub> is clearly seen in Ti-SBA-15-X-n samples which are typical due to the ligand-metal charge transfer (LMCT) between Ti<sup>4+</sup> and oxygen ligands, mainly attributable to the charge transfer in Si–O–Ti groups.[38] The adsorption band of Ti-SBA-15-X-n samples showed a blue (shorter wavelength) shift of 20-30 nm. [39] Even if a blue shift of the absorption edge of those samples is observed, it might due to the amorphous part of titania, not due to the quantum size effect.[40]

The TiO<sub>2</sub> particles size evaluated from XRD analysis are 21 nm and 30 nm for Degussa P-25 and bulk anatase respectively, whereas absence or not measurable anatase XRD reflections were found for the Ti-SBA-15-X-n samples, in agreement also with the bright field TEM images.

Therefore the pore channels of SBA-15 provide a size confinement for TiO<sub>2</sub> particles with average size probably below 2 nm, according also with previous authors which reported particles size in the range of 1.3-1.6 nm after three successive graftings.[36] The blue shift of the absorption edge for the composite samples clearly indicates an increase in the band gap of TiO<sub>2</sub> nanoparticles on the SBA-15 compare to the reference bulk materials.

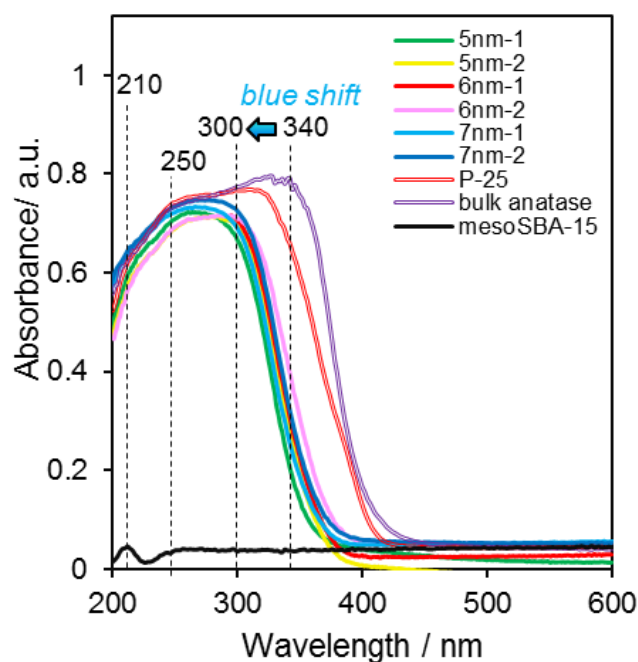


**Figure 3.18** UV-vis spectra of Ti-SBA-15-X-n samples, Degussa P-25, bulk anatase and mesoporous SBA-15.

Furthermore the band gap values were evaluated through the Kubelka-Munk function  $F(R)$  as shown in **(Figure 3.19a)** [41]. The band gap energies estimated from the intercept of the tangents to the plots are 3.1 and 3.2 eV for bulk anatase  $\text{TiO}_2$  and P-25 nanoparticles, respectively. The larger band gap of the Ti-SBA-15-X-n can be attributed to the quantum size effect as discussed above, due to the small crystalline size limited by SBA-15 channels. **Figure 3.19b** reports in detail the small region of absorbance of the parent support which shows a very wide band gap (5.5 eV).

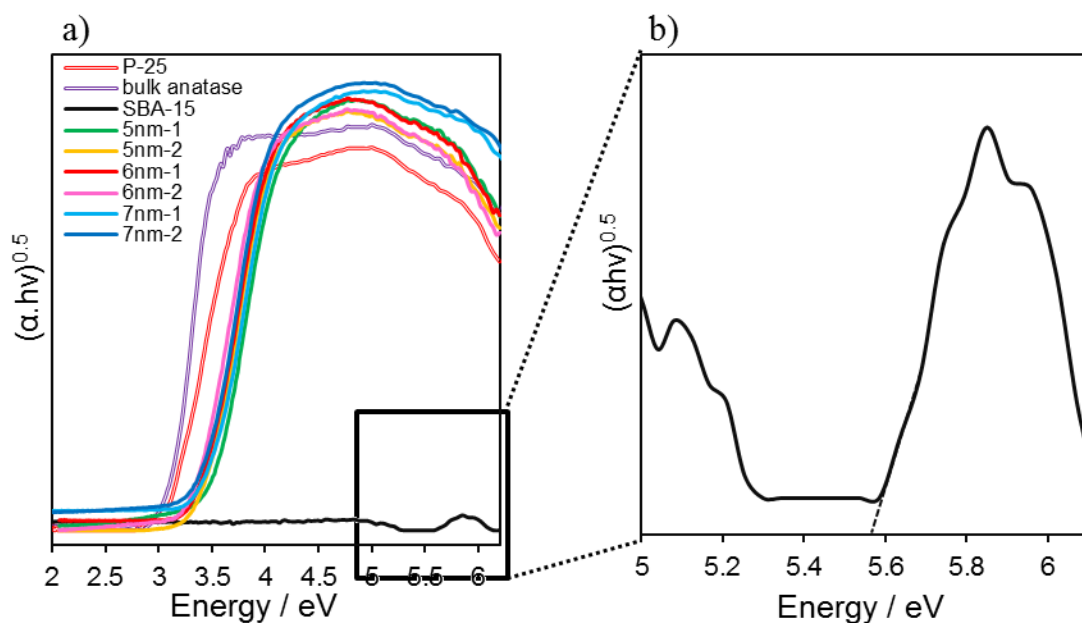


**Figure 3.19** Kubelka-Munk function for band gap evaluation (a), spectrum of SBA-15 (b).

The band gap values and the corresponding band edge are summarized in the **Table 3.8**.

**Table 3.8** Titania content (wt.%), band gap ( $E_g$ ), corresponding wavelengths value ( $\lambda_{Eg}$ ) and the band edge for the parent support, Ti-SBA-15-X-n and the bulk references materials.

Catalyst	$E_g$ / eV	$\lambda_{Eg}$ / nm	Band edge / nm
parent SBA-15	5.5	224	-
Ti-SBA-15 5-1	3.5	354	264
Ti-SBA-15 5-2	3.5	359	284
Ti-SBA-15 6-1	3.5	354	274
Ti-SBA-15 6-2	3.4	369	294
Ti-SBA-15 7-1	3.5	354	266
Ti-SBA-15 7-2	3.4	365	276
TiO <sub>2</sub> P-25	3.2	390	320
bulk anatase TiO <sub>2</sub>	3.2	390	340

### 3.2.2.2 Effect of titania loading

SBA-15-7 with larger pore size was chosen as support to prepare a series of composites catalyst with increasing TiO<sub>2</sub> loading in the range of 10-50 wt.%. The grafting of titania was achieved using a modified procedure by Landau et al.[42] describe in detail in **Chapter 2**. Five grafting cycles, each targeted to give a loading of ~10 wt. % of titania, were performed to obtain a layer-by-layer fashion deposition of TiO<sub>2</sub> on the silica support. Multiple grafting cycles were employed with the aim of avoiding pore blocking, ensuring a uniform covering of the parent SBA-15 and assessing the evolution of titania surface characteristics with film thickness (i.e. titania phase, particles size, band gap). The materials were then characterized in order to give a precise description of the composites catalysts and finally, the catalytic activity was evaluated by studying the photodegradation of methyl orange (MO) in water under UV-vis irradiation.

### 3.2.2.2.1 Elemental analysis

TiO<sub>2</sub> loadings were measured using XRF and ICP-OES analysis as shown in **Table 3.9**.

**Table 3.9.** Bulk elemental analysis for the Ti-SBA-15-n (n=1-5) composites.

Sample	TiO <sub>2</sub> loading / wt. %	
	XRF (% error)	ICP-OES
Ti-SBA-15-1	12.0 (1.4)	10.7
Ti-SBA-15-2	18.4 (0.61)	15.4
Ti-SBA-15-3	28.4 (0.46)	26.8
Ti-SBA-15-4	35.6 (0.43)	40.3
Ti-SBA-15-5	42.8 (0.7)	47.1

**Figure 3.20** shows the comparison of the two sets of data which are in very close agreement for the two techniques.

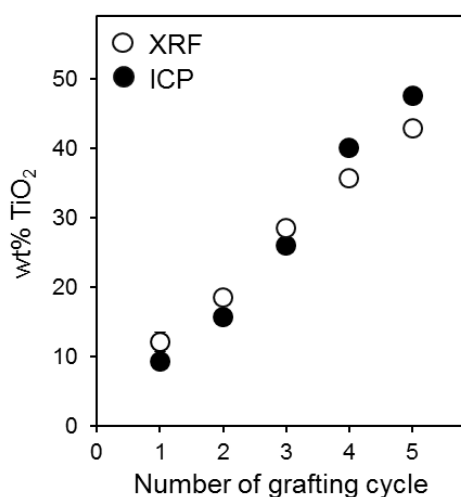


**Figure 3.20** Comparison on the wt. % of TiO<sub>2</sub> values obtained from XRF and ICP analysis.

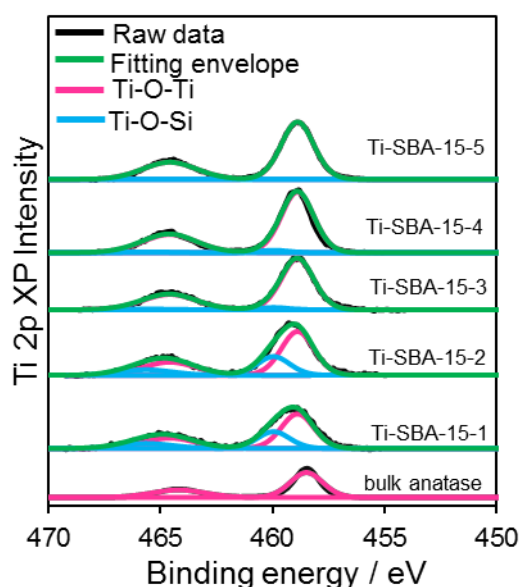
### 3.2.2.2.2 X-ray photoelectron spectroscopy

XPS analysis was employed to probe titania on the surface of the SBA-15 and determine any change in oxidation state as a function of Ti loading. A summary of the elemental composition is presented in **Table 3.10** which reports a significant increase titania content, indicative of surface species.

**Table 3.10** Surface composition of the Ti-SBA-15-n materials.

Sample	Si	O	Ti
	/ wt. %	/ wt. %	/ wt. %
SBA-15	47	51	-
Ti-SBA-15-1	45	47	7
Ti-SBA-15-2	41	48	10
Ti-SBA-15-3	32	46	14
Ti-SBA-15-4	26	45	22
Ti-SBA-15-5	24	45	25

**Figure 3.21** shows the Ti 2p spectra for the five grafting cycles. The Ti 2p<sub>3/2</sub> core level is characterized by binding energy (BE) values in the range of 458.7–459.3 eV which are indicative of octahedrally coordinated TiO<sub>2</sub> species.[43] The Ti 2p region for the synthesised catalysts was fit using line shapes obtained from a commercial bulk anatase, which recorded a Ti 2p<sub>3/2</sub> peak position of 458.5 eV, consistent with literature values.[27] A shift to higher binding energies is associated with the formation of Ti-O-Si bonds, resulting in the two sets of peaks exhibited in the Ti 2p spectra [44] caused by a decrease in the positive charge of the titania species within the Ti-O-Si formation compared to that of pure titania.[28]

**Figure 3.21** Ti 2p XPS spectra for the Ti-SBA-15-5-n samples and parent support.

The oxygen 1s region of the Ti-SBA-15-n samples and the bare support are shown in **Figure 3.22a**. The oxygen 1s region for the parent SBA-15 displayed the peak of silicon dioxide Si-O-Si at 532.8 eV and the feature at 533.3 eV assigned to oxygen in Si-OH. Increasing the titania loading resulted

in the emergence of a third feature centred at 530 eV, assigned to the oxygens in bulk titania, Ti-O-Ti.[28] It can be noticed that the increase of TiO<sub>2</sub> loading leads to a continuous increase in intensity of the 530.0–530.6 eV peak suggesting a larger presence of separate TiO<sub>2</sub> phases on the catalyst surface. **(Figure 3.22b)** It is evident that the surface Si-OH species decreases across the series with bulk titania loading, as titania species are grafted on the silica surface. The final percentage of Si-OH is zero after five following grafting procedures, indicative of formation of titania surface species.

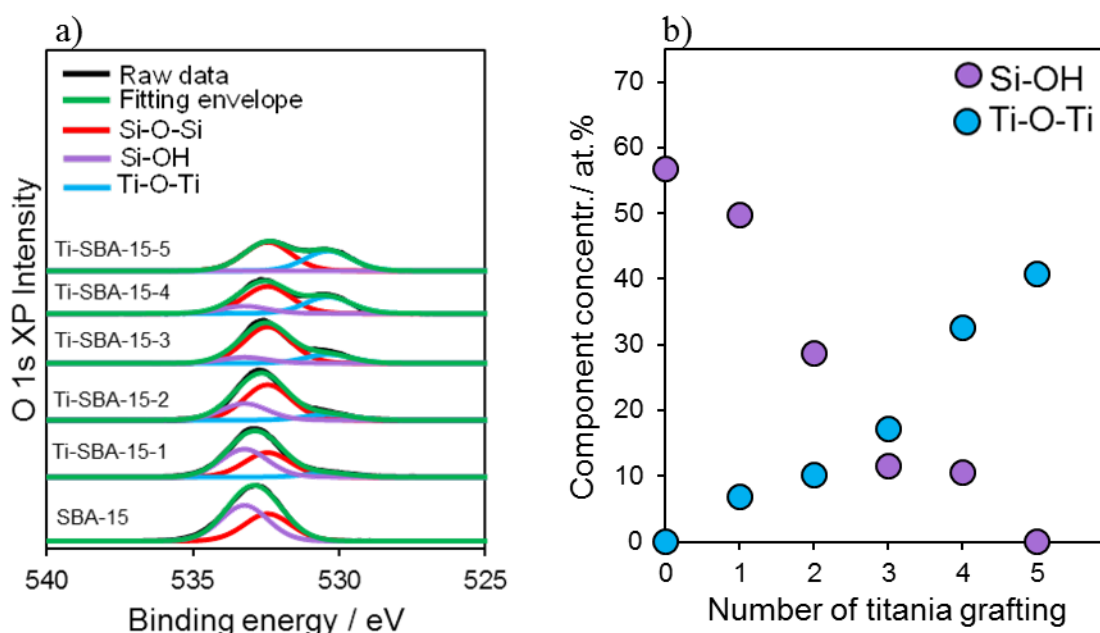


**Figure 3.22** O 1s XPS stack plot for Ti-SBA-15-*n* (*n*=1-5). The spectrum of the parent SBA-15 is reported for comparison (a); variation of surface species with increasing TiO<sub>2</sub> film thickness (b).

Finally the corresponding Si 2p XP spectra are shown in **Figure 3.23a** and fit with a Si 2p doublet ( $2p_{3/2}$  = 103.6 eV, doublet separation = 0.6 eV). The binding energy of the overall envelope progressively decreases from 103.6 eV for the bare silica support to a final value of 102.8 eV. The secondary silicon phase fit at a higher binding energy is attributed to Si-O-Ti species. This binding energy shift is in the opposite direction to that observed for the titanium signal for the same reason explained in **Section 3.2.2.1.2**. Moreover, as expected, the contribution from bulk silica is progressively screened by thicker titania ad layers. This leads to the emergence of the silica environment at the interface, in which silicon atoms are linked via oxygen to less electronegative titanium.[32]

The Ti:Si wt. % (from XPS) of the five grafted sample as function of their bulk ratio (obtained from the XRF data) is shown in **Figure 3.23b**.

It can be seen that the surface content of TiO<sub>2</sub> species increases with the TiO<sub>2</sub> loading. The solid line shows the expected values for a homogeneous distribution of titania phase within the support. An increase in the Ti:Si ratio above the predicted trend after the 3<sup>rd</sup> cycle of grafting (wt. %TiO<sub>2</sub> > 30) however, suggests that the TiO<sub>2</sub> species are located mainly on the external catalyst surface.



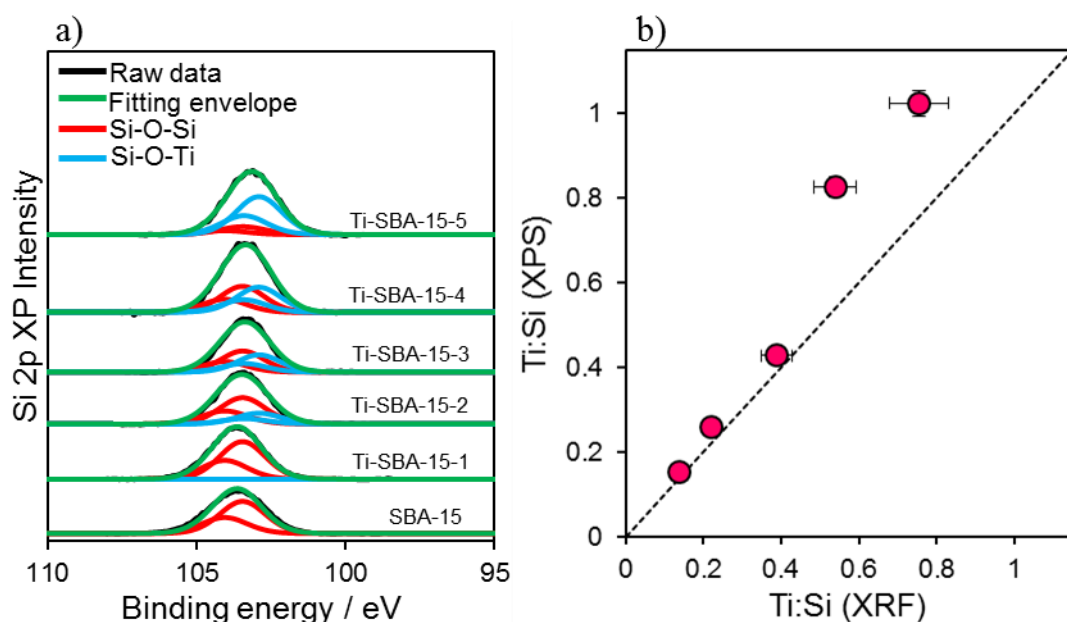


**Figure 3.23** Si 2p XPS spectra for the Ti-SBA-15-5-n samples and parent support (a). Surface Ti/Si atomic ratio (from XPS) versus bulk Ti/Si atomic ratio (from XRF). Solid line shows the expected values for a homogeneous Ti distribution within the solid (b).

### 3.2.2.2.3 Nitrogen porosimetry

Nitrogen porosimetry was performed on these materials to reveal the effect of titania loading on effective surface areas and pore dimensions. **Figure 3.24** demonstrates N<sub>2</sub> isotherms and pore size distribution for parent SBA-15 and the titania grafted SBA-15 catalysts. It can be observed that after grafting titania on the silica support, the structure of SBA-15 remains intact.

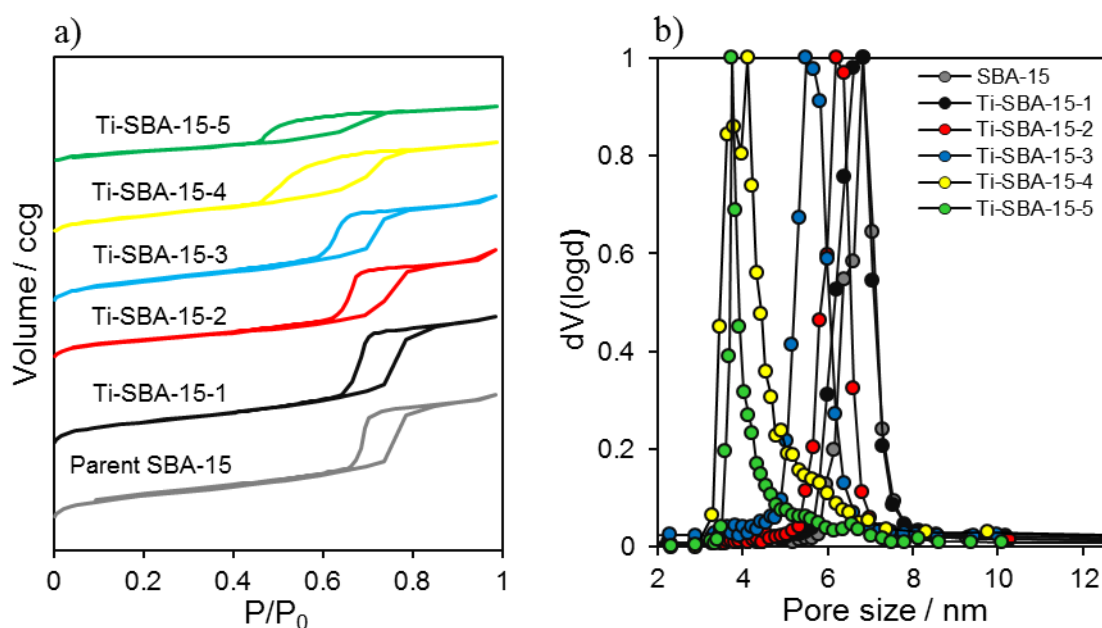


**Figure 3.24** Stacked isotherm plots (a) and BJH pore size distributions for Ti-SBA-15-5-n and the relative parent support (b).

In **Figure 3.24a** all the isotherms exhibit type IV characteristics according to IUPAC with H1-type hysteresis loops during the desorption step. This feature is the result of capillary condensation mechanism of filling and emptying pores in the mesopore region.

The isotherm of the parent SBA-15 shows a well-defined step around  $P/P_0 = 0.7$ , characteristic of capillary condensation within uniform pores. Whereas the Ti-SBA-15-n samples show the onset of the capillary condensation progressively shifted toward lower  $P/P_0$  values upon increasing of number of grafting. The pores of the parent SBA-15 exhibit an average diameter of 7 nm, and with increasing the number of graft cycles the pores become as narrow as ~4 nm. The presence of narrowed mesopores causes delayed evaporation, requiring a lower desorption pressure  $P/P_0$  and changes in the shape of the desorption branch of the isotherm.[29, 45] This result is confirmed by the BJH analysis of the desorption curve (**Figure 3.24b**) which shows a narrow pore size distribution with a progressive decrease in the average pore size. **Table 3.11** reports the textural properties of the parent and the composite material.

**Table 3.11** Structural and textural properties of the parent SBA-15 and the grafted samples.

Catalyst	$S_{\text{BET}}$ / $\text{m}^2.\text{g}^{-1}$	$d_p$ nm	$V_{\text{total}}$ / $\text{cc.g}^{-1}$	TiO <sub>2</sub> layer thickness / nm
Parent SBA-15	748	6.8	1.1	0
Ti-SBA-15-1	558	6.6	1.0	0.11
Ti-SBA-15-2	484	6.2	0.8	0.32
Ti-SBA-15-3	408	5.6	0.7	0.62
Ti-SBA-15-4	376	4.1	0.6	1.36
Ti-SBA-15-5	301	3.8	0.5	1.54

The trend of variation of textural properties and increasing of TiO<sub>2</sub> layer thickness with number of grafting cycles is shown in **Figure 3.25**.

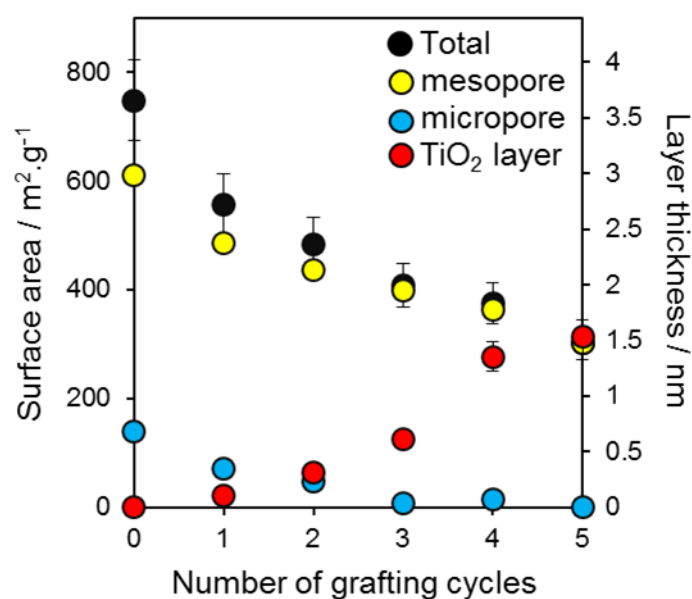


**Figure 3.25** Effect of Ti loading on mesopore and micropore volume and evolution of titania film thickness with the number of grafting cycles.

Micropores are almost completely filled after two grafting cycles. Mesopore surface area decreases steadily with each subsequent grafting cycle, suggesting uniform deposition of the TiO<sub>2</sub> film without undesired pore blockage.

The theoretical titania monolayer is assumed to have a thickness of 0.352 nm, from the interlayer spacing of the (101) plane of TiO<sub>2</sub> (anatase).[11] The calculated titania thickness is consistent with the theoretical layer-by-layer growth at the 3<sup>rd</sup> cycle of grafting.

#### 3.2.2.2.4 X-ray diffraction

**Figure 3.26a** shows the low-angle XRD patterns of pure SBA-15 and Ti-SBA-15 samples.

It can be seen that all the samples exhibited XRD patterns with one very intense diffraction peak and two weak peaks, which are characteristic of 2-D hexagonal (P6mm) structure with excellent textural uniformity.

The results indicated that Ti-SBA-15-n materials retained the ordered mesoporous structure of SBA-15. Moreover, the position of the (*d*<sub>10</sub>) reflection is unchanged and thus according with the Braggs law, the interplanar distance (*d*<sub>10</sub>) is not affected by the grafting procedure. Pore wall thickness has also been calculated subtracting average pore diameter (calculated from N<sub>2</sub> porosimetry experiments, see **Section 3.2.2.2.3**) from the unit cell size. Adding the successive loading of titanium dioxide leads to a thickening of the pore wall, confirming the preferential incorporation of metal oxide species onto the surface of the mesoporous system. (**Figure 3.26b**)

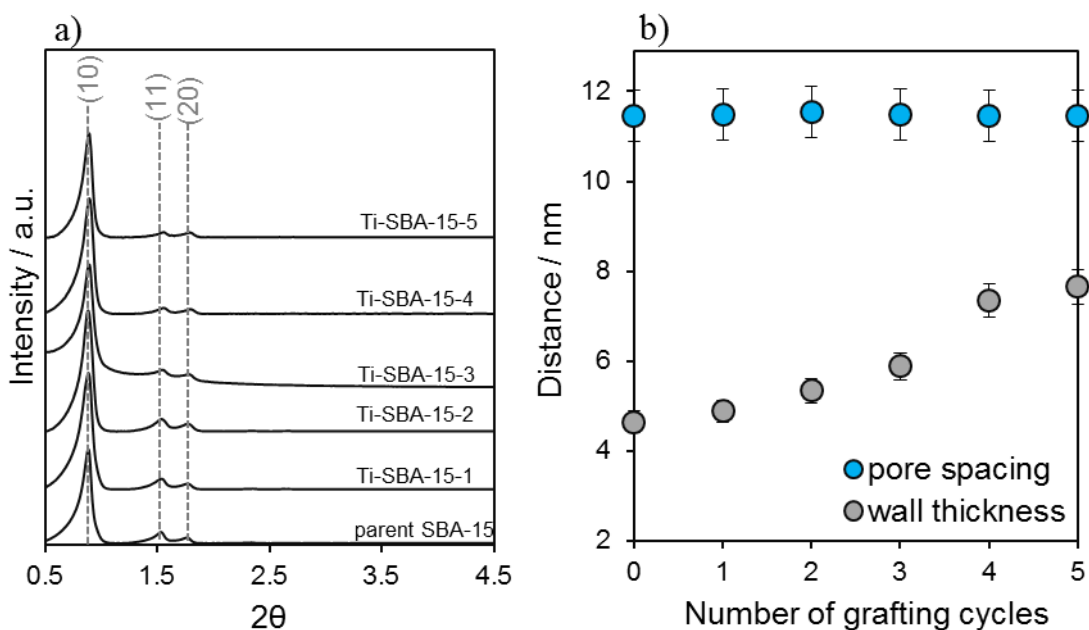


**Figure 3.26** Offset low angle XRD patterns of parent SBA-15 and the  $\text{TiO}_2$  grafted sample (a); evolution of the evaluated wall thickness ( $t_{\text{wall}}$ ) and pore spacing with the increasing of titania grafting cycles (b).

**Table 3.12** displays the unit cell sizes ( $a_0$ ) calculated for the different materials assuming a hexagonal array of pores with P6mm topology.

**Table 3.12** Pore spacing ( $a_0$ ) and pore wall thickness ( $t_{\text{wall}}$ ) calculated from XRD and  $\text{N}_2$  adsorption-desorption analyses.

Sample	$2\theta$	$d_{(10)}$ <sup>a</sup> / nm	$a_0$ <sup>b</sup> / nm	$d_{\text{pore}}$ <sup>c</sup> / nm	$t_{\text{wall}}$ <sup>d</sup> / nm
Parent SBA-15	0.89	9.9	11.4	6.8	4.6
Ti-SBA-15-1	0.89	9.9	11.5	6.6	4.9
Ti-SBA-15-2	0.88	10.0	11.5	6.2	5.3
Ti-SBA-15-3	0.89	9.9	11.5	5.6	5.9
Ti-SBA-15-4	0.89	9.9	11.4	4.1	7.3
Ti-SBA-15-5	0.89	9.9	11.4	3.8	7.6

<sup>a</sup>Interlayer spacing derived from Bragg's law, <sup>b</sup>pore spacing, <sup>c</sup>pore diameter from  $\text{N}_2$  desorption isotherm, <sup>d</sup>wall thickness =  $(2d_{10}/\sqrt{3})$ -pore diameter

**Figure 3.27** shows the wide angle XRD patterns over the range of  $20$  to  $80^\circ$  for bulk anatase, SBA-15 and Ti-SBA-15-n samples. The parent SBA-15 exhibits a broad diffraction at  $22.5^\circ$  corresponding to amorphous silica. No intense diffraction peaks corresponding to any  $\text{TiO}_2$  phase

were observed for the grafted samples up to the 3<sup>rd</sup> cycle of grafting. The absence of diffraction peaks on the XRD patterns of the Ti-SBA-15-n materials indicates that either TiO<sub>2</sub> is in the form of very small anatase particles or is amorphous. However, Ti-SBA-15-4 and Ti-SBA-15-5 exhibit diffractions attributable to anatase TiO<sub>2</sub>. Based on Scherrer equation (See **Chapter 2**), the crystallite size of anatase was calculated to be 8 and 9 nm, respectively.[46] As the pore size of the support is 7nm, the size of titania particles is too large to fit in the mesopores so the bigger nanoparticles are placed on the external surface.

Moreover the patterns of these two samples with the highest titania loading (35 and 43 wt.% of TiO<sub>2</sub>) clearly evidence that anatase is the only titania phase present in these systems, as indicated by the peaks at  $2\theta = 24.5^\circ, 38^\circ, 48^\circ, 54.5^\circ, 62.5^\circ, 70^\circ$  and  $75^\circ$ . For all Ti-SBA-15-n catalysts, no peak of (1 1 0) rutile reflection at  $27.4^\circ$  was detected.[47]

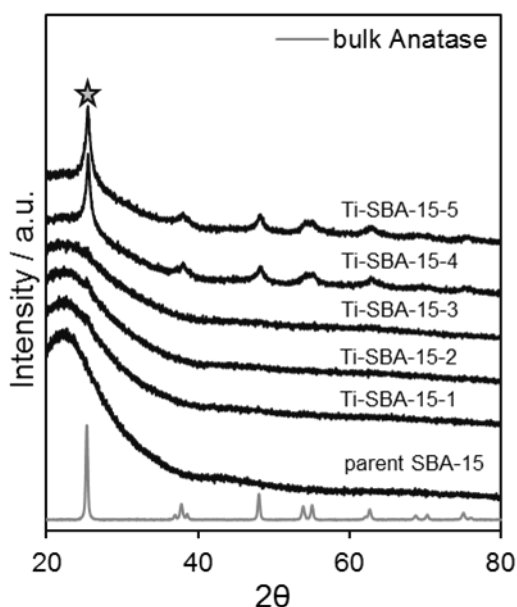


**Figure 3.27** Offset of wide angle XRD patterns of the composites materials and their support in comparison with the pattern of pure anatase (the gray star marks the (101) anatase reflection peaks).

### 3.2.2.2.5 Raman analysis

The crystal phase of the Ti-SBA-15-n photocatalysts for TiO<sub>2</sub> loading  $\leq 30$  wt. % was determined with Raman spectroscopy and the spectra are presented in **Figure 3.28**.

All the assignments were explained in detail in the previous section (See **Section 3.2.2.1.5**).

However the signal of SBA-15 is weak and only some of the typical silica vibrations could be identified (grey marked), on the other hand the four different bands at 145, 400, 520 and  $640\text{ cm}^{-1}$  are assigned to anatase crystallites (in red).

The characteristic peaks of anatase were already visible at low loading (below 10 wt. %). Up to the 3<sup>rd</sup> grafting cycle a weak and broad Raman band appears under ambient conditions at  $960\text{ cm}^{-1}$  which is characteristic of a surface titanium oxide over layer (blue marked).[33]

These anatase bands are more evident for the two final grafting cycles with the highest TiO<sub>2</sub> loading (~35-43wt. %). Ti-SBA-15-n samples with lower loading (~10-30%) show very low intensities indicating the presence of very small particles size ( $\leq 2$ nm).

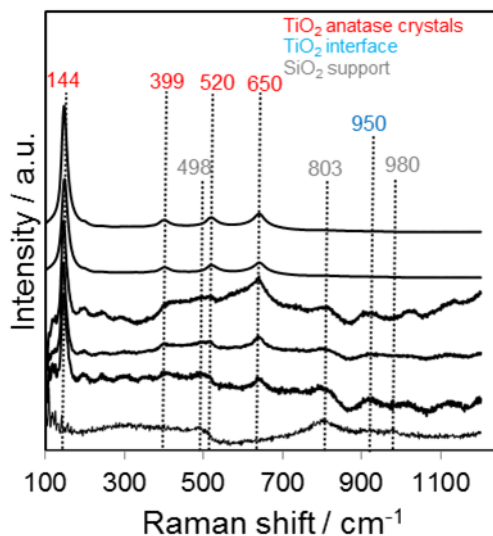


**Figure 3.28** Raman spectra of the parent SBA-15-7 and Ti-SBA-15-n (n=1-5).

### 3.2.2.2.6 ATR IR Spectroscopy

The ATR IR spectra of pure SBA-15 and Ti-SBA-15-n materials in the range of 1600-400 cm<sup>-1</sup> are shown in **Figure 3.29**. All the assignments were explained in detail in the previous section (See **Section 3.2.2.1.6**).

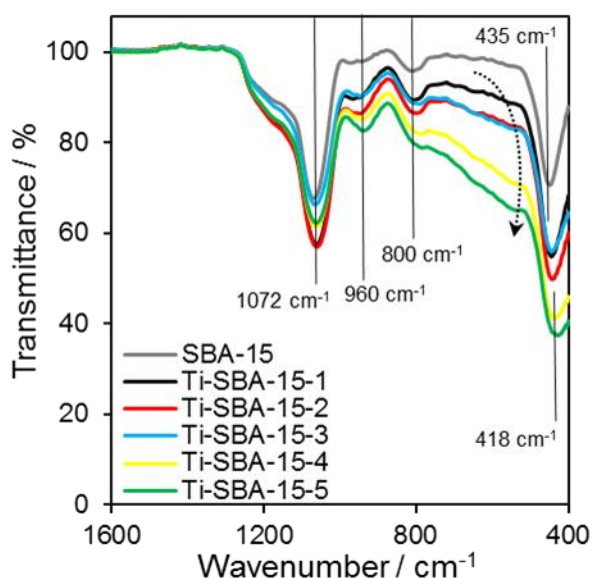


**Figure 3.29** ATR FT-IR spectra of Ti-SBA-15-n samples and the parent support.

The IR absorption peaks at 1072  $\text{cm}^{-1}$ , 800  $\text{cm}^{-1}$  and 435  $\text{cm}^{-1}$  are attributed to  $\nu_{\text{as}}(\text{Si-O-Si})$ ,  $\nu_{\text{s}}(\text{Si-O-Si})$  and  $\delta(\text{Si-O})$  vibrations of silica framework of SBA-15, respectively. [18, 35] These three peaks are well defined in the spectrum of the bare support (grey line).

The bands at c.a. 740  $\text{cm}^{-1}$  and 418  $\text{cm}^{-1}$  are commonly assigned to  $\nu(\text{Ti-O-Ti})$  and  $\nu(\text{Ti-O})$ , respectively. It can be observed that increasing the  $\text{TiO}_2$  loading a broad absorption band can be observed in the range 400–800  $\text{cm}^{-1}$  given by the contribution of the  $\nu(\text{Ti-O-Ti})$  stretching. In the meanwhile peak at 435  $\text{cm}^{-1}$  of  $\delta(\text{Si-O})$  is perturbed by the increasing of titania loading, with a shift to lower frequency up to the value of 418  $\text{cm}^{-1}$  characteristic of the stretching  $\nu(\text{Ti-O})$ . Also the band at 960  $\text{cm}^{-1}$  of  $\nu_{\text{as}}(\text{Si-O-Ti})$  grows with the titania loading. All these observations are evidences of the successful impregnation of  $\text{TiO}_2$  onto the silica support and the presence of  $\text{TiO}_2$  as a separate phase is more evident at higher  $\text{TiO}_2$  loading (wt. % > 30). The assigned vibrational mode are reported in **Table 3.13**.

**Table 3.13** Vibrational mode assignments of Ti-SBA-15-n catalysts.

Vibrational mode	Wavenumber
	/ $\text{cm}^{-1}$
$\nu_{\text{as}}(\text{Si-O-Si})$	1072
$\nu_{\text{sym}}(\text{Si-O-Si})$	800
$\delta(\text{Si-O})$	435
$\nu(\text{Ti-O-Ti})$	740
$\nu(\text{Ti-O})$	418
$\nu(\text{Si-O-Ti})$	960

### 3.2.2.2.7 Scanning transmission electron microscopy

Typical bright field TEM images of Ti-SBA-15-5 are shown in **Figure 3.30**.

These images are evidences that the pore walls of SBA-15 remain uniform upon five grafting cycles of  $\text{TiO}_2$ . Very small (ca. 2–3 nm) crystalline  $\text{TiO}_2$  particles can be detected, indicated with white arrows (**Figure 3.30a**) but they may not be representative of the whole sample. Indeed in spite of the high  $\text{TiO}_2$  loading of Ti-SBA-5, very few crystalline particles are observed.

**Figure 3.30b** shows deposited titania particles inside the SBA-15 channel (white square) with a measured particles size of ~6.4nm. The inset shows that at higher magnification was possible to measure the lattice parameter of anatase on the (101) plane, in agreement XRD wide angle and Raman analysis.

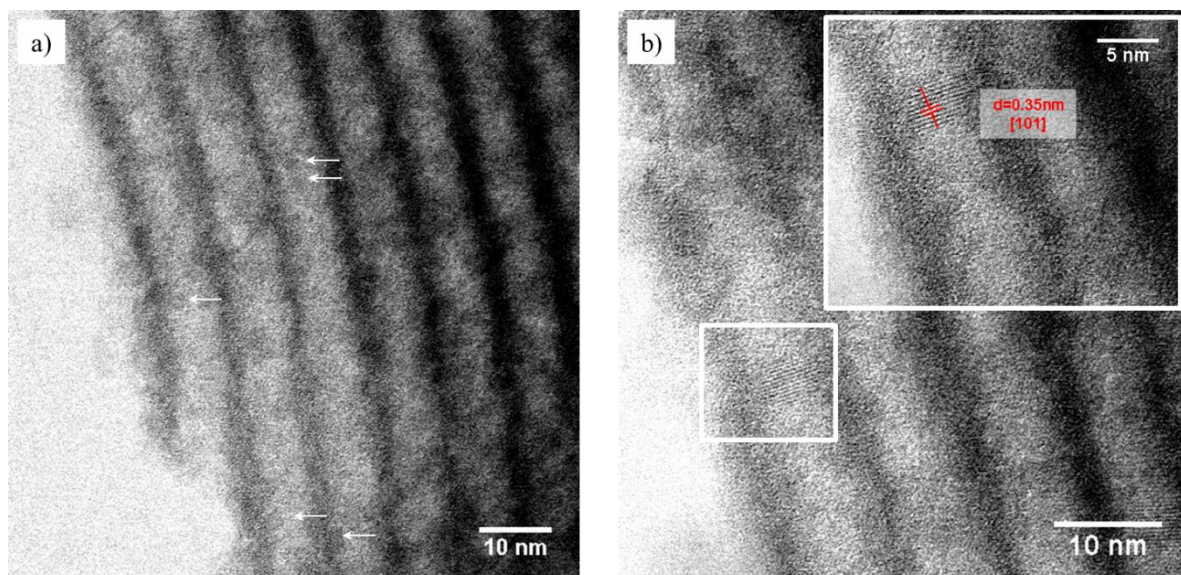


**Figure 3.30** Representative TEM images of Ti-SBA-15-5. Arrows show crystalline  $\text{TiO}_2$  nanoparticles (a); higher magnification and inset with detail of  $\text{TiO}_2$  nanoparticle observed inside the SBA-15 channel (b).

#### 3.2.2.2.8 UV-vis diffuse reflectance spectroscopy

**Figure 3.31a** shows the DRUV-Vis spectra of the  $\text{TiO}_2$  grafted SBA-15,  $\text{TiO}_2$  P-25, bulk anatase and the parent support SBA-15. Pure SBA-15 shows no pronounced absorption between 200 and 800 nm, only a weak absorption signal is seen at 210 nm. All the  $\text{TiO}_2$  and Ti-SBA-15-n spectra exhibit a characteristic adsorption band in region 350-400 nm, corresponding band transition. All the assignments were explained in details in **Section 3.2.2.1.8**. With increasing titanium content, the magnitude of blue shift of adsorption band is suppressed. The blue shift in the order of Ti-SBA-15  $1^{\text{st}} < 2^{\text{nd}} < 3^{\text{rd}} < 4^{\text{th}} \sim 5^{\text{th}} < \text{bulk TiO}_2$ , revealing growing coordination numbers of titanium with the  $\text{TiO}_2$  loading. (**Figure 3.31b**)



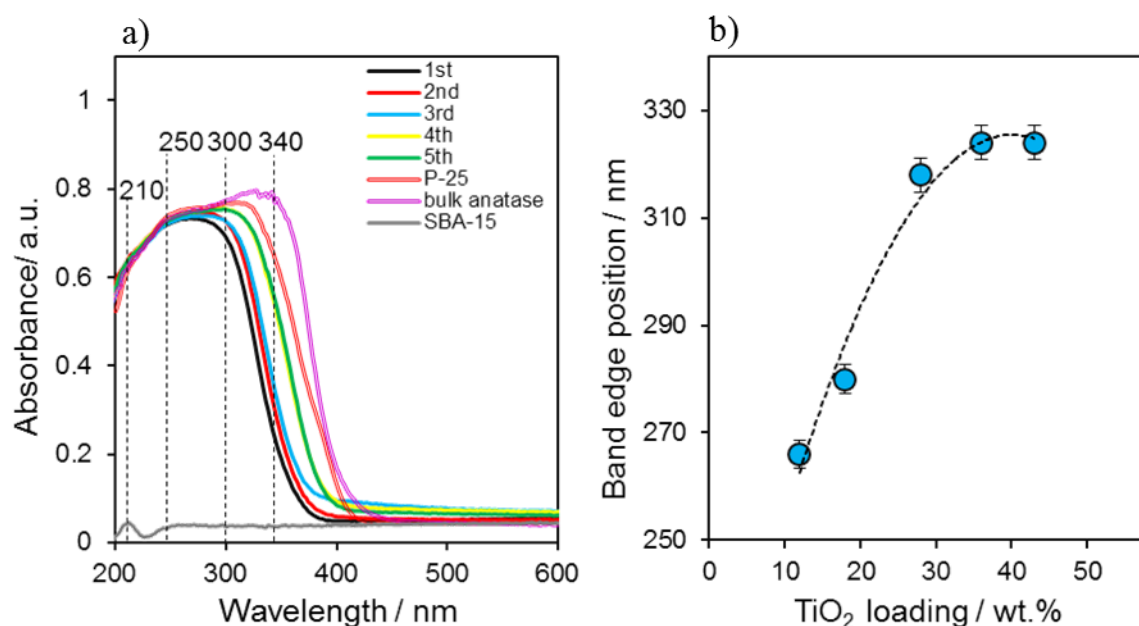


**Figure 3.31** UV-vis spectra of Ti-SBA-15-X-n samples, TiO<sub>2</sub> P-25, bulk anatase and parent SBA-15 (a) and evolution of UV absorption edge with the increasing of TiO<sub>2</sub> loading (b)

Using the Kubelka–Munk function  $F(R)$ , the band gap ( $E_g$ ) has been calculated from the plot of  $(\alpha h\nu)^{0.5}$  versus photon energy (eV). (Figure 3.32 a) The band gap energies estimated from the intercept of the tangents to the plots are in the range 3.5 -3.18 eV, with highest values for the TiO<sub>2</sub> nanoparticles to the smallest value found for the bulk anatase. Figure 3.32b shows that increasing of titania content, the band gaps are red shifted to longer wavelengths. With respect to the mixed oxide composites, this shift reflects to some extent an increase in the size of the TiO<sub>2</sub> domains.[48, 49]

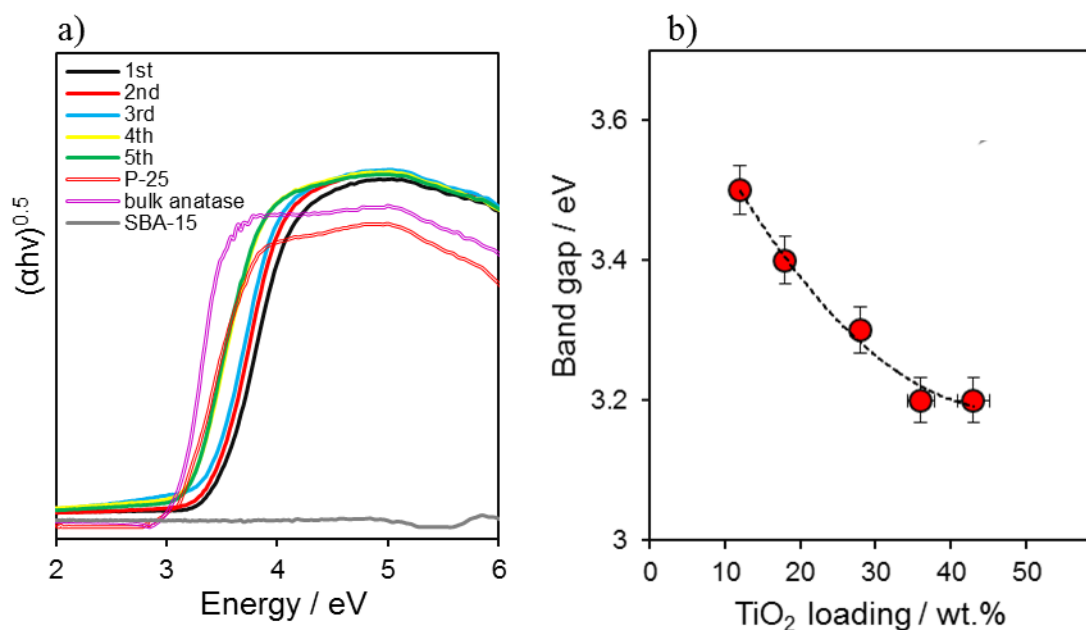


**Figure 3.32** Kubelka-Munk function for band gap evaluation of the TiO<sub>2</sub> based catalyst, the bare mesoporous support and two commercial references (a), trend of the band gap value with the increasing of titania loading (b).

The band edges and the corresponding band gap values are summarized in **Table 3.14**.

**Table 3.14** TiO<sub>2</sub> content, band gap ( $E_g$ ), corresponding wavelengths value ( $\lambda_{Eg}$ ) and the band edge for the parent support, Ti-SBA-15-X-n and the TiO<sub>2</sub> references.

Sample	$E_g$ / eV	$\lambda_{Eg}$ / nm	Band edge / nm
Parent SBA-15	5.5	225	-
Ti-SBA-15-1	3.5	354	266
Ti-SBA-15-2	3.4	365	276
Ti-SBA-15-3	3.3	376	318
Ti-SBA-15-4	3.2	388	324
Ti-SBA-15-5	3.2	388	324
TiO <sub>2</sub> P-25	3.2	390	332
Bulk anatase	3.2	390	340

### 3.2.3 Photocatalytic degradation of methyl orange

Photodegradation reactions of methyl orange (MO) were carried out under UV-vis irradiation in order to explore the impact of catalyst pore size and TiO<sub>2</sub> loading on the activities of the prepared photocatalysts. The operational set-up and reaction conditions can be found in **Chapter 2**.

#### 3.2.3.1 Effect of mesopore size

**Figure 3.33** shows the reaction profile for the loss of methyl orange, when using the synthesized catalysts as compared to the pure bulk anatase and commercial Degussa P-25. Blank experiments were carried out in the absence of catalyst (photolysis) and in the presence of bare SBA-15.

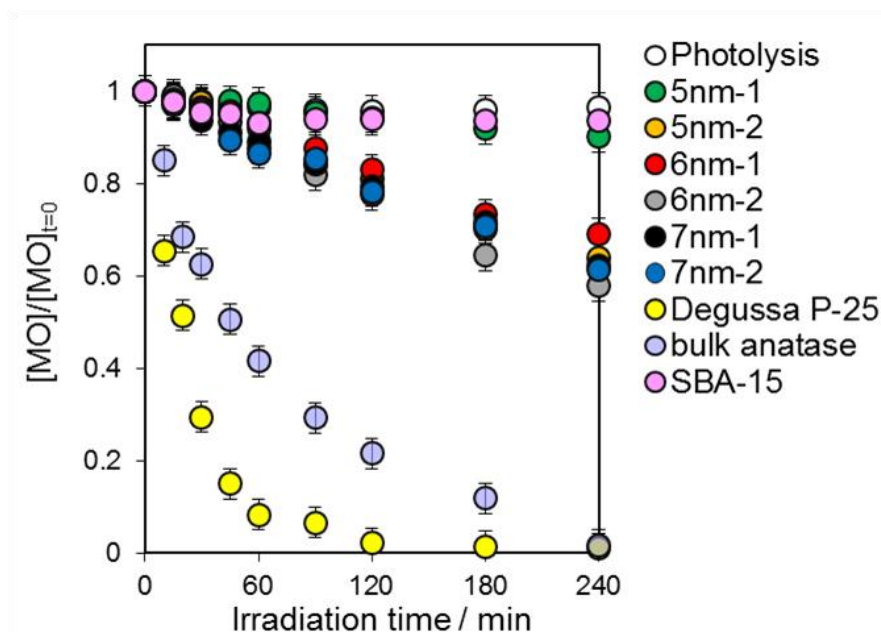


**Figure 3.33** Reduction of MO concentration with irradiation time over the three series of Ti-SBA-15-x-n, bulk anatase and Degussa P-25 and one of the parent support (SBA-15-7).

It must be noted that negligible conversion was observed for control experiments in the absence of titania. The final percentage of MO degradation for these two preliminary tests was 3.7% for the photolytic effect and 6.4% for the test performed with SBA-15 alone, confirming that the silica support exhibits a minor contribution to the degradation process.

As observed from the DR-UV/vis analysis (**Section 3.2.2.2.8**), the bare support shows a small absorption in the UV region and a very wide band gap of 5.5 eV. Because of its large band gap, SBA-15 provides a negligible contribution to photodegradation in the UV region which is most likely due to the high density of hydroxyl radical on the silica surface and/or the oxidation of water molecule, both sources of hydroxyl radicals (HO•) production.

**Figure 3.34** displays the values of the initial rate of MO degradation normalized for the mass of catalyst versus the pore size. It can be observed that increasing the pore size of the silica support

resulted in significant increase in the rate of the photocatalytic degradation of MO within the three series of catalysts (5 nm, 6 nm, 7 nm). This enhancement in degradation rate can be explain by the existence of mass-transport problems due to the accessibility of the dye molecule (molecular length ~1.2 nm) to the TiO<sub>2</sub> active sites located inside the small pores of the silica particles (<5 nm). The long diffusion path inside the channels of SBA-15 and small size of the pores could adversely affect the catalytic performance of the catalyst.[50] The linear correlation between the initial rate and the pore size shows that SBA-15-7 is the most suitable support for a composite catalyst as it benefits from minimised diffusion limitations and greater homogeneity in the TiO<sub>2</sub> dispersions compared with the other two host materials, as confirmed also from the XRD wide angle pattern. The linear correlation between the initial rate and the pore size shows that SBA-15-7 is the most suitable support for a composite catalyst as it benefits from minimised diffusion limitations and greater homogeneity in the TiO<sub>2</sub> dispersions compared with the other two host materials, as confirmed also from the XRD wide angle pattern.

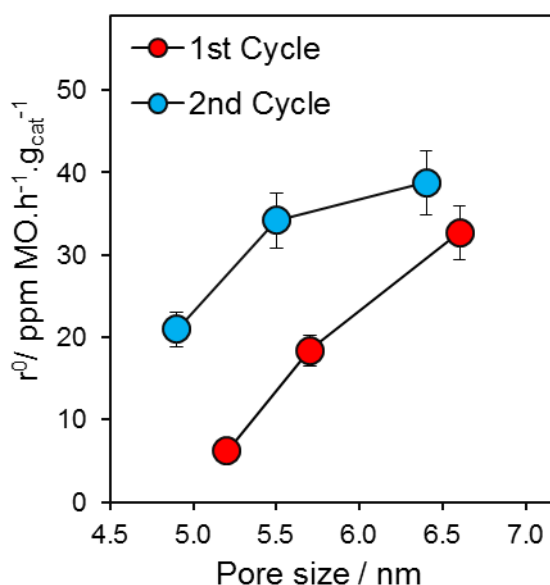


**Figure 3.34** Initial rate ( $r^0$ ) normalised for the mass of catalyst as function of the pore size.

**Figure 3.35** shows % of MO degradation during the irradiation time. In comparison with the control tests (photolysis and bare support) the addition of TiO<sub>2</sub> to SBA-15 substrate significantly improves the efficiency of MO photodegradation. However considering the experimental error, the final % of MO degradation reached is approximately the same for all the composites materials (~40%) independently from the titania loading.

Therefore it can be seen that 5nn-1 exhibits a significant deviation from this trend showing almost no activity, followed by 6nm-1. The latter is slightly more active but not completely in line with the trend of the other samples.

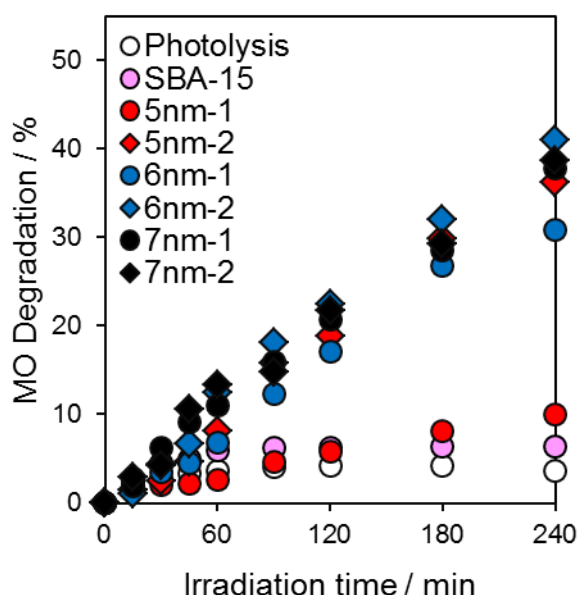


**Figure 3.35** Variation of the dye degradation rate with irradiation time of methyl orange solution.

These differences on catalytic behaviour found an explanation in the localization of titania nanoparticles during the grafting procedure, also in agreement with the characterization techniques previously shown. It was observed that there is no formation of separate  $\text{TiO}_2$  nanoparticles on the SBA-15 support up to a  $\text{TiO}_2$  loading of about 10 wt. % and the distribution of titania within the sample results homogeneous.

The three parent supports were prepared at different aging temperature and the removal of the surfactant by calcination leaves micropore areas inside the SBA-15 walls with high hydroxyl density. Porosimetry analysis confirm that the density of micropores varying with the aging temperature. (See **Section 3.2.2.1.3**) The support SBA-15-5 has the higher density of these micropores which is drastically reduced after the first grafting cycle. However the titania is present on the support (as confirmed by XRF, XPS, ICP analysis) but mainly located on the micropores, thus not available for the reaction.

Our reference experiments were performed with Degussa P-25 and the bulk anatase. Both samples reached more than 90% of total degradation of MO after 120 min of irradiation time, showing apparently higher activity than the supported titania.

However, normalizing the photodegradation rate by per gram of  $\text{TiO}_2$  contained in synthesized catalysts, the Ti-SBA-15-7 material show better photocatalytic activity than bulk anatase and comparable photoactive behaviour to the commercial P-25 Degussa. This exceptional activity is attributed to the high accessibility to the model compound to the active site. Results are shown in **Figure 3.36**.

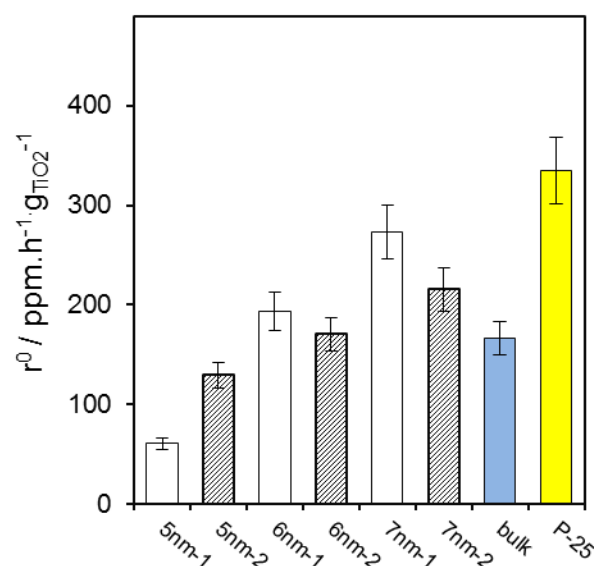


**Figure 3.36** Initial rate ( $r^0$ ) for the MO degradation normalised for the mass of  $\text{TiO}_2$ .

### 3.2.3.2 Effect of titania loading

The reduction of MO concentration vs. irradiation time over the series of composites under UV-vis irradiation is presented in **Figure 3.37**.

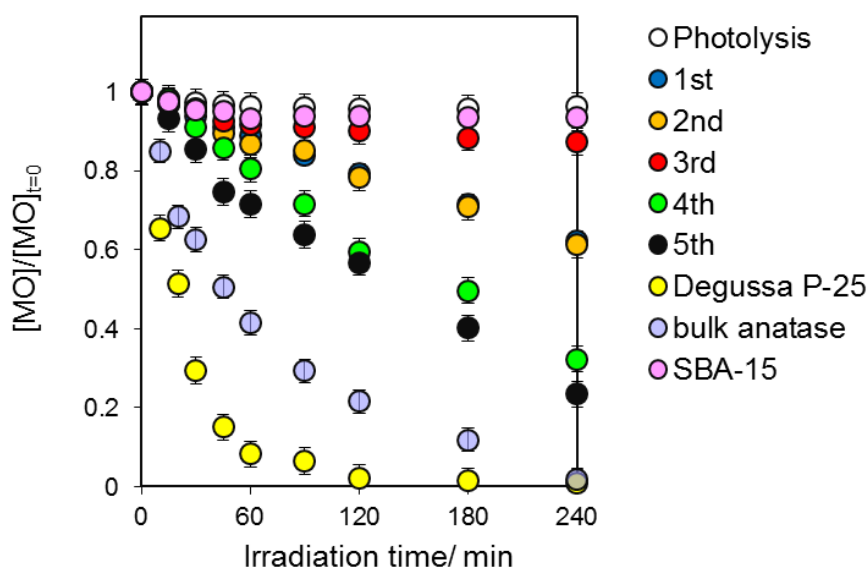


**Figure 3.37** Reduction in MO concentration with irradiation time by using different catalysts at different wt. % of  $\text{TiO}_2$  and two references (Degussa P-25 and bulk anatase).

From this figure it can be observed that the degree of degradation of MO using samples with low  $\text{TiO}_2$  content ( $\sim 10$  and  $30$  wt. %,  $1^{\text{st}}$ - $3^{\text{rd}}$  cycle of grating) is quite low and follows a slow rate compared with the samples at higher  $\text{TiO}_2$  loading ( $\sim 30$ - $40$  wt. %,  $4^{\text{th}}$  and  $5^{\text{th}}$ ).

The degradation efficiency is reported in **Figure 3.38**.

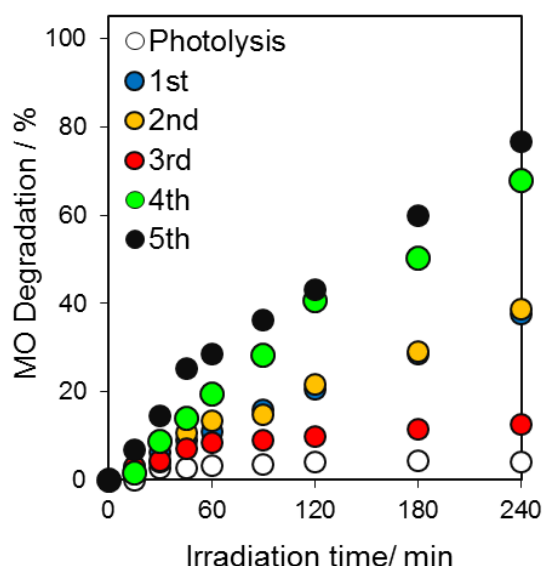


**Figure 3.38** Variation of the dye degradation rate with irradiation time of MO solution.

It is clear that the degradation of MO using samples with low  $\text{TiO}_2$  content (10 and 28 wt. %) is quite low and slow. After four hours of irradiation, the 1<sup>st</sup> and the 2<sup>nd</sup> grafting cycles reached only the 20 % of MO degradation, showing very similar photoactivity.

On the other hand the samples with the highest loading show about 80% of degradation of MO. However no relevant difference is observed between the samples with 35-43 wt. % of  $\text{TiO}_2$ . Interesting, the 3<sup>rd</sup> grafting cycle shows a very low activity with final degradation about 10 %.

It seems that the % of MO degradation first decreases and then increases by increasing the  $\text{TiO}_2$  content. This is due to the localization of  $\text{TiO}_2$  nanoparticles on the support and their accessibility to the target substrate. Up to the 3<sup>rd</sup> cycle of grafting,  $\text{TiO}_2$  nanoparticles are homogeneously dispersed on the internal and external surface of the support with very small anatase particles, consistent with the absence of any or very little diffraction anatase peak observed from the wide angle XRD pattern. While at high  $\text{TiO}_2$  loading it starts the formation of separate  $\text{TiO}_2$  nanoparticles located on the external surface and so more accessible to the target substrate. Therefore it can be postulated that the degradation rate is mainly dependent on the accessibility of the compound to the catalytic active sites.

However there are several factors, such as crystal phase, available surface area, crystalline size and band gap, which play an important role in influencing photoactivity. All these parameter are depending on the amount  $\text{TiO}_2$  loaded on the support. **Figure 3.39** shows the initial rate ( $r^0$ ) as function of the  $\text{TiO}_2$  loading.

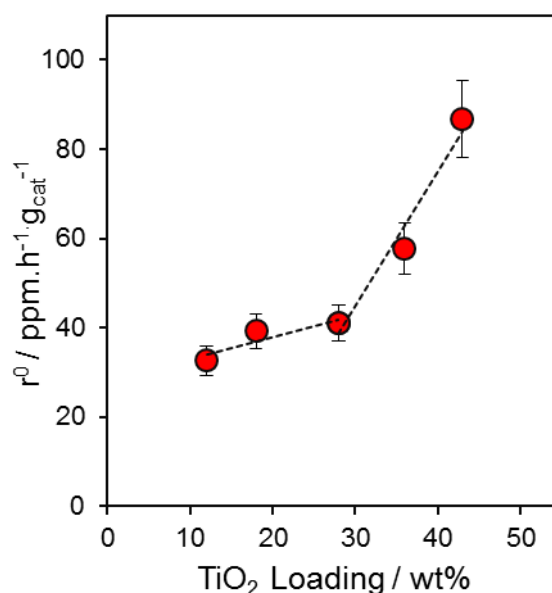


**Figure 3.39** Initial rate ( $r^0$ ) for the MO degradation normalised for the mass of catalyst as function of the TiO<sub>2</sub> loading.

First, it seems that the titania loading on the material produces only a slight increase in the rate of MO degradation, then a clear increase in the initial rate was found for TiO<sub>2</sub> loadings above 30 wt. %. An increasing of TiO<sub>2</sub> content led to an increase of crystallized anatase together with lower band gap energy values. Moreover at high loading, anatase particles (bigger than 6 nm) are located on the external surface area of the support providing a good accessibility of MO molecule to the TiO<sub>2</sub> active sites. Thus when MO molecules start to degrade, the diffusion of small subproducts within the TiO<sub>2</sub>-coated mesoporous network of SBA-15 may be facilitated.

From the analysis of the raw reaction profile the two bulk references (100% TiO<sub>2</sub>) show highest photoactivity compared to the composite materials (**Figure 3.37**). It should be also noticed that the two bulk references are characterized by different structural and electronic properties compared with the composites samples. This makes it complex to find the exact criteria with which to compare the activity of the bulk and the supported samples. Thus in order to compare the performance of the different catalysts with the same titania weight, the normalized initial rates for the actual TiO<sub>2</sub> mass are reported in **Figure 3.40**.



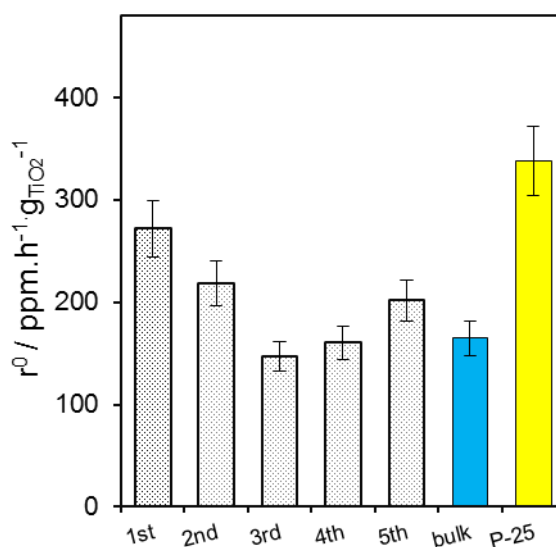


**Figure 3.40** Initial rate ( $r^0$ ) for the MO degradation normalised for the mass of TiO<sub>2</sub>.

Normalizing the obtained values for the actual mass of TiO<sub>2</sub> present in the system, it can be seen the anatase nanocrystal appear to be a more efficient photocatalyst when it is dispersed on the SBA-15 support with a high surface area. However the commercial reference, Degussa P-25 appears to be the best catalyst for MO degradation under the chosen experimental conditions. The high photocatalytic activity of TiO<sub>2</sub> P-25 is attributed to the complex structure of this material since it is a mixture of anatase and rutile phases.

### 3.3 Conclusions

Two different series of TiO<sub>2</sub>-coated SBA-15 composites were synthesized by grafting procedure. For the first series, three supports with three pore sizes were prepared at different aging temperatures (80, 100 and 120 °C). Further TiO<sub>2</sub> nanoparticles were grafted on each support with a target of TiO<sub>2</sub> loading in the range of 8-18 wt. % (Ti-SBA-15-X-n, X= aging temperature and n= number of grafting).

The aim was to investigate the influence of the pore size of the host support on the TiO<sub>2</sub> dispersion and on the photodegradation of MO. It was found that for the SBA-15 with the smaller mesopore size (5 nm) the deposition of TiO<sub>2</sub> meanly occurs inside the micropores, leading to a very low activity due to the fact that the active phase is less available for the target molecule. Moreover, considering the molecular length of MO (~1.2 nm), small pore size causes also mass-transport problems due to the accessibility of the dye molecule to the internal surface area of the host support. Therefore SBA-15 with the biggest pore size (7 nm) was the best candidate to study the influence of the TiO<sub>2</sub> loading effect. Hence, the same grafting method was applied for the second series of catalysts on the SBA-15-7 support and the TiO<sub>2</sub> loading was varied from 12-43 wt. % by five following grafting procedures (Ti-SBA-15-n, n=1-5). At loading below 30 wt. %, the titania

coating homogeneously occurs inside the mesopores and no crystalline anatase was observed by XRD and Raman. At higher loading, TiO<sub>2</sub> was found crystallized in anatase nanoparticles also outside the porosity (particle size ~8-10nm). The increasing of particle size brings to a more active phase available on the external surface and mainly to a sensible variation of the band gap energy. The results show that E<sub>g</sub> decreases with the increase of titania content, which affects the photoactivity of the samples. It clearly appeared that the Ti-SBA-17-5 composite with 43 wt. % of TiO<sub>2</sub> exhibits the highest MO degradation rate of both series. From these studies, it was determined that the mesoporous SBA-15 with a surface grafted layer of titania, exhibited a remarkable efficiency for dye degradation providing high surface area and good dispersion of the active phase.

### 3.4 References

- [1] X. Chen and S. S. Mao, "Titanium dioxide nanomaterials: Synthesis, properties, modifications, and applications," *Chemical Reviews*, vol. 107, pp. 2891-2959, Jul 2007.
- [2] M. R. Hoffmann, S. T. Martin, W. Y. Choi, and D. W. Bahnemann, "Environmental Applications of Semiconductor Photocatalysis," *Chemical Reviews*, vol. 95, pp. 69-96, Jan-Feb 1995.
- [3] G. Palmisano, E. Garcia-Lopez, G. Marci, V. Loddo, S. Yurdakal, V. Augugliaro, *et al.*, "Advances in selective conversions by heterogeneous photocatalysis," *Chemical Communications*, vol. 46, pp. 7074-7089, 2010.
- [4] A. Fujishima, T. N. Rao, and D. A. Tryk, "TiO<sub>2</sub>(2) photocatalysts and diamond electrodes," *Electrochimica Acta*, vol. 45, pp. 4683-4690, 2000.
- [5] Z. J. Li, B. Hou, Y. Xu, D. Wu, and Y. H. Sun, "Hydrothermal synthesis, characterization, and photocatalytic performance of silica-modified titanium dioxide nanoparticles," *Journal of Colloid and Interface Science*, vol. 288, pp. 149-154, Aug 1 2005.
- [6] D. S. Kim, S. J. Han, and S. Y. Kwak, "Synthesis and photocatalytic activity of mesoporous TiO<sub>2</sub> with the surface area, crystallite size, and pore size," *Journal of Colloid and Interface Science*, vol. 316, pp. 85-91, Dec 1 2007.
- [7] J. A. Shusterman, H. E. Mason, J. Bowers, A. Bruchet, E. C. Uribe, A. B. Kersting, *et al.*, "Development and Testing of Diglycolamide Functionalized Mesoporous Silica for Sorption of Trivalent Actinides and Lanthanides," *Acs Applied Materials & Interfaces*, vol. 7, pp. 20591-20599, Sep 23 2015.
- [8] J. J. Zhu, K. Kailasam, X. A. Xie, R. Schomaecker, and A. Thomas, "High-Surface-Area SBA-15 with Enhanced Mesopore Connectivity by the Addition of Poly(vinyl alcohol)," *Chemistry of Materials*, vol. 23, pp. 2062-2067, Apr 26 2011.
- [9] C. Galacho, M. M. L. R. Carrott, and P. J. M. Carrott, "Structural and catalytic properties of Ti-MCM-41 synthesised at room temperature up to high Ti content," *Microporous and Mesoporous Materials*, vol. 100, pp. 312-321, Mar 23 2007.

- [10] J. A. Melero, J. M. Arsuaga, P. G. de Frutos, J. Iglesias, J. Sainz, and S. Blazquez, "Direct synthesis of titanium-substituted mesostructured materials using non-ionic surfactants and titanocene dichloride," *Microporous and Mesoporous Materials*, vol. 86, pp. 364-373, Nov 28 2005.
- [11] G. Li and X. S. Zhao, "Characterization and photocatalytic properties of titanium-containing mesoporous SBA-15," *Industrial & Engineering Chemistry Research*, vol. 45, pp. 3569-3573, May 10 2006.
- [12] F. Berube, B. Nohair, F. Kleitz, and S. Kaliaguine, "Controlled Postgrafting of Titanium Chelates for Improved Synthesis of Ti-SBA-15 Epoxidation Catalysts," *Chemistry of Materials*, vol. 22, pp. 1988-2000, Mar 23 2010.
- [13] N. B. Lihitkar, M. K. Abyaneh, V. Samuel, R. Pasricha, S. W. Gosavi, and S. K. Kulkarni, "Titania nanoparticles synthesis in mesoporous molecular sieve MCM-41," *Journal of Colloid and Interface Science*, vol. 314, pp. 310-316, Oct 1 2007.
- [14] S. G. Zhang, Y. Fujii, K. Yamashita, K. Koyano, T. Tatsumi, and M. Anpo, "Photocatalytic reduction of CO<sub>2</sub> with H<sub>2</sub>O on Ti-MCM-41 and Ti-MCM-48 mesoporous zeolites at 328 K," *Chemistry Letters*, pp. 659-660, 1997.
- [15] A. M. Busuioc, V. Meynen, E. Beyers, P. Cool, N. Bilba, and E. F. Vansant, "Growth of anatase nanoparticles inside the mesopores of SBA-15 for photocatalytic applications," *Catalysis Communications*, vol. 8, pp. 527-530, Mar 2007.
- [16] W. Y. Dong, Y. J. Sun, Q. W. Ma, L. Zhu, W. M. Hua, X. C. Lu, *et al.*, "Excellent photocatalytic degradation activities of ordered mesoporous anatase TiO<sub>2</sub>-SiO<sub>2</sub> nanocomposites to various organic contaminants," *Journal of Hazardous Materials*, vol. 229, pp. 307-320, Aug 30 2012.
- [17] M. Besancon, L. Michelin, L. Josien, L. Vidal, K. Assaker, M. Bonne, *et al.*, "Influence of the porous texture of SBA-15 mesoporous silica on the anatase formation in TiO<sub>2</sub>-SiO<sub>2</sub> nanocomposites," *New Journal of Chemistry*, vol. 40, pp. 4386-4397, 2016.
- [18] F. X. Zhang, X. Carrier, J. M. Krafft, Y. Yoshimura, and J. Blanchard, "Insight into the structure and localization of the titania overlayer in TiO<sub>2</sub>-coated SBA-15 materials," *New Journal of Chemistry*, vol. 34, pp. 508-516, 2010.
- [19] V. Schwartz, D. R. Mullins, W. F. Yan, H. G. Zhu, S. Dai, and S. H. Overbury, "Structural investigation of au catalysts on TiO<sub>2</sub>-SiO<sub>2</sub> supports: Nature of the local structure of ti and au atoms by EXAFS and XANES," *Journal of Physical Chemistry C*, vol. 111, pp. 17322-17332, Nov 22 2007.
- [20] E. Santacesaria, M. Cozzolino, M. Di Serio, A. M. Venezia, and R. Tesser, "Vanadium based catalysts prepared by grafting: preparation, properties and performances in the ODH of butane," *Applied Catalysis a-General*, vol. 270, pp. 177-192, Aug 30 2004.

- [21] D. Zhao, J. Feng, Q. Huo, N. Melosh, G. H. Fredrickson, B. F. Chmelka, *et al.*, "Triblock Copolymer Syntheses of Mesoporous Silica with Periodic 50 to 300 Angstrom Pores," *Science*, vol. 279, pp. 548-552, 1998.
- [22] A. Galarneau, H. Cambon, F. Di Renzo, and F. Fajula, "True Microporosity and Surface Area of Mesoporous SBA-15 Silicas as a Function of Synthesis Temperature," *Langmuir*, vol. 17, pp. 8328-8335, 2001/12/01 2001.
- [23] A. Galarneau, N. Cambon, F. Di Renzo, R. Ryoo, M. Choi, and F. Fajula, "Microporosity and connections between pores in SBA-15 mesostructured silicas as a function of the temperature of synthesis," *New Journal of Chemistry*, vol. 27, pp. 73-79, 2003.
- [24] S. Ruthstein, V. Frydman, S. Kababya, M. Landau, and D. Goldfarb, "Study of the Formation of the Mesoporous Material SBA-15 by EPR Spectroscopy," *The Journal of Physical Chemistry B*, vol. 107, pp. 1739-1748, 2003/02/01 2003.
- [25] M. Imp  rator-Clerc, P. Davidson, and A. Davidson, "Existence of a Microporous Corona around the Mesopores of Silica-Based SBA-15 Materials Templated by Triblock Copolymers," *Journal of the American Chemical Society*, vol. 122, pp. 11925-11933, 2000/12/01 2000.
- [26] K. S. W. Sing, D. H. Everett, R. A. W. Haul, L. Moscou, R. A. Pierotti, J. Rouquerol, *et al.*, "Reporting Physisorption Data for Gas Solid Systems with Special Reference to the Determination of Surface-Area and Porosity (Recommendations 1984)," *Pure and Applied Chemistry*, vol. 57, pp. 603-619, 1985.
- [27] I. Georgiadou, N. Spanos, C. Papadopoulou, H. Matralis, C. Kordulis, and A. Lycourghiotis, "Preparation and Characterization of Various Titanias (Anatase) Used as Supports for Vanadia-Supported Catalysts," *Colloids and Surfaces a-Physicochemical and Engineering Aspects*, vol. 98, pp. 155-165, May 12 1995.
- [28] G. Lassaletta, A. Fernandez, J. P. Espinos, and A. R. Gonzalez-Elip  , "Spectroscopic Characterization of Quantum-Sized TiO<sub>2</sub> Supported on Silica - Influence of Size and TiO<sub>2</sub>-SiO<sub>2</sub> Interface Composition," *Journal of Physical Chemistry*, vol. 99, pp. 1484-1490, Feb 2 1995.
- [29] P. Van Der Voort, P. I. Ravikovitch, K. P. De Jong, M. Benjelloun, E. Van Bavel, A. H. Janssen, *et al.*, "A new templated ordered structure with combined micro- and mesopores and internal silica nanocapsules," *Journal of Physical Chemistry B*, vol. 106, pp. 5873-5877, Jun 13 2002.
- [30] J. Feng, G. M. An, B. H. Chen, Y. X. Li, K. L. Ding, Y. Xie, *et al.*, "Post-Synthesis of Ti-SBA-15 in Supercritical CO<sub>2</sub>-Ethanol Solution," *Clean-Soil Air Water*, vol. 37, pp. 527-533, Jul 2009.
- [31] V. Meynen, P. Cool, and E. F. Vansant, "Verified syntheses of mesoporous materials," *Microporous and Mesoporous Materials*, vol. 125, pp. 170-223, Oct 15 2009.

- [32] C. M. A. Parlett, L. J. Durndell, A. Machado, G. Cibin, D. W. Bruce, N. S. Hondow, *et al.*, "Alumina-grafted SBA-15 as a high performance support for Pd-catalysed cinnamyl alcohol selective oxidation," *Catalysis Today*, vol. 229, pp. 46-55, Jun 15 2014.
- [33] S. Srinivasan, A. K. Datye, M. Hampdensmith, I. E. Wachs, G. Deo, J. M. Jehng, *et al.*, "The Formation of Titanium-Oxide Monolayer Coatings on Silica Surfaces," *Journal of Catalysis*, vol. 131, pp. 260-275, Sep 1991.
- [34] R. L. Orefice and W. L. Vasconcelos, "Sol-gel transition and structural evolution on multicomponent gels derived from the alumina-silica system," *Journal of Sol-Gel Science and Technology*, vol. 9, pp. 239-249, 1997.
- [35] Y. J. Acosta-Silva, R. Nava, V. Hernandez-Morales, S. A. Macias-Sanchez, M. L. Gomez-Herrera, and B. Pawelec, "Methylene blue photodegradation over titania-decorated SBA-15," *Applied Catalysis B-Environmental*, vol. 110, pp. 108-117, Nov 2 2011.
- [36] X. C. Zheng, W. H. Ye, Z. Lin, B. J. Liu, X. J. Shi, and X. Y. Wang, "Synthesis, Characterization and Catalytic Efficiency of Ti-SBA-15 Mesoporous Materials," *Fundamental of Chemical Engineering, Pts 1-3*, vol. 233-235, pp. 2011-2014, 2011.
- [37] D. R. Sahu, L. Y. Hong, S. C. Wang, and J. L. Huang, "Synthesis, analysis and characterization of ordered mesoporous TiO<sub>2</sub>/SBA-15 matrix: Effect of calcination temperature," *Microporous and Mesoporous Materials*, vol. 117, pp. 640-649, Jan 15 2009.
- [38] V. A. de la Peña O'Shea, M. Capel-Sanchez, G. Blanco-Brieva, J. M. Campos-Martin, and J. L. G. Fierro, "The Usefulness of Time-Dependent Density Functional Theory to Describe the Electronic Spectra of Ti-Containing Catalysts," *Angewandte Chemie International Edition*, vol. 42, pp. 5851-5854, 2003.
- [39] X. T. Gao and I. E. Wachs, "Titania-silica as catalysts: molecular structural characteristics and physico-chemical properties," *Catalysis Today*, vol. 51, pp. 233-254, Jun 30 1999.
- [40] M. L. Pena, V. Dellarocca, F. Rey, A. Corma, S. Coluccia, and L. Marchese, "Elucidating the local environment of Ti(IV) active sites in Ti-MCM-48: a comparison between silylated and calcined catalysts," *Microporous and Mesoporous Materials*, vol. 44, pp. 345-356, Jun 2001.
- [41] S. Biswas, M. F. Hossain, T. Takahashi, Y. Kubota, and A. Fujishima, "Study of photocatalytic activity in sputter-deposited Cr-TiO<sub>2</sub> thin film," *Physica Status Solidi a-Applications and Materials Science*, vol. 205, pp. 2023-2027, Aug 2008.
- [42] M. Landau, E. Dafa, M. Kaliya, T. Sen, and M. Herskowitz, "Mesoporous alumina catalytic material prepared by grafting wide-pore MCM-41 with an alumina multilayer," *Microporous and mesoporous materials*, vol. 49, pp. 65-81, 2001.
- [43] C. L. Peza-Ledesma, L. Escamilla-Perea, R. Nava, B. Pawelec, and J. L. G. Fierro, "Supported gold catalysts in SBA-15 modified with TiO<sub>2</sub> for oxidation of carbon monoxide," *Applied Catalysis a-General*, vol. 375, pp. 37-48, Feb 26 2010.

- [44] R. Castillo, B. Koch, P. Ruiz, and B. Delmon, "Influence of Preparation Methods on the Texture and Structure of Titania-Supported on Silica," *Journal of Materials Chemistry*, vol. 4, pp. 903-906, Jun 1994.
- [45] J. C. Groen, L. A. A. Peffer, and J. Perez-Ramirez, "Pore size determination in modified micro- and mesoporous materials. Pitfalls and limitations in gas adsorption data analysis," *Microporous and Mesoporous Materials*, vol. 60, pp. 1-17, Jun 19 2003.
- [46] G. N. P. Scherrer, 1918, 2, 98, 1918.
- [47] K. Thamaphat, P. Limsuwan, and B. Ngotawornchai, "Phase characterization of TiO<sub>2</sub> powder by XRD and TEM."
- [48] H. Lin, C. P. Huang, W. Li, C. Ni, S. I. Shah, and Y. H. Tseng, "Size dependency of nanocrystalline TiO<sub>2</sub> on its optical property and photocatalytic reactivity exemplified by 2-chlorophenol," *Applied Catalysis B-Environmental*, vol. 68, pp. 1-11, Oct 26 2006.
- [49] C. d. M. Donega, "Synthesis and properties of colloidal heteronanocrystals," *Chemical Society Reviews*, vol. 40, pp. 1512-1546, 2011.
- [50] T. Kamegawa, Y. Ishiguro, H. Seto, and H. Yamashita, "Enhanced photocatalytic properties of TiO<sub>2</sub>-loaded porous silica with hierarchical macroporous and mesoporous architectures in water purification," *Journal of Materials Chemistry A*, vol. 3, pp. 2323-2330, 2015.

## *Chapter 4*

### *Titania grafted on hierarchical silica support*

## 4 Titania grafted on macro-mesoporous silica support

### 4.1 Introduction

**Chapter 3** evidences the crucial role of support structure on the synthesis of  $\text{TiO}_2$  based photocatalysts. Mesoporous silicas are a well understood and versatile material, for which advances in control over their pore structure and surface properties [1] have made them an ideal choice as supports for  $\text{TiO}_2$  nanoparticles for photocatalytic processes. [2-4]

A further challenge is to design hierarchical structures which can not only improve the molecular diffusion/ transport kinetics but also enhance light harvesting. Primarily the generation of ordered macropores within the SBA-15 architecture is predicted to benefit internal mass diffusion kinetics through a more open support structure and shorter length mesopore domains.[5] Additionally, ordered macroporous materials are of significant interest because of their optical properties as three dimensional photonic crystals (PC),[6-8] but their effect have not been fully investigated yet.

The photonic crystals are periodic dielectric structures, which can prohibit the propagation of a certain frequency range of light, called photonic band gap (PBG). At the frequency edges of the stop-band, photons propagate with strongly reduced speed and this phenomena reinforces the light-matter interaction, thus the consequent probability of light absorption is increased.[9] So far several research groups focused their attention on the design and synthesis of hierarchical materials for photocatalytic application. However, it is very difficult to obtain high control of the hierarchical morphology. Porous materials with three-dimensionally ordered macroporous are mainly synthesized using spherical polymers as a hard template. [2, 10, 11] These particles are easily removed from the target material by thermal treatment or solvent extraction.[12]

Chen et al.[13-15] demonstrate the importance of the highly ordered structure for a macroporous anatase, establishing the unique property of the photonic crystal to improve the light harvesting. Oxidative decomposition of methyl blue was performed under monochromatic UV light. A study on the slow photon effect were also performed by Liu et al. and Chen et al. in the application of  $\text{TiO}_2$  PC to the photocatalytic degradation of Rhodamine B and phenol, respectively.[9, 16]

Lu et al.[17] obtained a highly ordered  $\text{TiO}_2$  PC using two sizes of polystyrene beads (193 and 240 nm) as hard templates, removed by a calcination step at  $550^\circ\text{C}$ . The augmented photocatalytic performance of the  $\text{TiO}_2$  PC was demonstrated by comparison with the same  $\text{TiO}_2$  synthesised without the template, and applied as the control experiments in the photodegradation of 2,4-dichlorophenol (2,4-DCP).

Wen et al.[18] optimized the position of the photonic stop band of macroporous ZnO catalysts by tuning the diameter of the hard template.



Yamashita et al.[2, 12] explored different kind of siliceous material as a support for a  $\text{TiO}_2$  photocatalyst, investigating the effect of hierarchical structure for different loadings of titania obtained by conventional impregnation method. The utilization of a hierarchically porous architecture exhibited superior photocatalytic performances for the degradation of relatively large organic compounds compare to the mesoporous supported material. However, beside the unique structural properties of the hierarchical structure, such as well-ordered architecture, high surface area and the large pore volume together with the evidence of reduced diffusion limitation, the role of macropores was not fully investigated for their optical properties.

In contrast, Mitchell et al.[19] performed a detailed study on the optical properties of coated photonic macroporous supports using different kind of nanoparticles ( $\text{TiO}_2$ ,  $\text{Fr}_3\text{O}_4$  or  $\text{CdS}$ ) onto macroporous  $\text{SiO}_2$  and  $\text{ZrO}_2$  deposited by the wet impregnation method. It was found that the PBG position strongly depended on the loading and the distribution of the active phase on the photonic support. Thus the results showed that by tuning the position of the stop band of the host support with the absorption edge of the photoactive phase it was possible to obtain an enhancement in light absorption and consequentially in the photocatalytic efficiency of the material. Moreover it was found the importance of control over the nanoparticle dispersion in order to retain the photonic properties also after the coating with the active phase.

The following chapter builds upon these investigations by introducing  $\text{TiO}_2$  on hierarchical SBA-15 by a grafting procedure in order to have a strong stability of the active phase on the host support and much control on the nanoparticles dispersion. An innovative synthetic route utilising the true liquid crystal templating (TLCT) has been investigated to observe the effect of incorporating macropores, to form an ordered macroporous-mesoporous support.[20] The aim of the study was to investigate the effect of structural and optical properties of this particular structure on the photooxidation rate of organic pollutants in water.

In this chapter three ordered hierarchical materials were prepared using different polystyrene beads size (200, 400 and 600nm). On this series of supports only one grafting procedure was performed in order to study the effect of the macropore size on the grafting procedure and on the activity of the composite materials. Subsequently the effect of  $\text{TiO}_2$  loading was explored on the support synthesized with 400 nm PS beads size. The catalytic activity of the composites was evaluated by studying the photodegradation of methyl orange (MO) in water under UV-vis irradiation and compared with the photocatalytic performance of the Ti-SBA-15 samples.

## 4.2 Results and discussion

### 4.2.1 Characterisation of polystyrene beads

The emulsion polymerisation protocol devised by Vaudreuil et al[21] was used to produce mono-disperse polystyrene spheres, for use as a hard template for macropore incorporation into SBA-15. Three different PS beads sizes were obtained: 200 nm, 400 nm and 600 nm, with STEM used to establish the successful synthesis of monodispersed polystyrene spheres. **Figure 4.1**, **Figure 4.2** and **Figure 4.3** confirm a successful synthesis, with spherical morphologies exclusively synthesised and good mono-dispersity. All values are in excellent agreement with reported literature values under similar synthesis conditions.[5]

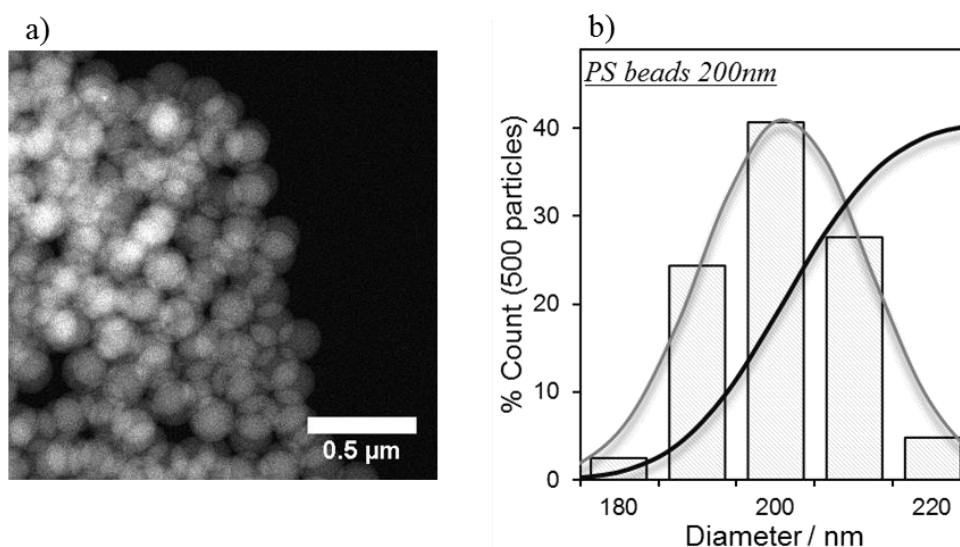


**Figure 4.1** Representative STEM images of polystyrene beads of 200nm size (before the centrifuge step) (a) and the relative particle size distributions for 500 particles (b).

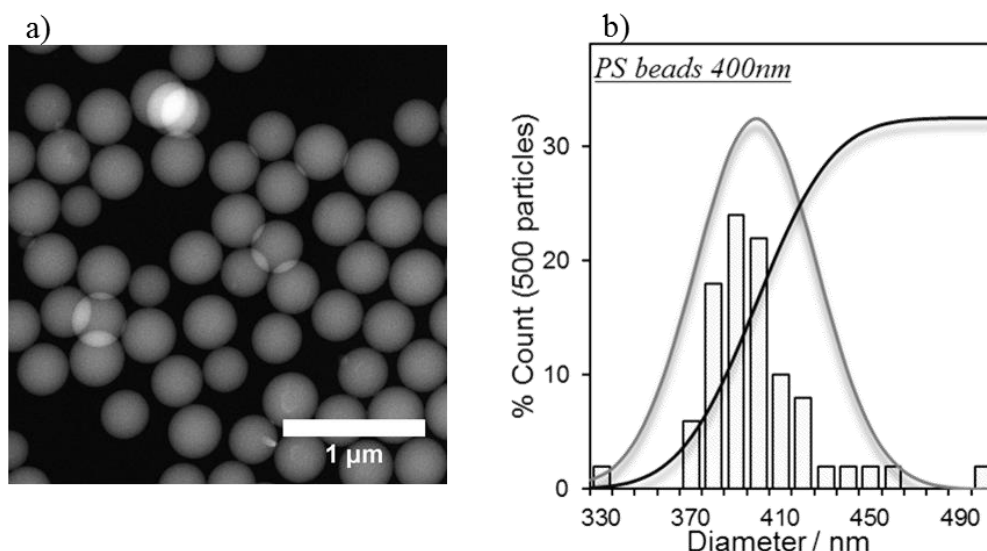


**Figure 4.2** Representative STEM images of polystyrene beads of 400nm size (before the centrifuge step) (a) and the relative particle size distributions for 500 particles (b).

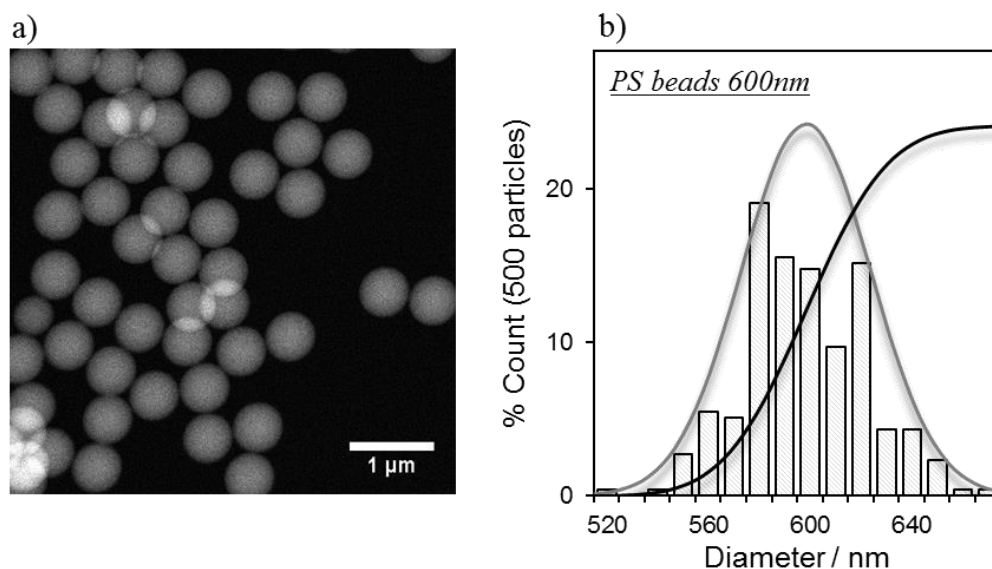


**Figure 4.3** Representative STEM images of polystyrene beads of 600nm size (before the centrifuge step) (a) and the relative particle size distributions for 500 particles (b).

#### 4.2.2 Characterisation of the TLCT-MM-SBA-15 supports

TLCT-MM-SBA-15 with three macropore sizes were synthesised using methodologies developed by Parlett et al.[22] Successful synthesis was verified using a variety of characterisation techniques. Textural properties were explored by N<sub>2</sub> porosimetry, resulting isotherms shown in **Figure 4.4a**. As previously established for SBA-15, TLCT-MM-SBA-15 exhibits a type IV, isotherm and H1 hysteresis, inherent to the preservation of SBA-15 mesostructure and pore uniformity.[23] A second hysteresis is shown for this material at higher pressures due to the incomplete

filling/emptying of the macropores. BJH analysis of desorption curve shows a very similar value of mesopore pore diameter (~6-7 nm) of the three supports. (**Figure 4.4b**)

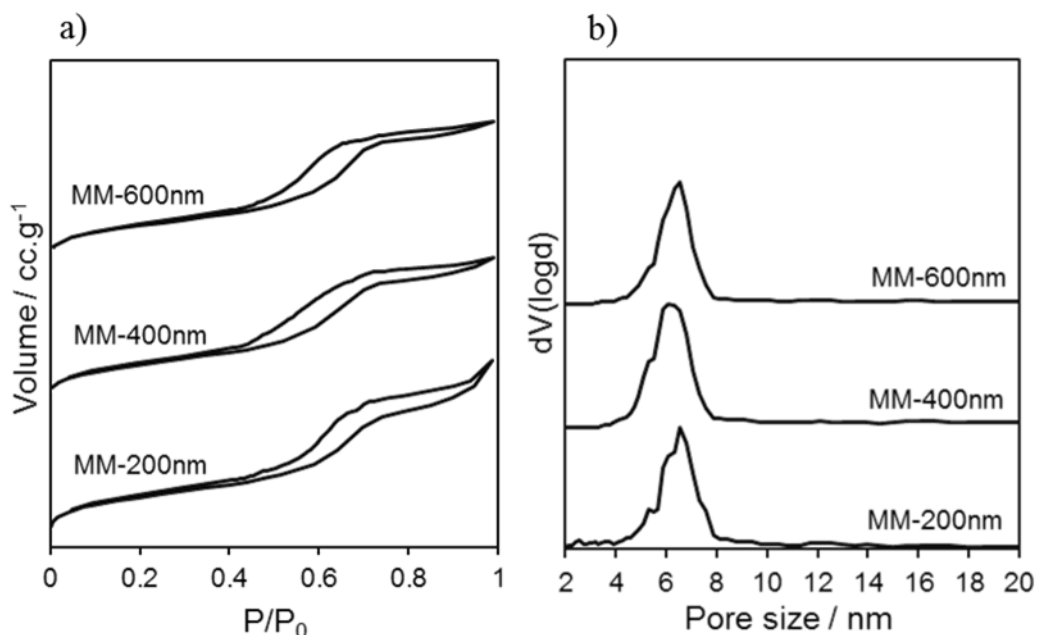


**Figure 4.4** Stacked isotherms of MM-SBA-15 supports (a) and stacked BJH pore size distribution plots (b).

The BET and BJH methods were used to determine respective surface areas and average mesopore diameters, with the results presented in **Table 4.1**.

**Table 4.1** Textural properties of the MM- SBA-15 support.

Sample	Pore size / nm	S <sub>BET</sub> / m <sup>2</sup> .g <sup>-1</sup>	V <sub>pore</sub> / cc.g <sup>-1</sup>	V <sub>micro</sub> / cc.g <sup>-1</sup>
MM-200	6.6	301	0.4	0.02
MM-400	6.1	340	0.5	-
MM-600	6.9	334	0.6	-

The BET surface areas for TLCT-SBA-15 (~320 m<sup>2</sup>/g) is significantly lower than for SBA-15 (~700 m<sup>2</sup>/g, reported in **Chapter 3**), which appears to result from a decrease in their microporosity, as determined by the t-plot method.[20, 24] This observation can be explained by the removal of the hydrothermal treatment in TLCT synthetic protocols; thus altering pore-swelling dynamics.

Additionally, the presence of the polystyrene bead-macropore template restricts the formation and swelling of the mesophase to cavities around said template, thus explaining the smaller unit cell parameter and fall in XRD peak intensity, as displayed in **Figure 4.5**.

**Figure 4.5a** shows the low angle XRD patterns of the MM-SBA-15 supports in comparison with SBA-15-7. The MMSBA-15 demonstrates a broadened SBA-15 ( $d_{10}$ ) reflection only. The other two characteristic peaks of the ( $d_{11}$ ) and ( $d_{20}$ ) diffraction planes of the 2D hexagonal pore structure typical of the mesoporous SBA-15 are not visible or reduced to a weak shoulder for the MM-SBA-15 due to the lower number of pore repeat units, a consequence of the macropores disrupting the mesopore framework. It must be noted that macropore ordering within the support framework was undetectable via traditional low angle powder diffraction due to the extremely large repeat unit distances ( $\sim 30$  times that of the mesopores) between each macropore. Moreover it can be noticed that the first order reflection ( $d_{10}$ ) is shifted to higher angle TLCT MM-SBA-15 with respect to SBA-15.

**Figure 4.5b** shows the trend of pore spacing ( $a_0$ ) and wall thickness ( $t_{\text{wall}}$ ) with the macropores size. The observed parameters tend to increase with increasing of macropores size in the following order: MM-200 < MM-400 < MM-600 ~ mesoSBA-15.

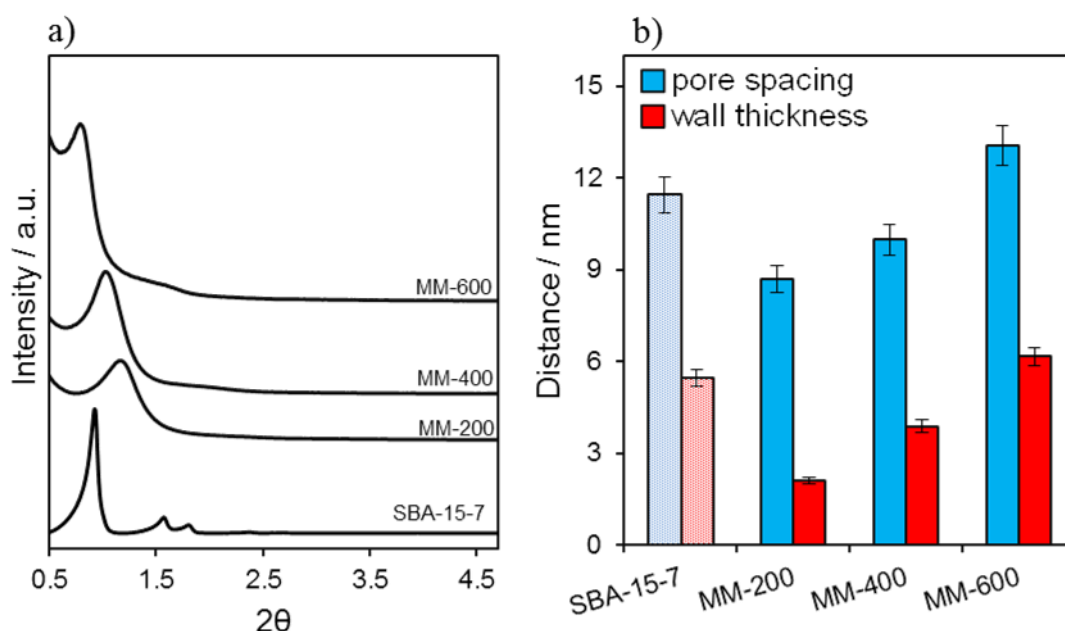


**Figure 4.5** Low angle XRD patterns of the silica supports (a), trend of increasing of  $t_{\text{wall}}$  and  $a_0$  with increasing of macropore size in comparison with the values found for the SBA-15 (b).

The parameters evaluated from the XRD low angle are reported in **Table 4.2**. [5, 24, 25]

**Table 4.2** Pore spacing ( $a_0$ ), interlayer spacing ( $d_{10}$ ) and wall thickness ( $t_{\text{wall}}$ ) of the hierarchical supports with different macropores size. The sample SBA-15-7 is reported for comparison.

Sample	$2\theta$	$d_{(10)}^a$ / nm	$a_0^b$ / nm	$d_p^c$ / nm	$t_{\text{wall}}^d$ / nm
SBA-15-7	0.8	10.2	11.8	6.8	5.0
MM-200	1.2	7.5	8.7	6.6	2.1
MM-400	1.0	8.7	10.0	6.1	3.9
MM-600	0.8	11.3	13.1	6.9	6.2

<sup>a</sup> Interlayer spacing derived from Bragg's law, <sup>b</sup> pore spacing, <sup>c</sup> pore diameter from  $N_2$  desorption isotherm, <sup>d</sup> wall thickness =  $(2d_{(10)}/\sqrt{3})$ -pore diameter

SEM analysis was used to provide concrete evidence for the successful generation of macroporous architecture. (**Figure 4.6a**, **Figure 4.6b** and **Figure 4.6c**) Moreover, the images reveal macropores are slightly smaller than the PS bead templates used in synthesis. (**Figure 4.6d**) The macropores are formed due to the removal of polystyrene beads from the silica walls by calcination, thus it is proposed that the size of the macro voids is slightly less than the size of the original polystyrene because of shrinkage of silica walls during melting of polystyrene latex.[26] The diameter of macropores formed from 200 nm PS beads is ca. 150 nm, indicating a shrinking of about 25% when compared to the size of the parent PS beads. A similar degree of shrinkage of 15% and 28% respectively is observed for silicas prepared with PS beads of 400 and 600 nm diameters, with average macropores size of 340 and 428 nm.

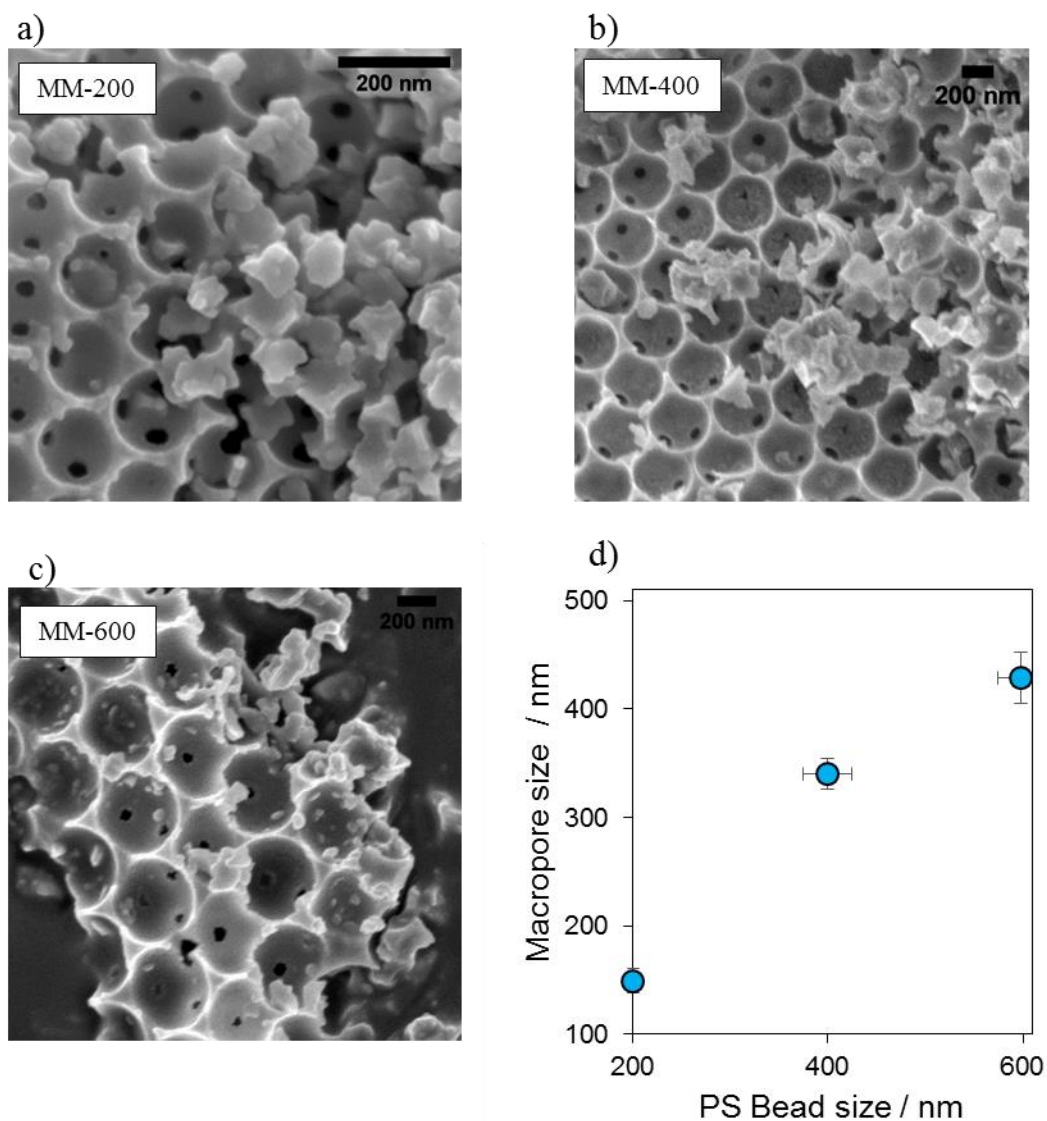


**Figure 4.6** SEM image of macro-mesoporous SBA-15 obtained with PS beads of different sizes: 200 nm(a), 400 nm (b) and 600 nm (c). The plot shows that measured macropores are smaller than the size of PS bead templates previously measured from the STEM pictures (d).

## 4.2.3 Characterisation of TiO<sub>2</sub> grafted supports

### 4.2.3.1 Effect of macropores size

Upon successful characterisation of each support, TiO<sub>2</sub> was introduced onto the surface using the grafting procedure describe on **Chapter 2**, aiming to TiO<sub>2</sub> loadings of 6-10 wt. %. The motivation of this study was to prepare a photoactive material evaluating the advantages resulting from the introducing of hierarchical structure and investigate the effect of different macropore size on the mass transfer limitation and on the optical properties of the material as photonic crystal coated with an active phase. The nomenclature used for the composites catalyst is defined as follows: X-n, with X the size of the macropores (nm) and n the number of grafting cycles.

#### 4.2.3.1.1 Elemental analysis

XRF and ICP-OES analysis were conducted on the composite materials to quantify their bulk composition. The values of wt.% of TiO<sub>2</sub> obtained from the two techniques are shown in **Table 4.3**.

**Table 4.3** Bulk elemental analysis for the hierarchical composites with different macropores size.

Sample	TiO <sub>2</sub> loading / wt.%	
	XRF (%error)	ICP-OES
200-1	8.1 (0.9)	9.7
400-1	9.5 (1.1)	10.3
600-1	6.0 (0.8)	8.3

#### 4.2.3.1.2 X-ray photoelectron spectroscopy

XPS was employed to probe the surface composition and the oxidation state of the supported TiO<sub>2</sub> nanoparticles. A summary of the elemental surface composition is presented in **Table 4.4**, which reports the wt. % of the surface species for each of the grafted MM-SBA-15 support.

**Table 4.4** Surface composition of the hierarchical composites.

Sample	Si	O	Ti
	/ wt. %	/ wt. %	/ wt. %
200-1	49	46	4
400-1	48	47	5
600-1	49	47	3



High-resolution XPS spectra for Ti2p and O1s of the sample 200-1 are displayed in **Figure 4.7**. **Figure 4.7a** shows that Ti 2p<sub>3/2</sub> corresponds to a binding energy of 458.9 eV, which is slightly higher than that of TiO<sub>2</sub> bulk anatase (458.8 eV) [46]. The shift to higher binding energies is associated with the formation of Ti-O-Si chemical bonds, resulting in the two sets of peaks exhibited in the Ti 2p spectra. [27, 28] The peaks centred at 459.9 eV and 465.7 eV were assigned to cross-linking Ti–O–Si bonds and the shift is due to a decrease in the positive charge of the titania species within the Ti-O-Si formation compared to that of anatase.[29]

Analysis of the oxygen 1s regions (**Figure 4.7b**) indicates that there were multiple components that may be fitted into three peaks: oxygen species in Si–O–Si groups (532.4 eV) in the form of silicon dioxide, those in interfacial Si–O–Ti cross-linking bonds (530.4 eV) and those from surface hydroxyl groups (533.3 eV).[29, 30] Compared with the XPS of the bare support MM-200, the contributions of OH groups in O1s shows lower hydroxyl content and the presence of the cross-linking Ti–O–Si bonds, suggesting that Ti and Si are combined through a shared oxide.

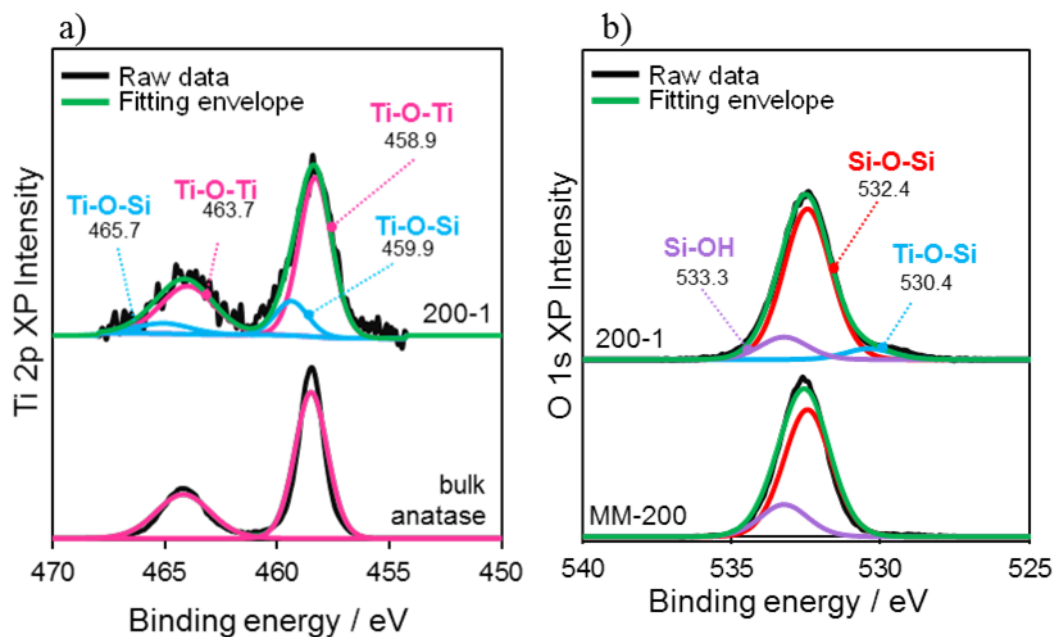


**Figure 4.7** Ti 2p region from XPS analysis of 200-1 and bulk anatase (a), and O 1s region from of titania grafted on macroporous SBA-15 and the correspondent bare support.

The corresponding Si 2p XP spectra for the composite material and the bare support are shown in **Figure 4.8**. The Si2p spectrum was fit with two sets of Si 2p doublets with a doublet separation of ~0.6 eV.[31] The peak at 103.41 eV corresponds to Si-O-Si and it is attributed to the pure silica (red line). An additional peak at 102.9 eV (blue line) is only present in the grafted sample. This assigned to silicon atoms at the silica-titania interface.

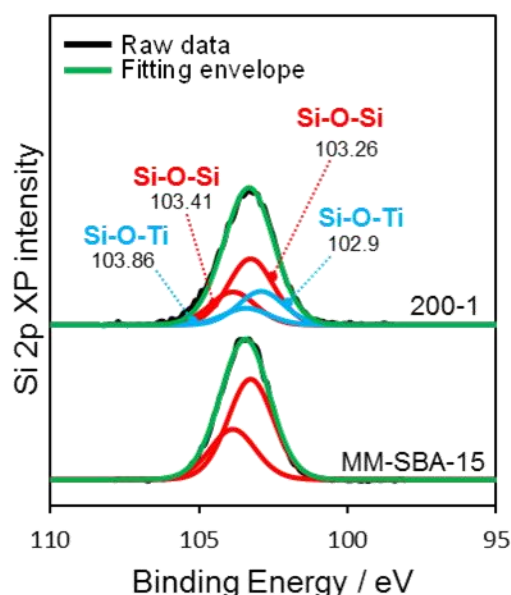


**Figure 4.8** Si 2p region from XPS analysis of 200-1 and parent support.

The bulk and surface compositions of the composite catalysts evaluated by ICP and XPS are summarised in **Table 4.5** below and the wt. % Ti bulk:surface ratio is reported. The bulk and surface values result identical, indicating that for low TiO<sub>2</sub> loading (ca. ≤10 wt. %) it is possible to obtain a homogeneous coverage on the porous support.

**Table 4.5** Comparison of the surface and bulk Ti wt. % content for the hierarchical composites.

Sample	Surface Ti <sup>a</sup> / wt. %	Bulk Ti <sup>b</sup> / wt. %	Surface : Bulk
200-1	3.8	3.9	1.0
400-1	4.8	4.5	1.1
600-1	3.2	3.5	0.9

<sup>a</sup> XPS, <sup>b</sup> XRF

#### 4.2.3.1.3 Nitrogen porosimetry

Textural differences between the bare supports and grafted samples were explored by N<sub>2</sub> porosimetry. The resulting isotherms are shown in **Figure 4.9a**. The isotherms retain a type IV shape, characteristic of SBA-15 mesostructure and pore uniformity, including a H1 hysteresis loop associated with the bottle-necked pore openings and an increasing adsorption at high partial pressure, suggesting the presence of macropores.[24, 25, 32] A second hysteresis is shown for these materials at higher partial pressures ( $P/P_0 > 0.8$ ) due to the incomplete filling/emptying of the macropores. The hysteresis loop size increases after the grafting procedure (See isotherms 2-4-6 in **Figure 4.9a**), which may be due to the TiO<sub>2</sub>-coating of the internal surface area of the pores that

could slightly limit the diffusion of N<sub>2</sub> during desorption cycle. In general, the preserved hysteresis and isotherm shape of the parent material upon the grafting confirms there is negligible pore collapse or change in support infrastructure.

Pore size distributions, calculated from the desorption branch of the isotherm, are presented in **Figure 4.9b**. BJH pore size distribution plots show a shift of the maximum value to lower pore diameters after one grafting cycle. The difference in mesopore size between the parent and the grafted materials is in the range of ~0.5-1 nm. Considering that the titania monolayer is assumed to have a thickness of 0.352 nm, which is the interlayer spacing for the (101) plane of TiO<sub>2</sub> (anatase), the results suggested the formation of thicker layer or agglomeration of TiO<sub>2</sub> nanoparticles on the silica surface.

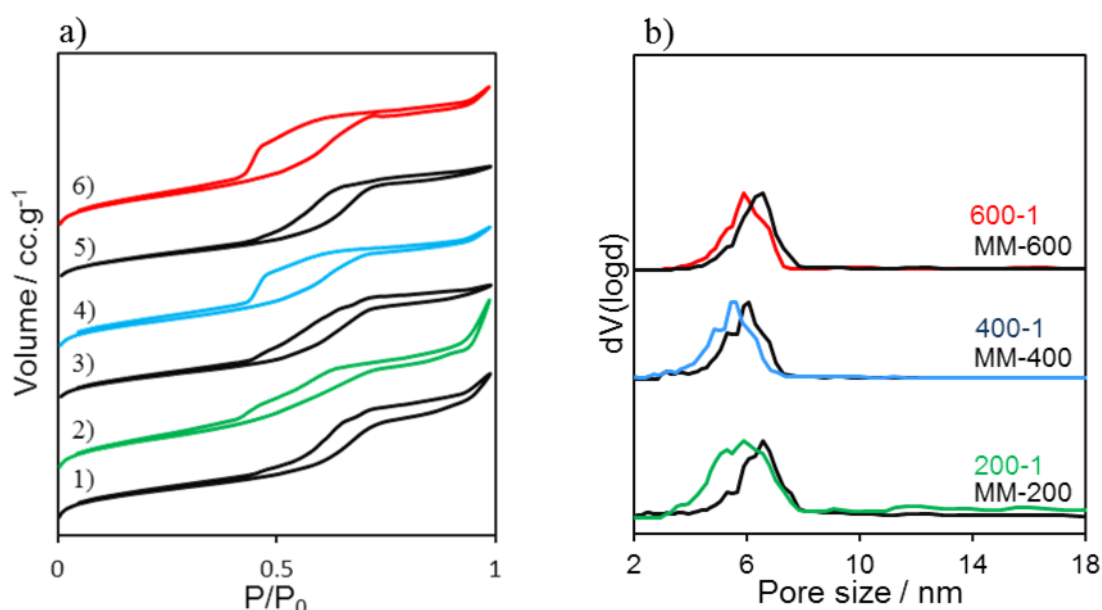


**Figure 4.9** Stacked isotherm plots of hierarchical SBA-15 with different macropore sizes (black lines): MM-200 (1), MM-400 (3) and MM-600 (5); and the relative grafted composite samples (200-1(2), 400-1 (4) and 600-1 (6)) (a); stacked BJH mesopore size distributions (b).

**Table 4.6** reports the textural properties of the grafted samples in comparison with the relative parent supports.

**Table 4.6** Textural properties of the parent MM- SBA-15 and the grafted samples.

Sample	$S_{\text{BET}}$ / m <sup>2</sup> .g <sup>-1</sup>	$d_p$ / nm	$\Delta_{\text{pore size}}$ / nm	$V_{\text{total}}$ / cc.g <sup>-1</sup>
MM-200	301	6.6		0.4
200-1	300	5.9	0.7	0.4
MM-400	340	6.1		0.5
400-1	322	5.7	0.5	0.4
MM-600	334	6.9		0.6
600-1	267	5.9	1.0	0.4

#### 4.2.3.1.4 Powder X-ray diffraction

**Figure 4.10a** shows the wide angle XRD patterns for the three TiO<sub>2</sub> grafted MM-SBA-15.

A broad reflection at angles  $\theta < 35^\circ$  was attributed to amorphous silica and a weak peak at 24.5 degrees was assigned to (101) reflection of anatase. A decrease in particle size was observed with increasing diameter of macropore size of the support. (**Figure 4.10b**) This trend may arise from the genesis of large TiO<sub>2</sub> crystallites during the grafting procedure which may block pores (more easily for smaller macropores) hindering permeation of the titania precursor solution through the pore network, leading to low dispersion of TiO<sub>2</sub> nanoparticles on the internal silica surface.

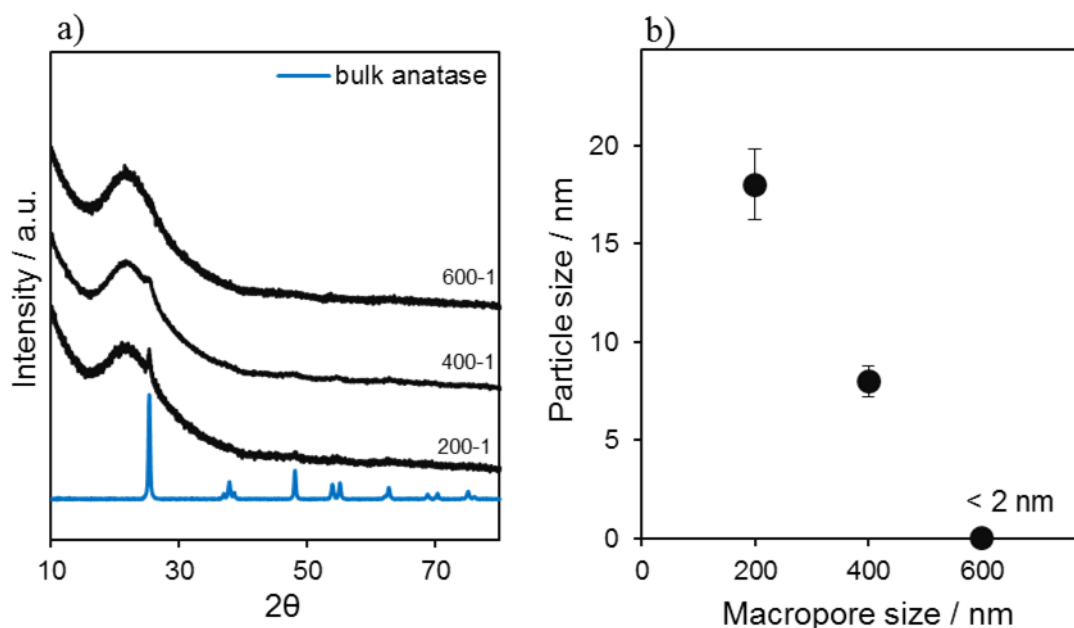


**Figure 4.10** Offset of wide angle XRD patterns of the grafted materials in comparison with the spectrum of bulk anatase (a). Evolution of the anatase crystallite size with the number of titania graftings evaluated by the Scherrer equation (b).

#### 4.2.3.1.5 ATR-IR spectroscopy

The ATR IR spectra of pure MM-SBA-15 and the grafted materials are shown in **Figure 4.11**. The TiO<sub>2</sub> P-25 and the mesoporous SBA-15 7 spectra are reported for comparison. These results reported for the spectra of the composites materials provide further evidence of the successful grafting of TiO<sub>2</sub> onto the silica support along with the formation of a separate TiO<sub>2</sub> phase. The band at around 960 cm<sup>-1</sup>, which has been widely used to characterize the bond between the metal ions and the silica framework and is typical of the Ti-O-Si vibration for the interface species, is very weak compared to the peaks attributed to the single SiO<sub>2</sub> and TiO<sub>2</sub> phases. This observation is further evidence for the presence of TiO<sub>2</sub> crystallites on the hierarchical SBA-15 support even at low TiO<sub>2</sub> loading, in agreement with the XRD and XPS data.

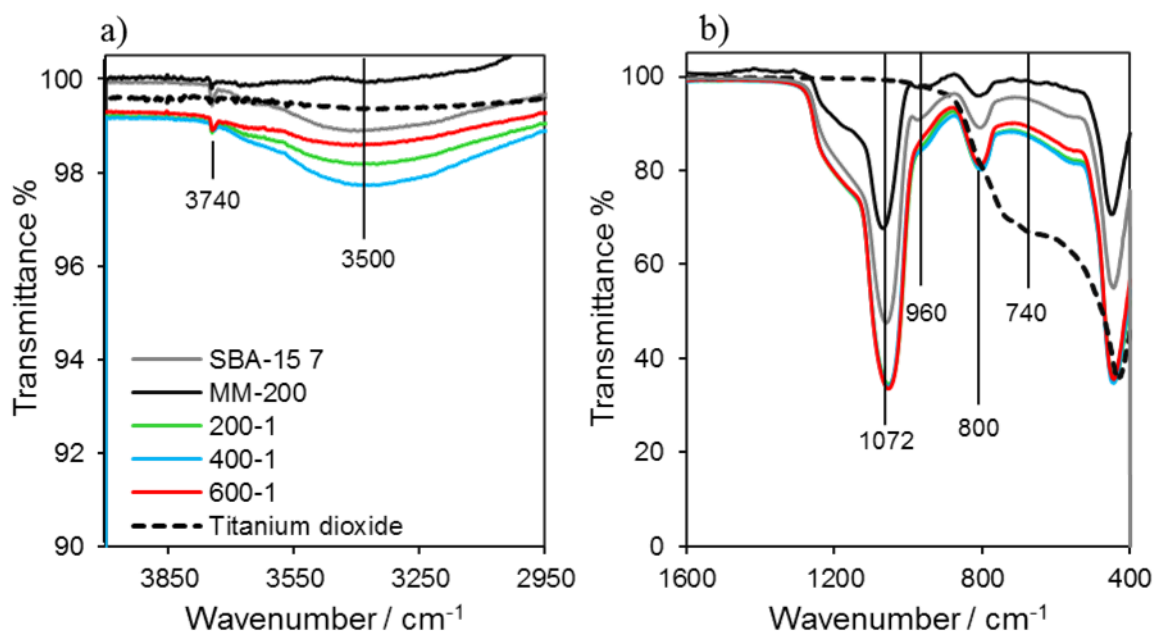


**Figure 4.11** ATR IR spectra of the grafted samples, the MM-200 support, the mesoporous support (SBA-15 7) and the TiO<sub>2</sub> P-25 in the range of 2950-4000 cm<sup>-1</sup> (a), 400-1600 cm<sup>-1</sup> (b).

The observed frequencies and assignments are reported in **Table 4.7** and are in good accord with the results presented in **Chapter 3**.

**Table 4.7** Assigned vibrational modes for the TiO<sub>2</sub> grafted MM-SBA-15.

Vibrational Mode	Frequency /cm <sup>-1</sup>
$\nu_{as}$ (Si-O-Si)	1072
$\nu_{sym}$ (Si-O-Si)	800
$\delta$ (Si-O)	435
$\nu$ (Si-OH)	3740
$\nu$ (Ti-O-Ti)	740
$\nu$ (Ti-O)	418
$\nu$ (Ti-OH)	3500
$\nu$ (Si-O-Ti)	960

#### 4.2.3.1.6 Scanning transmission electron microscopy

TEM was used to examine the structural architecture of the TiO<sub>2</sub> grafted catalysts with representative bright field TEM images. **Figure 4.12** depicts representative TEM images of the 200-1 synthesized sample. Macropores are clearly incorporated throughout MM-SBA-15, with an average diameter of 185 nm. Moreover the high resolution TEM images confirm the ordered mesopore structure is retained and that the pore walls of SBA-15 channels remain uniform upon grafting of TiO<sub>2</sub>. The sample displays both the channel structures and the hexagonal mesopore



packing of a typical SBA-15 within the framework, and thus successful synthesis of hierarchical macroporous-mesoporous silica and not two independent phases.

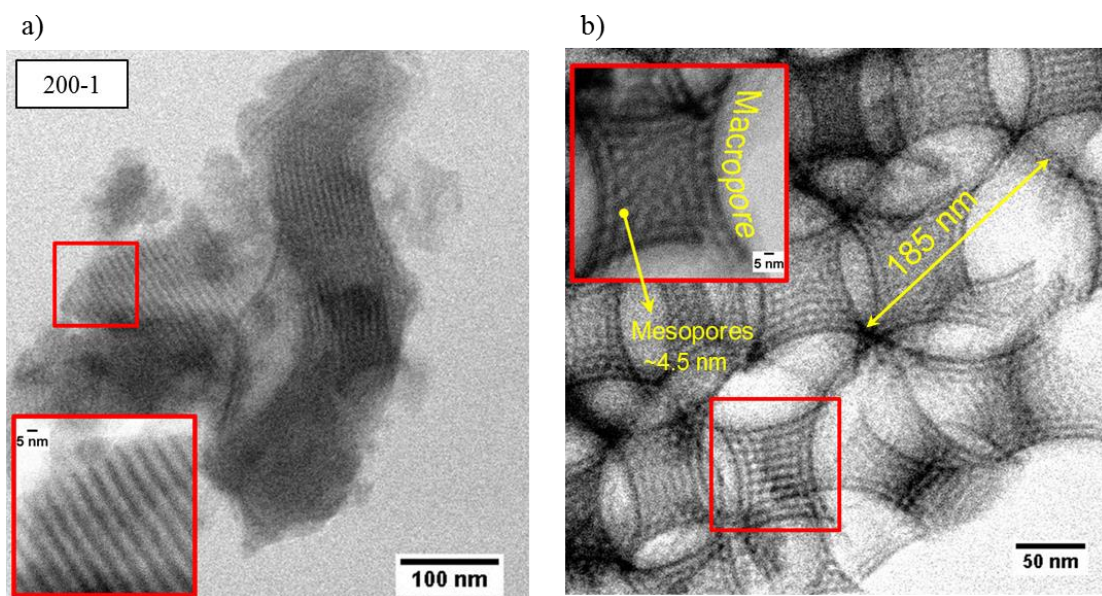


**Figure 4.12** Representative bright field TEM images of channel (a) and the hierarchical macro/mesoporous structure of the 200-1(b).

Representative TEM images of 400-1 and 600-1 are shown in **Figure 4.13**.

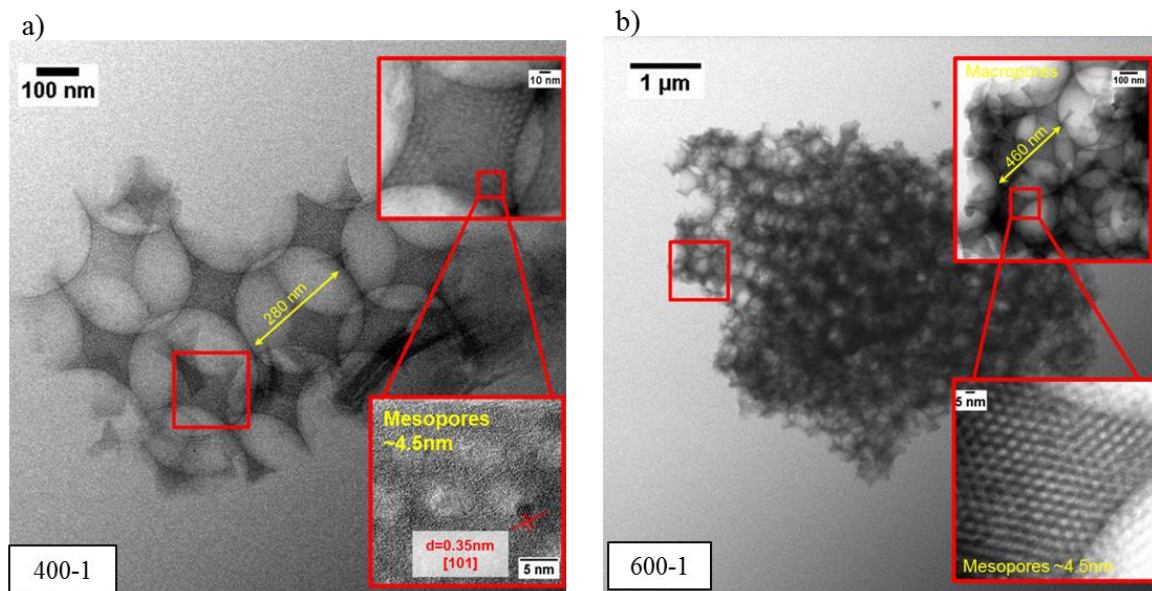


**Figure 4.13** Representative bright field TEM images of the hierarchical macro/mesoporous structure of the 400-1(a) and the 600-1 (b) samples.

For all the reported TEM images it is interesting to observe the presence of the mesopore structure within the macropore network. In **Figure 4.13a** the insert highlights a selected area with a presence of a small anatase nanoparticle ( $d \sim 2\text{ nm}$ ). The spherical morphology and the arrows indicate the

(101) lattice spacing with d-spacing of 0.35 nm are both evidence of the presence of TiO<sub>2</sub> nanoparticles in anatase phase, in agreement with the XRD analysis. [33]

#### 4.2.3.1.7 UV-vis diffuse reflectance spectroscopy

Diffuse reflectance (DR) UV-vis spectroscopy was used to characterize the electronic structure and the optical proprieties of hierarchical composite catalysts.

Three-dimensionally ordered macroporous (3DOM) materials have drawn much attention in the field of photocatalysis, because the periodic pore structure, with its large porosity, introduces new interesting optical properties, as three dimensional photonic crystals (PC).[6, 7, 34, 35] To be specific, the synthesised hierarchical supports (MM-SBA-15) are photonic crystal with an inverse opal structure (IOS). Photonic crystals are materials characterized by a periodic structure with ordered spatial variation of the refractive index ( $n$ ) between the solid matrix (i.e. silica,  $n_{\text{SiO}_2} = 1.45$ ) and the voids (air,  $n_{\text{air}} = 1$ ), which cause a modification of propagation of light for specific wavelength.[19] This range of wavelengths that cannot propagate through the PC structure is called photonic band gap (PBG or stop band) and its variation is due to the refractive index contrast. [8, 36] **(Figure 4.14)** Specifically, inverse opals are created by the infiltration of synthetic opals (i.e. PS beads) with a material of high refractive index (silica) and subsequent removal of the spheres to produce a structure of periodic voids (air) surrounded by a continuously silica matrix. This creates a large refractive index contrast that has the potential to produce a PBG. Photons within this particular range of energy cannot be absorbed by the PC structure and are, consequently, reflected. The resulting effect is an internal multiple scattering.[37] Another important feature of inverse opals, together with the PBG, is the existence of the slow photons (SP) effect. The light at the frequency edge of the PBG propagate with strongest reduced velocity in the solid matter and these photons are usually called “slow photons”. This effect can significantly enhance the light absorption within the material (light harvesting).[7]

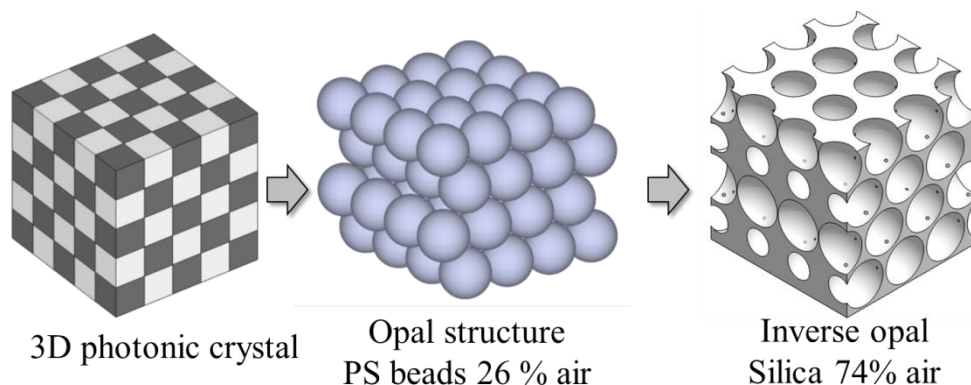


**Figure 4.14** Schematic figure of photonic crystal with silica inverse opal structure.

The optical behaviour of the synthesised photonic crystals with an inverse opal structure (IOs) was further investigated by diffuse reflectance (DR) UV-visible spectroscopy. In particular the stop bands can be conveniently measured and the position of slow photons can be identified by approximating slopes at the edge of the stop bands. Diffuse reflectance spectra of the MM-SBA-15 supports with different macropores size and the corresponding stop band positions are reported in **Figure 4.15**. The dotted circles indicate the maximum reflectance of the stop bands, while the black arrows indicate the expected region of the slow photon formation at the blue edge of the stop band (BPG –blue photonic gap). **Figure 4.15a** shows the most evident difference between the two kind of silica supports: mesoporous SBA-15-7, with 100% of reflectance in the UV-Vis region (black line), and the hierarchical materials with broad reflectance bands (stop band) characteristic of the photonic structure. The position of the stop bands shifts to longer wavelength for bigger macropores, as shown in **Figure 4.15b**. The PBG are located in the visible region and centred at 412 (MM-200), 494 (MM-400) and 654 (MM-600) nm. Thus, PBG of the three hierarchical supports is evidently modulated by changing the macropore diameters.[38] This trend confirms that the hierarchical silica structure can block light in a certain wavelength range, allowing the confinement and manipulation of photons within the materials. [7] The stop band, the consequent internal scattering, together with the slow photons effect of support material play a key role in improving the light absorption and thereby the photocatalytic activity of semiconducting materials (i.e.  $\text{TiO}_2$ ) when the wavelength of slow photons overlaps with the band gap of a semiconductor and/or the incident light wavelength. Only if these conditions are satisfied, an enhancement of the light absorption by slow photons can be observed.[37]

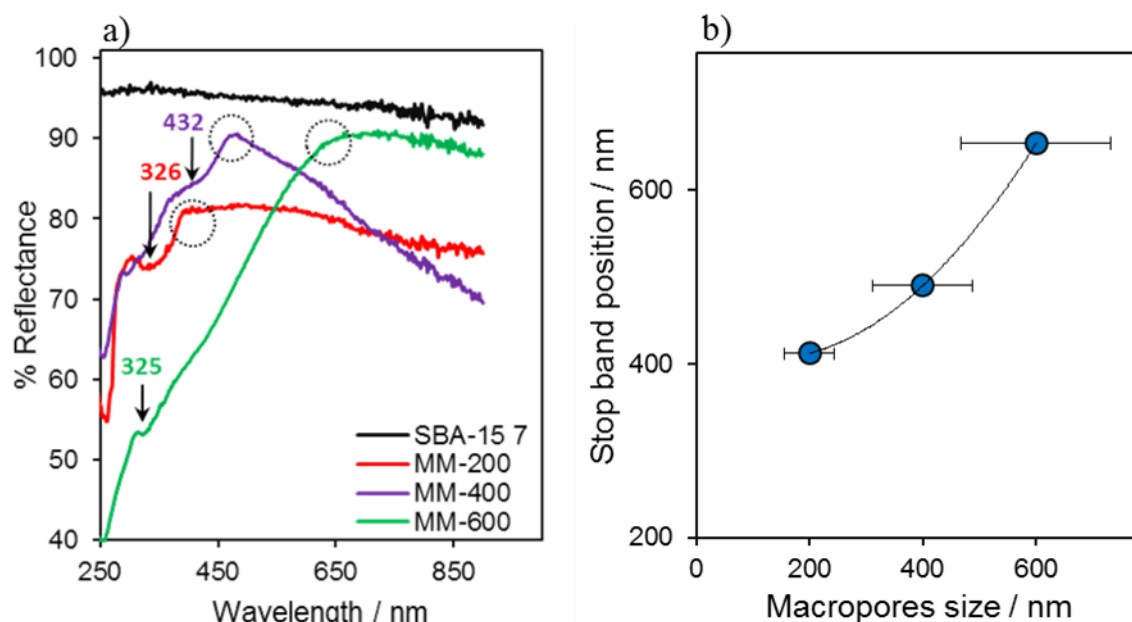


**Figure 4.15** DRUV-vis reflectance spectra (%R) of hierarchical silica supports with different macropores size in comparison with the mesoporous SBA-15 (a) shift of the stop band position as function of the macropore size (b).



The band gap energies ( $E_g$ ) of the three hierarchical support grafted with  $\text{TiO}_2$  (~10 wt. %) were calculated using Kubelka-Munk function  $F(R)$  as shown in **Figure 4.16a** (the  $E_g$  values indicated by the black arrows). **Figure 4.16b** shows the absorption spectra of the three composites and the reflectance spectra of the corresponding supports. The yellow region represents the electronic band gap of the  $\text{TiO}_2$  nanoparticles grafted on each support and the black arrows are the positions of blue edges of the PBG. The blue edge of the PBG of the sample 200-1 and 600-1 is tuned with the electronic band gap of  $\text{TiO}_2$  and this can increase the probability to produce a slow photon effect.

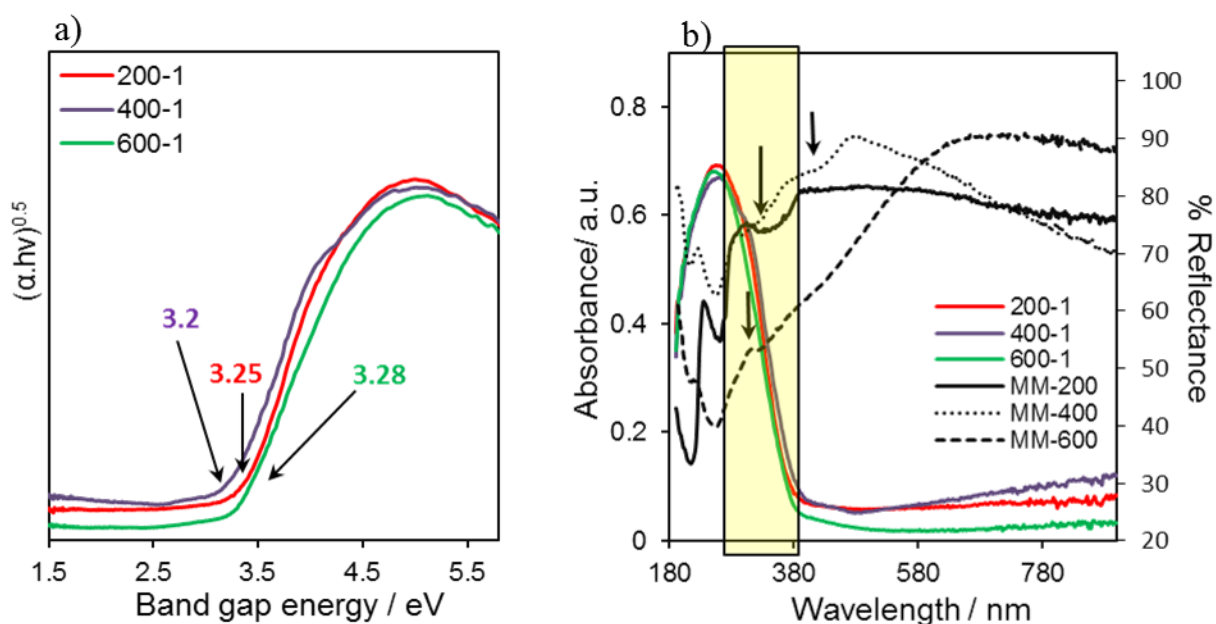


**Figure 4.16** Kubelka-Munk function for band gap evaluation (a) and absorption spectra (primary y-axis) of the  $\text{TiO}_2$  on MM-SBA-15 support and the reflectance spectra (secondary y-axis) for the corresponding supports (b).

#### 4.2.3.2 Effect of titania loading

The previous section has highlighted the influence that support materials can exert upon supported metal nanoparticle catalysts and the photoactivity of the composite catalysts. Varying support properties can induce considerable changes in the photonic properties of these materials, and in turn affect their photocatalytic performance. The macro-mesoporous SBA-15 synthesized using a PS beads template of 400 nm diameter was chosen as support to investigate the impact of the titania loading. Three grafting cycles were performed to obtain a gradually and uniform  $\text{TiO}_2$ -coating of the silica support, avoiding pore blocking and monitoring the evolution of titania surface properties. The nomenclature used for the composites catalyst is defined as follows: MM-400, for the parent hierarchical support, and 400-n, with n = number of grafting cycles, for the composites catalysts.

#### 4.2.3.2.1 Elemental analysis

Titania was introduced to hierarchical silica support (MM-400) using the grafting procedure outlined in **Chapter 2**, covering a range of weight loadings of 10% to 23%. Three different loadings of TiO<sub>2</sub> on MM- 400 were prepared and the bulk titania content was measured using XRF and ICP analysis. (**Table 4.8**)

**Table 4.8** Bulk elemental analysis for the hierarchical composites with different TiO<sub>2</sub> loading.

Sample	TiO <sub>2</sub> loading / wt. %	
	XRF (%error)	ICP-OES
400-1	9.5 (1.12)	10.3
400-2	19.0 (0.8)	15.0
400-3	23.1 (0.96)	18.0

#### 4.2.3.2.2 X-ray photoelectron spectroscopy

The impact of the three consecutive grafting procedures onto MM-400 support was explored by XPS to determine surface composition of the samples with increasing titania loading.

**Table 4.9** presents detailed information about surface composition of 400-n (n = 1-3) catalysts.

**Table 4.9** Surface composition of the 400-n materials (n=1-3).

.Sample	Si	O	Ti
	wt. %	wt. %	wt. %
MM-400	48	52	-
400-1	48	47	5
400-2	43	47	9
400-3	42	47	11

From high resolution XP spectra, the evolution of Ti, O, Si species on the surface of MM-400 can be observed, confirming that as the titanium content of the materials is increased, interfacial species (Si-O-Ti) are present on the surface of silica support. The Ti 2p region was fit using line shapes obtained from bulk anatase, which recorded a Ti 2p<sub>3/2</sub> peak position of 458.8 eV, consistent with literature values.[39] (**Figure 4.17a**) A shift to slightly higher binding energies is associated with the formation of Ti-O-Si bonds, resulting in the two sets of peaks exhibited in the Ti 2p spectra[40] caused by a decrease in the positive charge of the titania species within the Ti-O-Si formation compared to that of the bulk reference.[29]

The Oxygen 1s region (**Figure 4.17b**) displayed an asymmetry which was accounted for by fitting the spectra with peaks for bulk silicon dioxide at 532.4 eV and for titanium dioxide at 530 eV, with the line shapes and positions taken from analysis of the parent SBA-15 and bulk anatase. The

contributions of OH groups from surface hydroxyl group at 533.3 eV drastically decreases already at the 1<sup>st</sup> grafting cycle, indicating that also at low titania loading (wt.% TiO<sub>2</sub> ≤ 10) the MM-SBA-15 surface is almost completely covered.

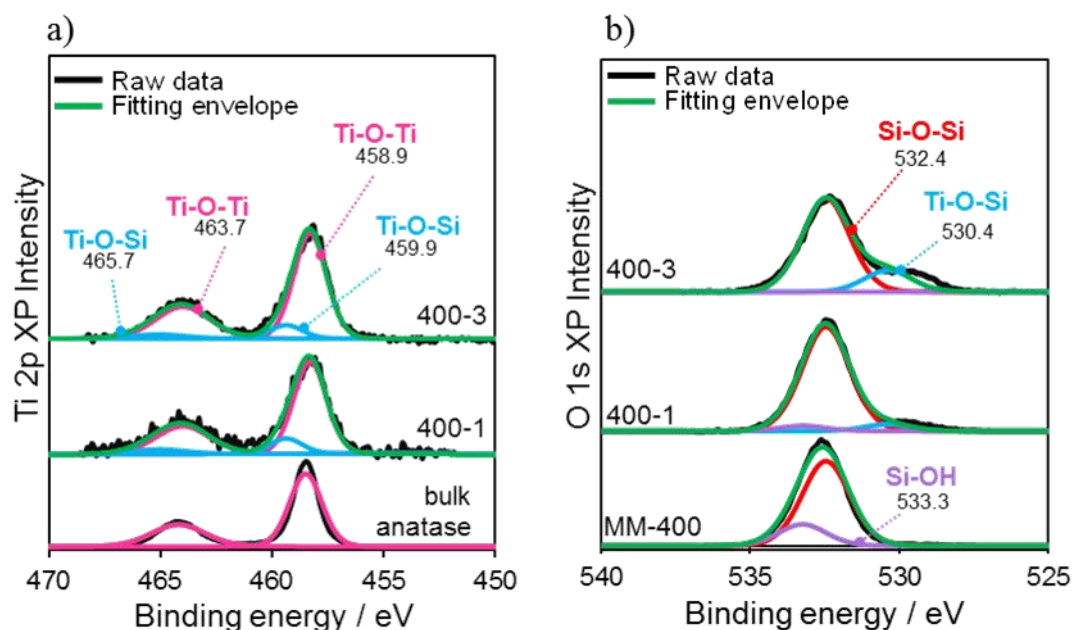


**Figure 4.17** Ti 2p XPS stack plots of the composites catalysts obtained from the 1<sup>st</sup> and the 3<sup>rd</sup> grafting cycles. The spectrum of bulk anatase is reported for comparison (a) O 1s XPS stack plots of the three grafting cycles and the relative bare support (b).

The XPS spectra from of the silicon regions are reported in **Figure 4.18a**. These Si spectra also exhibit two distinct chemical environments with BE = 0.61 eV.[31] The state at 103.4 eV is attributed to the pure silica (red line), and is the only species in SBA-15, whereas an additional peak at 102.9 eV (blue line) is present in the grafted samples. This is assigned to silicon atoms of the Si-O-Ti interface specie. After the 3<sup>rd</sup> grafting cycle the interface layer eventually becomes the dominate silica species, with the pure silica signal decreases with grafting cycle.(**Figure 4.18b**) This results from the suppression of the bulk silica signal, from the growing titania coating.

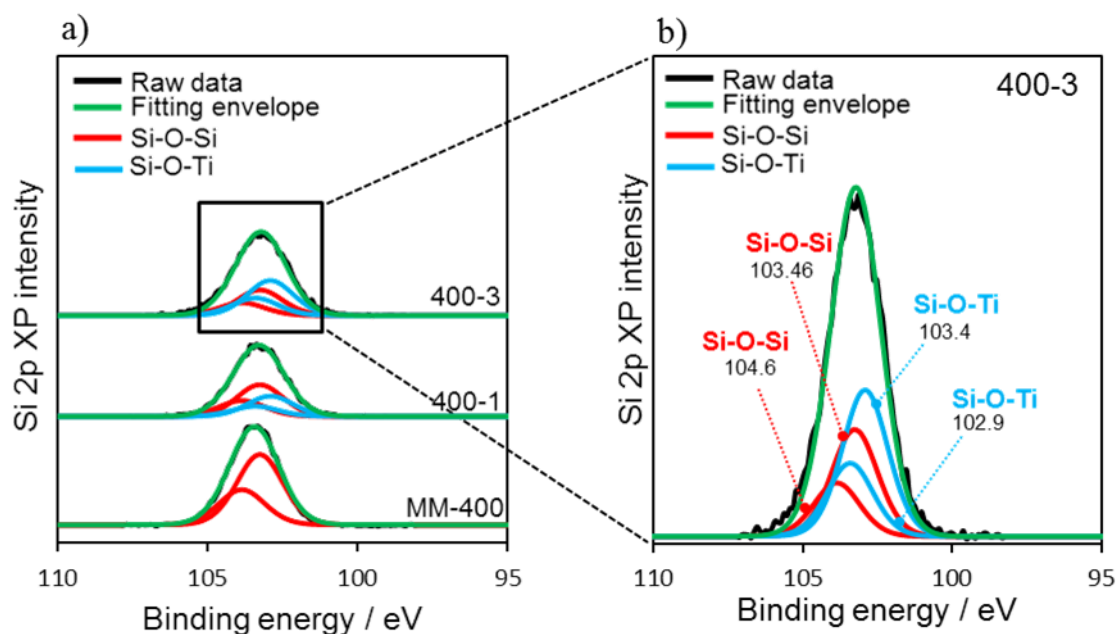


**Figure 4.18** Si 2p XPS stack plots for the 1<sup>st</sup> and the 3<sup>rd</sup> grafting cycle of the composites catalyst. The spectrum of the bare support MM-400 is reported for comparison (a) highlight of the Si 2p region for the 3<sup>rd</sup> grafting cycle (b).

**Table 4.10** reports the bulk and surface wt. % Ti for each grafting cycle, revealing that increasing the loading the bulk/surface ratio is not really changing among the series, suggesting more agglomeration or aggregation of TiO<sub>2</sub> crystallites on the support rather than growing a uniform film.

**Table 4.10** Comparison of the surface and bulk Ti wt. % content for the MM-n composites.

Sample	Surface Ti <sup>b</sup> wt. %	Bulk Ti <sup>a</sup> wt. %	Surface : Bulk
400-1	4.8	4.8	1.0
400-2	8.8	9.5	1.1
400-3	11.2	11.9	1.1

<sup>a</sup>XPS, <sup>b</sup>XRF

#### 4.2.3.2.3 Nitrogen porosimetry

N<sub>2</sub> porosimetry allows evaluation of textural properties of the grafted samples and the correspondent support. The recorded isotherms shown in

**Figure 4.19a** possess type IV shape with an H1 hysteresis, [41] characteristic of mesoporous supports with uniform mesopore diameters. Furthermore the isotherms display a second hysteresis at elevated relative pressures reflecting partial filling/emptying of the macropore network.

The BJH method was applied to the desorption branches of these isotherms to observe the pore size distribution. (**Figure 4.19b**) The pore size distributions indicate that the prepared materials do not have an entirely monodisperse pore network, with a small amount of pores existing at a lower diameter to those of the average ( $\sim 6$  nm), possibly due to contraction of the P-123 micelles near to the polystyrene bead regions. The grafting of titania appears to reduce the overall pore size, initially at the first grafting cycle by an insignificant margin, contrary to that observed in the mesoporous material, possibly due to condensation occurring mainly within the large macroporous voids. Subsequently, after the second and third grafting cycles the pore diameter is significantly reduced to 3.5 nm.[42]

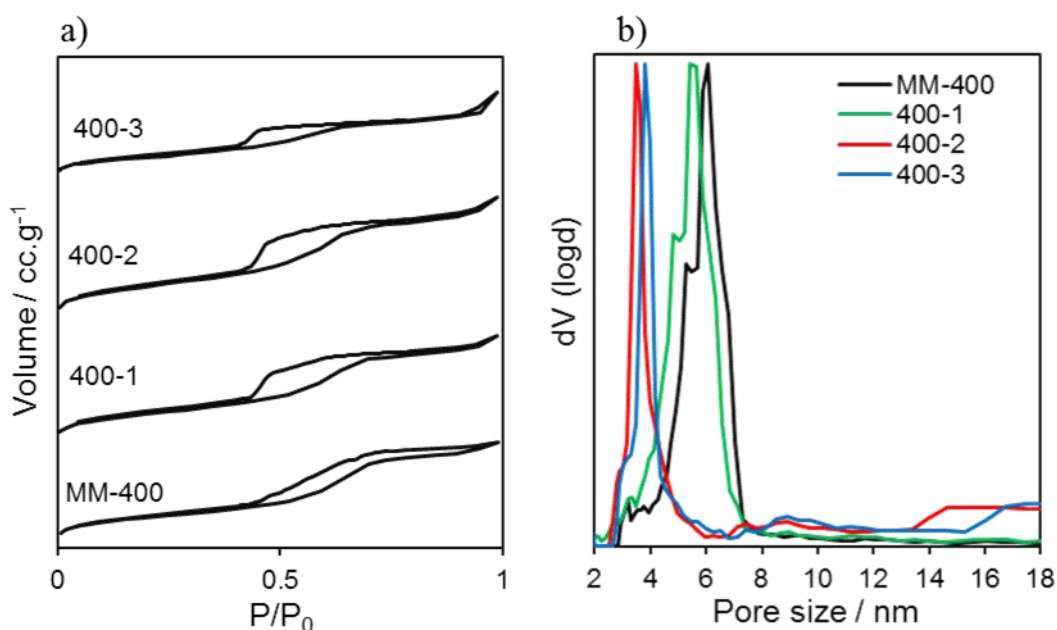


**Figure 4.19** Stacked isotherm plots of MM-n (n=1-3) composites samples and the parent MM-400 (a) BJH pore size distributions (b)

The BET and BJH methods were used to determine respective surface areas and average mesopore diameters and pore volume, with the results presented in **Table 4.11**. The BET surface areas gradually decrease with the grafting cycles.

**Table 4.11** Textural properties of the parent MM- SBA-15 and the grafted samples

Sample	TiO <sub>2</sub> / wt. %	S <sub>BET</sub> / m <sup>2</sup> .g <sup>-1</sup>	d <sub>p</sub> nm	V <sub>total</sub> / cc.g <sup>-1</sup>
MM-400	-	340	6.1	0.5
400-1	9.5	322	5.7	0.4
400-2	19	312	3.5	0.4
400-3	23.1	243	3.5	0.3

#### 4.2.3.2.4 Powder X-ray diffraction

**Figure 4.20a** shows the wide angle XRD patterns for the TiO<sub>2</sub> grafted MM-400 series, with evidence of the TiO<sub>2</sub> crystalline anatase phase. The (101) anatase diffraction peak at 25° was discernible at the first cycle of grafting and at higher TiO<sub>2</sub> loading XRD patterns exhibited strong diffraction peaks at 35°, 48° and 52° indicating TiO<sub>2</sub> in the anatase phase. The dominant (101) reflection at 25° was used to investigate the average of particles size through application of the Scherrer equation (See **Chapter 2**), [43] and an increase in size with the increasing of TiO<sub>2</sub> loading was observed (**Figure 4.20b**).

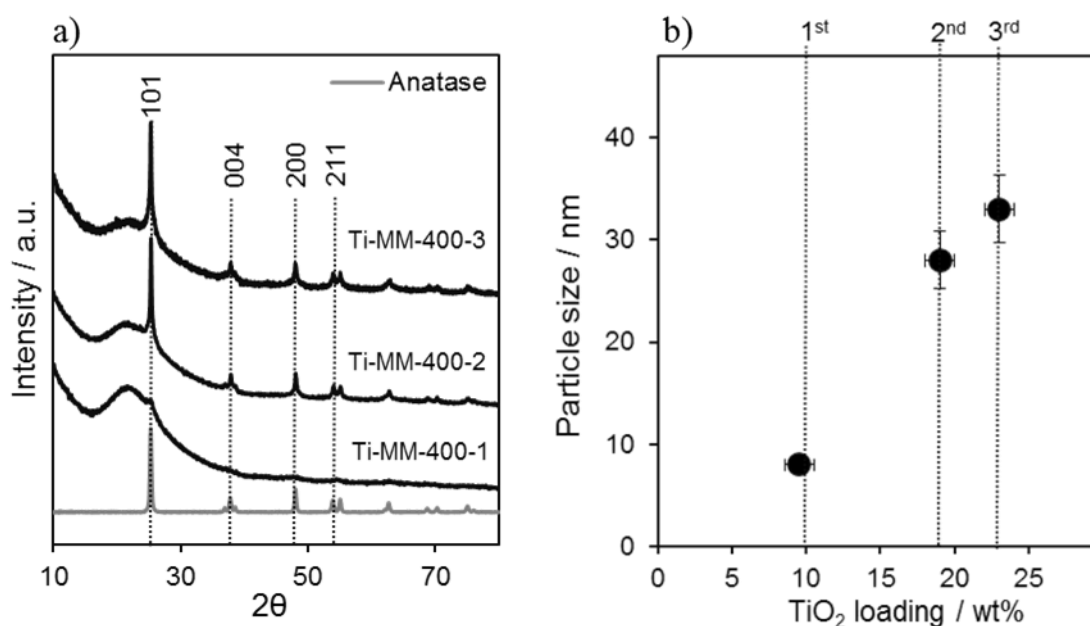


**Figure 4.20** Offset of wide angle XRD patterns of the grafted materials in comparison with the spectrum of pure anatase (a); evolution of the anatase crystallite size with the number of titania graftings evaluated by the Scherrer equation (b).

#### 4.2.3.2.5 ATR IR spectroscopy

The ATR IR spectra of pure MM-400 and 400-n ( $n = 1-3$ ) composite materials are shown in **Figure 4.21**. All the assignments were reported and explained more in detail in the **Section 4.2.3.1.5**.

In **Figure 4.21a** the broad signal centred at c.a.  $3500\text{ cm}^{-1}$  is due to the stretching vibration of hydroxyl groups Ti–OH, whereas the small sharp peak at  $3740\text{ cm}^{-1}$  is assigned to the Si–OH stretching.[44] In **Figure 4.21b** the characteristic bands of Si–O–Si vibrations dominate in the IR spectra. The peak around  $1072\text{ cm}^{-1}$  and  $800\text{ cm}^{-1}$  are attributed to the asymmetric and symmetric Si–O–Si stretching modes, respectively.[45] The bands at c.a.  $418\text{ cm}^{-1}$ , commonly assigned to  $\nu(\text{Ti-O})$  stretching, together with the shoulder at c.a.  $740\text{ cm}^{-1}$ , characteristic of the  $\nu(\text{Ti-O-Ti})$  mode, are increasing with the  $\text{TiO}_2$  loading.[46] Moreover the band at  $960\text{ cm}^{-1}$  of  $\nu_{\text{as}}(\text{Si-O-Ti})$  grows with the titania loading. All of these observations are further evidences of the successful impregnation of  $\text{TiO}_2$  onto the silica support

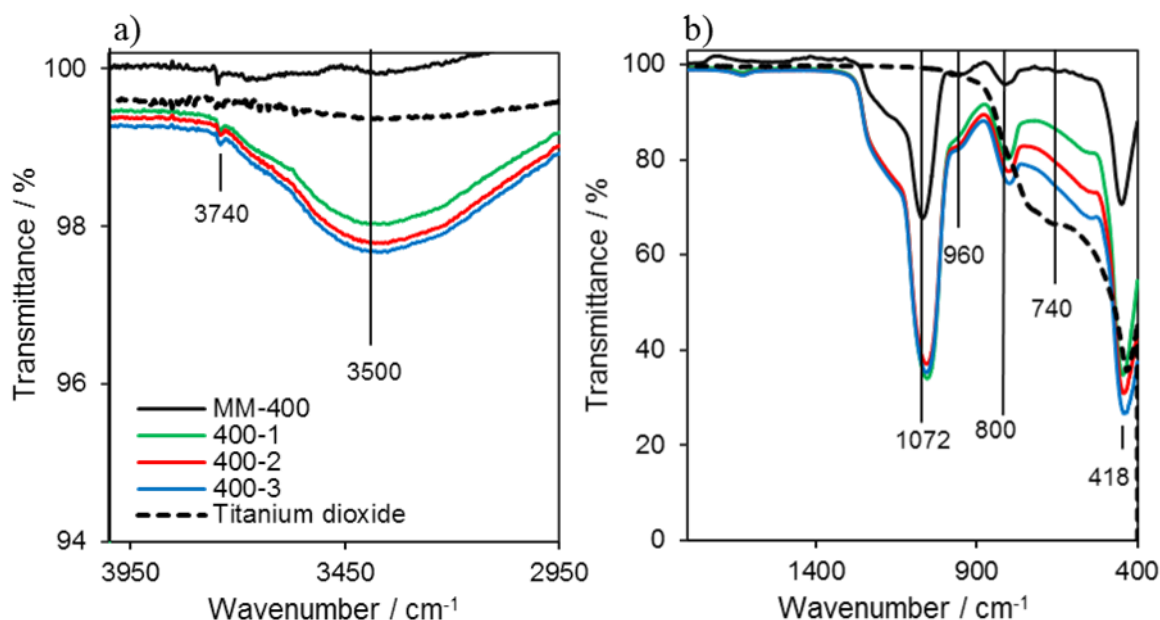


**Figure 4.21** ATR IR spectra of  $\text{TiO}_2$  grafted samples and the bare support MM-400 in the range of wavenumber of  $2950\text{--}4000\text{ cm}^{-1}$  (a) and of  $400\text{--}1600\text{ cm}^{-1}$  (b).

#### 4.2.3.2.6 Scanning transmission electron microscopy

Following the successful grafting of titania onto the surface of the hierarchically porous structure, the sample was studied using TEM, to confirm the retained presence of macropores and the uniform coating of the support. (**Figure 4.22**) The low magnification micrograph (a) shows the preserved morphology of the ordered macropores within the sample after three grafting procedures. The yellow circles indicate the presence of some titania particles aggregating throughout the material after three cycles of grafting, in agreement with XRD analysis. The high resolution images (b, c & d) highlight the highly-organised hexagonal mesopore area in between the macropore



network at the 1<sup>st</sup> (b), 2<sup>nd</sup> (c) and 3<sup>rd</sup> (d) cycle of grafting. In these bright fields TEM images the titania nanoparticles can be distinguished due to the differences in titania/silica contrast and the yellow arrows indicates the formation of a thin coating of titania on the surface of the hierarchically porous SBA-15 which increase with the grafting cycles.

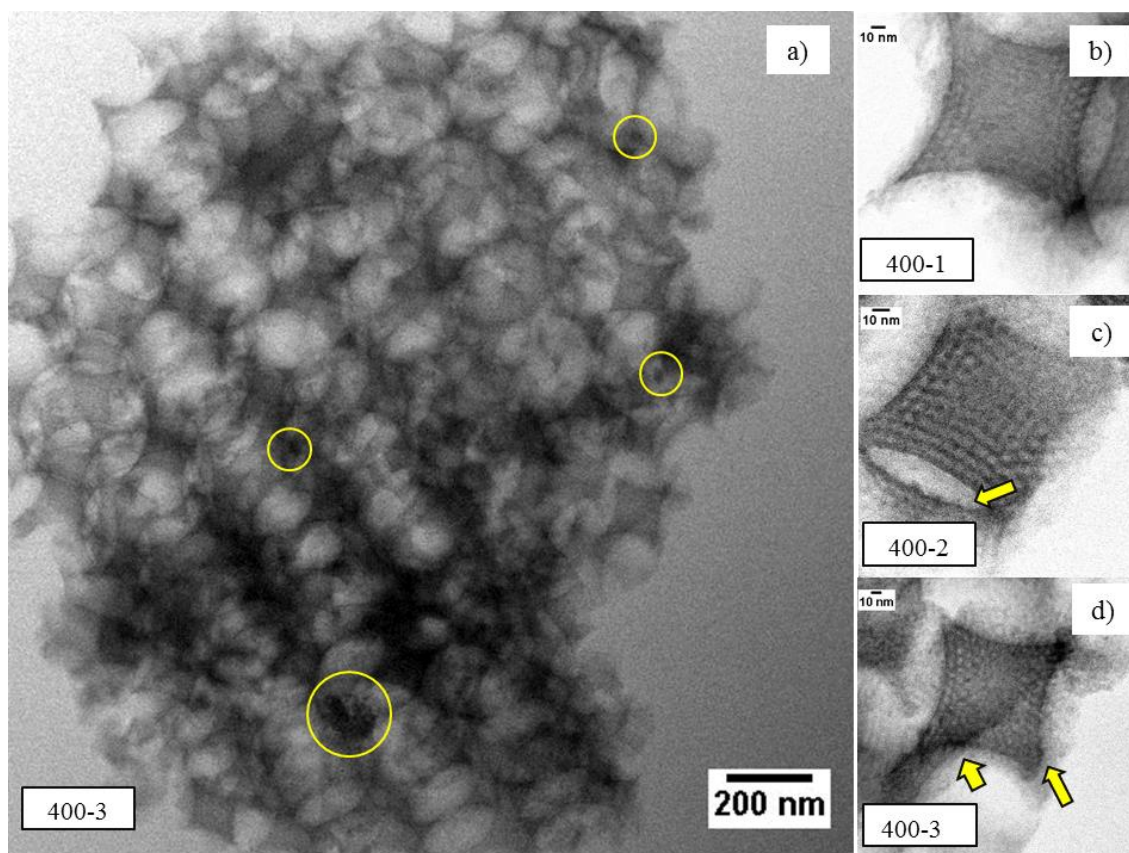


**Figure 4.22** Representative HRTEM images of MM-400 after titania 400-3 (a and d), 400-1 (b) and 400-2 (c).

#### 4.2.3.2.7 UV-vis diffuse reflectance spectroscopy

**Figure 4.23** shows DRUV-vis spectra of 10-23 wt. % TiO<sub>2</sub> grafted hierarchical macro-mesoporous silica support (MM-400). All the TiO<sub>2</sub> grafted MM-400 samples showed similar absorption in the UV region ( $\lambda \sim 300-390$  nm), with a red shift of band edge position ( $\lambda_{\max}$ ) depending by the titania content. (**Figure 4.23a**) As observed from the XRD wide angle (Section 4.2.3.2.4), the TiO<sub>2</sub> particle sizes rapidly increased even for a narrow range of TiO<sub>2</sub> loading.[29] **Figure 4.23b** reveals the spectra obtained by the Kubelka-Munk function for the evaluation of the band gaps, which were determined to be  $E_g \sim 3.1-3.2$  eV for all the TiO<sub>2</sub> grafted MM-400 samples. As mentioned earlier in this chapter (See **Section 4.2.3.1.7**), the hierarchical silica support MM-400 behaves as photonic crystal and also the photonic band gap (PBG) is affected by the TiO<sub>2</sub> loading.



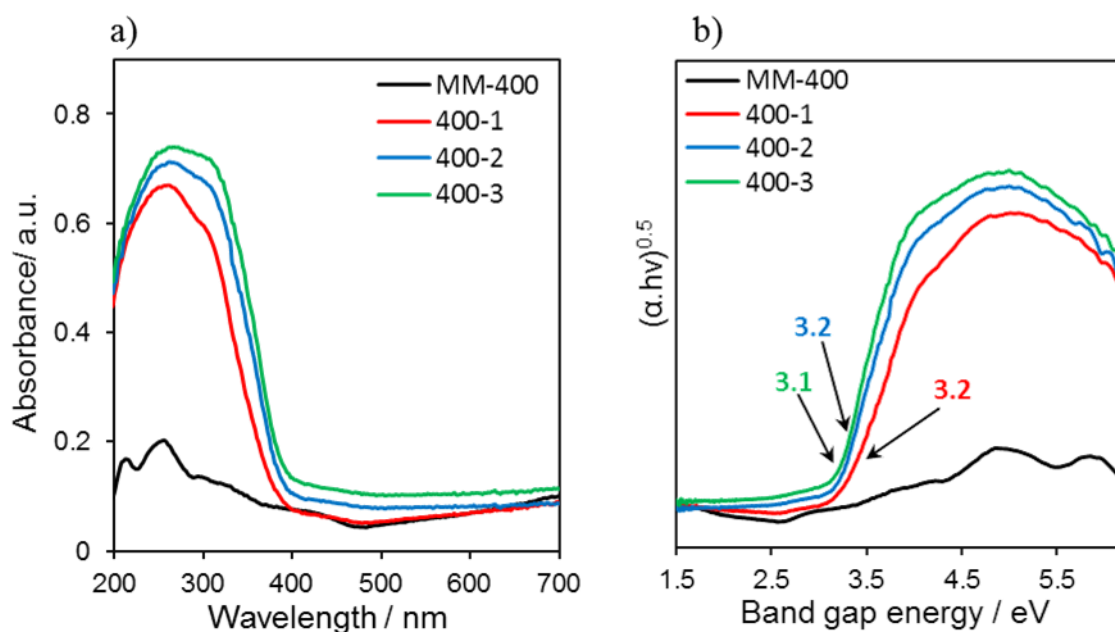


**Figure 4.23** Absorption spectra of all the  $\text{TiO}_2$  grafted MM-400 samples (a); Kubelka-Munk functions for the band gap evaluation (b).

Further diffuse reflectance spectra (%R) of the  $\text{TiO}_2$  grafted silica supports and the corresponding silica photonic crystal supports are shown in **Figure 4.24**.

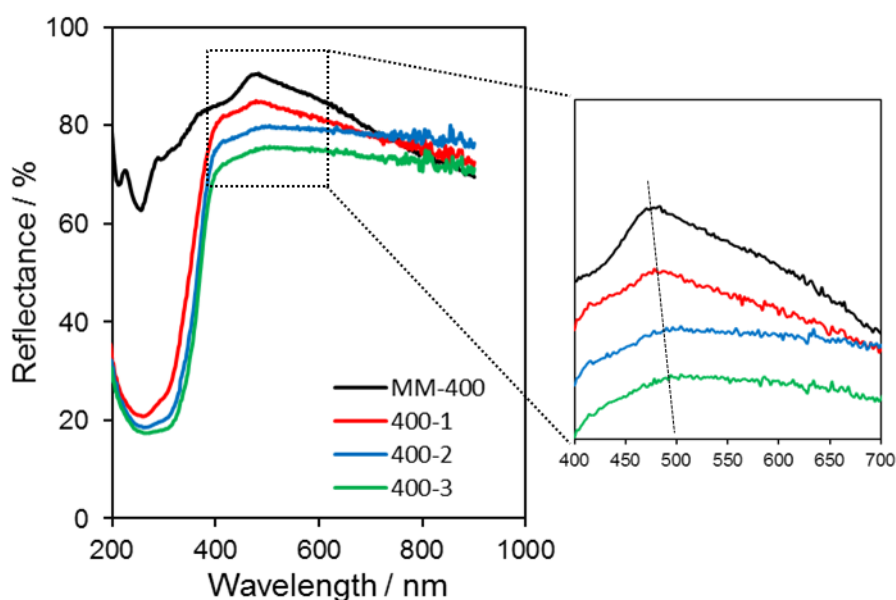


**Figure 4.24** Diffuse reflectance spectra (%R) of the  $\text{TiO}_2$  grafted MM-400 samples with different  $\text{TiO}_2$  loading and the corresponding support MM-400. The PBG region has been enhanced for clarity.

The PBG intensity was observed to significantly broaden and reduce with increasing titania loading, indicating a non-uniform coverage after the 1<sup>st</sup> grafting cycle, in agreement with the

porosimetry and XRD data. [19] However with respect to the bare support MM-400, increasing the  $\text{TiO}_2$  loading red shifts the PBG to longer wavelengths. (**Figure 4.25**) This red shift is related to the introduction of an increasing amount of  $\text{TiO}_2$ , characterized by an higher refractive index compared to the silica walls and the voids ( $n_{\text{TiO}_2} = 2.49 > n_{\text{SiO}_2} = 1.45 > n_{\text{air}} = 1$ ).

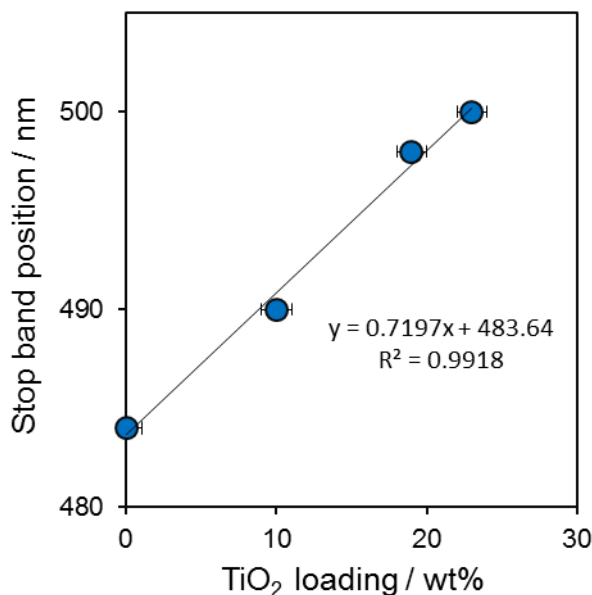


**Figure 4.25** The stop band position as a function of the titania loading.

The broadening of the PBG and the red shift of the electronic band gap ( $E_g$ ) with increasing of  $\text{TiO}_2$  loading can enhance the probability to have a slow photon effect as result of the overlap between the blue edges of the PBG and the absorption spectrum of the material. (**Figure 4.26**) The shaded area shows the wavelength range corresponding to the electronic state of  $\text{TiO}_2$  grafted MM-400 samples and the black arrow points to the expected region of slow photon formation at the blue edge of the PBG. It can be seen that the higher the loading the higher the probability to have slow photon effect due to the red shift of  $E_g$ . These results show that for ordered MM-400 support the photonic properties are retained and the shape and the position of the PBG can be tuned based on the  $\text{TiO}_2$  loading and the kind of coverage (i.e. nanoparticles deposition or uniform coating).

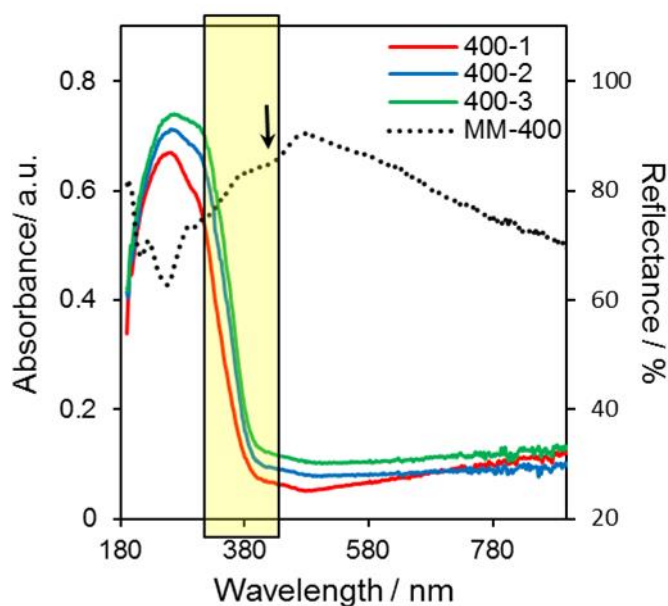


**Figure 4.26** Absorption spectra (primary y-axis) of the  $\text{TiO}_2$  grafted MM-400 samples and the reflectance spectra (secondary y-axis) for the correspondent support.

#### 4.2.4 Photocatalytic degradation of methyl orange (MO)

The photocatalytic activity of all the samples with different macropore diameters and titania loading were examined in the photodegradation of methyl orange, to correlate structural and photonic properties with the activity. The operational set-up and reaction conditions can be found in **Chapter 2**.

##### 4.2.4.1 Effect of macropores size

**Figure 4.27** shows degradation rate curves of samples synthesized by using three different PS template spheres (200, 400 and 600 nm) in comparison with that of the commercial P-25, the bulk anatase and the mesoporous grafted sample (Ti-SBA-15-7-1).

A blank experiment under UV was performed in the presence of the parent support MM-SBA-15 (MM-400) and the result obtained with meso SBA-15 is also reported for comparison. (See **Chapter 3**) The reaction profiles of the support with three different macropores shown the same trend and the reported values (black dots) are an average of the three experiments (MM-200/UV, MM-400/UV and MM-600/UV).

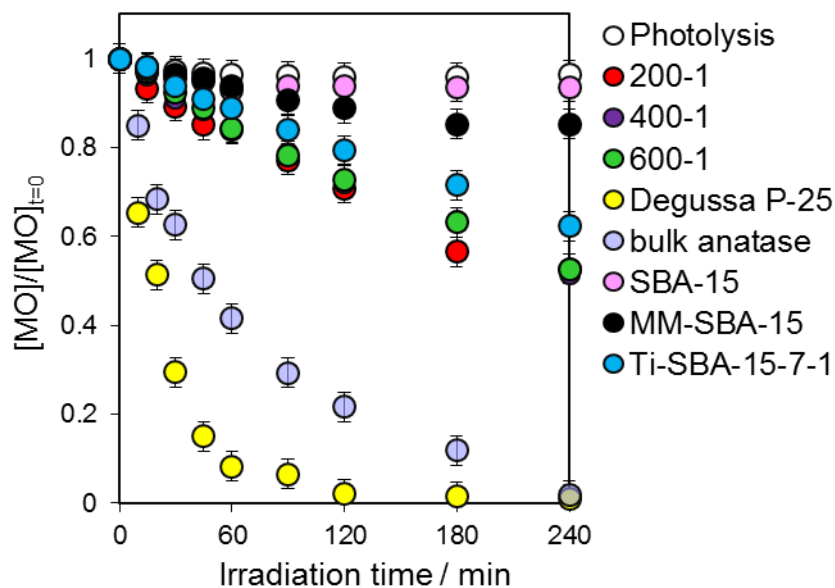


**Figure 4.27** Degradation of MO concentration with irradiation time over the three series of synthesized catalyst from supports with different macropores size, two references (bulk anatase and Degussa P-25) and two parent supports (MM-SBA-15 and SBA-15). Photolysis test of MO under UV without catalyst is also reported together with the comparison with the 1<sup>st</sup> grafting cycle on SBA-15-7.

**Figure 4.28** shows % of MO degradation during the irradiation time. The parent support shows a final percentage of MO degradation of 14%, significantly higher than the purely mesoporous SBA-15-7 (~6.4 %). (See Chapter 3)

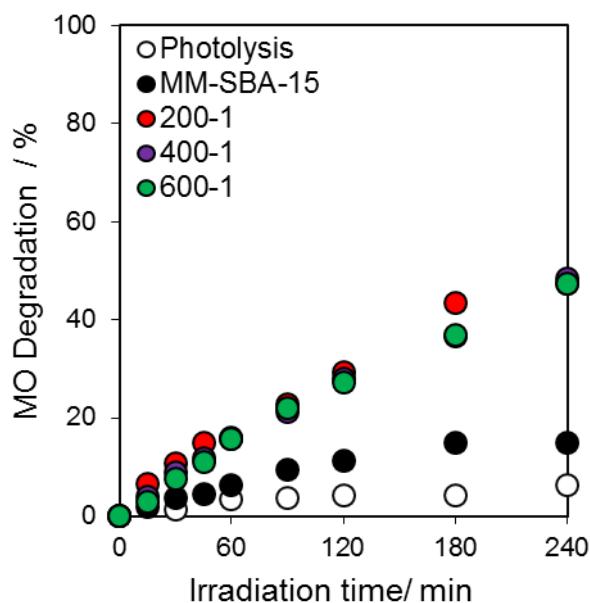


**Figure 4.28** Variation of the dye degradation rate with irradiation time of methyl orange solution for the grafted samples with different macropores size.

As explained in the previous chapter, despite the wide band gap, the silica surface is slightly photoactive in the far UV ( $E_g \sim 5.5$  eV) and it can generate electron-hole-pairs to initiate radical reactions starting from water and oxygen.[47, 48] The evaluated initial rate constants are the same for the two silica supports ( $\sim 19 \text{ ppm.h}^{-1}.\text{g}_{\text{cat}}^{-1}$ ) but the hierarchical SBA-15 showed the highest final percentage of MO degradation most probably due to the differences in structural and optical properties of the two samples.

Although the highest surface area, the catalytic behaviour of the mesoporous SBA-15 is influenced by the accessibility of the compounds to site of radical production. The long diffusion path and small size of the pores could explain the lower percentage of MO degradation compare to the hierarchical MM-SBA-15.[49, 50] The introduction of macropore inside the ordered mesoporous generated the formation of many apertures and short mesoporous channels, which are effective for improving the diffusion of the reactant. In addition the open structure of the MM-SBA-15 also has a better response to light, improving the probability of electron-hole pair formation and thus of active centres for radical attacks. On the other hand, the reaction profiles of the three grafted hierarchical catalysts show a similar photocatalytic performances, with final degradation of  $\sim 47\%$  after four hours of irradiation. The same trend was observed for the initial rate ( $r^0$ ).

**Figure 4.29a** depicts the evaluated  $r^0$  as function of the macropore diameters in comparison with the Ti-SBA-15-7-1 mesoporous catalyst, with comparable mesopore size ( $\sim 6.8$  nm) and  $\text{TiO}_2$  loading ( $\sim 10$  wt. %).

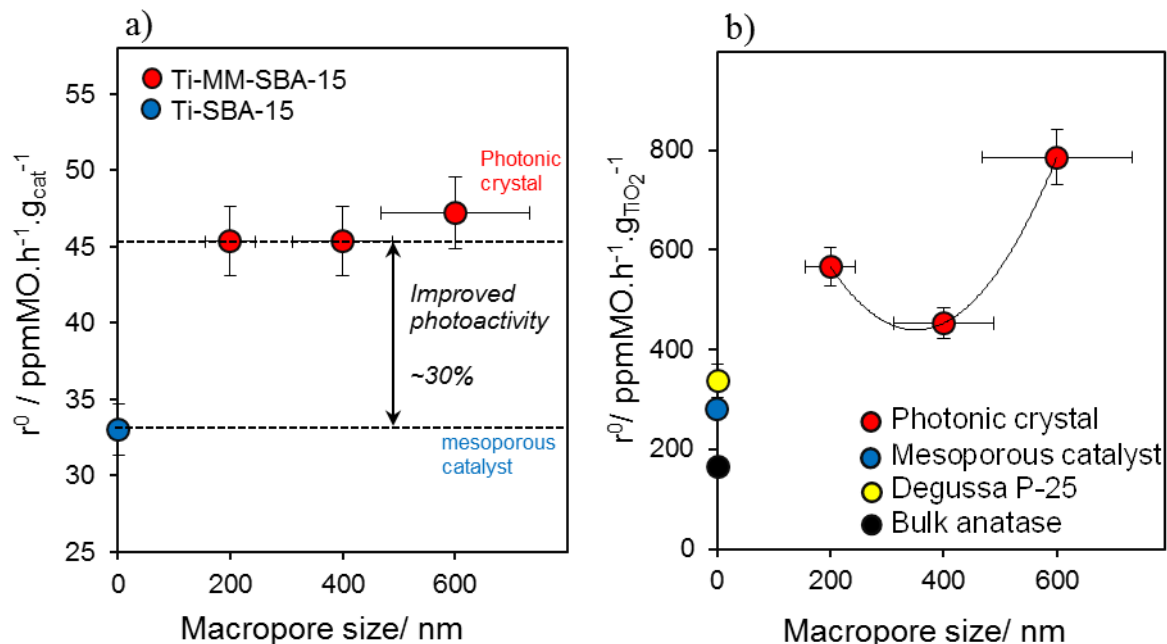


**Figure 4.29** Initial rate ( $r^0$ ) normalised for the mass of catalyst (a) and the mass of  $\text{TiO}_2$  (b) as function of the macropore diameters.

The hierarchical structure of these TiO<sub>2</sub> grafted photonic crystal provides an enhancement of the photocatalytic performance of about ~30% compared to the TiO<sub>2</sub> grafted mesoporous SBA-15. The photocatalytic enhancement of the MO degradation is clearly affected by the structural and optical differences of the two families of support used for the TiO<sub>2</sub> photocatalyst. In the first place the catalytic performance is influenced by the accessibility of compounds to the active sites and for the hierarchical catalysts the highly ordered channels possess high connectivity which efficiently facilitates the mass transport. Secondly the enhancement of light harvesting resulting from photonic crystal structure must be considered. The relative position of the stop band (PBG) and the slow photon (SP) is crucial to have a real contribution on the photocatalytic performance of the catalysts. [37] For example, if the high reflectivity due to the PBG is centred in the region of strong absorption of TiO<sub>2</sub>, the reflection can be disadvantageous as the photons suitable for the reaction tend to be reflected instead of absorbed to form e<sup>-</sup>/h<sup>+</sup> pair, mandatory step to initiate the photocatalytic process. However for the three samples the maximum of the PBG is located in the visible region, so the wavelength range of strong light absorption of TiO<sub>2</sub> is avoided and the slow photon effect can be still considered as a contributor to the overall process.

Normalizing for the amount of the active phase present on each support (grams of TiO<sub>2</sub> evaluated from the XRF analysis), it can be seen that  $r^0$  first decreases and then increases with macropore size. (**Figure 4.29b**) The initial rate follows the trend: 400-1 < 200-1 < 600-1. For the samples 200-1 and 600-1, the edge of the stop band of the support overlaps the absorption region of the active phase and the slowing of the photons is expected to occur. [51] (See **Figure 4.16a**) Slow photons leads to an increasing of light absorption, consequently contributing to a higher photocatalytic activity.[7] Furthermore the 600-1 sample demonstrates the best initial rate probably due to the lowest reflectivity in the light absorption region of TiO<sub>2</sub> compared to the 200-1 catalyst. Finally the initial rates normalised for the mass of active sites indicate that the hierarchical catalysts exhibit even higher photoactivity than the commercial P-25 and bulk anatase. This is probably owed to a combination of highly dispersed nanocrystals on high surface area (~300 m<sup>2</sup>.g<sup>-1</sup>), excellent accessibility to the active phase, enhanced of light harvesting due to the well-ordered macroporous structure and its photonic properties.

#### 4.2.4.2 Effect of titania loading

The reduction of MO concentration vs. irradiation time over the series of composites under UV-vis irradiation is presented in **Figure 4.30**.

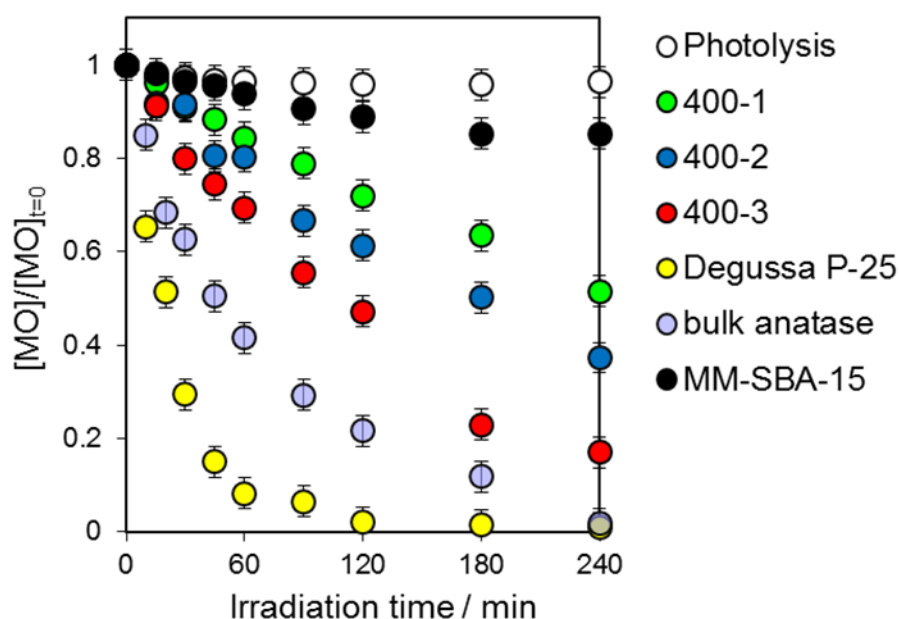


**Figure 4.30** Degradation of MO concentration with irradiation time over the three TiO<sub>2</sub>-grafted catalysts from the support MM-400, two references (bulk anatase and Degussa P-25) and the parent support. Photolysis test of MO under UV without catalyst is also reported.

The photocatalytic degradation of MO with TiO<sub>2</sub> P-25 and bulk anatase were conducted for comparison, and the direct photolysis of MO without any catalyst served as a control test. The loss of MO was around 50% after 4 h of irradiation in presence of the catalyst with the lowest loading of TiO<sub>2</sub> (~10 wt. %). Among the three catalysts, the 3<sup>rd</sup> grafting cycle (~30 wt. % TiO<sub>2</sub>) exhibited the most powerful photocatalytic activity with a degradation efficiency of 83%. (**Figure 4.31**)

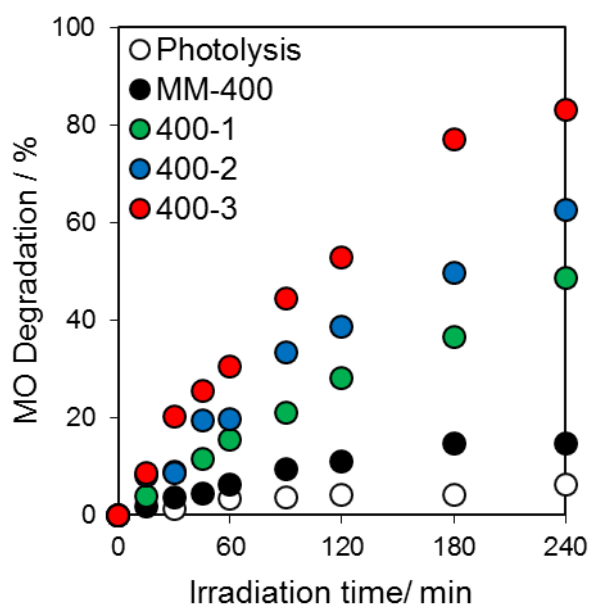


**Figure 4.31** Variation of the dye degradation rate with irradiation time of methyl orange solution for the grafted samples with different TiO<sub>2</sub> loading, the MM-400 support and UV-vis test.

Comparison of the photocatalytic performances of mesoporous and hierarchical series of catalysts is shown in **Figure 4.32a**, where the initial rate ( $r^0$ ) is plotted as a function of the  $\text{TiO}_2$  loading. Between these two families of materials, the macro/meso-porous structures have a large influence on the photocatalytic activity. It can be noticed that already for the lowest loading ( $\leq 10$  wt. %  $\text{TiO}_2$ ) the trend is  $400-1$  ( $r^0 \sim 45 \text{ ppm MO.h}^{-1}.\text{g}^{-1}$ )  $>$   $\text{Ti-SBA-15-7-1}$  ( $r^0 \sim 33 \text{ ppm MO.h}^{-1}.\text{g}^{-1}$ ). For the second grafting cycle ( $\sim 20$  wt. %  $\text{TiO}_2$ ), this difference between the two systems markedly increases, thus the activity for the hierarchical catalyst is higher of a factor of 1.5. Following this trend, the 3<sup>rd</sup> grafting cycle ( $\text{TiO}_2 \geq 20$  wt. %) the hierarchical catalyst reached the highest initial rate value ( $r^0 \sim 90 \text{ ppm MO.h}^{-1}.\text{g}^{-1}$ ) over the all mesoporous family of catalysts. Consequently, the combined structure of ordered mesoporous and hierarchical macroporous architectures exhibited greater photocatalytic performance among the mesoporous catalysts due to the combination of structural and optical properties. On one hand the bimodal macro-mesoporous architecture provide a solution for the mass transport limitation encountered in the treatment of waste water containing big molecular size compounds. The MO molecule ( $\sim 1.2$  nm) can easily access to the active sites present in the macropores, breaking down in smaller products that can consequentially diffuse faster inside the mesopores proceeding in the photooxidation process. On the other hand the ordered macroporosity provides an enhancement of light harvesting through the photonic crystal properties, while retaining a considerably high surface area ( $\sim 300 \text{ m}^2.\text{g}^{-1}$ ) due to the presence of the mesoporous structure. As mentioned in the previous chapter, a proper comparison between the synthesized materials and the bulk references suffers from an intrinsic level of difficulty. The initial rates of MO degradation normalized for  $\text{TiO}_2$  mass present in each catalyst are reported in **Figure 4.32b**. The results show that the more efficient photocatalysts is obtained when  $\text{TiO}_2$  is dispersed on the hierarchical SBA-15, due to the unique structural and optical properties of the support. The normalised activity of 400-1 and 400-3 results to be even higher of the commercial Degussa P-25.



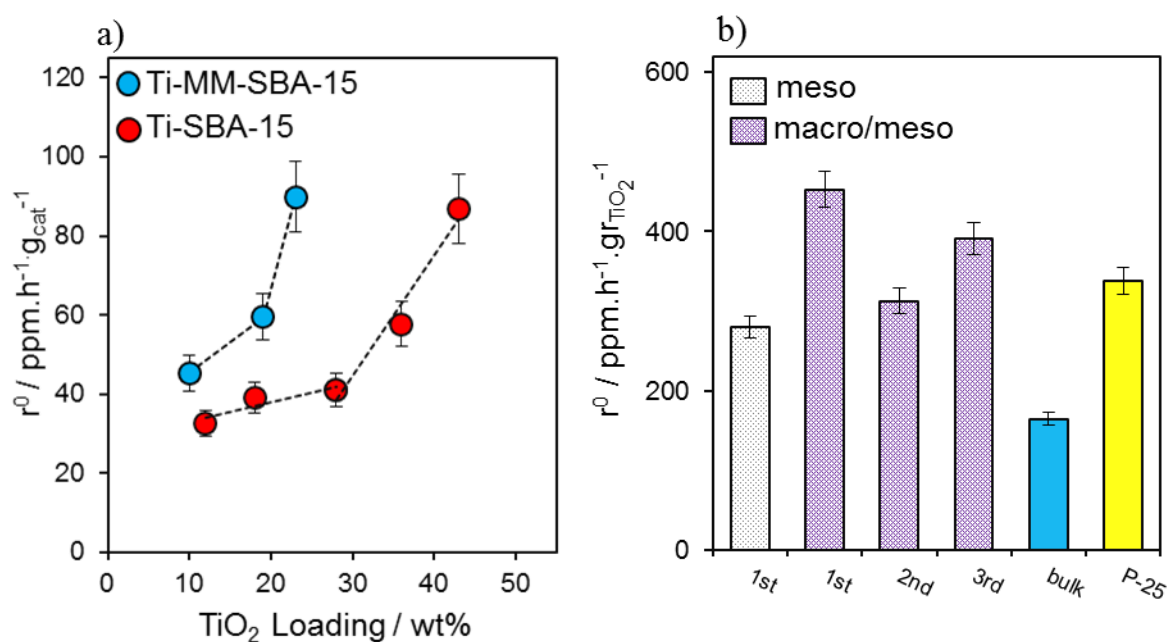


**Figure 4.32** Initial rate ( $r^0$ ) of MO degradation normalised for the mass of catalyst as function of the TiO<sub>2</sub> loading for the two families of catalyst (meso and macro/meso TiO<sub>2</sub>-coated SBA-15) (a); initial rate ( $r^0$ ) normalised for the mass of TiO<sub>2</sub> (b).

### 4.3 Conclusions

In this chapter the successful generation of hierarchical SBA-15 through TLCT method was demonstrated. The macropore size was tuned with three different PS beads size and two series of titania based photocatalysts were synthesised by grafting procedure.

Firstly, the macropore size effect (200, 400 and 600 nm) was investigated and on each support a single grafting cycle was performed in order to obtain similar titania loading (~10 wt. %). The three catalysts were fully characterised and their activity tested on the photodegradation of MO. It was found that introducing the hierarchical structure markedly increases the photocatalytic activity of the composite samples of about ~30 % compared to the mesoporous catalysts. However among the series with different macropores, the differences in the photocatalytic were mainly attributed to optical properties of the supports, which are proper inverse opals photonic crystals. Their photonic band gap (PBG) was dependent on the voids volume and the probability of slow photon effect was found to be higher for the 200-1 and 600-1 samples where the blue edge overlaps with the electronic band gap of the deposited TiO<sub>2</sub>. Therefore a further study was performed on the MM-400 support to investigate the effect of the TiO<sub>2</sub> loading on the optical properties and catalytic performances of the composite materials.

Hence, a second family of photocatalyst was synthesized applying three times the grafting method on the chosen support in order to obtain a range of TiO<sub>2</sub> loading of 10-23 wt. %. DR-UV data showed a change in the PBG together with the red shift of the electronic band gap with the

increasing of TiO<sub>2</sub> loading. Modification of optical properties leads to an increasing of the efficiency in the photocatalytic oxidation of MO and the results show that the most active catalysts resulted to be 400-3 with the highest TiO<sub>2</sub> loading.

#### 4.4 References

- [1] A. Galarneau, H. Cambon, F. Di Renzo, R. Ryoo, M. Choi, and F. Fajula, "Microporosity and connections between pores in SBA-15 mesostructured silicas as a function of the temperature of synthesis," *New Journal of Chemistry*, vol. 27, pp. 73-79, 2003.
- [2] T. Kamegawa, Y. Ishiguro, H. Seto, and H. Yamashita, "Enhanced photocatalytic properties of TiO<sub>2</sub>-loaded porous silica with hierarchical macroporous and mesoporous architectures in water purification," *Journal of Materials Chemistry A*, vol. 3, pp. 2323-2330, 2015.
- [3] W. Wei, C. Yu, Q. Zhao, G. Li, and Y. Wan, "Improvement of the Visible-Light Photocatalytic Performance of TiO<sub>2</sub> by Carbon Mesostructures," *Chemistry – A European Journal*, vol. 19, pp. 566-577, 2013.
- [4] T. Kamegawa, D. Yamahana, and H. Yamashita, "Graphene Coating of TiO<sub>2</sub> Nanoparticles Loaded on Mesoporous Silica for Enhancement of Photocatalytic Activity," *The Journal of Physical Chemistry C*, vol. 114, pp. 15049-15053, 2010/09/09 2010.
- [5] J. Dhainaut, J.-P. Dacquin, A. F. Lee, and K. Wilson, "Hierarchical macroporous-mesoporous SBA-15 sulfonic acid catalysts for biodiesel synthesis," *Green Chemistry*, vol. 12, pp. 296-303, 2010.
- [6] J. I. L. Chen and G. A. Ozin, "Tracing the Effect of Slow Photons in Photoisomerization of Azobenzene," *Advanced Materials*, vol. 20, pp. 4784-4788, 2008.
- [7] M. Wu, Y. Li, Z. Deng, and B. L. Su, "Three-Dimensionally Ordered Macroporous Titania with Structural and Photonic Effects for Enhanced Photocatalytic Efficiency," *ChemSusChem*, vol. 4, pp. 1481-1488, 2011.
- [8] R. C. Schroden, M. Al-Daous, C. F. Blanford, and A. Stein, "Optical Properties of Inverse Opal Photonic Crystals," *Chemistry of Materials*, vol. 14, pp. 3305-3315, 2002/08/01 2002.
- [9] H. Chen, S. Chen, X. Quan, and Y. Zhang, "Structuring a TiO<sub>2</sub>-Based Photonic Crystal Photocatalyst with Schottky Junction for Efficient Photocatalysis," *Environmental Science & Technology*, vol. 44, pp. 451-455, 2010/01/01 2010.
- [10] A. Stein and R. C. Schroden, "Colloidal crystal templating of three-dimensionally ordered macroporous solids: materials for photonics and beyond," *Current Opinion in Solid State & Materials Science*, vol. 5, pp. 553-564, Dec 2001.
- [11] A. Stein, B. E. Wilson, and S. G. Rudisill, "Design and functionality of colloidal-crystal-templated materials-chemical applications of inverse opals," *Chemical Society Reviews*, vol. 42, pp. 2763-2803, 2013.

- [12] T. Kamegawa, Y. Kuwahara, and H. Yamashita, "Design of TiO<sub>2</sub>-loaded Porous Siliceous Materials and Application to Photocatalytic Environmental Purification," *Journal of the Japan Petroleum Institute*, vol. 59, pp. 165-173, Sep 2016.
- [13] J. I. L. Chen, G. von Freymann, S. Y. Choi, V. Kitaev, and G. A. Ozin, "Amplified photochemistry with slow photons," *Advanced Materials*, vol. 18, pp. 1915-+, Jul 18 2006.
- [14] J. I. L. Chen, G. von Freymann, V. Kitaev, and G. A. Ozin, "Effect of Disorder on the Optically Amplified Photocatalytic Efficiency of Titania Inverse Opals," *Journal of the American Chemical Society*, vol. 129, pp. 1196-1202, 2007/02/01 2007.
- [15] J. I. L. Chen, E. Loso, N. Ebrahim, and G. A. Ozin, "Synergy of slow photon and chemically amplified photochemistry in platinum nanocluster-loaded inverse titania opals," *Journal of the American Chemical Society*, vol. 130, pp. 5420-+, Apr 23 2008.
- [16] J. Liu, M. Li, J. Wang, Y. Song, L. Jiang, T. Murakami, *et al.*, "Hierarchically Macro-/Mesoporous Ti-Si Oxides Photonic Crystal with Highly Efficient Photocatalytic Capability," *Environmental Science & Technology*, vol. 43, pp. 9425-9431, 2009/12/15 2009.
- [17] Y. Lu, H. Yu, S. Chen, X. Quan, and H. Zhao, "Integrating Plasmonic Nanoparticles with TiO<sub>2</sub> Photonic Crystal for Enhancement of Visible-Light-Driven Photocatalysis," *Environmental Science & Technology*, vol. 46, pp. 1724-1730, 2012/02/07 2012.
- [18] S. G. Meng, D. Z. Li, P. Wang, X. Z. Zheng, J. X. Wang, J. Chen, *et al.*, "Probing photonic effect on photocatalytic degradation of dyes based on 3D inverse opal ZnO photonic crystal," *Rsc Advances*, vol. 3, pp. 17021-17028, 2013.
- [19] R. Mitchell, R. Brydson, and R. E. Douthwaite, "Homogeneous coating of photonic macroporous oxides with inorganic nanocrystals," *Nanoscale*, vol. 6, pp. 4043-4046, 2014.
- [20] S. G. Wainwright, C. Parlett, R. A. Blackley, W. Zhou, A. F. Lee, K. Wilson, *et al.*, "True liquid crystal templating of SBA-15 with reduced microporosity," *Microporous and Mesoporous Materials*, vol. 172, pp. 112-117, 5/15 2013.
- [21] S. Vaudreuil, M. Bousmina, S. Kaliaguine, and L. Bonnevot, "Synthesis of Macrostructured Silica by Sedimentation-Aggregation," *Advanced Materials*, vol. 13, pp. 1310-1312, 2001.
- [22] C. M. A. Parlett, M. A. Isaacs, S. K. Beaumont, L. M. Bingham, N. S. Hondow, K. Wilson, *et al.*, "Spatially orthogonal chemical functionalization of a hierarchical pore network for catalytic cascade reactions," *Nat Mater*, vol. 15, pp. 178-182, 02//print 2016.
- [23] K. S. W. Sing, D. H. Everett, R. A. W. Haul, L. Moscou, R. A. Pierotti, J. Rouquerol, *et al.*, "Reporting Physisorption Data for Gas Solid Systems with Special Reference to the Determination of Surface-Area and Porosity (Recommendations 1984)," *Pure and Applied Chemistry*, vol. 57, pp. 603-619, 1985.
- [24] C. M. A. Parlett, P. Keshwalla, S. G. Wainwright, D. W. Bruce, N. S. Hondow, K. Wilson, *et al.*, "Hierarchically Ordered Nanoporous Pd/SBA-15 Catalyst for the Aerobic Selective

- Oxidation of Sterically Challenging Allylic Alcohols," *ACS Catalysis*, vol. 3, pp. 2122-2129, 2013/09/06 2013.
- [25] T.-W. Kim, R. Ryoo, M. Kruk, K. P. Gierszal, M. Jaroniec, S. Kamiya, *et al.*, "Tailoring the Pore Structure of SBA-16 Silica Molecular Sieve through the Use of Copolymer Blends and Control of Synthesis Temperature and Time," *The Journal of Physical Chemistry B*, vol. 108, pp. 11480-11489, 2004/08/01 2004.
- [26] T. Sen, G. J. T. Tiddy, J. L. Casci, and M. W. Anderson, "Synthesis and Characterization of Hierarchically Ordered Porous Silica Materials," *Chemistry of Materials*, vol. 16, pp. 2044-2054, 2004/06/01 2004.
- [27] R. Castillo, B. Koch, P. Ruiz, and B. Delmon, "Influence of Preparation Methods on the Texture and Structure of Titania-Supported on Silica," *Journal of Materials Chemistry*, vol. 4, pp. 903-906, Jun 1994.
- [28] D. H. Sun, Z. M. Liu, J. He, B. X. Han, H. L. Zhang, and Y. Huang, "Surface sol-gel modification of mesoporous silica molecular sieve SBA-15 with TiO<sub>2</sub> in supercritical CO<sub>2</sub>," *Microporous and Mesoporous Materials*, vol. 80, pp. 165-171, May 2 2005.
- [29] G. Lassaletta, A. Fernandez, J. P. Espinos, and A. R. Gonzalez-Elipe, "Spectroscopic characterization of quantum-sized TiO<sub>2</sub> supported on silica: influence of size and TiO<sub>2</sub>-SiO<sub>2</sub> interface composition," *The Journal of Physical Chemistry*, vol. 99, pp. 1484-1490, 1995/02/01 1995.
- [30] M. Q. Wang, B. Gong, X. Yao, Y. P. Wang, and R. N. Lamb, "Preparation and microstructure properties of Al-doped TiO<sub>2</sub>-SiO<sub>2</sub> gel-glass film," *Thin Solid Films*, vol. 515, pp. 2055-2058, Dec 5 2006.
- [31] N. X.-R. P. s. database, "NIST Standard Reference Database 20, Version 3.5.: p. [online] Available at: < <http://srdata.nist.gov/xps/>> ", ed, 2003.
- [32] P. Van Der Voort, M. Benjelloun, and E. F. Vansant, "Rationalization of the Synthesis of SBA-16: Controlling the Micro- and Mesoporosity," *The Journal of Physical Chemistry B*, vol. 106, pp. 9027-9032, 2002/09/01 2002.
- [33] K. Thamaphat, P. Limsuwan, and B. Ngotawornchai, "Phase characterization of TiO<sub>2</sub> powder by XRD and TEM."
- [34] G. I. N. Waterhouse and M. R. Waterland, "Opal and inverse opal photonic crystals: Fabrication and characterization," *Polyhedron*, vol. 26, pp. 356-368, 1/22/ 2007.
- [35] F. Marlow, Muldarisnur, P. Sharifi, R. Brinkmann, and C. Mendive, "Opals: Status and Prospects," *Angewandte Chemie-International Edition*, vol. 48, pp. 6212-6233, 2009.
- [36] A. Mihi, F. J. López-Alcaraz, and H. Míguez, "Full spectrum enhancement of the light harvesting efficiency of dye sensitized solar cells by including colloidal photonic crystal multilayers," *Applied Physics Letters*, vol. 88, p. 193110, 2006.

- [37] M. Curti, J. Schneider, D. W. Bahnemann, and C. B. Mendive, "Inverse Opal Photonic Crystals as a Strategy to Improve Photocatalysis: Underexplored Questions," *Journal of Physical Chemistry Letters*, vol. 6, pp. 3903-3910, Oct 1 2015.
- [38] M. Wu, J. Liu, J. Jin, C. Wang, S. Z. Huang, Z. Deng, *et al.*, "Probing significant light absorption enhancement of titania inverse opal films for highly exalted photocatalytic degradation of dye pollutants," *Applied Catalysis B-Environmental*, vol. 150, pp. 411-420, May 5 2014.
- [39] I. Georgiadou, N. Spanos, C. Papadopoulou, H. Matralis, C. Kordulis, and A. Lycourghiotis, "Preparation and characterization of various titanias (anatase) used as supports for vanadia-supported catalysts," *Colloids and Surfaces A: Physicochemical and Engineering Aspects*, vol. 98, pp. 155-165, 5/12/ 1995.
- [40] R. Castillo, B. Koch, P. Ruiz, and B. Delmon, "Influence of preparation methods on the texture and structure of titania supported on silica," *Journal of Materials Chemistry*, vol. 4, pp. 903-906, 1994.
- [41] P. Webb, C. Orr, and C. Micromeritics Instrument, *Analytical methods in fine particle technology*. Norcross, Ga.: Micromeritics Instrument Corp., 1997.
- [42] X.-C. Guo and P. Dong, "Multistep Coating of Thick Titania Layers on Monodisperse Silica Nanospheres," *Langmuir*, vol. 15, pp. 5535-5540, 1999/08/01 1999.
- [43] G. N. P. Scherrer, 1918, 2, 98, 1918.
- [44] F. X. Zhang, X. Carrier, J. M. Krafft, Y. Yoshimura, and J. Blanchard, "Insight into the structure and localization of the titania overlayer in TiO<sub>2</sub>-coated SBA-15 materials," *New Journal of Chemistry*, vol. 34, pp. 508-516, 2010.
- [45] R. L. Orefice and W. L. Vasconcelos, "Sol-gel transition and structural evolution on multicomponent gels derived from the alumina-silica system," *Journal of Sol-Gel Science and Technology*, vol. 9, pp. 239-249, 1997.
- [46] V. Zelenák, V. Hornebecq, S. Mornet, O. Schäf, and P. Llewellyn, "Mesoporous Silica Modified with Titania: Structure and Thermal Stability," *Chemistry of Materials*, vol. 18, pp. 3184-3191, 2006/07/01 2006.
- [47] J. C. Yu, J. G. Yu, and J. C. Zhao, "Enhanced photocatalytic activity of mesoporous and ordinary TiO<sub>2</sub> thin films by sulfuric acid treatment," *Applied Catalysis B-Environmental*, vol. 36, pp. 31-43, Feb 8 2002.
- [48] L. Skuja, "Time-Resolved Low-Temperature Luminescence of Nonbridging Oxygen Hole-Centers in Silica Glass," *Solid State Communications*, vol. 84, pp. 613-616, Nov 1992.
- [49] K. Egeblad, C. H. Christensen, M. Kustova, and C. H. Christensen, "Templating mesoporous zeolites," *Chemistry of Materials*, vol. 20, pp. 946-960, Feb 12 2008.
- [50] M. Choi, K. Na, J. Kim, Y. Sakamoto, O. Terasaki, and R. Ryoo, "Stable single-unit-cell nanosheets of zeolite MFI as active and long-lived catalysts," *Nature*, vol. 461, pp. 246-U120, Sep 10 2009.

- [51] A. Imhof, W. L. Vos, R. Sprik, and A. Lagendijk, "Large Dispersive Effects near the Band Edges of Photonic Crystals," *Physical Review Letters*, vol. 83, pp. 2942-2945, 10/11/ 1999.

## *Chapter 5*

*In situ ATR IR study of liquid phase  
propanoic acid photooxidation on  
TiO<sub>2</sub> nanoparticles*

## 5 In situ ATR IR study of liquid phase propanoic acid photooxidation on TiO<sub>2</sub> nanoparticles

### 5.1 Introduction

**Chapter 3** and **4** were focused on developing nanostructured photocatalysts with the aim of maximising the activity of titania supported on silica by increasing the surface area, improving the molecular/diffusion transfer and enhanced the light harvesting.

However the development of a successful photocatalyst requires not only detailed understanding of material's structure and its performance, but also a more detailed investigation of the reaction mechanism at the catalyst surface. In heterogeneous photocatalysis it is, therefore, of crucial importance to understand the processes that take place at solid-liquid interfaces. In light of this infrared (IR) spectroscopy is a powerful tool to investigate interfacial chemistry in heterogeneous systems and the attenuated total reflection (ATR) sampling method allows for investigation of the adsorption of organic molecules onto a metal oxide surface under a wide range of conditions.

In this chapter the photodegradation of propionic acid over different titania nanoparticles was investigated by *in-situ* attenuated total reflection infrared (ATR-IR) spectroscopy in a flow-through cell. The aim of the presented study is to validate a methodology to explore the solid-liquid interface in a time-resolved manner during photocatalytic decomposition of organic molecules. The biggest asset of the use of *in-situ* techniques is the fact that the properties of an interface during the process of interest may be drastically different from the properties determined prior to, or post-reaction. However IR spectroscopic methods are difficult to apply to solid – liquid and in particular solid – water interfaces due to the strong IR absorption of the solvent.

The reliability of information obtained from the IR spectra is dependent mainly upon the correct assignment of the vibrational modes by comparison with published spectroscopic data and computational studies.[1, 2] Several experimental and theoretical studies on the adsorption of aliphatic mono- and di-carboxylic acids on metal oxide surfaces have been performed.[3] Di-carboxylic acids are the most widely studied because they adsorb much more strongly to oxide surfaces due to both electrostatic and chemical interactions and the ability to form bridging or chelating adsorption structures.[2, 4-7] Oxalic acid is the simplest polyacid molecule and its adsorption on metal oxide has been studied in a wide range of experimental conditions (pH, concentration, temperature)

Hug et al. [2] studied the adsorption of oxalic acid on P-25 identifying several surface complexes in a bidentate bridging or monodentate modes with surface Ti<sup>4+</sup> sites and focusing their study on the measurement of adsorbed oxalate to plot an isotherm curve. A similar study was performed by Young et al. [4], they use pure anatase to investigate the adsorption/desorption kinetics of oxalic acid and extract the pseudo-first-order rate constants corresponding to the three expected adsorbed species: monodentate and bidentate, in bridging and chelating configuration.



Subsequently, Mendive et al. published several papers introducing the study of photodegradation of oxalic acid over different titania phases, combining spectroscopy and theoretical investigation.[6, 8] Furthermore, they also propose the mechanism of oxidation under UV (A) with the possible photo-induced surface complexes and reaction pathway.[7, 9] These works highlight the importance of the strong relation between species which form on the surface in the dark and the overall reaction pathway. However all of these investigations were performed using a simple and well-known model compound in oxalic acid. In the past ten years, similar studies have also been performed using more complex molecules. For example, Dolamic and Burgi [10] introduced the investigation on di-carboxylic acids using a combination of ATR-IR spectroscopy, modulation excitation spectroscopy and isotope labelling to study the mechanism of mineralization over TiO<sub>2</sub> P-25 under UV(A) irradiation. They found that the photooxidation of malonic acid adsorbed to the TiO<sub>2</sub> surface as malonate can follow two routes: one ends up in an oxalate before reaching the complete mineralization to CO<sub>2</sub>, the other one leads to the formation of acetic acid after the first photo-Kolbe reaction, which easily desorbs from the surface without being further oxidized.

Analogous to this study, more recent investigations were also performed on several monocarboxylic acids (i.e. formic acid or acetic acid). The resulting IR signals were found to be weaker due to the single-site attack of the probe molecule and for this reason most of these studies were undertaken in the gas phase, with an additional investigation of water-surface interactions.[11-13] Mattson and Osterlund [14] studied the adsorption and photoinduced decomposition of acetone and acetic acid on anatase, brookite, and rutile TiO<sub>2</sub> Nanoparticles. The in-situ FTIR transmission in gas-solid phase was used to define the spectral change under UV (A) irradiation on the different titania phases which suggested a TiO<sub>2</sub> phase-dependent reaction pathways.

Several studies were performed with acetic and formic acid and were also supported by DFT calculations. Liao et al.[15] determined that molecular acetic acid and acetate groups adsorbed onto TiO<sub>2</sub> surfaces, the first by H-bonding or Lewis acid-base interaction and the latter by chemical bidentate bonding. Based on the detected adsorbed species they proposed a reaction mechanism of acetic acid photodegradation and the effect of water addition was investigated to mimic the reaction in the solution phase. CO<sub>2</sub> was detected as a photoproduct in the UV irradiation of surface acetate and in the presence of water; some surface acetate was converted into acetic acid.

Similar results were founded by Nanayakkera et al.[16] They focused on the understanding of formic acid adsorption on TiO<sub>2</sub> nanoparticles, and especially on the effect of relative humidity and adsorbed water on surface coordination, adsorption kinetics, and the rate of photooxidation of adsorbed formate. Their results showed that gas-phase formic acid adsorbs dissociatively on TiO<sub>2</sub> forming adsorbed formate mainly in a bridged bidentate coordination. Co-adsorbed water changes the coordination of formate to solvated, monodentate formate and this will make carbon dioxide formation favourable in the presence of water vapor.

This observation was confirmed and supported by the computational results of Miller et al. [17] They found that monodetate formate and adsorbed water favour the oxidation at the hole sites of  $\text{TiO}_2$ , increasing the reduction rate of oxygen by the electrons in the conduction band. This will produce a great number of radical species, enhancing the mineralization rate of formic acid to  $\text{CO}_2$  and water. There is not yet a general agreement on the mechanism of the adsorption of organic molecules and water on  $\text{TiO}_2$  surfaces and the following photodegradation mechanism and for this reason the best approach to understand this complex system is to combine the experimental results obtained by ATR-FTIR spectroscopy and other techniques.

Several studies have been reported in the literature regarding the application of IR techniques in photocatalytic systems but the ATR *in-situ* spectroscopy in a liquid-solid phase is still not widely studied due to difficulties relating to setting the optimal working conditions and correctly processing and assigning the vibrational modes in the final spectra. In this chapter, a full investigation of propanoic acid degradation over  $\text{TiO}_2$  is reported. A schematic drawing of the experimental setup for solid-liquid interface investigations is shown in the **Figure 5.1**.

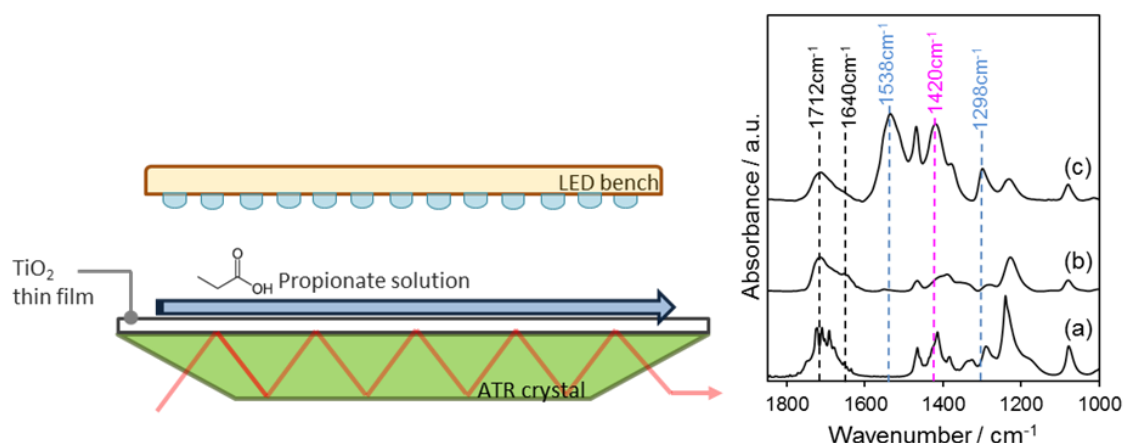


**Figure 5.1.** Schematic drawing of the experimental setup of the ATR IR cell for solid-liquid interface investigations and an example of the IR spectra collected for pure PA (a), PA in liquid phase (b) and PA adsorbed on P-25 surface (c).

Preliminary studies with the purpose of validating the correct working conditions of the ATR flow cell involved experiments using propionic acid at different concentrations, temperatures and flow conditions. After these initial screening tests the photocatalytic oxidation of propionic acid was investigated in parallel by *in-situ* ATR FT-IR spectroscopy in a bespoke flow cell reactor and by high pressure liquid chromatography (HPLC) for experiments performed in a batch reactor using Degussa P-25, anatase and rutile  $\text{TiO}_2$  nanoparticles as catalysts. The adsorption kinetics in the dark and the surface intermediates formed during the photocatalytic oxidation of propionic acid have been investigated.

The aim of this study is to gain the understanding of the surface reaction mechanism during photocatalytic processes and obtain a model reaction which can be applied to predict the influence of physicochemical parameters on the catalyst performance.

## 5.2 Results and Discussions

### 5.2.1 Adsorption kinetics and equilibrium studies

Adsorption kinetics and equilibrium constants were evaluated in relation to the Langmuir adsorption model, which is based on the assumptions of reversible adsorption/desorption mechanism, all adsorption sites being equivalent, monolayer as maximum adsorption and no interaction between adsorbed species.[18] Fitting the experimental data into Langmuir kinetic model enables to evaluate the adsorption/desorption rate ( $k_a$ ,  $k_d$ ) and the half-life ( $t_{1/2}$ ) of the identified adsorbed species using the **Equation 5.1**:

—

**Equation 5.1** Langmuir kinetic model.

where  $\theta$  is the surface coverage function of time,  $\theta_0$  is the coverage when the desorption commences (saturation coverage),  $k$  is the kinetic constant and  $t_{1/2}$  is the half-life.

In general, for ATR-IR spectroscopic experiments, the surface coverage  $\theta$  is proportional to the absorbance of spectral peak due to the adsorbed species,  $A$ , **Equation 5.2**:

—

**Equation 5.2** Surface coverage.

where  $A_{\max}$  is the maximum value reached at the equilibrium point.

This kinetic theory is ideal for a single adsorbed species system, however the system in this work, propionic acid /  $\text{TiO}_2$ , includes at least three different molecule configurations. The Langmuir model does however provide the best fit to the experimental data with a correlation coefficient which is always  $R^2 > 0.98$ . The Langmuir-type isotherms were obtained by plotting absorbance versus time, where absorption is measured as peak areas of the adsorbed species collected at set time intervals during a 30 minute period of propanoic acid flow ( $0.4 \text{ ml.min}^{-1}$ ) over the  $\text{TiO}_2$  thin film in the dark. The spectra were recorded until the adsorption had reached an equilibrium, then deionized water was passed over the catalyst to study desorption kinetics. **Figure 5.2** shows an

example of data fitting for adsorption and desorption data relative to the peak at  $1712\text{ cm}^{-1}$  (physisorbed propanoic acid on  $\text{TiO}_2$ ).

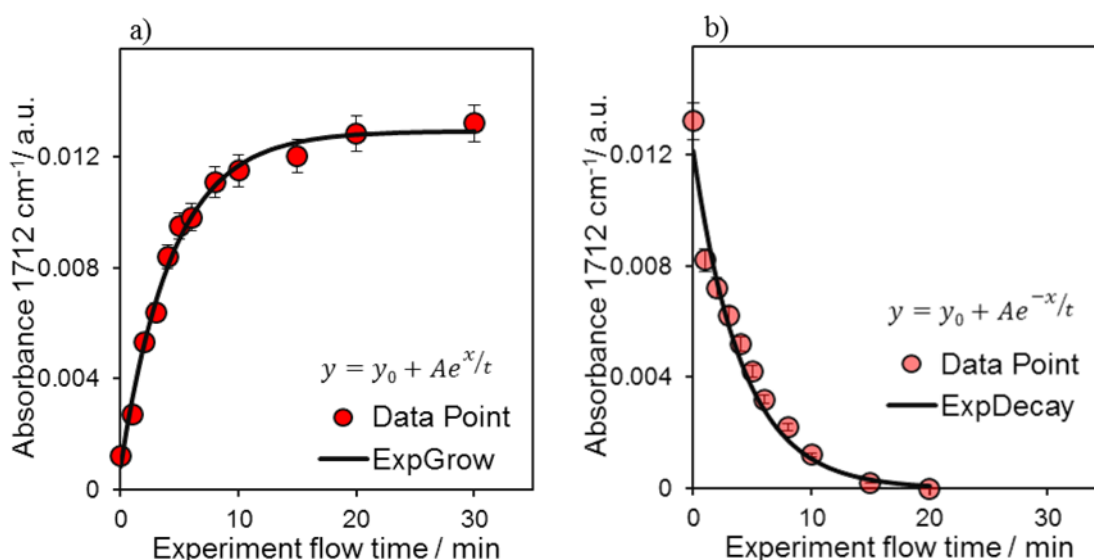


**Figure 5.2** Time dependence of absorbance (at  $1712\text{ cm}^{-1}$ ) during the adsorption (a) and desorption (b) time and the relative fitting obtained with exponential function in Origin 9.

Moreover the equilibrium constant ( $k_{eq}$ ) was derived from the adsorption/desorption rate constants ( $k_a, k_d^{-1}$ ), while the Langmuir adsorption (affinity) constant  $K_L$  was defined as function of the concentration of adsorbate (ligand)  $[L]$  using **Equation 5.3**.

$$K_L = \frac{k_a}{k_d[L]}$$

**Equation 5.3** Langmuir affinity constant

**Equation 5.3** indicates that a more strongly bound adsorbed species (i.e. chemisorbed species) is expected to have a larger adsorption rate constant and a smaller desorption rate constant than a more weakly bound adsorbed species.

### 5.2.2 Optimization of working conditions

The adsorption of propanoic acid in the dark onto  $\text{TiO}_2$  P-25 was explored under several operative conditions (acid concentration, flow rate and temperature). These tests were critical to establish the optimum working conditions in order to have a good interpretation of the spectra and determine reproducibility of later tests. Common reaction conditions of  $0.05\text{ M}$  acid solution and  $0.4\text{ ml.min}^{-1}$  flow rate at room temperature were used unless otherwise stated. For full details of flow cell set-up see **Chapter 2**.

### 5.2.2.1 Effect of propanoic acid concentration

The purpose of these experiments was to identify the optimum acid concentration for the study of adsorption of the acid on  $\text{TiO}_2$  surface and photo-degradation under UV(A).

A crucial step prior to the collection of adsorbed spectra is to identify the relative absorption intensity and the frequency of the vibrational modes for the acid in the liquid phase. In addition, a concentration range of acid solution was prepared to identify the target concentration for which the contribution from the liquid phase species were negligible compared to those from adsorbed species. Prior to spectral analysis, any contributions from water must be correctly subtracted.

As shown in **Figure 5.3** the  $\nu_s(\text{O-H})$  and  $\delta(\text{H-O-H})$  at  $3280$  and  $1645\text{ cm}^{-1}$  are intense peaks coming from the absorption of water which can cover the signals from other species, therefore in all analysis a blank subtraction is carried out, using as a background the spectrum of deionized water on the ATR crystal for measurements in the liquid phase and the spectrum of water adsorbed on  $\text{TiO}_2$  for subsequent adsorption studies.

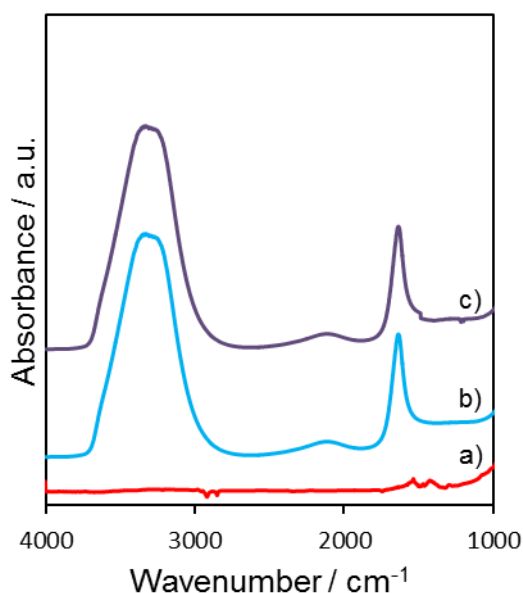


**Figure 5.3** ATR-IR spectra of a dried  $\text{TiO}_2$  thin film on a ZnSe crystal (a), pure water on a ZnSe crystal (b) and a water saturated thin film of dried  $\text{TiO}_2$  on a ZnSe crystal (c).

In **Figure 5.4a** the ATR IR spectra of solutions in the range of 1M and 0.01M of propanoic acid are depicted. The intensity of each peak increases with increasing of concentration as indicated by the calibration curves wherein each data point is calculated from the peak area of the corresponding absorption. **Figure 5.4b** illustrates calibration curves obtained using peak area of the two peaks in the finger print region of propionic acid at  $1227\text{ cm}^{-1}$  and  $1080\text{ cm}^{-1}$ ,  $\nu(\text{C-O})$  and  $\nu(\text{C-C})$  respectively.

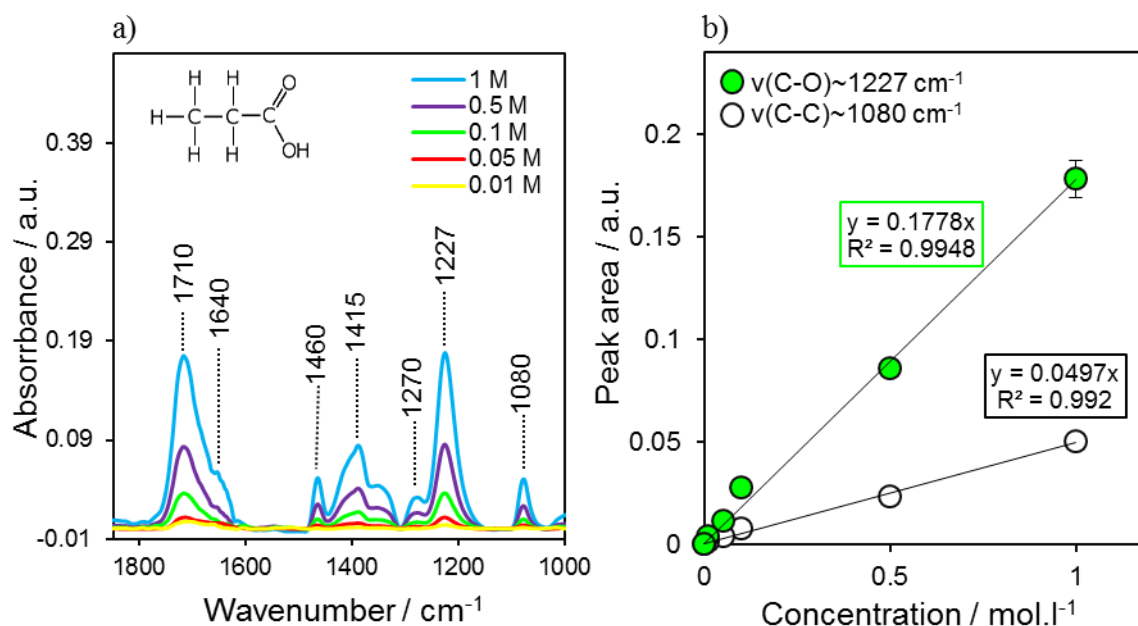


**Figure 5.4** ATR-IR spectra of propanoic acid dissolved in water in the range of concentration between 0.1 M and  $10^{-2}$  M (a) and calibration lines calculated from the peak area of the characteristic vibrational modes of propanoic acid in solution (b).

**Table 5.1** gives a summary of assigned vibrational mode of propanoic acid.

**Table 5.1** IR absorption bands and vibrational mode assignments of propanoic acid.

Mode assignment	Frequencies / $\text{cm}^{-1}$	Description
$\nu(\text{C}=\text{O})_{\text{m}}$	1710	monomer stretching
$\nu(\text{C}=\text{O})_{\text{d}}$	1640	dimer stretching
$\nu_{\text{as}}(\text{CH}_2)$	1460	asymmetric stretching
$\delta(\text{C}-\text{O}-\text{H})$	1415	bending
$\nu_{\text{s}}(\text{CH}_2)$	1270	symmetric stretching
$\nu(\text{C}-\text{O})$	1227	
$\nu(\text{C}-\text{C})$	1080	
$\nu(\text{C}-\text{H})$	2850-2950	
$\nu(\text{O}-\text{H})$	2500-3500	

For the adsorption studies a narrower range of concentration was chosen, with the aim of avoid the strong absorption signal from the liquid phase (0.1, 0.05 and 0.01M).

**Figure 5.5** depicts the spectra of propanoic acid at the equilibrium conditions in comparison with the solution phase and the adsorption affinity constant ( $k_L$ ) evaluated from the kinetic studies. In **Figure 5.5a** the bold black lines represent the adsorbed acid (ads) and the dotted lines represent the propionic acid in solution (w) at the same concentrations. The spectra of adsorbed species are

markedly different from that of the acid in solution due to the impact of strong IR absorbance of the surface-coordinate species. The strongest adsorbed species shows characteristic peaks which are clearly distinct from the acid in solution phase (range 1600-1400  $\text{cm}^{-1}$ ), while the species weakly bonded or only physisorbed on the catalyst surface exhibit negligible changes (1800-1600  $\text{cm}^{-1}$ ). The most prominent absorption occurs in the carboxylate region and the identified peaks have been assigned to propionate bonded to the surface in two different configurations:

- bridging mode, via the two oxygen molecules of the carboxyl group in a bi-dentate configuration, with the carbon chain perpendicular to the surface. ( $\nu_{\text{as}} \sim 1538 \text{ cm}^{-1}$  and  $\nu_{\text{s}} \sim 1298 \text{ cm}^{-1}$ ,  $\Delta\nu \sim 200 \text{ cm}^{-1}$ );[19]
- monodentate mode, with one oxygen bonded to the titania surface and the characteristic stretching band at  $1420 \text{ cm}^{-1}$ . [20]

In the carbonyl region (1800-1600  $\text{cm}^{-1}$ ), it is hard to distinguish the contribution between solution phase and surface bound species. Only a very small shift of  $\sim 2 \text{ cm}^{-1}$  to a higher wavenumber of  $\nu(\text{C}=\text{O})$  stretching at  $1700 \text{ cm}^{-1}$  can be reported, suggesting there is H-bonding through the carbonyl group. On the other hand, the shoulder at  $1640 \text{ cm}^{-1}$  is more difficult to discern. According to the literature, this band could be associated with the dimeric forms of carboxylic acids in solution, or the carboxylates or to the  $\nu(\text{C}=\text{O})$  stretching of chemisorbed acid at Lewis acid sites ( $\text{Ti}^{4+}$ ) through the oxygen lone-pair electrons of the carbonyl group.[2, 5]

The  $K_L$  values evaluated from the kinetic experiments for the identified adsorbed species are reported in **Figure 5.5b**. The trend shows that at the highest concentration the adsorption on the catalyst surface is dominated by the bridging bidentate configuration, whereas for the monodentate species the affinity with the catalyst surface appears to be linearly dependent from the concentration value. It is clear that the physisorbed propanoic acid is the more weakly adsorbed species in all range of concentrations.

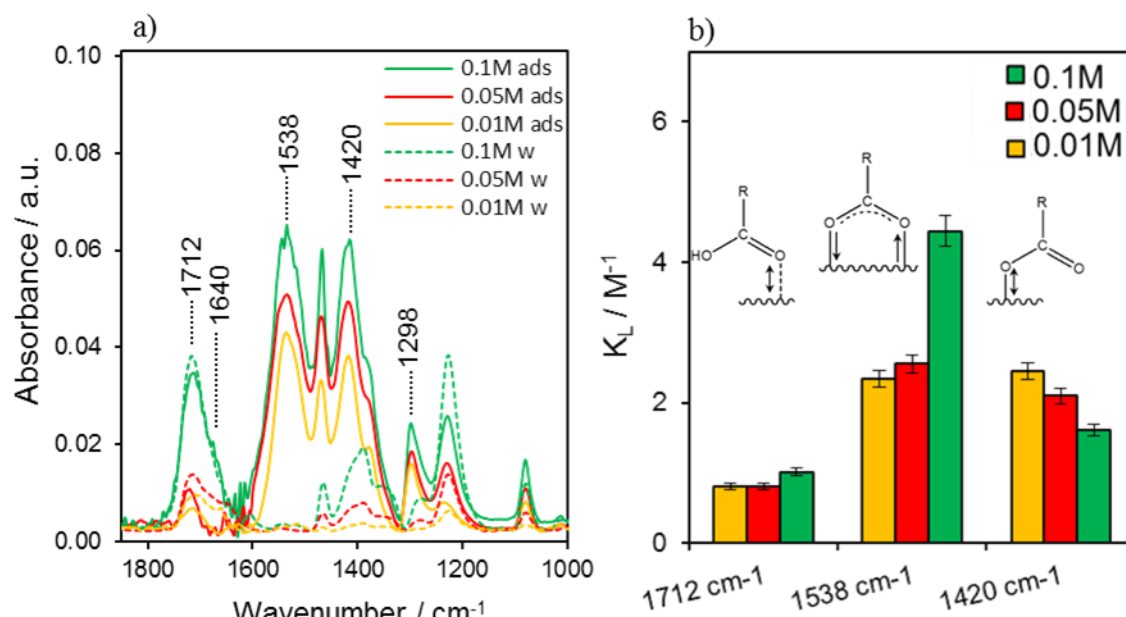


**Figure 5.5** ATR-IR spectra of propanoic acid adsorbed on TiO<sub>2</sub> P-25 under equilibrium conditions (bold line) and spectra of the acid at the same concentration in solution (dotted line) (a). Adsorption affinity constant ( $k_L$ ) from the kinetic experiment performed at different propanoic acid concentrations (b).

The four different possible configurations of a propanoic acid molecule on a TiO<sub>2</sub> surface are reported in **Figure 5.6**.

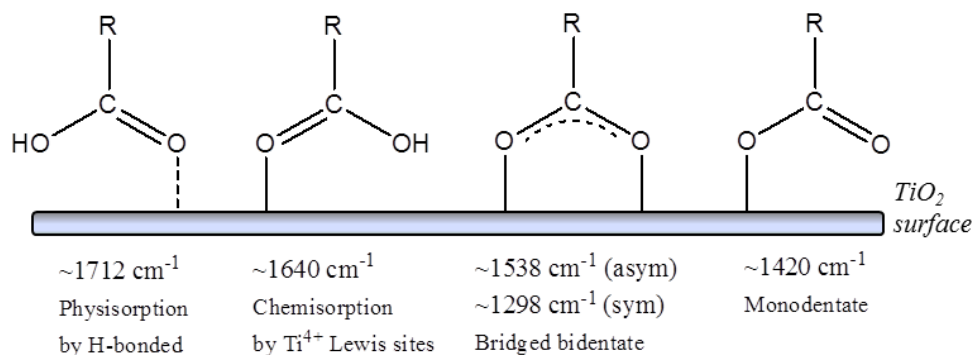


**Figure 5.6.** Different adsorption modes of propanoic acid on TiO<sub>2</sub>.

### 5.2.2.2 Effect of flow rate

An aqueous solution of 0.1M propanoic acid was passed over the catalyst at rates of 0.1, 0.4 and 0.8 ml.min<sup>-1</sup> across the TiO<sub>2</sub> films. The purpose of these experiments was to investigate the effect of flow rate on the adsorption kinetics and evaluate the optimum working conditions for the following studies.



**Figure 5.7a** shows the spectra collected at equilibrium for propanoic acid adsorbed on P-25 after flowing a solution of the acid at different rates over a thin film. The spectrum of propanoic acid in solution is reported for comparison (dotted line).

**Figure 5.7b** shows that the equilibrium constant  $k_{eq}$  for the three adsorbed species first increases and then decreases with flow rate. The values of the equilibrium constants are higher at  $0.4 \text{ ml.min}^{-1}$  and the calculated  $k_{eq}$  values follow the order: bidentate (4.9) > monodentate (3.9) > physisorbed (1.9) acid. Similar trends, but lower values, were estimated at a lower flow rate  $0.1 \text{ ml.min}^{-1}$ . Using a higher flow rate ( $0.8 \text{ ml.min}^{-1}$ ) results in a reduction of all equilibrium constants with a similar value for the three the spectral components suggesting an increasing of desorption and a decreasing of the adsorption kinetics of all adsorbed species. Flow rates lower than  $0.1 \text{ ml.min}^{-1}$  gave negligible adsorption signals and higher than  $1 \text{ ml.min}^{-1}$  were found to physically remove the films in contact with the ATR crystal, and hence both rates are not reported. The intermediate flow rate also provides the best-fit values of  $k_{eq}$  evaluated from the Langmuir model. Thus all the reported experiments in the following chapter were performed at flow rate of  $0.4 \text{ ml.min}^{-1}$ .

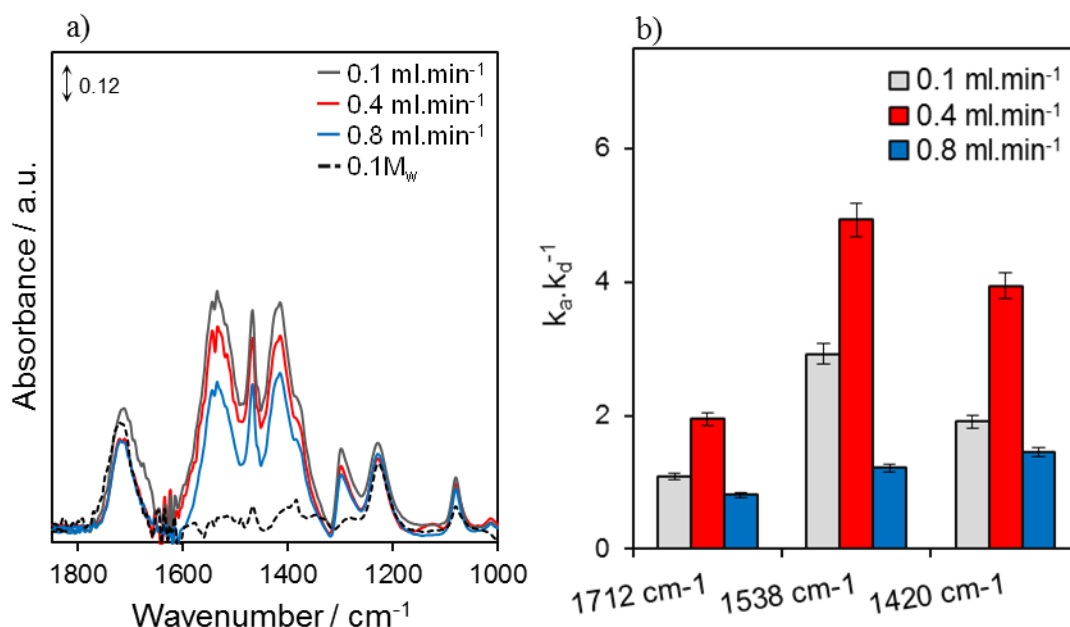


**Figure 5.7** ATR IR spectra of 0.1M propanoic acid solution adsorbed on TiO<sub>2</sub> P-25 under equilibrium conditions (bold line) reached at different flow rates and spectra of the acid at the same concentration in solution (dotted line)(a). Equilibrium constant ( $k_{eq}$ ) evaluated from the Langmuir model for the three surface complexes (b).

### 5.2.2.3 Effect of temperature

Kinetic studies were conducted at 0.1M propanoic acid concentration in the range of temperature of 25-70 °C. Values of equilibrium constant ( $k_{eq}$ ) and Gibbs free energies of adsorption ( $\Delta G_{ads}^\circ$ ) were experimentally calculated from fitting the Langmuir model to evaluate the effect of temperature of the adsorption mechanism on each surface complex.

**Figure 5.8a** shows the spectra collected at equilibrium for adsorbed propanoic acid on P-25 at different temperatures. The recorded peak heights in the carboxylate region clearly decrease with increasing of the temperature, while the intensity of the peak at  $1712\text{ cm}^{-1}$  does not show any significant changes within this temperature range, because the peak of physisorbed acid overlaps with the vibrational stretching of the acid in liquid phase ( $\nu(\text{C}=\text{O}) \sim 1710\text{ cm}^{-1}$ ) and at equilibrium it is hard to distinguish the two contributions.

**Figure 5.8b** depicts the equilibrium constants ( $k_{\text{eq}}$ ) evaluated from the ratio between the adsorption/desorption equilibrium constants. It can be seen that  $k_{\text{eq}}$  of the physisorbed complex ( $1712\text{ cm}^{-1}$ ) is strongly affected by the temperature and desorption rate drastically rises at  $35^\circ\text{C}$ . On the other hand, for the two chemisorbed configurations, the adsorption is favoured at room temperature, while the  $k_{\text{eq}}$  shows a decrease to lower values in the range of  $35\text{--}50^\circ\text{C}$ . It can be seen that in this range the equilibrium constants are quite similar however the values drastically decrease with increasing temperature at  $75^\circ\text{C}$ .

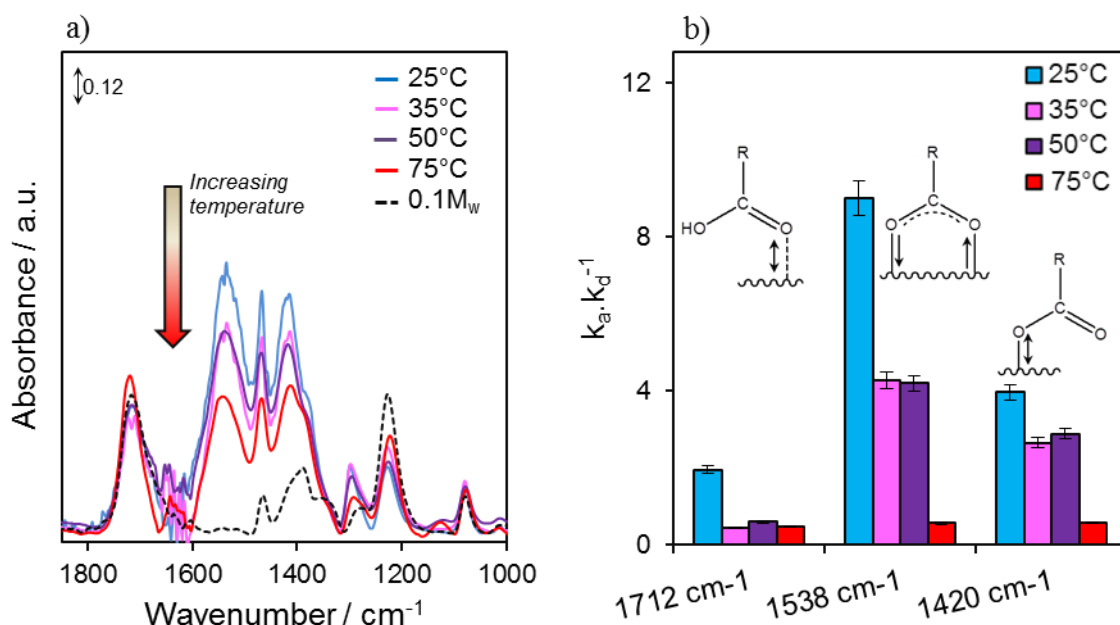


**Figure 5.8** ATR-FTIR spectra of adsorbed propionic acid over TiO<sub>2</sub> P-25 collected at the equilibrium ( $t = 30\text{ min}$ ) at different temperature. The spectrum of propanoic acid in solution at room temperature (black dotted line) was reported for comparison (a). Value of equilibrium constants (evaluated from the Langmuir model) are reported for the three surface complexes (b).

Using these results, Gibbs free energy ( $\Delta G^\circ$ ) was calculated from the Langmuir equilibrium constants. The Gibbs energy change ( $\Delta G^\circ$ ) indicates the degree of spontaneity of an adsorption process, and a higher negative value reflects a more energetically favourable adsorption. According to thermodynamic law,  $\Delta G^\circ$  of adsorption is calculated as follows:

$$\ln(k_{eq})$$

**Equation 5.4** Gibbs free energy

in which  $k_{eq}$  is the thermodynamic equilibrium constant without units,  $T$  is the absolute temperature in Kelvins, and  $R$  is the gas constant with a value of  $8.314 \text{ J.mol}^{-1}.\text{K}^{-1}$ .

**Figure 5.9** shows the dependency of  $\Delta G_{ads}^{\circ}$  on temperature calculated from the Langmuir  $k_{eq}$  values as a function of spectral components for adsorbed propanoic acid on P-25. Results show adsorption of all three surface complexes at room temperature. The  $\Delta G_{ads}^{\circ}$  for the formation of bidentate propionate was calculated to be  $-61 \text{ kJ mol}^{-1}$ , which is more negative than monodentate propionate and physisorbed acid ( $-38$  and  $-19 \text{ kJ mol}^{-1}$ ), respectively. Furthermore the Langmuir model predicts an exothermic adsorption of physisorbed propanoic acid at  $35^{\circ}\text{C}$ , resulting in a net increase of  $\Delta G_{ads}^{\circ}$  to positive values which remain approximately constant in all this temperature range ( $\sim 19 \text{ kJ mol}^{-1}$ ), meaning that the adsorption is no longer spontaneous.

This result further confirms the weak interaction of the physisorbed complex with the catalyst surface which is also strongly affected by the temperature.

On the other hand, the  $\Delta G_{ads}$  values for the two chemisorbed species were all found to be negative in the range from  $-61$  to  $-26 \text{ kcal/mol}$  up to  $50^{\circ}\text{C}$ . Above this temperature the Gibbs free energy were found to be positive ( $\sim 14 \text{ kJ mol}^{-1}$ ) and very close to the  $\Delta G_{ads}$  value calculated for the physisorbed acid, indicating that at  $70^{\circ}\text{C}$  the adsorption is not a spontaneous process anymore.

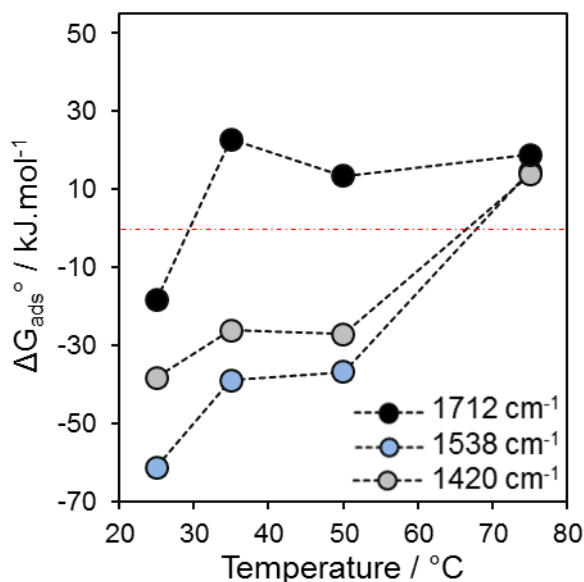


**Figure 5.9** Temperature dependence of  $\Delta G_{ads}^{\circ}$  calculated from the Langmuir  $k_{eq}$ .

The above study regarding the Gibbs free energy values from the liquid phase is similar to that found for adsorption of carboxylic acid in gas phase. Because of the interactions of dissolved species with the bulk water, the  $\Delta G_{ads}$  values in liquid phase are found to be generally lower

compared to the gas-phase values.[21] These results show that in order to perform adsorption kinetic studies for the three surface complexes the effective adsorption should take place at room temperature (298.15 K).

### **5.2.3 Adsorption and photodecomposition of propanoic acid on P-25, anatase and rutile TiO<sub>2</sub> nanoparticles**

In the previous section three operational parameters (initial adsorbate concentration, flow rate and temperature) were optimized in order to have the best conditions on the ATR IR flow cell to perform adsorption and photocatalytic kinetic studies related to propanoic acid over TiO<sub>2</sub> nanoparticles. Based on the obtained results, the highest spectra resolution for the adsorbed species was observed at 0.05 M initial concentration of propanoic acid. The highest equilibrium constant ( $k_{eq}$ ) for the three surface complexes was obtained at 0.4 ml.min<sup>-1</sup> flow rate at room temperature. Moreover equilibrium data analysed reveal the Langmuir isotherm to be the best fitted model.

In the following sections a comparative study of the adsorption and photodegradation of propanoic acid on TiO<sub>2</sub> nanoparticles by *in-situ* ATR IR spectroscopy is presented. The photocatalytic oxidation of propanoic acid was investigated in parallel in a batch reactor and analysis concentrations were performed by high pressure liquid chromatography (HPLC).

The adsorption kinetics in the dark and the surface intermediates formed during the photocatalytic oxidation of propanoic acid has been investigated. In the final section the effect of pH has also been explored.

The aim of this study is to gain an understanding of the surface reaction mechanism during photocatalytic processes and obtain a model reaction which can be applied to predict the influence of physicochemical parameters on the catalyst performance.

### 5.2.3.1 Propanoic acid adsorption

**Figure 5.10** shows the two main regions of interest of the ATR-IR spectra collected during flow of propanoic acid solution over P-25 TiO<sub>2</sub> for 30 min in the dark.

**Figure 5.10a** depicts the region at higher wavenumbers, from 2500 to 3850 cm<sup>-1</sup>, mainly dominated by signals attributable to the stretching mode of OH and C-H groups. In **Figure 5.10b** the characteristic peaks of propionic acid due to  $\delta(\text{CH}_2)$ ,  $\nu(\text{C-O})$ , and  $\nu(\text{C-C})$  bands at ~1472, ~1227 and ~1080 cm<sup>-1</sup> (grey font), respectively and the strong vibrational modes of the adsorbed acid (black font) are marked. All the assignments for the adsorbed species have been previously discussed. (See **Section 5.2.2.1**)

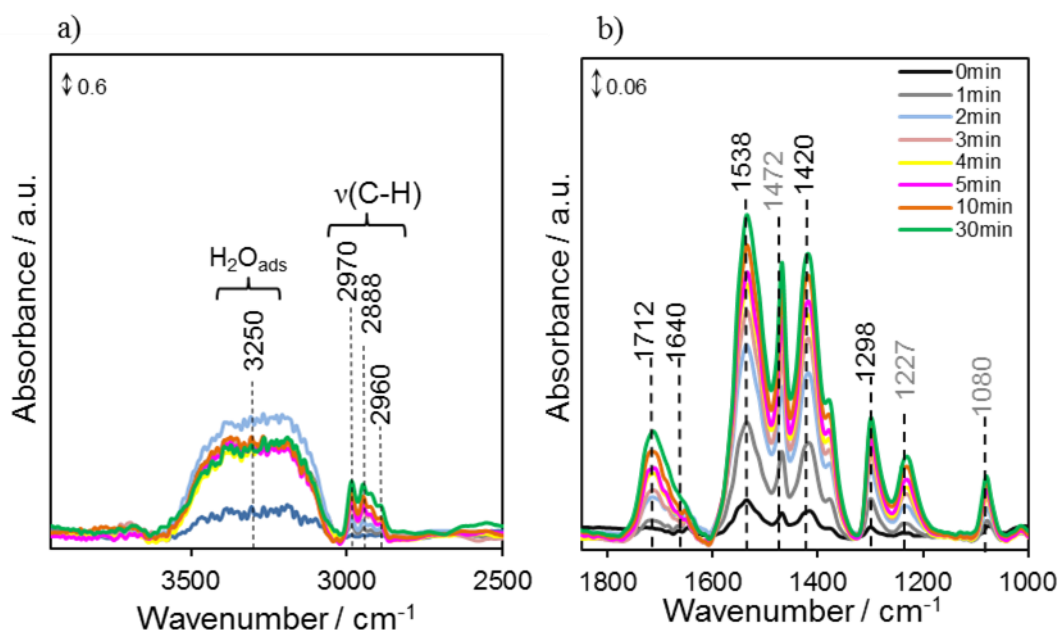


**Figure 5.10** Series of ATR-IR spectra recorded during adsorption of propanoic acid solution on TiO<sub>2</sub> P-25 in the dark for 30 min. IR region: 2500-3850 cm<sup>-1</sup> (a) and 1000-1850 cm<sup>-1</sup> (b).

Moreover **Figure 5.10a** is reported in order to clarify the interaction of water with TiO<sub>2</sub> surface even after the background subtraction. It is well known that TiO<sub>2</sub> exhibits amphoteric characteristics and when it is in contact with an aqueous solution the formation of surface species is strongly related with pH. It is very important, especially in adsorption studies, to know the surface charge of the material in aqueous media as, if the catalyst and the adsorbate have the same charge, the adsorption between the two phases is limited.

The point of zero charge (PZC) or isoelectric point (IEP) is referred to the condition when the electrical charge density on a surface is zero. For TiO<sub>2</sub> the PZC has been reported between 4 and 6.[22] Based on the pH value, the amphoteric surface of TiO<sub>2</sub> will be positively or negatively charged because of the acid-base equilibrium as **Equation 5.5** and **5.6** show:

$$\text{pH} \leq 5$$

**Equation 5.5** Surface protonation of  $\text{TiO}_2$  at acidic pH.

$$\text{pH} > 5$$

**Equation 5.6** Surface deprotonation of  $\text{TiO}_2$  at basic pH.

A background spectrum was recorded using deionised water at  $\text{pH} = 5 \sim \text{pzc}_{\text{TiO}_2}$  where the  $\text{TiO}_2$  surface was weakly positive due to predominant species  $\text{TiOH}_2^+$  and  $\text{TiOH}$ . During the adsorption experiment, the measured value of the propanoic acid solution was  $\text{pH} = 3$  (no pH corrections were applied) and propanoic acid was partially deprotonated ( $\text{pH} < \text{pK}_a = 4.87$ ). This pH value results in more positive species on the catalyst surface ( $\text{TiOH}_2^+$ ) and the opposite charges of adsorbent and adsorbate favours the interaction between the two phases.

In **Figure 5.10a** a broad band centred at  $3250 \text{ cm}^{-1}$  can be seen, characteristic of the O-H stretching. This band was assigned to the adsorbed water or more precisely to the stretching of the bidentate  $\text{O-H}_2^+$  group on the  $\text{TiO}_2$  surface due to the protonation of the hydroxyl group of  $\text{TiO}_2$  in contact with acidic media (**Figure 5.11**).[23, 24]

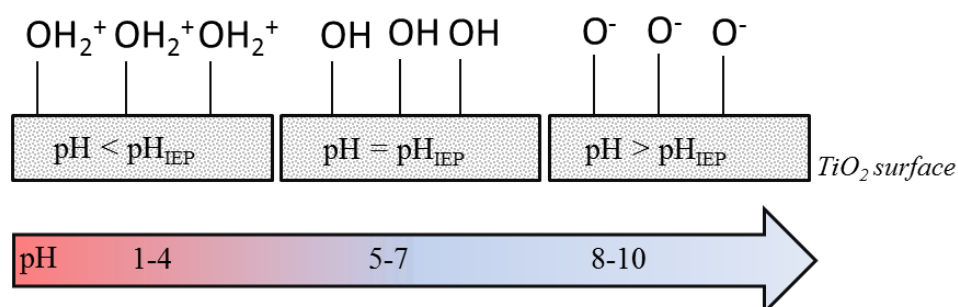


**Figure 5.11** Simplified figure of the protonation and deprotonation of hydroxylated  $\text{TiO}_2$  surface leading to positive and negative net charge at the surface.

This region ( $3000\text{-}3500 \text{ cm}^{-1}$ ) also contains the O-H stretching of carboxylic acids but this band is less likely due to the adsorbed molecular acid for two main reasons; firstly, at  $\text{pH} = 3$  propionic acid is mainly present in its dissociated form ( $\text{C}_2\text{H}_5\text{COO}^-$ ) and secondly this band readily increases within the first minute of solution/catalyst contact but does not grow simultaneously with the characteristic band of adsorbed propionic acid. Meanwhile, as propanoic acid was adsorbed on  $\text{TiO}_2$  surface, the positive bands at  $2960$ ,  $2920$ , and  $2888 \text{ cm}^{-1}$ , which characterize C-H stretching of the acid, were observed.

**Figure 5.12** shows the intensities of each of the most important bands belonging to adsorbed acid in the characteristic adsorption isotherm shape. All the assigned bands reached the saturation point within the first 10 min with a rapid initial rise tending to plateaux.

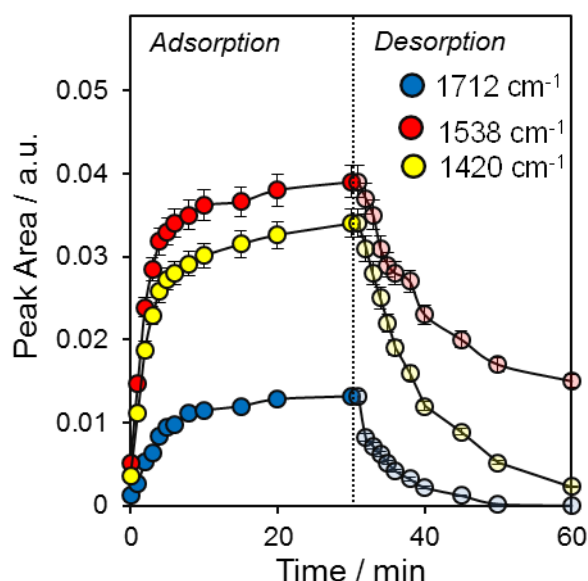


**Figure 5.12** Adsorption/desorption time profile of the most relevant bands of adsorbed propanoic acid on TiO<sub>2</sub> P-25 obtained by measuring the peak area at different times.

Previous discussion showed that the adsorption affinity for the three identified species follow the order: bridging bidentate > monodentate > physisorbed propanoic acid. (See **section 5.2.2.1**) The band of the bridging bidentate ( $\nu_a(\text{COO}) \sim 1538 \text{ cm}^{-1}$ ) configuration reaches a plateau with the highest intensity in the adsorption phase and doesn't decay totally in the desorption step while the band of the monodentate configuration ( $\nu(\text{CO}) \sim 1420 \text{ cm}^{-1}$ ) grows along with it but the lower intensity and the lower adsorption rate suggests less of this formation. Finally the evolution of the band  $\nu(\text{C=O})$  at  $1712 \text{ cm}^{-1}$  shows the lowest absorption and more rapid decay at the early stage of desorption. As expected the physisorbed specie is weakly bonded to the surface in comparison with the chemisorbed propionate.

TiO<sub>2</sub> P-25 is a mixture of anatase (80%) and rutile (20%), and hence the two sets of carboxylate bands could originate from adsorption on the two crystal phases. Using the same experimental conditions, adsorption/desorption tests were performed on different titania samples to investigate the interaction behaviour of propionic acid over different titania phases.

**Figure 5.13** shows the IR spectra of propionic acid adsorbed on TiO<sub>2</sub> P-25, anatase (A), rutile (R) and a physical mixture of the two pure phases in the same mass ratio (4:1) of P-25.

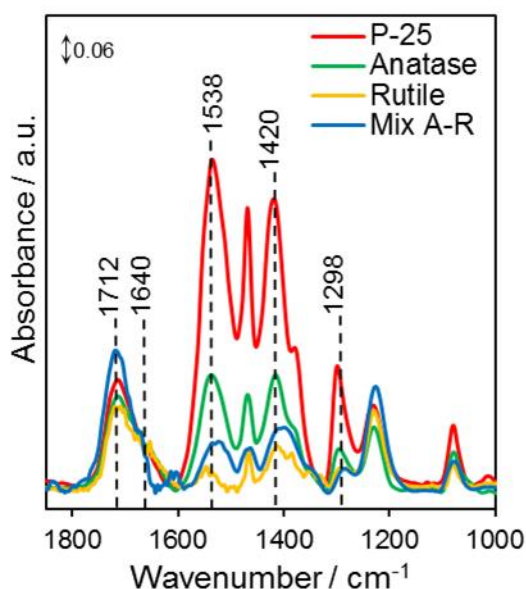


**Figure 5.13** ATR-IR absorption spectra of propanoic acid adsorbed on P-25, anatase, rutile and physical mix 80% A-20% R TiO<sub>2</sub> nanoparticle thin film

As expected distinct spectral differences become apparent in the region of adsorbed propionate, whereas the intensity and the position of the vibrational mode of molecular adsorbed acid  $\nu(\text{C}=\text{O}) \sim 1712 \text{ cm}^{-1}$  retains the same intensity and position for all the samples. The high band of bridging bidentate mode ( $\nu_a(\text{COO}^-) \sim 1538 \text{ cm}^{-1}$ ) observed on anatase is almost completely absent on rutile. Previous theoretical and computational studies confirmed the experimental observation present in this work, showing that the bridged bidentate bonding mode is more favoured on anatase (101) over monodentate configuration.[25-27]

The experiment performed with the physical mixture of anatase and rutile in the (4:1) ratio did not show the same behaviour as the P-25 sample, suggesting that the strong interaction of anatase/rutile interface in P-25 is critical in the adsorption of organic acid on the catalyst surface.[28]

**Figure 5.14, Figure 5.15 and Figure 5.16** show the time evolution of the spectra resulting from flowing 0.05M propanoic acid solution over anatase, rutile and the mixed 80%anatase-20%rutile (adsorption step) and the corresponding time evolution obtained during the desorption step from the same samples exposed to a water flow for 30 min. Such ATR-IR desorption data have not been previously reported in liquid phase for an organic acid over different titania phases.



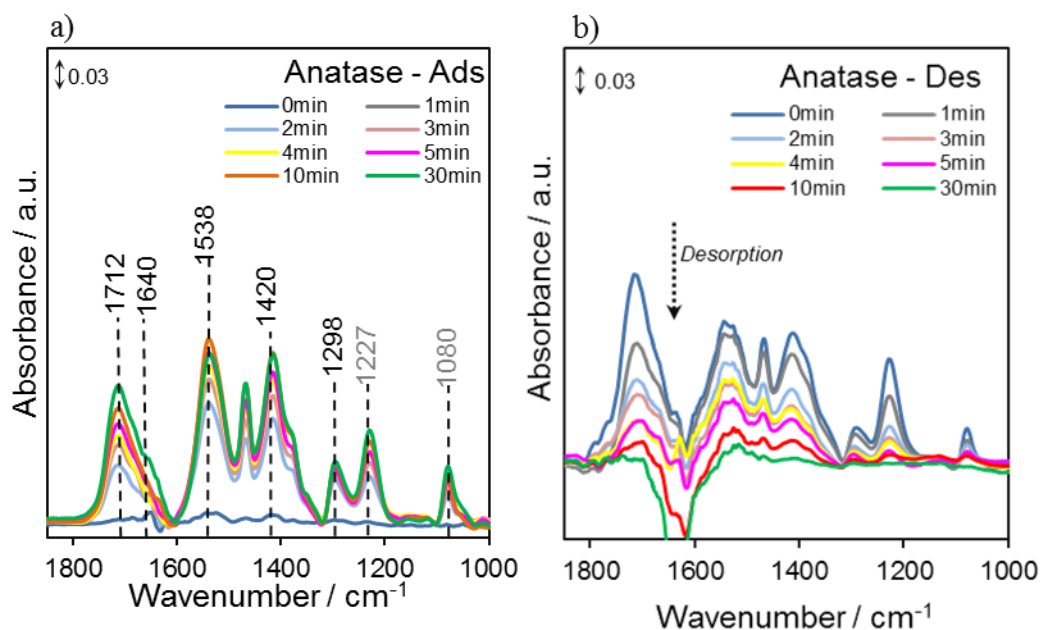


**Figure 5.14** ATR IR spectra changes obtained during the adsorption of propanoic acid on anatase, (a) and the corresponding spectra in the desorption step (b). The arrow indicates evolution of spectra with increasing time.

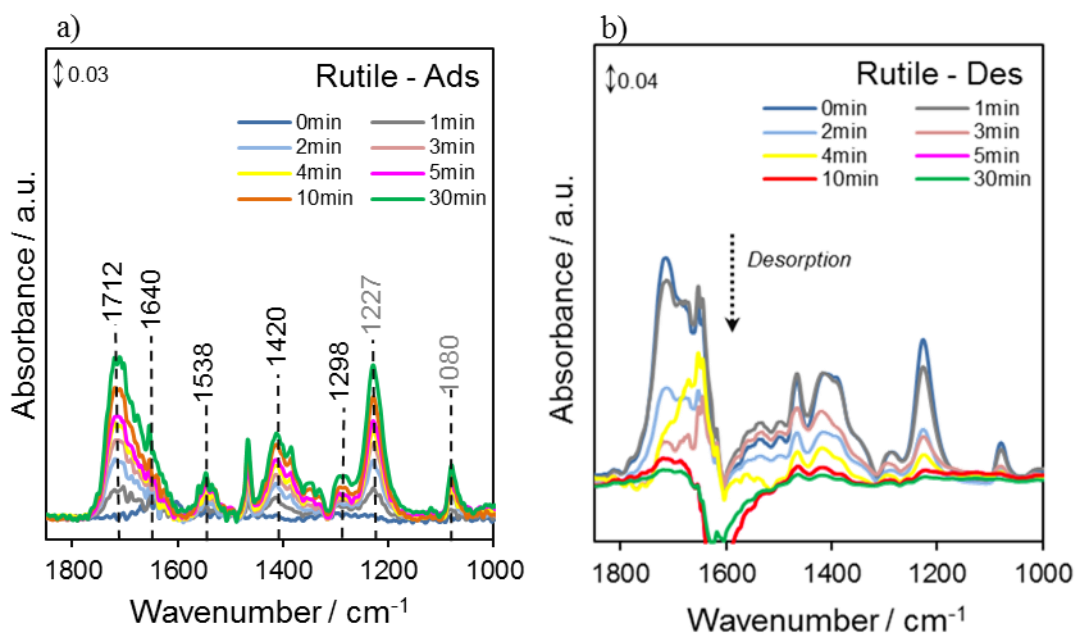


**Figure 5.15** ATR IR spectra changes obtained during the adsorption of propanoic acid on rutile, (a) and the corresponding spectra in the desorption step (b). The arrow indicates evolution of spectra with increasing time.

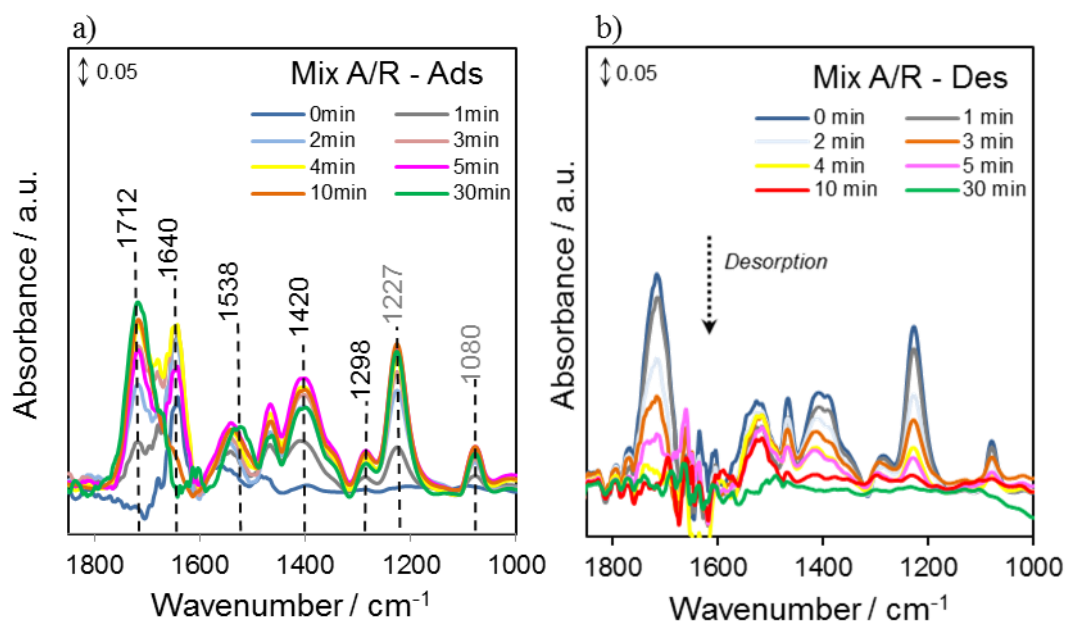


**Figure 5.16** ATR IR spectra changes obtained during the adsorption of propanoic acid on physical mixture 80% anatase-20% rutile, (a) and the corresponding spectra in the desorption step (b). The arrow indicates evolution of spectra with increasing time.

In the comparison of the adsorption behaviour on the two pure  $\text{TiO}_2$  phases is evident that the time scale to reach the adsorption equilibrium is very different potentially owing to differences in textural properties and crystalline domain of the two samples. On anatase, propanoic acid exhibited very rapid adsorption and reached the equilibrium within 5 minutes with a prominent band of adsorbed bridging propionate ( $\nu_a(\text{COO}^-) \sim 1548 \text{ cm}^{-1}$ ); whereas on rutile the acid displayed slower adsorption and took more than 10 minutes to reach the equilibrium with the strongest band intensity in the carbonyl region ( $1600\text{--}1800 \text{ cm}^{-1}$ ) and highest carboxylate vibration at  $1472 \text{ cm}^{-1}$  for the stretching of monodentate mode ( $\nu(\text{CO})$ ). For all the samples the comparison between adsorption and desorption step shows a different time scale for the evolution of the peaks. During the adsorption step in the carbonyl region the  $1714 \text{ cm}^{-1}$  peak (H-bonded propionic acid) grows more slowly compared to the  $1640 \text{ cm}^{-1}$  peak (chemisorbed acid) but clearly decays more rapidly in the desorption, suggesting a less strongly adsorbed species.

This observation is further supported by the examination of the spectra of the physical mixture 80% anatase- 20% rutile. (**Figure 5.16**) In this case it seems that the adsorption is clearly characterized from two stages process, as result of the separate contribution of the two phases.

The first stage occurs within the first 5 minutes in which the spectra is dominate by the  $\nu(\text{C=O}) \sim 1640 \text{ cm}^{-1}$  stretching of chemisorbed acid at Lewis acid sites ( $\text{Ti}^{4+}$ ). [29] This first step is followed by a slower process in which the absorption peak at  $1720 \text{ cm}^{-1}$  gains further intensity. The final equilibrated spectrum recorded at 30 minutes corresponds to three different complexes of

propanoic acid on the  $\text{TiO}_2$  surface: H-bonded propanoic acid ( $1712\text{ cm}^{-1}$ ) and propionate in bidentate ( $1538\text{ cm}^{-1}$ ) and monodentate configuration ( $1420\text{ cm}^{-1}$ ). In agreement with previous studies performed through SVD global analysis on dicarboxylic acids, the spectral changes are associated with the build-up of the least stable species which has in this case a characteristic band at  $1712\text{ cm}^{-1}$ . [6, 30]

**Figure 5.17a,b,c** show the time dependence of absorbance of IR peaks for the identified surface species on different titania nanoparticles in the characteristic isotherm shape. The peak at  $1640\text{ cm}^{-1}$  was not included due to the difficulty of isolating the absorption of water which occurs in the same region and the strong absorbance of the adjacent peak at  $1712\text{ cm}^{-1}$ . It is evident that the peak of physisorbed acid ( $1712\text{ cm}^{-1}$ ) disappears more quickly in the desorption step for all the samples, whereas the chemisorbed species show slower desorption suggesting that are more strongly bonded to the surface (**Figure 5.17d**).

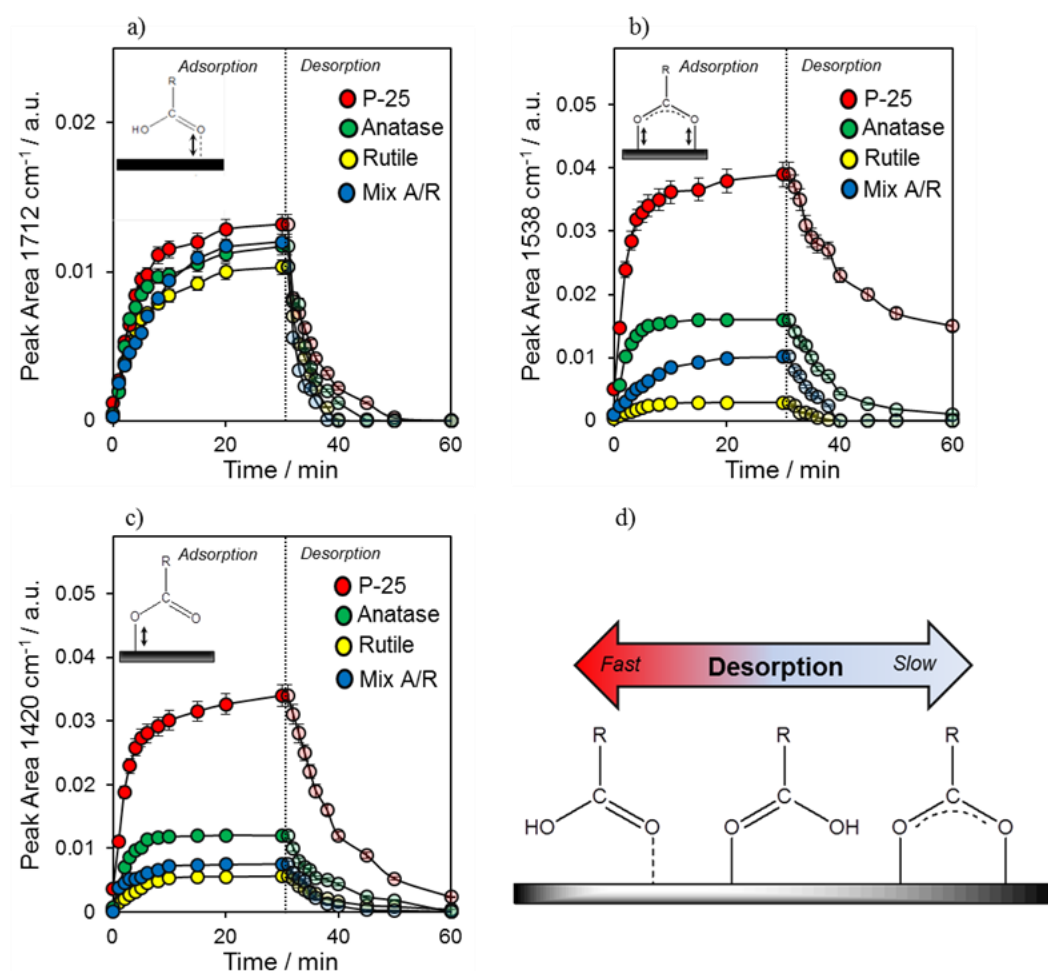


**Figure 5.17** Time dependence of absorbance of propanoic acid on different  $\text{TiO}_2$  nanoparticles. Adsorption and desorption data points were obtained from the measured area of the absorption peaks of propionic acid and propionate bonded to the surface (a, b, c). Schematic representation of surface bound species related with the desorption rate (d).

Such contributions are also seen in the kinetic analysis of the adsorption/ desorption data, shown in **Table 5.2**. Data shows that for P-25 and anatase the peak at  $1538\text{ cm}^{-1}$  (bridged bidentate) is characterised by a faster adsorption rate but a slower decay of absorbance on the desorption step, with a residual coverage of 38% and 6% respectively after 30 minutes of flowing water on the acid-saturated catalyst film. This suggests that for the samples containing anatase the most strongly adsorbed species is the bidentate propionate bonded to the surface via donor atoms from the carboxylate group, as previous studies show for some carboxylic and dicarboxylic compounds.[3] The analysis of the monodentate mode ( $1420\text{ cm}^{-1}$ ) indicates a smaller adsorption/ desorption ratio compared to the bidentate configuration, indicative of less affinity with the catalyst surface. On the other hand, on the rutile thin film the  $k_{\text{ads}}/k_{\text{des}}$  ratio is higher for the monodentate ( $1420\text{ cm}^{-1}$ ) with a residual coverage of 6.3%, absent for the pure anatase. Finally the kinetic data confirmed the weaker adsorption for the physisorbed acid ( $1714\text{ cm}^{-1}$ ) with an average of half-live of  $\sim 3$  minutes and no residual coverage reported in the end of the test for any of the samples.

**Table 5.2** Maximum absorbance value for each component ( $A_{\text{max}}$ ), value for each component normalised for the surface area( $A_{\text{max}}\cdot SA^{-1}$ ), residual coverage in the end of the desorption step ( $\theta_r$ ), adsorption/desorption rate constant ( $k_a$ ,  $k_d$ ) and half-life value ( $t_{1/2}$ ).

Band $\text{cm}^{-1}$	Sample	$A_{\text{max}}$	$A_{\text{max}}\cdot SA^{-1}$ $/\text{m}^{-2}\cdot\text{g}\cdot 10^3$	$\theta_r$ %	$k_{\text{ads}}$ $/\text{min}^{-1}$	error	$k_{\text{des}}$ $/\text{min}^{-1}$	error	$k_{\text{ads}}/k_{\text{des}}$	$t_{1/2}$ $/\text{min}$
1712	P-25	0.013	0.26	-	0.23	$\mp 0.016$	0.23	$\mp 0.03$	1.0	4.3
	anatase	0.012	0.29	-	0.27	$\mp 0.025$	0.26	$\mp 0.026$	1.0	3.7
	rutile	0.010	0.79	-	0.21	$\mp 0.015$	0.30	$\mp 0.024$	0.7	3.2
	phys mix	0.012	-	-	0.13	$\mp 0.018$	0.50	$\mp 0.024$	0.3	2.0
1538	P-25	0.039	0.78	38	0.41	$\mp 0.025$	0.11	$\mp 0.012$	3.7	8.9
	anatase	0.016	0.40	6	0.45	$\mp 0.018$	0.20	$\mp 0.018$	2.3	4.9
	rutile	0.003	0.22	-	0.22	$\mp 0.015$	0.32	$\mp 0.026$	0.7	3.1
	phys mix	0.010	-	-	0.14	$\mp 0.018$	0.21	$\mp 0.023$	0.7	4.8
1420	P-25	0.034	0.68	7	0.35	$\mp 0.015$	0.12	$\mp 0.018$	2.9	8.4
	anatase	0.012	0.30	-	0.39	$\mp 0.018$	0.14	$\mp 0.022$	2.8	6.9
	rutile	0.006	0.43	6	0.21	$\mp 0.016$	0.16	$\mp 0.022$	1.3	6.0
	phys mix	0.008	-	-	0.35	$\mp 0.016$	0.21	$\mp 0.02$	1.7	4.6

These observations confirm preferential adsorption modes of the probe molecule based on the different titania phases. Different mechanisms of chemisorption could be related to the density of

Lewis acid sites on the surface of different titania materials. FT-IR spectroscopy of pyridine adsorption was used to characterize the acidity of the samples.

As presented in **Figure 5.18a**, five IR peaks are observed in the spectra. Two sharp and intense peaks at  $1445\text{ cm}^{-1}$  and  $1605\text{ cm}^{-1}$  correspond to the coordinated pyridine adsorbed on Lewis acid sites on  $\text{TiO}_2$ . The characteristic peak of pyridine adsorbed on Brønsted acid sites on  $\text{TiO}_2$  (at  $1540\text{ cm}^{-1}$ ) is broad and weak for the samples containing anatase and not present on rutile. Therefore the peaks at  $1575\text{ cm}^{-1}$  and  $1491\text{ cm}^{-1}$  assigned to the combined Brønsted/Lewis acidity can be attributed only to the Lewis acid sites on  $\text{TiO}_2$ . [26, 31]

In **Figure 5.18b** it can be noticed that the higher amount of Lewis acid sites corresponds to a higher final absorbance value of the bridging bidentate mode ( $A_{\text{max}}$ ), except for P-25 which shows higher affinity with propanoic acid despite the lower amount of acid sites compare to pure anatase. The surface density of acidic sites offers a potential explanation for the prominent peak at  $1538\text{ cm}^{-1}$  (bridging bidentate mode) for anatase and the physical mixture of the two phases (80% anatase), which is not evident on rutile. The higher number of adjacent Lewis acid sites increases the probability of having the molecule bonded to the surface in the bidentate configuration [26].

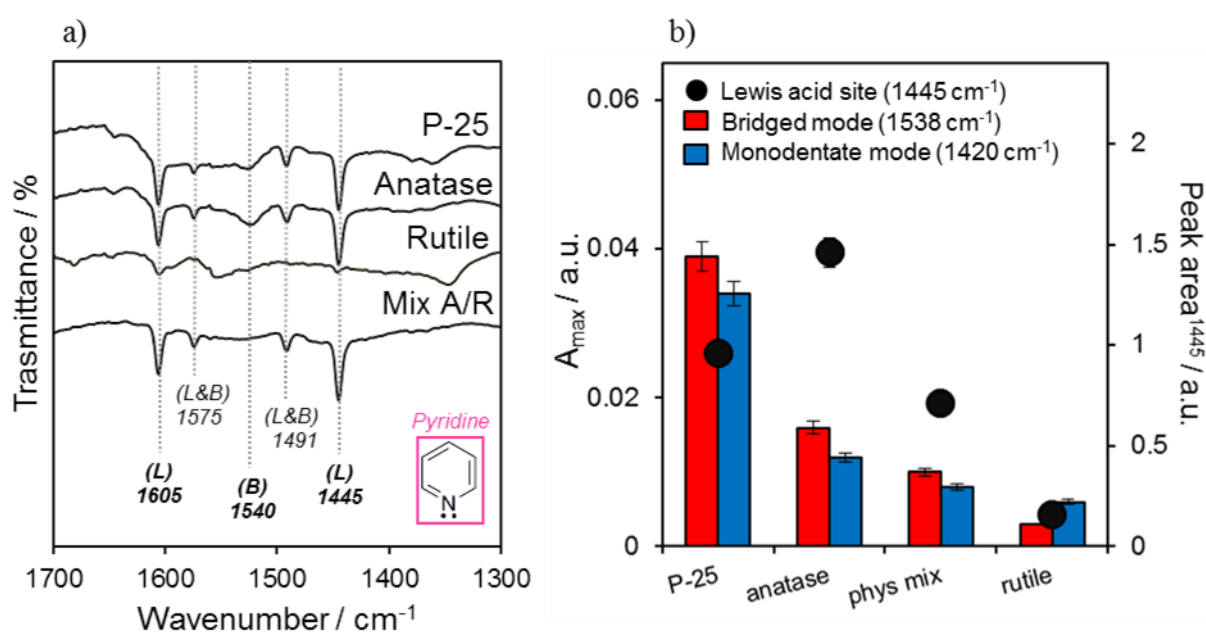


**Figure 5.18** IR spectra in  $1300\text{--}1700\text{ cm}^{-1}$  spectral region for pyridine adsorbed on P-25, anatase and rutile (a) and plot of surface Lewis acid density for the different  $\text{TiO}_2$  samples (b).

In the following section, further experiments with physical mixtures of anatase and rutile phases were not reported due to the reproducibility problem. During the adsorption/desorption tests the thin film of the physical mixture of anatase-rutile suffered of poor stability under flow conditions on the ZnSe crystal, attributed to marked differences in particle size and density of the two mixed

crystal phases. The different interactions of propanoic acid molecules with the surface of the titania nanoparticles might lead to differences on photocatalytic properties.

The goal of this study is to investigate how the different adsorption modes of propanoic acid on  $\text{TiO}_2$  surfaces affect the photocatalytic efficiency of the oxidation process in aqueous media by ATR IR spectroscopy. To achieve this, the study *in-situ* of chemisorbed reaction intermediates was performed supported by the identification of photodegradation pathways by experiments carried out in a batch reactor under similar reaction conditions.

### **5.2.3.2 Propanoic acid photodecomposition**

The three  $\text{TiO}_2$  catalysts (P-25, anatase and rutile) were evaluated for the photodegradation of propanoic acid in aqueous solution under UV LED light ( $\lambda \sim 365 \text{ nm}$ ). ATR-IR spectroscopy, facilitating the detection of surface bound species, was applied to study the liquid phase photooxidation of propanoic acid on  $\text{TiO}_2$  thin film and identify the reaction mechanism.

In parallel, samples were tested in a batch reactor equipped with an array comprised of 34 LEDs and the degradation of propionic acid and the generated intermediates were measured by HPLC chromatography as a function of time. The innovative aspect of this work is to present a parallel study of propionic acid ( $\text{C}_3$ ) degradation between a batch and an ATR flow photo-reactors both in liquid phase, unlike most of the previous investigations that were performed in gas phase and for shorter acid chain lengths.[15, 32, 33]

### 5.2.3.2.1 Batch reactor

**Figure 5.19a** shows the normalised reaction profile of photocatalytic degradation of propionic acid. The time evolution of the target substrate and the detected reaction intermediates is reported in **Figure 5.19b**, **Figure 5.19c** and **Figure 5.19d** for P-15, anatase and rutile respectively.

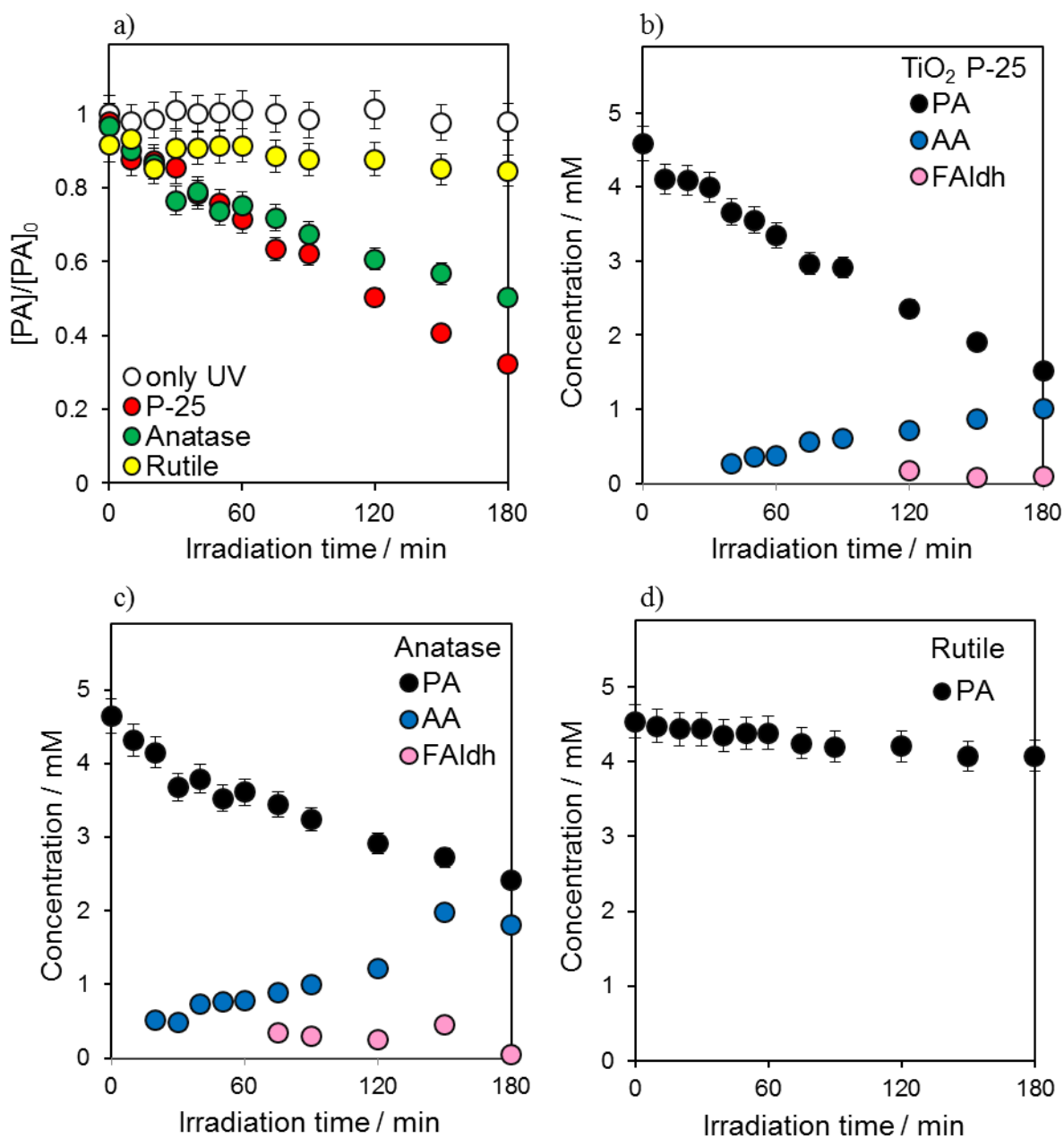


**Figure 5.19** Comparison of the photocatalytic activity of the different photocatalysts under UV light (a) and reaction profile of propionic acid with relative formed intermediates detected by HPLC analysis of TiO<sub>2</sub> P-25 (b), anatase (c) and rutile (d).

As evidenced within **Table 5.3**, despite the higher initial rate of anatase, the final conversion of propionic acid was lower compared to P-25, but a higher acetic acid yield was measured. This result can be attributed to deactivation of the catalyst. For both samples the main detected

intermediate was acetic acid, followed by the formation of a small percentage of formaldehyde. On the other hand rutile shows a very low reaction rate, with only 10% of final conversion and no intermediates detected in solution

**Table 5.3** Experimental results of the propanoic acid photooxidation over TiO<sub>2</sub> samples.

Sample	$r^0$ <sup>a</sup> / mmol.h <sup>-1</sup>	Conversion <sup>b</sup> %	Intermediates	Yields <sup>c</sup> %	Selectivity <sup>c</sup> %
P-25	0.12	67	CH <sub>3</sub> COOH	22	33
			CH <sub>2</sub> O	2	3
anatase	0.13	48	CH <sub>3</sub> COOH	39	81
			CH <sub>2</sub> O	1	2
rutile	0.03	10	-	-	-

[a] Initial reaction rate evaluated in the first 40 mins

[b] Final propanoic acid conversion

[c] Final values of yield and selectivity of the detected intermediates

#### 5.2.3.2.2 ATR flow reactor

**Figure 5.20** ATR-IR spectra recorded at different time during the photodegradation of propanoic acid on TiO<sub>2</sub> P-25 under UV (365 nm) in the 2500-3900 cm<sup>-1</sup> (a) and 1000–1850 cm<sup>-1</sup> (b) region. Spectra were collected during 2 hours of illumination at different times and spectra of TiO<sub>2</sub> samples saturated with propanoic acid solution prior to illumination were used as background in each measurement. **Figure 5.20a** shows an increase of the band centred at 3250 cm<sup>-1</sup> during the first hour of irradiation (green arrow). This band was attributed to the formation of water on the TiO<sub>2</sub> surface as reaction product. Furthermore the shoulder appearing at 3480 cm<sup>-1</sup> could be assigned to the formation of H<sub>2</sub>O<sub>2</sub>, which has been speculated to be another possible photoproduct.[12] The band of water eventually decreases after 2h of irradiation (red arrow). At the same time the carboxylate region showed a continuous change due to an increase of absorption bands at 1590 cm<sup>-1</sup> and 1384 cm<sup>-1</sup> assigned to the typical  $\nu_a(\text{COO}^-)$  and  $\nu_s(\text{COO}^-)$  vibration of the coordinate formate.[19] (**Figure 5.20b**)



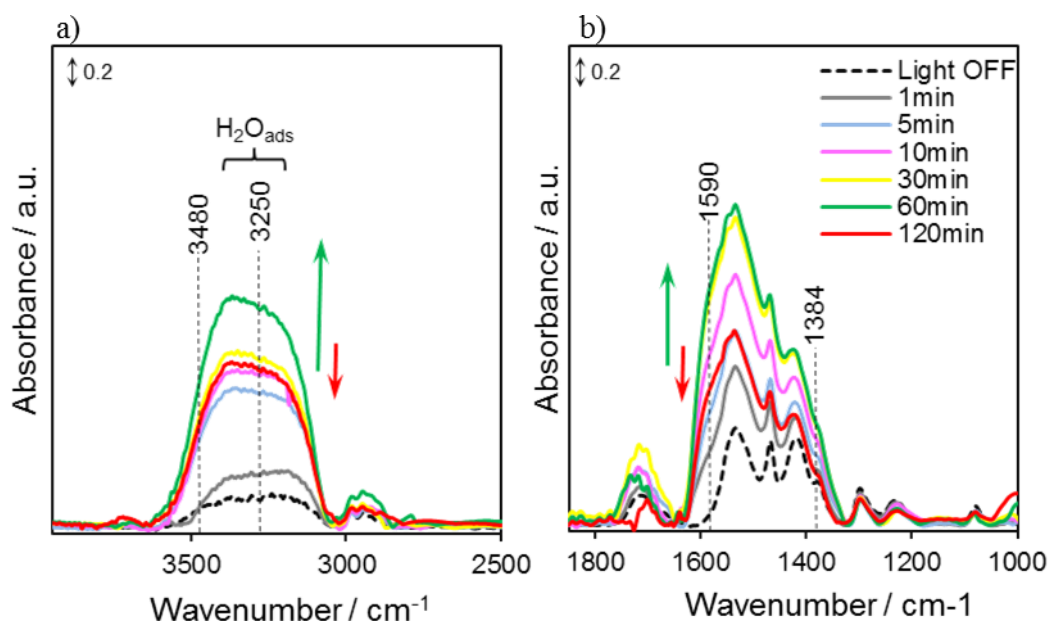


**Figure 5.20** shows the ATR IR spectra obtained during photodegradation of propanoic acid on TiO<sub>2</sub> P-25.

**Figure 5.21** confirms the presence of formate as reaction adsorbed intermediate. The subtraction of the spectrum of propanoic acid adsorbed on P-25 after 60 min of irradiation (1) from the spectrum collected in the dark at equilibrium (2) provides the evidence of positive bands of  $\nu_a(\text{COO}^-)$ ~1590 and  $\nu_s(\text{COO}^-)$ ~1384 cm<sup>-1</sup> (see 1-2 spectrum), confirming the presence of formate as reaction adsorbed intermediate (spectrum 1-2). The spectrum of adsorbed formic acid (3), used as reference for the peaks assignment, was obtained by flowing for 30 minutes a 0.05 M aqueous solution of acid over a TiO<sub>2</sub> P-25 thin film in the dark. The characteristic bands of propanoic acid in the finger print region of  $\nu(\text{C-C})$  ~1227 cm<sup>-1</sup> and  $\nu(\text{C-O})$ ~1080 cm<sup>-1</sup> were seen to decrease, and this further proved the photodecomposition of the acid.

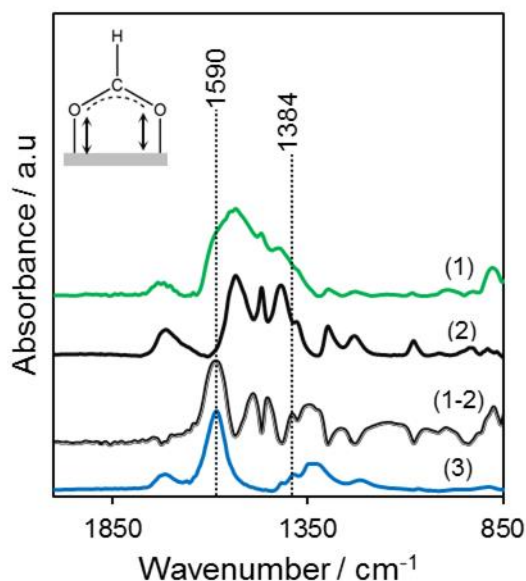


**Figure 5.21** Stacked ATR IR spectra obtained in different conditions (from the top): (1) after 60 min of irradiation, (2) equilibrium in the dark, (1-2) spectrum obtained from the difference of the latter two, (3) equilibrium in the dark of formic acid over P-25.

To gain more information about the evolution of the generated intermediate (formate and water), the spectrum of propanoic acid adsorbed on P-25 collected before UV irradiation was further subtracted from all the spectra collected during the irradiation time. (See **Figure 1, Appendix**) **Figure 5.22** shows the evolution of the peak area of fingerprint of propanoic acid (p), adsorbed formate (f) and water (w) on the TiO<sub>2</sub> P-25 surface during the irradiation time. During the first 10 min of irradiation, the  $\nu(\text{C-C})$  and  $\nu(\text{C-O})$  propionic acid peaks decrease and vibrational bands of adsorbed formate and water initially increase and then eventually start to decrease after extended illumination time (~90 min).[19]

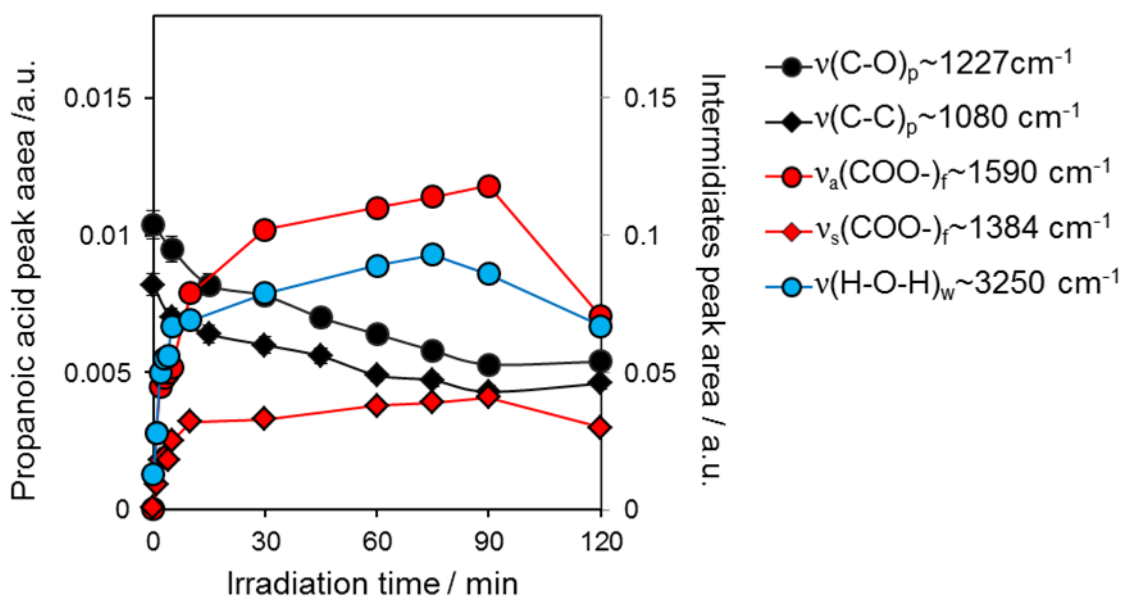


**Figure 5.22** Evolution of the peak areas of propanoic acid at  $v(C-O) \sim 1227 \text{ cm}^{-1}$  and  $v(C-C) \sim 1080 \text{ cm}^{-1}$  (p, in black) and formate (f, in red) and water (w, in blue), during the irradiation time.

**Figure 5.23** shows the ATR IR spectra obtained during photodegradation of propanoic acid on anatase. **Figure 5.23a** shows a very weak and noisy signal in the region of adsorbed water ( $\sim 3250 \text{ cm}^{-1}$ ), whilst two peaks at ca.  $2950 \text{ cm}^{-1}$  and  $2850 \text{ cm}^{-1}$  are assigned to the  $v_a(COO) + \delta(CH)$  and  $v(CH)$  respectively typical of adsorbed formate.[16] Formate formation on anatase is further supported by the appearance of the two shoulders at  $1590 \text{ cm}^{-1}$  and  $1384 \text{ cm}^{-1}$ . (**Figure 5.23b**)

On anatase, the  $v_a(COO^-)$  band at  $\sim 1590 \text{ cm}^{-1}$  is broader than the one observed on P-25 and it can be assigned to formate ions signalling formation of aqueous-like clusters.[20] This suggests weaker adsorbate-surface interactions on anatase and displacement by water formed in the course of the photoreaction, in agreement with previous studies.[34] At the same time the disappearance of the bands  $v(C=O) \sim 1712 \text{ cm}^{-1}$  and  $v(CO)$  at  $1420 \text{ cm}^{-1}$  (black arrows) seems to correlate to the broadening of the bands at  $1538 \text{ cm}^{-1}$ , suggesting that under illumination propionic acid in the monodentate configuration is gradually converted to propionate.

Such an assignment is based on two aspects: the observation of the difference spectra obtained by subtraction of the spectrum of propanoic acid adsorbed in the dark from the spectra collected during the irradiation time (See **Figure 2, Appendix**) and some previous studies performed on alkanes and dicarboxylic acids which confirm the evolution of the surface species under illumination and the dependence of photo-oxidation reaction on  $\text{TiO}_2$  with the structure of the surface intermediates.[6, 14]

In particular, on anatase the rearrangement of propionic acid molecule from the monodentate to a bidentate configuration can be considered the rate-determining steps (RDS) of the

photodegradation reaction which then easily leads to the formation and accumulation of reaction intermediates.[14]

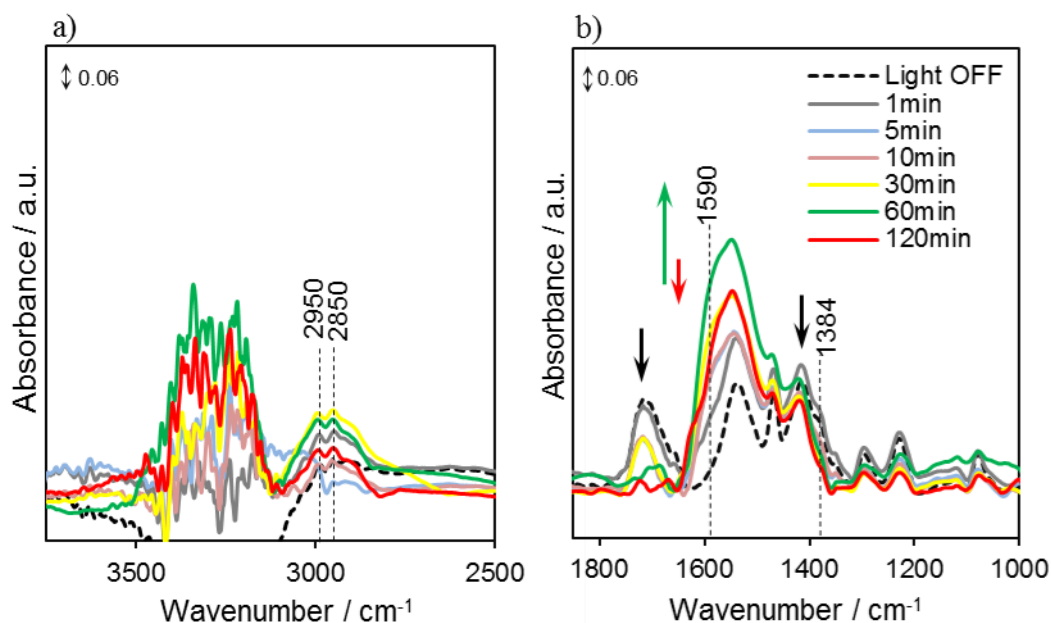


**Figure 5.23** ATR-IR spectra recorded at different time during the photodegradation of propanoic acid on anatase under UV (365 nm) in the 2500–3900cm<sup>-1</sup> (a) and 1000–1850 cm<sup>-1</sup> (b) region.

In contrast, on rutile, where most propanoic acid is adsorbed in monodentate configuration, only negligible spectral differences are observed after extended illumination; and the propionate appears to be photostable on the surface. **(Figure 5.24)** **Figure 5.24a** shows that the OH stretching band increased and shifted towards a higher wavenumber ( $\sim 3632$  cm<sup>-1</sup>) during UV irradiation. Although only a small percentage of the substrate is degraded over rutile, the photo-excitation of the catalyst under UV leads the formation of reactive oxygen species (ROS) from the reduction/oxidation of water and oxygen by means of the electron/hole pair. This indicates that formation of this band can be attributed to photocatalytically generated H<sub>2</sub>O<sub>2</sub> as more stable photoproduct compared to the other ROS (HO<sup>•</sup>, HO<sub>2</sub><sup>•</sup>).[35] This observation is confirmed from some recent chemiluminescence studies performed by Kakuma et al.[36] They found that the generation rate and the adsorption of H<sub>2</sub>O<sub>2</sub> under UV light were significantly larger for rutile. In **Figure 5.24b** it can be clearly seen that the band of  $\nu(\text{C}=\text{O}) \sim 1712$  cm<sup>-1</sup> gradually decreases (black arrow) and in the meantime the band at 1538 cm<sup>-1</sup> of chemisorbed propionate show an increase in intensity (red arrows).

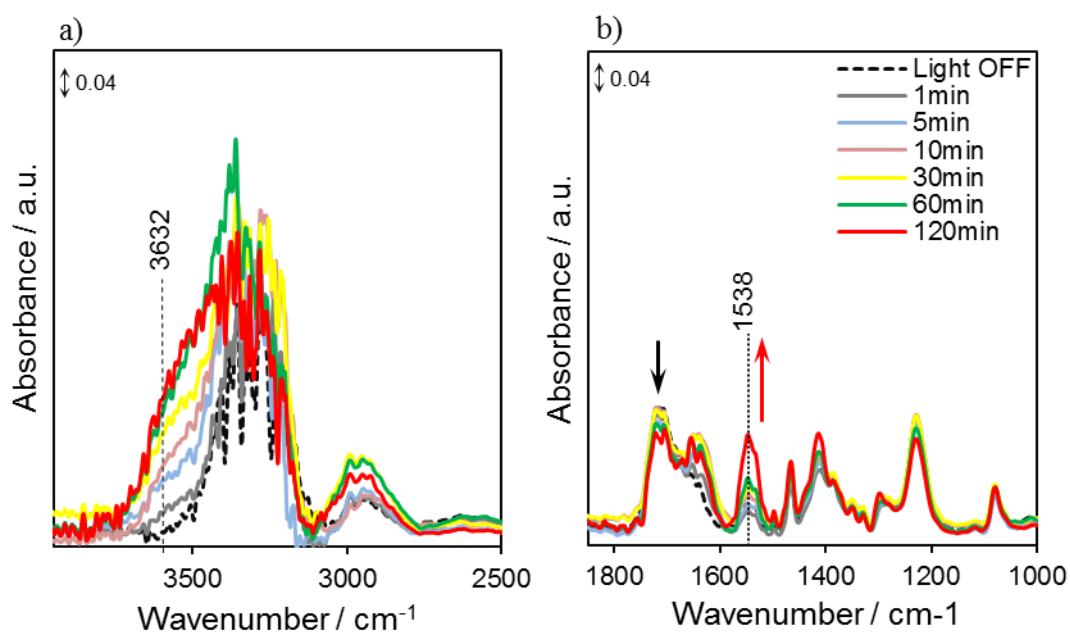


**Figure 5.24** ATR-IR spectra recorded at different time during the photodegradation of propanoic acid on rutile under UV (365 nm) in the 2500–3900 $\text{cm}^{-1}$  (a) and 1000–1850  $\text{cm}^{-1}$  (b) region.

**Figure 5.25** shows the time evolution of the measured peak areas of the physisorbed, the monodentate and bidentate configurations. The peak areas were measured from the subtracted spectra shown in **Figure 3, Appendix**.

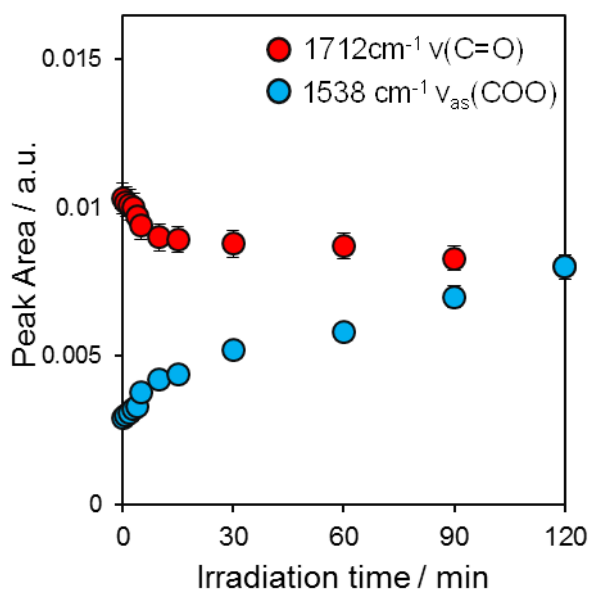


**Figure 5.25** Evolution of the peak areas related to the H-bonded acid  $\nu(\text{C}=\text{O})$  and propionate in bridging  $\nu(\text{COO}^-)$  configuration.

In agreement with previous studies the formation of bridging bidentate under irradiation is favoured but photo-stable on rutile. [14, 19, 37] Contrarily to anatase, the reaction does not proceed to photo-oxidized products. On rutile the most exposed surface is the (110) planes and propanoic acid dissociates on this facet as propionate remaining strongly bonded to the surface and this mechanism is exclusively detectable only by IR spectroscopy measurements.

Furthermore, even though there is the production of radical, active species, the photocatalytic oxidation of organic substrates on rutile seems to be limited to adsorbed substrates, with a very limited reaction zone confined on the surface. The higher photoactivity of anatase can be explained by its ability to generate more mobile radical species capable of migrating to the bulk solution and reacting with both surface-bound and unbound substrates/intermediates. (**Figure 5.26**) [38] These observations are consistent with the reaction profile detected by HPLC in the batch reaction. The rutile catalyst exhibited low activity, achieving only 10% conversion after 3 hours of irradiation and no intermediates could be detected in solution



**Figure 5.26** Illustration of OH-radical-mediated photocatalysis on anatase (left) and rutile (right), image from Reference [38].

#### 5.2.3.2.3 Proposed reaction mechanism

The proposed reaction mechanism summarize the results obtained from the photo-oxidation of propanoic acid performed in the batch reactor (HPLC data) and the surface species identified under irradiation by ATR IR spectroscopy for the three different TiO<sub>2</sub> catalysts. For the samples containing anatase, this parallel studies lead to the identification of three main organic intermediates: acetic acid (in solution), formic acid (adsorbed on the surface) and formaldehyde (weakly adsorbed on the surface and present in small concentration in solution). In **Figure 5.27** a schematic drawing of the reaction pathways for the photodegradation of propionic acid on TiO<sub>2</sub> P-25 sample is shown. The high propionic acid conversion (67%) measured by HPLC and the relatively low selectivity of acetic acid in solution compared to pure anatase (**Table 5.3**) can be explained as follows.

Initially, propionic acid ( $C_3$ ) was strongly bonded to the surface of  $TiO_2$  P-25 in the bridged bidentate configuration which is recognised as the main precursor for the photo-Kolbe decarboxylation.[39] This route (1) is initiated by a photo-generated hole ( $h^+$ ) and leads to  $CO_2$  and a carbon centred radical ( $C_2^\bullet$ ). In the presence of  $O_2$ , the formed alkyl radicals react with peroxy radicals ( $HO_2^\bullet$ ), and then decomposes to water and carbonylated intermediates (i.e. acetic acid) following the well-known Russell mechanism (route 3).[40, 41] Acetic acid can easily desorb from the surface [9] and in fact there are no signs in the ATR IR spectra of adsorbed acetic acid/acetate during the irradiation time whilst this oxidation product was measurable in solution after 40 min of irradiation.[9] However a low concentration of formaldehyde in solution and strong adsorbed formate signal from the ATR IR spectra were detected and these observations suggest other possible mechanisms. The second possible route (2) involves the hydroxylation by H-atom abstraction from the  $\alpha$ -carbon, followed by the formation of pyruvic acid. This intermediate was not detected in the present work but previous studies and isotopic investigation confirm the presence of this intermediate in the photocatalytic decomposition of propionic acid.[24, 41, 42] Pyruvic acid is not only a precursor of acetic acid (route 2-4-5) but offers a reasonable explanation for the formation of the other intermediates. Thus the proposed route (2-4-6) is consistent with the strong formate signal shown by the ATR IR measurements. It was observed that after the first 10 minutes of irradiation, the characteristic peaks of adsorbed formate grow more slowly and then start to decay for the extent of the illumination time because the formate species further decompose to  $CO_2$  in a single step reaction without forming long lived intermediates. [43] (**Figure 5.22**) On the other hand, the generation of formaldehyde dissolved in solution can be explained by the hydroxylation process followed by a photo-Kolbe decarboxylation (route 2-4-7-8). Finally, for completeness, the possibility of hydroxyl radicals attack at the  $\beta$ -carbon (route 9) is reported but in this system no evidence of the possible intermediates deriving from this mechanism was observed.

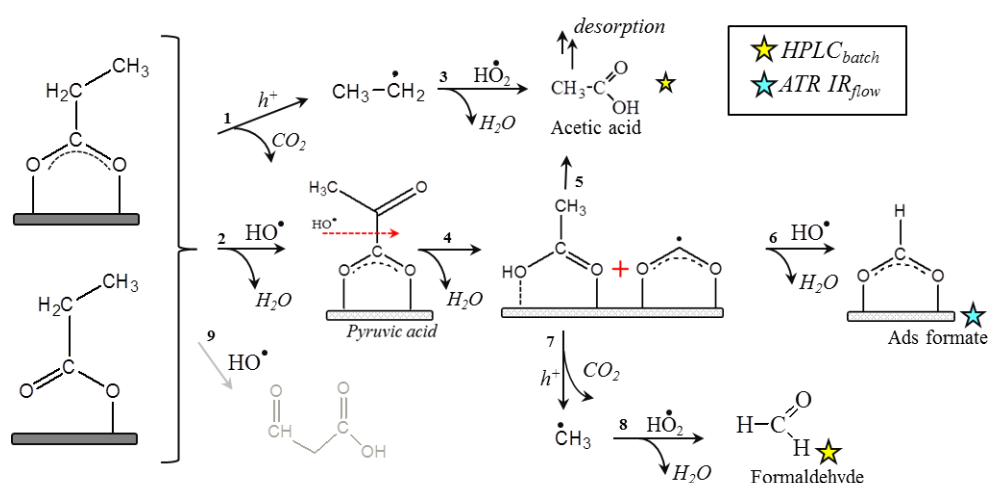


**Figure 5.27** Proposed reaction mechanism for of propanoic acid over  $TiO_2$  P-25.

The comparative study between P-25 and pure anatase leads to the conclusion that, for the latter, degradation of propanoic acid mainly proceeds through direct photo-Kolbe decarboxylation with higher production of acetic acid [19] and CO<sub>2</sub> (route 1-3). Thus on anatase propanoic acid readily oxidizes to acetic acid but the reaction cannot proceed further due to the low affinity of this product with the TiO<sub>2</sub> surface. On P-25 the presence of rutile (~20 %) might contribute to stabilize the adsorbed intermediates allowing the reaction to proceed to different routes. The synergistic effect between the two phases can explain the higher propanoic acid conversion and the formation of smaller intermediates (i.e. formaldehyde and strong adsorbed formate). These observations are supported by the HPLC analysis and further confirmed by the measurements of the CO<sub>2</sub> peak area of the IR spectra, as shown in **Figure 5.28**.

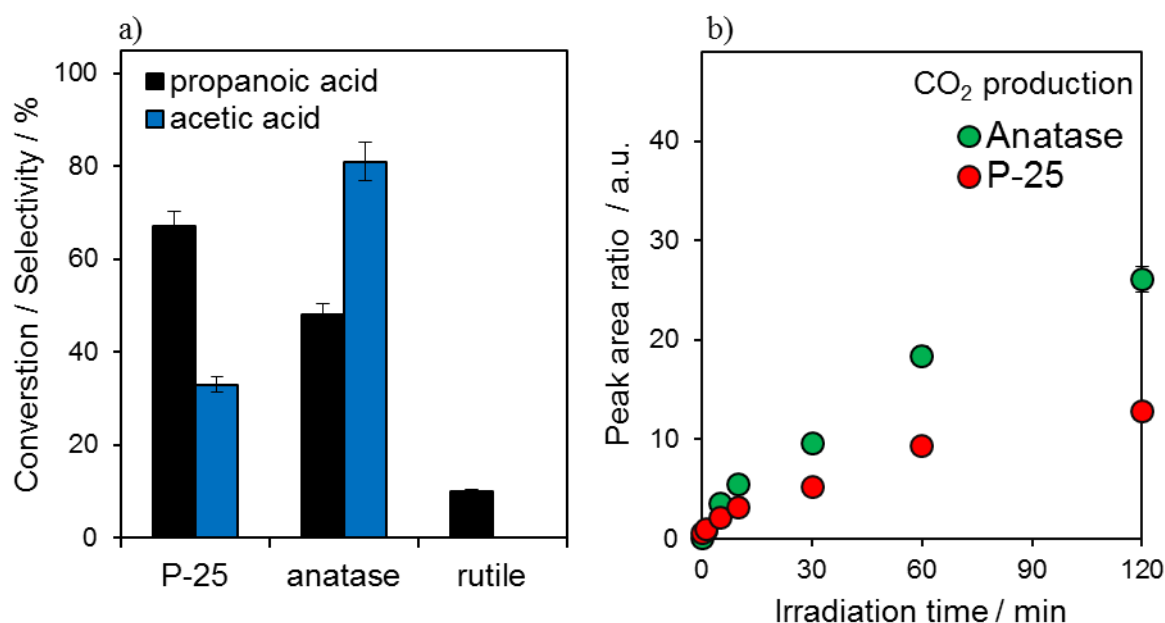


**Figure 5.28** Conversion-selectivity plot for the three TiO<sub>2</sub> samples (a); evolution during the irradiation time of the peak area ratio  $\nu(\text{CO}_2)/\nu(\text{C-C})$  evaluated for P-25 and anatase (b).

#### 5.2.4 Effect of pH

The pH effect was investigated because it may influence the surface charge on the photocatalyst, the amount of produced HO<sup>•</sup>, the state of ionization of the substrate and its adsorption efficacy.[12]

The effect of pH on the photodegradation of propanoic acid was studied in the pH range 3-8. An aqueous solution of ammonia was added to adjust the pH of the propanoic acid solution. With no pH correction the stock solution has measured pH value of 3. Values of pH 6.3 and 8 were obtained after ammonia correction. The solution at higher pH was used for a photocatalytic test in the ATR flow cell to investigate the effect of pH on the surface interactions. **Figure 5.29a-b** show the normalised reaction profile of photocatalytic degradation of propanoic acid and the initial rates in the range of pH 3-8, respectively.



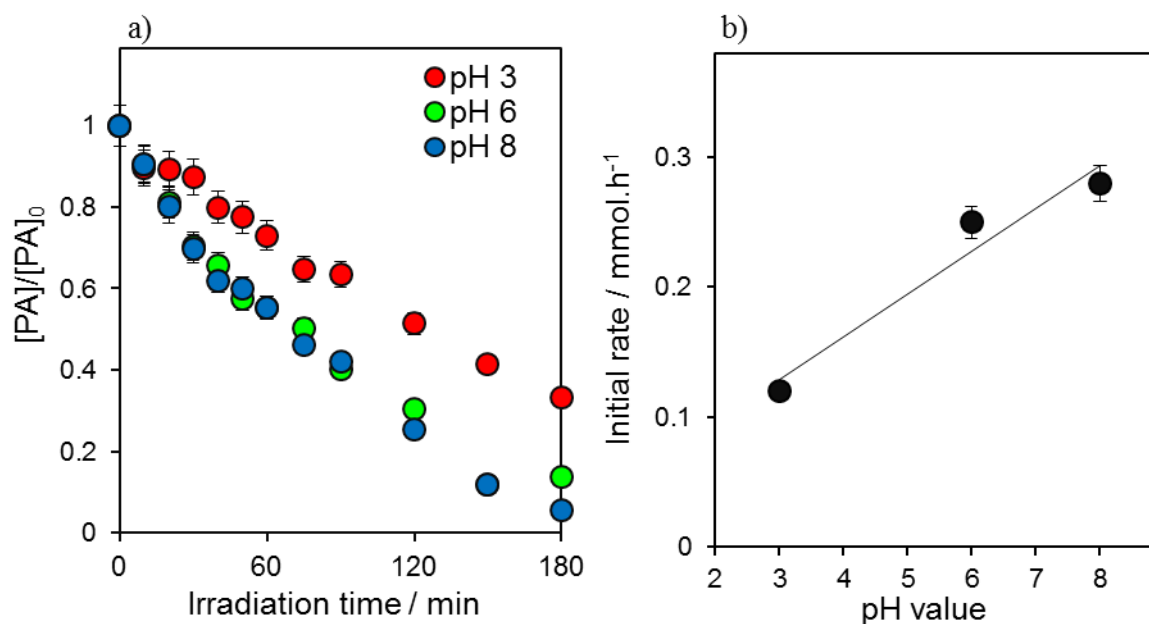


**Figure 5.29** Comparison of the photocatalytic degradation of propionic acid over TiO<sub>2</sub> P-25 at different pH under UV light (a) Trend of the initial rate with the pH value (b).

The reaction profiles of propanoic acid degradation and detected intermediates at pH 6 and 8 are reported in **Figure 5.30**. It is interesting to note that increasing the pH, the initial rates and the propanoic acid conversions increase. In addition also the acetic acid selectivity increases with the pH, suggesting that the product distribution is pH dependent.

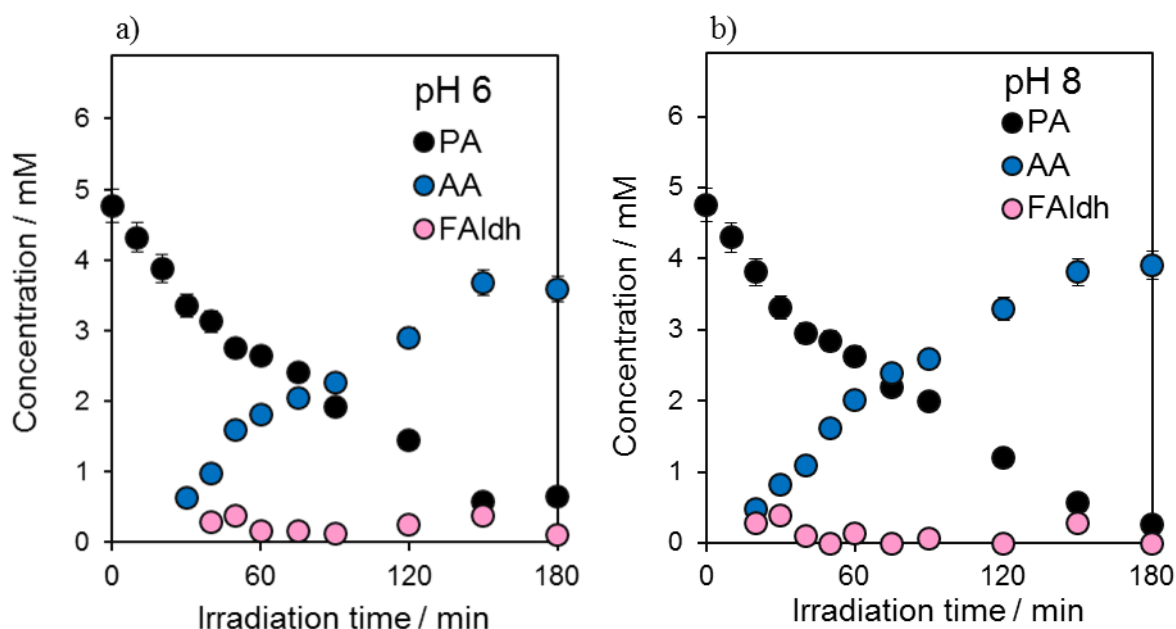


**Figure 5.30** Reaction profile of oxidation propionic acid over TiO<sub>2</sub> P-25 with relative intermediates detected by HPLC analysis at pH 6 (a) and 8 (b).

**Table 5.4** summarises the initial rate, conversions and the yields of the photodegradation reactions.

**Table 5.4** Experimental results of the propanoic acid photooxidation over P-25 at different pH.

pH	$r^0$ <sup>a</sup> / mmol.h <sup>-1</sup>	Conversion <sup>b</sup> %	Intermediates	Yields <sup>c</sup> %	Selectivity <sup>c</sup> %
3	0.12	67	CH <sub>3</sub> COOH	22	33
			CH <sub>2</sub> O	2	3
6	0.25	86	CH <sub>3</sub> COOH	75	87
			CH <sub>2</sub> O	0	2
8	0.28	94	CH <sub>3</sub> COOH	82	87
			CH <sub>2</sub> O	-	-

[a] Initial reaction rate evaluated in the first 40 mins

[b] Final propanoic acid conversion

[c] Final values of yield and selectivity of the detected intermediates

In first place the pH modification can induce changes in the adsorption mode of propanoic acid. In **Figure 5.31** the spectra at adsorption equilibrium are reported in order to compare the different affinity of propanoic acid with TiO<sub>2</sub> surface, the spectra of acid in solution are reported for comparison. At pH 8 the solution is well above the pK<sub>a</sub> (4.87) of the carboxylic acid group and thus all the acid is deprotonated. Observing the spectrum of propanoic acid in solution (dotted blue line) it can be seen that the peak at 1712 cm<sup>-1</sup> of carbonyl stretching  $\nu(\text{C=O})$  is weakened by the neighbouring COO<sup>-</sup> group which shows a sharp absorption peak at ~1538 cm<sup>-1</sup>, absent at pH 3 where only the 1.3% of the acid is deprotonated. In presence of catalyst, the relative peaks intensity change (bold lines). It is well known that the affinity of carboxylate for the surface of metal oxides increases with decreasing pH.[12] The isoelectric point (IEP) of the TiO<sub>2</sub> (Degussa P-25) is at pH 6.8, thus in acidic media TiO<sub>2</sub> surface is positively charged and the electrostatic attraction between the surface and the acid promotes the adsorption. In alkaline conditions (pH > 6.8), there is an increasing of the TiO<sup>-</sup> groups density and also the acid molecules are negatively charged, thus, due to electrostatic repulsion, the acid is scarcely adsorbed.

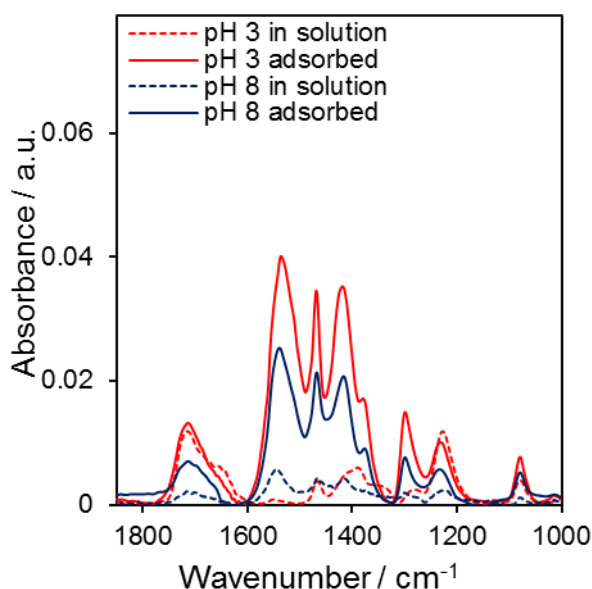


**Figure 5.31** ATR-FTIR spectra of propionic acid at pH 3 and 8 in aqueous solution (dotted lines) and adsorbed on TiO<sub>2</sub> P-25 nanoparticle (bold lines).

**Figure 5.32** shows a schematic drawing of the affinity of propionic acid in solution and the surface of metal oxide with the varying of pH.

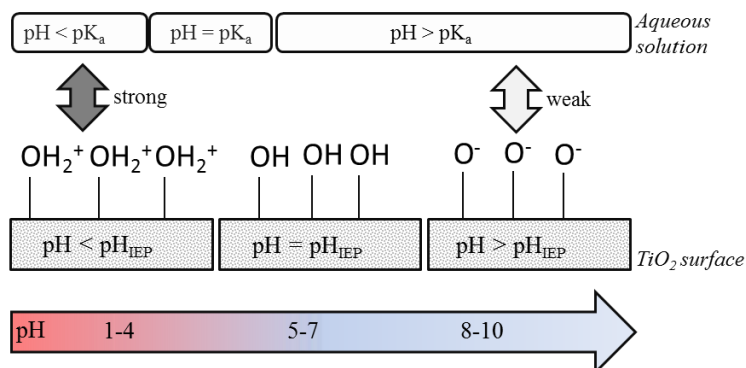


**Figure 5.32** Schematic illustration of the adsorption of carboxylic acid on the TiO<sub>2</sub> surface relatively to the pH of the solution and isoelectric point (IEP) of TiO<sub>2</sub>.

Despite the low affinity between the target molecule and catalyst surface, the photodegradation was significantly enhanced at high pH. The high activity can be explained with more efficient formation of hydroxyl radicals in alkaline solution, due to the high concentration of HO<sup>-</sup> ions.[44] Previous studies also confirm that the activity of hydroxyl radicals is higher on dissociated species (i.e. propionate).[45] In the previous section (**Figure 5.27** in **Section 5.2.3.2.3**) two main pathways were identified for the photodegradation of propanoic acid over TiO<sub>2</sub> P-25.

The ATR IR spectroscopy can help to elucidate which route is favoured under UV at different pH. The spectral development of propionic acid adsorption under UV illumination at pH 8 is shown in **Figure 5.33**. Under UV, the band of adsorbed water centred at  $3250\text{ cm}^{-1}$  drastically decreases in the first 10 minutes of irradiation, as shown in **Figure 5.33a** (black arrow). For extended irradiation time the OH band decreases and shifts towards higher wavenumber ( $\sim 3480\text{ cm}^{-1}$ ) which can be due to the production of hydrogen peroxide ( $\text{H}_2\text{O}_2$ ) species.[11, 46] On the other hand, the carboxylate region under UV shows more affinities with the spectra recorded in acidic conditions, as shown in **Figure 5.33b**. However at pH 8 the spectral changes show a small evolution in the carboxylate region, with initial rapid increasing of the absorption band of formate ( $1590\text{ cm}^{-1}$  and  $1384\text{ cm}^{-1}$ ) in the first 30 min of irradiation and a negligible decreasing in peak intensities for extended irradiation time. This observation is in line with the reduced adsorption affinity between the acid and the catalyst surface in alkaline conditions, suggesting that at pH 8 the small amount of adsorbed propionic acid initially reacts through photo-Kolbe mechanism with formation of  $\text{CO}_2$  to then proceed to other routes.

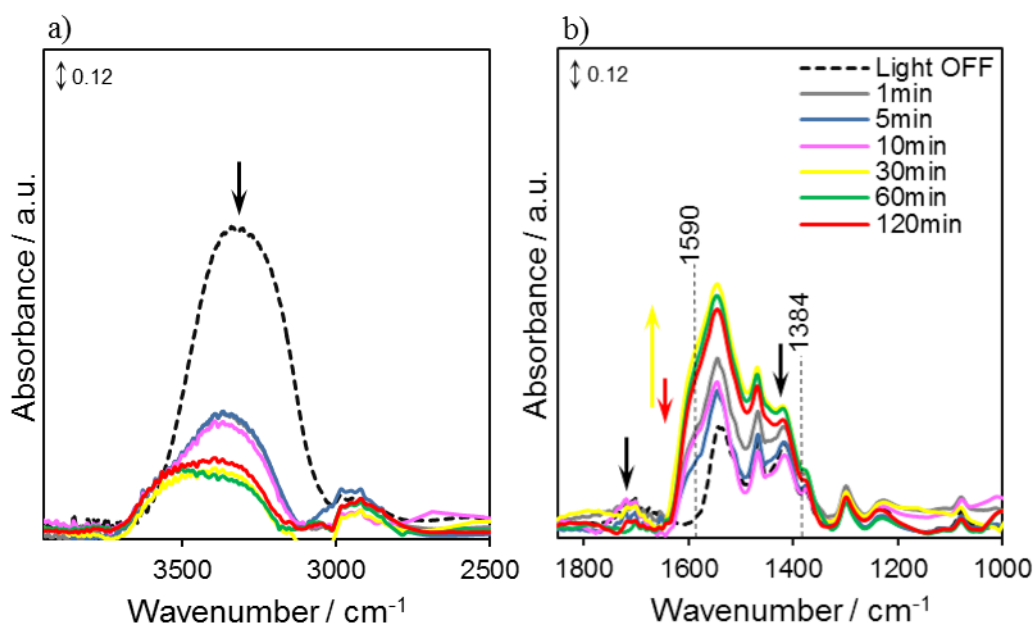


**Figure 5.33** ATR-IR spectra recorded at different time during the photodegradation of propionic acid on  $\text{TiO}_2$  P-25 under UV (365 nm) at pH 8 in the  $2500\text{--}3900\text{ cm}^{-1}$  (a) and  $1000\text{--}1850\text{ cm}^{-1}$  (b) region. Spectra were collected during 2 hours illumination at different times and spectra of  $\text{TiO}_2$  samples saturated with propionic acid solution prior to illumination were used as background in each measurement.

**Figure 5.34b** shows the HPLC data with higher propionic acid conversion and acetic acid selectivity at pH 6 and 8. In **Figure 5.34b** the peak ratio  $\text{CO}_2 / \text{v(C-C)}$  highlights that in alkaline condition the formation of  $\text{CO}_2$  results to be faster in the first 30 min until reached a constant value, lower than the one observed at pH 3.

Considering that  $\text{CO}_2$  is the product of direct hole oxidation through the photo-Kolbe mechanism, these results suggest that at pH 8 the favourite route for oxidation of propanoic acid is through hydroxyl radical attack. This observation could explain the high acetic acid selectivity, due to a double contribution of hole and  $\text{HO}^\bullet$  attack (See route 1-3 and 2-4-5, **Figure 5.27**), and also the formation of formaldehyde in solution within the first hour of irradiation (route 2-8, **Figure 5.27**). All these results confirm the strongly dependence of the fate of the photocatalytic reaction from the pH conditions which influence the interaction substrate-catalyst, the adsorption of water on catalyst surface and subsequently the formation of reactive species and sub-products.

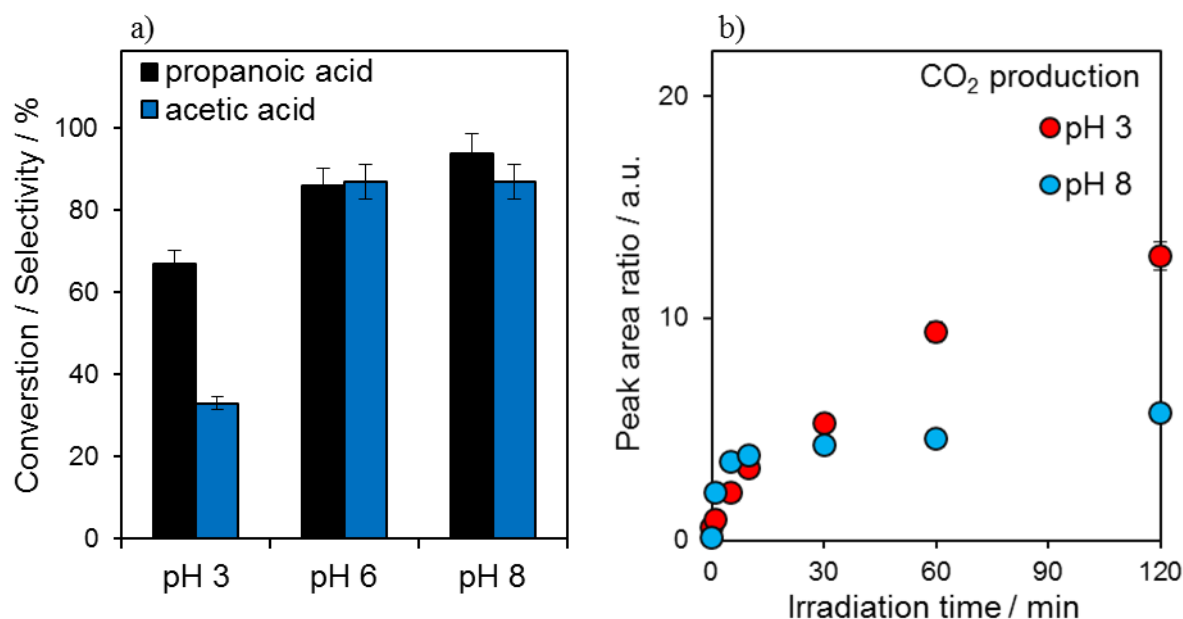


**Figure 5.34** Conversion-selectivity plot for the three pH values (a); evolution during the irradiation time of the peak area ratio  $\nu(\text{CO}_2)/\nu(\text{C-C})$ .

### 5.3 Conclusions

In this chapter the adsorption and photodecomposition of propanoic acid over a  $\text{TiO}_2$  film was investigated by *in situ* ATR-IR spectroscopy, aiming at identifying different surface complexes for propanoic acid adsorbed on the surface of P-25, anatase and rutile and demonstrating the dependence of the reaction mechanism from the adsorption modes. Significantly, the identification of a reaction mechanism was achieved by simultaneous but separate detection of reaction intermediates in liquid phase (batch reactor) and as surface species (ATR flow reactor).

Adsorption kinetic studies reveal that propanoic acid bonds more strongly to P-25 and anatase in bidentate configuration and more weakly to rutile in monodentate mode. The surface density of acidic sites offers a potential explanation for differences of adsorptions modes, thus the higher number of adjacent Lewis acid sites on the anatase surface increases the probability of having the molecule bonded to the surface in the bidentate configuration.

This configuration is recognised as the main precursor for the direct hole oxidation through photo-Kolbe mechanism, which leads to CO<sub>2</sub> and acetic acid. Upon illumination the coverage of adsorbed propanoic acid on P-25 and anatase decreased and adsorbed CO<sub>2</sub> was observed and measured on the TiO<sub>2</sub> surface and acetic acid detected in solution. On rutile the formation of bridging bidentate configuration is a rate determining step for photo-decomposition of propanoic acid and after 3 hours of irradiation only ATR spectral change were observed and no intermediates detected in solutions. The second possible identified route was the hydroxyl attack with H-abstraction and formation of water. Formate was a main intermediate surface product on P-25 and anatase. It was observed that coordinated formate is preferred on P-25, whereas formate ions form on anatase, which is displayed by the typical broad peak at  $\nu_a(\text{COO}) \sim 1590 \text{ cm}^{-1}$ . More molecular water on the surface of anatase tends to displace acetic acid, which was detected with high selectivity in solution compared to P-25. In general, surface IR spectra showed that P-25 exhibits large similarities with anatase but the highest final conversion of propanoic acid and the higher formaldehyde selectivity suggest the possibility of more reaction pathway for P-25, probably due to the contribution of rutile which is able to stabilize the adsorption of intermediates to the catalyst surface. Finally, the role of pH on the reaction mechanism was investigated. In alkaline media the reaction rate showed an increasing in activity with high propanoic acid conversion and acetic acid yield, with formation of formaldehyde within the first 30 minutes of irradiation. At pH 8 molecules and catalyst surface are negatively charged but, despite the low adsorption affinity, alkaline media promote the formation of hydroxyl radicals which are the main responsible of acid degradation.

## 5.4 References

- [1] A. J. McQuillan, "Probing solid-solution interfacial chemistry with ATR-IR spectroscopy of particle films," *Advanced Materials*, vol. 13, pp. 1034-+, Jul 4 2001.
- [2] S. J. Hug and B. Sulzberger, "In-Situ Fourier-Transform Infrared Spectroscopic Evidence for the Formation of Several Different Surface Complexes of Oxalate on TiO<sub>2</sub> in the Aqueous-Phase," *Langmuir*, vol. 10, pp. 3587-3597, Oct 1994.
- [3] K. D. Dobson and A. J. McQuillan, "In situ infrared spectroscopic analysis of the adsorption of aliphatic carboxylic acids to TiO<sub>2</sub>, ZrO<sub>2</sub>, Al<sub>2</sub>O<sub>3</sub>, and Ta<sub>2</sub>O<sub>5</sub> from aqueous solutions," *Spectrochimica Acta Part a-Molecular and Biomolecular Spectroscopy*, vol. 55, pp. 1395-1405, Jul 1999.
- [4] A. G. Young and A. J. McQuillan, "Adsorption/Desorption Kinetics from ATR-IR Spectroscopy. Aqueous Oxalic Acid on Anatase TiO<sub>2</sub>," *Langmuir*, vol. 25, pp. 3538-3548, Mar 17 2009.
- [5] S. J. Hug and D. Bahnemann, "Infrared spectra of oxalate, malonate and succinate adsorbed on the aqueous surface of rutile, anatase and lepidocrocite measured with in situ ATR-FTIR," *Journal of Electron Spectroscopy and Related Phenomena*, vol. 150, pp. 208-219, Feb 2006.

- [6] C. B. Mendive, D. W. Bahnemann, and M. A. Blesa, "Microscopic characterization of the photocatalytic oxidation of oxalic acid adsorbed onto TiO<sub>2</sub> by FTIR-ATR," *Catalysis Today*, vol. 101, pp. 237-244, Apr 15 2005.
- [7] C. B. Mendive, T. Bredow, J. Schneider, M. Blesa, and D. Bahnemann, "Oxalic acid at the TiO<sub>2</sub>/water interface under UV(A) illumination: Surface reaction mechanisms," *Journal of Catalysis*, vol. 322, pp. 60-72, Feb 2015.
- [8] C. B. Mendive, T. Bredow, A. Feldhoff, M. Blesa, and D. Bahnemann, "Adsorption of oxalate on rutile particles in aqueous solutions: a spectroscopic, electron-microscopic and theoretical study," *Physical Chemistry Chemical Physics*, vol. 10, pp. 1960-1974, 2008.
- [9] C. B. Mendive, T. Bredow, A. Feldhoff, M. A. Blesa, and D. Bahnemann, "Adsorption of oxalate on anatase (100) and rutile (110) surfaces in aqueous systems: experimental results vs. theoretical predictions," *Physical Chemistry Chemical Physics*, vol. 11, pp. 1794-1808, 2009.
- [10] I. Dolamic and T. Burgi, "Photocatalysis of dicarboxylic acids over TiO<sub>2</sub>: An in situ ATR-IR study," *Journal of Catalysis*, vol. 248, pp. 268-276, Jun 10 2007.
- [11] H. Belhadj, A. Hakki, P. K. J. Robertson, and D. W. Bahnemann, "In situ ATR-FTIR study of H<sub>2</sub>O and D<sub>2</sub>O adsorption on TiO<sub>2</sub> under UV irradiation," *Physical Chemistry Chemical Physics*, vol. 17, pp. 22940-22946, 2015.
- [12] M. A. Blesa, A. D. Weisz, P. J. Morando, J. A. Salfity, G. E. Magaz, and A. E. Regazzoni, "The interaction of metal oxide surfaces with complexing agents dissolved in water," *Coordination Chemistry Reviews*, vol. 196, pp. 31-63, Jan 2000.
- [13] W. K. Li, X. Q. Gong, G. Lu, and A. Selloni, "Different reactivities of TiO<sub>2</sub> polymorphs: Comparative DFT calculations of water and formic acid adsorption at anatase and brookite TiO<sub>2</sub> surfaces," *Journal of Physical Chemistry C*, vol. 112, pp. 6594-6596, May 1 2008.
- [14] T. van der Meulen, A. Mattson, and L. Osterlund, "A comparative study of the photocatalytic oxidation of propane on anatase, rutile, and mixed-phase anatase-rutile TiO<sub>2</sub> nanoparticles: Role of surface intermediates," *Journal of Catalysis*, vol. 251, pp. 131-144, Oct 1 2007.
- [15] L. F. Liao, C. F. Lien, and J. L. Lin, "FTIR study of adsorption and photoreactions of acetic acid on TiO<sub>2</sub>," *Physical Chemistry Chemical Physics*, vol. 3, pp. 3831-3837, 2001.
- [16] C. E. Nanayakkara, J. K. Dillon, and V. H. Grassian, "Surface Adsorption and Photochemistry of Gas-Phase Formic Acid on TiO<sub>2</sub> Nanoparticles: The Role of Adsorbed Water in Surface Coordination, Adsorption Kinetics, and Rate of Photoproduct Formation," *Journal of Physical Chemistry C*, vol. 118, pp. 25487-25495, Nov 6 2014.
- [17] L. W. Miller, M. I. Tejedor-Tejedor, and M. A. Anderson, "Titanium dioxide-coated silica waveguides for the photocatalytic oxidation of formic acid in water," *Environmental Science & Technology*, vol. 33, pp. 2070-2075, Jun 15 1999.
- [18] A. W. Adamson and A. P. Gast, "Physical chemistry of surfaces."

- [19] F. P. Rotzinger, J. M. Kesselman-Truttmann, S. J. Hug, V. Shklover, and M. Gratzel, "Structure and vibrational spectrum of formate and acetate adsorbed from aqueous solution onto the TiO<sub>2</sub> rutile (110) surface," *Journal of Physical Chemistry B*, vol. 108, pp. 5004-5017, Apr 22 2004.
- [20] A. Mattsson and L. Osterlund, "Adsorption and Photoinduced Decomposition of Acetone and Acetic Acid on Anatase, Brookite, and Rutile TiO<sub>2</sub> Nanoparticles," *Journal of Physical Chemistry C*, vol. 114, pp. 14121-14132, Aug 26 2010.
- [21] G. Busca, J. Lamotte, J. C. Lavalley, and V. Lorenzelli, "FT-IR study of the adsorption and transformation of formaldehyde on oxide surfaces," *Journal of the American Chemical Society*, vol. 109, pp. 5197-5202, 1987/08/01 1987.
- [22] N. Jaffrezicrenault, P. Pichat, A. Foissy, and R. Mercier, "Effect of Deposited Pt Particles on the Surface-Charge of TiO<sub>2</sub> Aqueous Suspensions by Potentiometry, Electrophoresis, and Labeled Ion Adsorption," *Journal of Physical Chemistry*, vol. 90, pp. 2733-2738, Jun 5 1986.
- [23] J. F. Fan and J. T. Yates, "Infrared Study of the Oxidation of Hexafluoropropene on TiO<sub>2</sub>," *Journal of Physical Chemistry*, vol. 98, pp. 10621-10627, Oct 13 1994.
- [24] B. Wen, Y. Li, C. C. Chen, W. H. Ma, and J. C. Zhao, "An Unexplored O-2-Involved Pathway for the Decarboxylation of Saturated Carboxylic Acids by TiO<sub>2</sub> Photocatalysis: An Isotopic Probe Study," *Chemistry-a European Journal*, vol. 16, pp. 11859-11866, 2010.
- [25] F. Nunzi and F. De Angelis, "DFT Investigations of Formic Acid Adsorption on Single-Wall TiO<sub>2</sub> Nanotubes: Effect of the Surface Curvature," *Journal of Physical Chemistry C*, vol. 115, pp. 2179-2186, Feb 10 2011.
- [26] S. Manzhos, G. Giorgi, and K. Yamashita, "A Density Functional Tight Binding Study of Acetic Acid Adsorption on Crystalline and Amorphous Surfaces of Titania," *Molecules*, vol. 20, pp. 3371-3388, Feb 2015.
- [27] D. C. Grinter, M. Nicotra, and G. Thornton, "Acetic Acid Adsorption on Anatase TiO<sub>2</sub>(101)," *Journal of Physical Chemistry C*, vol. 116, pp. 11643-11651, May 31 2012.
- [28] R. Su, R. Bechstein, L. So, R. T. Vang, M. Sillassen, B. Esbjornsson, *et al.*, "How the Anatase-to-Rutile Ratio Influences the Photoreactivity of TiO<sub>2</sub>," *Journal of Physical Chemistry C*, vol. 115, pp. 24287-24292, Dec 15 2011.
- [29] Y. K. Chen, Y. F. Lin, Z. W. Peng, and J. L. Lin, "Transmission FT-IR Study on the Adsorption and Reactions of Lactic Acid and Poly(lactic acid) on TiO<sub>2</sub>," *Journal of Physical Chemistry C*, vol. 114, pp. 17720-17727, Oct 21 2010.
- [30] P. Z. Araujo, C. B. Mendive, L. A. G. Rodenas, P. J. Morando, A. E. Regazzoni, M. A. Blesa, *et al.*, "FT-IR-ATR as a tool to probe photocatalytic interfaces," *Colloids and Surfaces a-Physicochemical and Engineering Aspects*, vol. 265, pp. 73-80, Sep 1 2005.
- [31] O. M. Busch, W. Brijoux, S. Thomson, and F. Schuth, "Spatially resolving infrared spectroscopy for parallelized characterization of acid sites of catalysts via pyridine



- sorption: Possibilities and limitations," *Journal of Catalysis*, vol. 222, pp. 174-179, Feb 15 2004.
- [32] N. Serpone, J. Martin, S. Horikoshi, and H. Hidaka, "Photocatalyzed oxidation and mineralization of C1-C5 linear aliphatic acids in UV-irradiated aqueous titania dispersions-kinetics, identification of intermediates and quantum yields," *Journal of Photochemistry and Photobiology a-Chemistry*, vol. 169, pp. 235-251, Feb 5 2005.
- [33] M. R. Hoffmann, S. T. Martin, W. Y. Choi, and D. W. Bahnemann, "Environmental Applications of Semiconductor Photocatalysis," *Chemical Reviews*, vol. 95, pp. 69-96, Jan-Feb 1995.
- [34] M. J. Backes, A. C. Lukaski, and D. S. Muggli, "Active sites and effects of H<sub>2</sub>O and temperature on the photocatalytic oxidation of C-13-acetic acid on TiO<sub>2</sub>," *Applied Catalysis B-Environmental*, vol. 61, pp. 21-35, Oct 27 2005.
- [35] H. Belhadj, S. Melchers, P. K. J. Robertson, and D. W. Bahnemann, "Pathways of the photocatalytic reaction of acetate in H<sub>2</sub>O and D<sub>2</sub>O: A combined EPR and ATR-FTIR study," *Journal of Catalysis*, vol. 344, pp. 831-840, Dec 2016.
- [36] Y. Kakuma, A. Y. Nosaka, and Y. Nosaka, "Difference in TiO<sub>2</sub> photocatalytic mechanism between rutile and anatase studied by the detection of active oxygen and surface species in water," *Physical Chemistry Chemical Physics*, vol. 17, pp. 18691-18698, 2015.
- [37] M. Andersson, A. Kiselev, L. Osterlund, and A. E. C. Palmqvist, "Microemulsion-mediated room-temperature synthesis of high-surface-area rutile and its photocatalytic performance," *Journal of Physical Chemistry C*, vol. 111, pp. 6789-6797, May 10 2007.
- [38] W. Kim, T. Tachikawa, G. H. Moon, T. Majima, and W. Choi, "Molecular-Level Understanding of the Photocatalytic Activity Difference between Anatase and Rutile Nanoparticles," *Angewandte Chemie-International Edition*, vol. 53, pp. 14036-14041, Dec 15 2014.
- [39] B. Kraeutler and A. J. Bard, "Heterogeneous Photocatalytic Decomposition of Saturated Carboxylic-Acids on TiO<sub>2</sub> Powder - Decarboxylative Route to Alkanes," *Journal of the American Chemical Society*, vol. 100, pp. 5985-5992, 1978.
- [40] G. A. Russell, "Deuterium-isotope Effects in the Autoxidation of Alkyl Hydrocarbons. Mechanism of the Interaction of Peroxy Radicals," *Journal of the American Chemical Society*, vol. 79, pp. 3871-3877, 1957.
- [41] X. B. Pang, W. Chang, C. C. Chen, H. W. Ji, W. H. Ma, and J. C. Zhao, "Determining the TiO<sub>2</sub>-Photocatalytic Aryl-Ring-Opening Mechanism in Aqueous Solution Using Oxygen-18 Labeled O<sub>2</sub> and H<sub>2</sub>O," *Journal of the American Chemical Society*, vol. 136, pp. 8714-8721, Jun 18 2014.
- [42] Y. Ogata, K. Tomizawa, and K. Takagi, "Photo-Oxidation of Formic, Acetic, and Propionic Acids with Aqueous Hydrogen-Peroxide," *Canadian Journal of Chemistry-Revue Canadienne De Chimie*, vol. 59, pp. 14-18, 1981.

- [43] D. S. Muggli and L. F. Ding, "Photocatalytic performance of sulfated TiO<sub>2</sub> and Degussa P-25TiO<sub>2</sub> during oxidation of organics," *Applied Catalysis B-Environmental*, vol. 32, pp. 181-194, Aug 1 2001.
- [44] M. Trillas, J. Peral, and X. Domenech, "Photocatalyzed degradation of phenol, 2,4-dichlorophenol, phenoxyacetic acid and 2,4-dichlorophenoxyacetic acid over supported TiO<sub>2</sub> in a flow system," *Journal of Chemical Technology and Biotechnology*, vol. 67, pp. 237-242, Nov 1996.
- [45] G. V. Buxton, C. L. Greenstock, W. P. Helman, and A. B. Ross, "Critical-Review of Rate Constants for Reactions of Hydrated Electrons, Hydrogen-Atoms and Hydroxyl Radicals (.Oh/.O-) in Aqueous-Solution," *Journal of Physical and Chemical Reference Data*, vol. 17, pp. 513-886, 1988.
- [46] R. Nakamura, A. Imanishi, K. Murakoshi, and Y. Nakato, "In situ FTIR studies of primary intermediates of photocatalytic reactions on nanocrystalline TiO<sub>2</sub> films in contact with aqueous solutions," *Journal of the American Chemical Society*, vol. 125, pp. 7443-7450, Jun 18 2003.

## *Chapter 6*

### *Conclusions and future work*

## 6. Conclusions and future work

### 6.1. Conclusions

Heterogeneous photocatalysis has been found to be an effective solution for the removal of organic contaminants from wastewater. This thesis set out to explore the structure reactivity correlations in nanostructured titania photocatalysts for the degradation of aqueous organic pollutants, combined with *in-situ* ATR studies.

During the course of this research work, a number of conclusions have been reached, regarding the preparation, characterization and reactivity of TiO<sub>2</sub> based photocatalysts. Two approaches were taken utilising first mesoporous SBA-15 and then macro-mesoporous SBA-15 as a scaffolds to obtain a uniform titania coating via a grafting method. The photoactivity of these materials was explored through their application in dye degradation under UV-vis light which is an important reaction for the waste water treatment.

In the first approach TiO<sub>2</sub>-SBA-15 materials were prepared by successive graftings of titanium isopropoxide on dehydrated mesoporous SBA-15. A series of three supports was synthesized at different aging temperatures in order to systematically tune the pore size and the TiO<sub>2</sub> content was set at 8-18 wt. %.

The influence of the pore size of silica supports on the dispersion of TiO<sub>2</sub> was demonstrated and SBA-15 with large mesopores of around 7 nm (synthesized at 120°C) produced the most effective catalyst. Characterization of the catalysts by N<sub>2</sub> porosimetry confirmed that the grafting of TiO<sub>2</sub> exhibits a systematic decreasing of pore size with no bimodal distribution observed in the BJH plot compared to the other two supports with smaller mesopores size. Moreover no crystalline anatase was observed by XRD analysis. Considering also the molecular length of methyl orange (~1.2 nm), large mesopore size avoids mass-transport problems due to the accessibility of the dye molecule to the internal surface area of the photocatalyst.

Going forwards, SBA-15 synthesized at 120°C was used as an optimal host support and the TiO<sub>2</sub> content of the composites was varied from 12 to 43 wt. %. At TiO<sub>2</sub> loadings higher than 30 wt.%, crystalline anatase was observed by XRD and Raman. The results show that E<sub>g</sub> decreases with the increase of titania content, which affects the photoactivity of synthesized material on the degradation of MO.

After five successive grafting procedures, the sample with highest TiO<sub>2</sub> loading (43 wt.%) was found to possess a relatively high surface area (~300 m<sup>2</sup>.g<sup>-1</sup>), readily accessible mesopore for the target molecule (~3.8 nm) and a band gap value comparable to the commercial titania references (3.2 eV). These properties affect the photoactivity of the composite which exhibits the highest initial rate of MO degradation (87 ppm.h<sup>-1</sup>.gr<sub>cat</sub><sup>-1</sup>) over both synthesised series of mesoporous photocatalysts.

In the second approach enhancement of textural and optical properties of these materials was attempted and achieved through grafting of titania on hierarchical SBA-15 support.

The aims in this stage were to develop an ordered hierarchical photocatalyst through grafting of  $\text{TiO}_2$  nanoparticle in photonic supports (macro-mesoporous SBA-15), and investigate the effects of the photonic structure on the photocatalytic activity.

Initially the grafting method was applied on supports with three different macropores size with a titania loading set at ~10 wt. %. It was found that introducing the hierarchical structure markedly increases the photocatalytic activity of the composite samples of about ~30 % compared to the mesoporous catalysts with the same  $\text{TiO}_2$  loading and similar mesopores size. Enhancements of initial reaction rates relevant to dye degradation by slow photons at the blue edge of a photonic stop band have been reported for the samples with 200 and 600 nm macropore size.

Secondly a further study was performed on the support with 400 nm macropore size to investigate the effect of the  $\text{TiO}_2$  loading on the photonic support. The PBG intensity was observed to significantly broaden and reduce with increasing titania loading in the range of 10-23 wt. %.

Modification of optical properties leads to an increasing of the efficiency in the photocatalytic oxidation of MO in terms of initial rate and the results show that the most active catalysts resulted to be 400-3 with the highest  $\text{TiO}_2$  loading.

In conclusion this work reports the successful synthesis of ordered hierarchical system with high specific surface area and a three-dimensionally continuous structure with the properties of a photonic crystal. These features make the new material a highly effective photocatalyst since the diffusion resistance is minimized and the efficiency of photoabsorption is enhanced.

In the final section of this research work, attenuated total reflection infrared (ATR-IR) spectroscopy was used to study the adsorption and photodegradation processes of carboxylic acids onto titanium dioxide film. The photodegradation of propanoic acid on P-25  $\text{TiO}_2$  and on pure anatase and rutile phases was followed in situ. Analysis of ATR IR spectra indicates that propanoic acid bonds stronger to P-25 and anatase in bidentate configuration and weaker to rutile. Upon illumination the spectral evolution of adsorbed propanoic acid demonstrates adsorption mode-dependent reaction pathways.

For example formate is the main intermediate species detected on P-25 and anatase surface when propanoic acid is photodecomposed; whereas on rutile, coordinated propionate in bidentate configuration is formed and it is not photodegraded even after 120 min of illumination. This result was consistent with the performance evaluated in the batch photo-reactor, in which the propanoic acid conversion was only 10% after 3 hours of illumination and no intermediates were detected in solution. Coordinated formate is preferred on P-25, whereas formate ions form on pure anatase, which is proved by the typical broadening of the  $\nu_a(\text{COO})$ . In general, the surface ATR IR spectra show that P-25 exhibits large similarities with anatase compared with rutile but the former shows more molecular

water evolves on the surface, which tends to displace propanoic acid and hinder the interfacial charge transfer to the adsorbed organic molecules. Lower propanoic acid conversion but higher quantum yield of acetic acid was detected in solution for pure anatase compared with P-25. This suggests that on anatase adsorbed propanoic acid rapidly evolves to acetic acid by photo-Kolbe decarboxylation, which is weakly bonded to the surface and tends to accumulate in solution without further interaction with the catalyst surface. For P-25 the concentration in solution of acetic acid is lower despite the higher conversion of propanoic acid. This indicates that upon illumination the reaction pathways for propanoic acid decomposition involve both the direct hole oxidation and the hydroxyl radical attack and that care must be taken when deriving reaction mechanisms based only on stable intermediate species observed in solution. The presented study highlights that a molecular level understanding of processes occurring at catalytic solid liquid interfaces is of great importance for the rational design of solid catalysed liquid phase reactions. Thus the cell design and the developed protocol with catalysts benchmark to follow photodegradation reactions at solid-liquid interface offers great opportunities for mechanistic investigations of interfacial processes and provide a great basis for future developments.

## **6.2. Future work**

In this thesis, nanostructure titania based catalysts were studied for the application in photocatalysis for water treatment.

Although hierarchical nanostructures have been widely characterized together their unique properties such as increased light harvesting and mass transport, further investigation on charge separation mechanism and adsorption capacity are required to deeply understand all the advantages that these materials can offer in the field of environmental applications.

An interesting future development of this work could be the evaluation of these hierarchical photocatalysts in various photocatalytic reactions such as  $H_2$  production,  $CO_2$  reduction and degradation of different classes of pollutants.

Also modification strategies such as doping, forming hetero-junctions and the loading of suitable co-catalyst could be of great interest since they offer the possibility to develop visible-light photocatalyst. In addition, further studies may include the analysis and determination of possible degradation pathways of pollutants in water by IR spectroscopy techniques. This will contribute to the understanding of the photocatalytic degradation process on the surface of synthesised catalyst in order to develop any possible strategy for the design of a smart photocatalysts.

# *Appendix*

**Figure 1** shows the evolution of formate on the TiO<sub>2</sub> P-25 surface during the irradiation time (2 hours). The black lines refer to the increasing spectra collected at different time (0-60 min), whereas the red line is the last spectrum (120 min) which indicates a decrease in formate adsorbed on the surface following an extended period of irradiation.

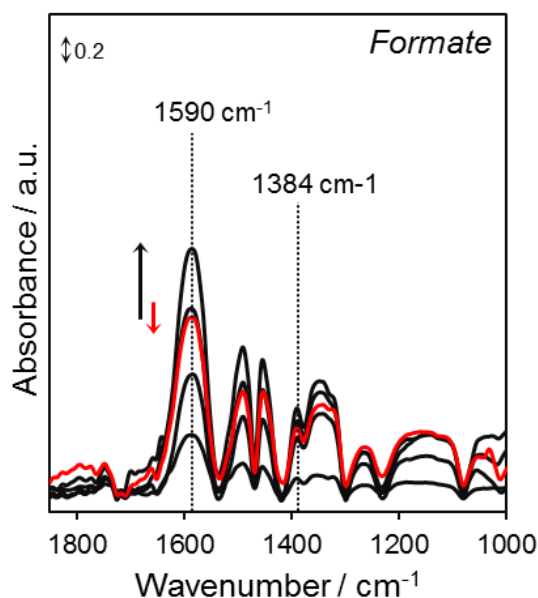


**Figure 1** Evolution during the time of the spectra obtained from the subtraction ( $UV_{\text{time}} - Ads_{\text{dark}}$ ) from flowing propanoic acid over TiO<sub>2</sub> P-25.

**Figure 2** shows the disappearance of peak at  $1712\text{ cm}^{-1}$  (physisorbed acid) which seems to be related to the broadening of the bands at  $1538\text{ cm}^{-1}$ , suggesting that under illumination, the monodentate configuration is gradually converted to propionate. Moreover for extended illumination time the band intensity of adsorbed formate ( $1590\text{ cm}^{-1}$ ) increases at the expense of the propionate, which eventually also starts to disappear after 60 min. The band of formate is much broader compare to the defined and intense peak observed on TiO<sub>2</sub> P-25, suggesting a weak interaction of this species with the catalyst surface.



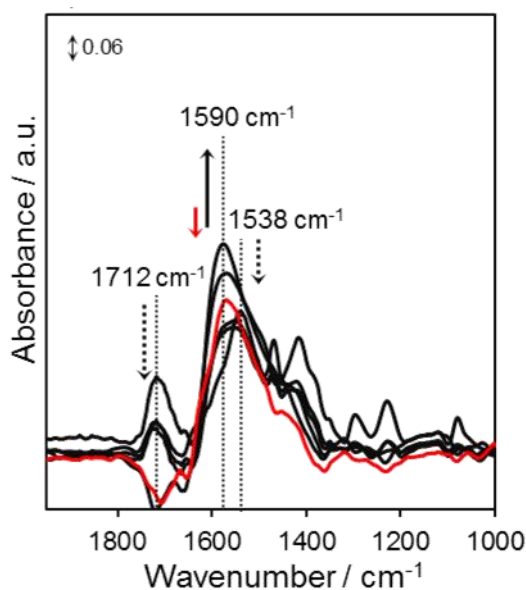


**Figure 2** Evolution during the time of the spectra obtained from the subtraction ( $UV_{\text{time}} - Ads_{\text{dark}}$ ) from the experiment of propanoic acid over anatase.

**Figure 3** shows that the physisorbed monodentate acid (peak at  $1712\text{ cm}^{-1}$ ) gradually disappears and converts to bidentate propionate with the two characteristic bands at  $1538\text{ cm}^{-1}$  and  $1297\text{ cm}^{-1}$ , asymmetric and symmetric stretching respectively. The blue dot indicates the peak at around  $1625\text{ cm}^{-1}$  which is due to the  $\delta(\text{HOH})$  vibrational mode of the small amounts of adsorbed water forming during the irradiation time.

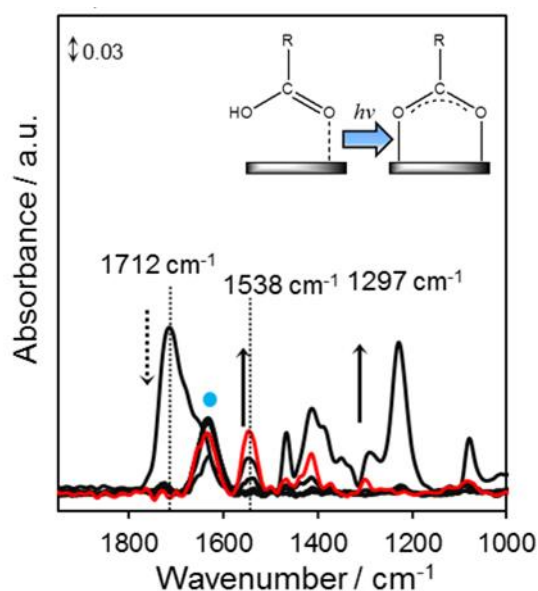


**Figure 3** Evolution during the time of the spectra obtained from the subtraction ( $UV_{\text{time}} - Ads_{\text{dark}}$ ) from the experiment of propanoic acid over rutile.